

The background of the entire cover is a scanning electron micrograph (SEM) of illite shale. It shows a complex, layered, and somewhat fibrous structure with varying shades of gray, representing the mineral's surface morphology.

Chemical Compaction of Illite Shale: An Experimental Study

**by
Rolf H.C. Bruijn**

2012

Zurich, Switzerland

Cover image: a broken surface SE image of PAT1 (C) sample P1328. It shows a high magnification of the characteristic, yet complex microstructure of synthesized metapelite comprised of silty and clayey quartz clasts and occasionally folded ultrafine mica and illite crystals as matrix material.

DISS. ETH NO. 20144

**Chemical compaction of illite shale: An
experimental study**

A dissertation submitted to

ETH ZURICH

for the degree of

Doctor of Sciences

presented by

ROLF HENDRIK CORNELIS
BRUIJN

M.Sc. Earth Sciences,
Utrecht University, the Netherlands

Date of birth 05.05.1983

Citizen of the Netherlands

accepted on the recommendation of

Prof. Dr. Jean-Pierre Burg	examiner
Dr. Philip M. Benson	co-examiner
Dr. Dan Faulkner	co-examiner

This work was financially supported by the Swiss National Science Foundation grants 200020-132772 and 200021-116153, awarded to Prof. Dr. J-P. Burg, Dr. L. Burlini and Dr. S. Misra.

On this thesis rests copyright.

The entire thesis except chapter 4
Copyright © 2012, R.H.C. Bruijn, following ‘Ordinance on Doctoral Studies, art. 34’, issued by ETH Zurich, Switzerland.

Chapter 4
Copyright © 2011, Elsevier B.V., following ‘Journal Publishing Agreement’ issued by Elsevier B.V., the Netherlands, for article “*Mechanical and microstructural development of Carrara marble with pre-existing strain variation*”, with PII-number: S0040-1951(10)00390-2.

Cover and book design: R.H.C. Bruijn

Printed by printenbind.nl, Amsterdam

*Dedicated to Luigi Burlini
may he rest in peace,
and my mother and sisters,
for allowing me to go on this adventure
far away from home*

Table of contents

Abstract	1
Kurzfassung	3
Chapter 1: Introduction	7
<hr/>	
1.1: Literature background	8
1.2: Problem statement	10
1.3: Rationale	11
1.4: Thesis outlook	12
Chapter 2: Sediment compaction	15
<hr/>	
2.1: Compaction kinetics in nature and experiments	16
2.2: Shale/mudstone compaction	24
2.3: Sandstone compaction	28
2.4: Limestone compaction	30
2.5: Very low-grade metamorphism	31
2.6: Rock magnetism	33
Chapter 3: Methods and analytical tools	35
<hr/>	
3.1: Sample preparation and experiments	36
3.2: Compaction apparatus	38
3.3: Data recording and processing for compaction stage 3b	44
3.4: Methods for chemical analysis	47
3.5: Porosity and density measurements	49
3.6: SEM imaging	50
3.7: Magnetic properties	53
Chapter 4: Evaluation of instrumentation precision	57
<hr/>	
Mechanical and microstructural development of Carrara marble with pre-existing strain variation	
4.1: Introduction	59
4.2: Method	61
4.3: Results	65
4.4: Discussion	78
4.5: Conclusions	89
4.6: Acknowledgements	90

Chapter 5: Material: illite shale 91

5.1: Illite shale selection	92
5.2: Physical state of the shales	92
5.3: Mineral phases and microstructure	94
5.4: Porosity/density and pores	98
5.5: Major element composition	100
5.6: Powder grain size	103
5.7: Choice of Maplewood Shale	105
5.8: Geological setting of Maplewood Shale	106

Chapter 6: Chemical model 109

6.1: Phase stability modeling	110
6.2: Pseudosection	110
6.3: Water dependency	112
6.4: Dehydration and dehydroxylation	114
6.5: Summary	115

Chapter 7: Results 117

7.1: Porosity and density	118
7.2: Finite volumetric strain	119
7.3: Finite sample deformation	120
7.4: Mechanical data and rheology	121
7.5: Chemistry	125
7.6: SEM mineral phase characterization	127
7.7: Microstructures	130
7.8: Pores	132

Chapter 8: Magnetism 135

Chemical compaction of illite shale powder: magnetic characterization	
8.1: Introduction	137
8.2: Method	137
8.3: Results	139
8.4: Discussion and conclusions	143
8.5: Acknowledgements	145

Chapter 9: Discussion 147

9.1: Porosity and density	148
9.2: Accommodation of finite volumetric strain	150
9.3: Sample deformation path	151
9.4: Deformation mechanisms	153
9.5: Chemistry	156
9.6: Microfabric elements	157

10.1: Problem statement	162
10.2: Main findings	163
10.3: Conclusions	164
10.4: Recommendation for further research	165
References	169
Appendix A: List of physical quantities and established constants	187
Appendix B: List of compaction stage 3b experiments	190
Appendix C: Sample properties after compaction stage 2 and 3a	192
Appendix D: Sample properties after compaction stage 3b experiments	194
Appendix E: KFT water content	196
Acknowledgements	199
Curriculum Vitae	201

Abstract

Sediment diagenesis has been classified nearly a century ago as a key process for the formation of rocks. In response to burial by overlying younger deposits, both mechanical and chemical processes contribute to the compaction and consolidation of sediments, the degree of which is controlled by both intrinsic and extrinsic parameters such as time, effective pressure, temperature, mineral composition and grain size distribution. Rock physical properties are strongly affected by clay diagenesis. So far, only the mechanical processes during clay diagenesis that dominate in the top 2-3 km of the sedimentary column have been simulated in the laboratory. However, studies on natural shales and mudstones have also emphasized the importance of chemical processes for diagenesis, although occurring in deeper domains and controlled more by temperature than by effective stress. Foreland basins are typical examples of a tectonic setting where sediments are buried deep enough for the activation of chemical processes. The effect of tectonic forces (deformation) on diagenesis is however enigmatic and to date poorly constrained by experimental simulation. The present study simulates the chemical processes in the laboratory and examines how tectonic forces affect compaction processes that transform porous illite shale powder into compact crystalline metapelite.

The experimental compaction procedure consists of three stages. In the first compaction stage, dry illite shale powder (originating from Maplewood Shale, New York, USA) was mechanically compacted in a hydraulic cold-press with a vertical load of 200 MPa. The second stage employed a hot isostatic press (HIP) set at 170 MPa confining pressure and 590 °C, and ensured powder lithification. In the final stage, further compaction was achieved by either repeating HIP treatment or by performing confined deformation tests in a Paterson-type gas-medium apparatus. During the second HIP event temperature and pressure were set at 490 °C and 172 MPa. In the Paterson apparatus three different stress regimes were applied: confined compression, confined torsion or isostatic stress. For the first two regimes, deformation was enforced by applying a constant strain rate ranging from 7×10^{-6} to $7 \times 10^{-4} \text{ s}^{-1}$. Experiments were performed at 300 MPa confining pressure and a fixed temperature of 500 °C, 650 °C, 700 °C or 750 °C. These conditions were chosen from a thermodynamic forward simulation of the stability of mineral phases. In some Paterson apparatus tests, the effects of fluid availability and effective pressure were tested by respectively venting the sample or applying a 50 MPa argon pore pressure.

Lithified samples were analyzed for their microstructural, chemical and physical development with compaction using scanning electron microscopy, Karl Fisher Titration, X-ray diffraction and gas pycnometry. Sample strength evolution was recorded during Paterson apparatus tests and strain measured afterwards. The magnetic signature of the compacting metapelites was quantified by measuring low and high-field anisotropy of magnetic susceptibility (AMS), and the ferrimagnetic contributions were identified using rock magnetic methods.

The three-stage compaction resulted in synthetic metapelites ranging in porosity from 1.0 % to 17.1 %. Linear increase in density and strong correlation between volumetric strain and pore reduction indicate that compaction was accommodated primarily by pore space closing. In deformation experiments axial strain was accommodated first by uniaxial shortening following pore collapse and later by radial extension, which in some cases resulted in total decompaction. Illite transformation to phengite and fluid assisted mass transfer resulted in diffusion creep type strain accommodation. Mechanical pore closing is characterized by pronounced compaction hardening and partial pore recovery upon unloading. Porosity reflects the progress of illite transformation, which is accompanied by enhanced mica alignment and shape preferred authigenic quartz. The AMS signal carried by the phyllosilicates increases linearly with compaction, quantifying the development of texture and reflecting illite preservation. Deformation structures accommodate strain as alternative to exhausted or delayed pore space reduction processes. The smallest visible pores in SEM, associated with illite flakes, diminished as compaction progressed; larger pores were preserved.

Chemical compaction can be simulated in the laboratory provided mineral transformation processes are sufficiently enhanced. In this, differential stress (tectonic force) acts merely as accelerant. There is no evidence for otherwise altered fabric and porosity/density development with the application of differential stress, in comparison with isostatically compacted metapelites.

Kurzfassung

Die Sedimentdiagenese gilt schon seit fast einem Jahrhundert als Schlüsselfaktor für die Gesteinsbildung. Mechanische und chemische Prozesse führen zu einer Kompaktion und Konsolidation der Sedimente aufgrund von Überlagerung durch jüngere Sedimente. Dieser Prozess wird durch innere und äussere Parameter wie effektiver Druck, Temperatur, Mineralzusammensetzung und Korngrößenverteilung kontrolliert. Die physikalischen Eigenschaften toniger Sedimente verändern sich während der Diagenese sehr stark. Bis anhin wurde im Labor nur die mechanischen Prozesse während der Diagenese von Tonsedimente simuliert. Studien über natürliche Tonsteine jedoch heben die Wichtigkeit chemischer Prozesse während der Diagenese vor allem in tieferen Lagen hervor, welche hauptsächlich von der Temperatur und weniger vom effektiven Druck kontrolliert wird. Vorlandbecken sind typische Beispiele für tektonische Settings, wo Sedimente tief genug versenkt werden, um chemische Prozesse zu aktivieren. Der Einfluss tektonischer Kräfte (Deformation) auf die Diagenese ist jedoch weitgehend unbekannt und bis jetzt experimentell nur wenig untersucht. Diese Studie simuliert die chemischen Prozesse der Diagenese im Labor und untersucht, wie sich tektonische Kräfte auf Kompaktionsprozesse auswirken, bei denen porenreiches Illitpulver in kompakte kristalline Metapelite umgewandelt wird.

Die experimentelle Kompaktion besteht aus drei Schritten: Im ersten Kompaktionsschritt wurde das trockene Illitpulver (Material aus Maplewood Shale, New York, USA) mechanisch in einer hydraulischen Presse bei Raumtemperatur mit einer vertikalen Belastung von 200 MPa verdichtet. Für den zweiten Schritt wurde eine Sinter-HIP-Kompaktanlage (HIP) mit 170 MPa Druck und 590 °C verwendet. Dieser Schritt garantiert die Lithifizierung des Pulvers. Eine stärkere Kompaktion im letzten Schritt wurde entweder durch Wiederholung des zweiten Schrittes mit der HIP oder durch Deformationstests in einem Apparat vom Typ Paterson erreicht. Im zweiten HIP-Durchgang wurden Temperatur und Druck auf 490 °C und 172 MPa eingestellt. Mit dem Paterson-Apparat wurden drei verschiedene Belastungszustände getestet: Kompression, Torsion oder Druck. Die Proben wurden für die ersten beiden Zustände mit einer konstanten Verformungsrate zwischen $7 \times 10^{-6} \text{ s}^{-1}$ und $7 \times 10^{-4} \text{ s}^{-1}$ deformiert. Die Experimente wurden bei 300 MPa Druck und bei konstanten Temperaturen von 500 °C, 650 °C, 700 °C oder 750 °C durchgeführt. Diese Bedingungen wurden aufgrund eines thermodynamischen Modells gewählt, das die Stabilitäten der Mineralphasen berechnet. Bei einigen Tests mit dem Paterson-Apparat wurde der Einfluss von Fluiden und effektivem Druck getestet.

Die lithifizierten Proben wurden auf mikrostrukturelle, chemische und physikalische Veränderungen mit zunehmender Kompaktion analysiert. Die Analysen wurden mit dem Rasterelektronenmikroskop, Karl-Fischer-Titration, Röntgenbeugung und einem Pyknometer durchgeführt. Die Veränderung der Probenfestigkeit wurde während der Tests im Paterson-Apparat ermittelt und die Deformation jeweils nachträglich bestimmt. Das magnetische Gefüge des kompakten

Metapelites wurde als magnetische Anisotropie (AMS) in hohem und tiefem magnetischem Feld gemessen und der ferromagnetische Beitrag mit Hilfe von petromagnetischen Methoden identifiziert.

Mit diesem Drei-Schritte-Kompaktionsverfahren wurden Metapelite mit einer Porosität von 1.0% bis 17.1% hergestellt. Die lineare Zunahme der Dichte und eine starke Korrelation zwischen Volumenänderung und Porenreduktion weist darauf hin, dass die Kompaktion primär auf Porenschliessung zurückzuführen ist. In den Deformationsexperimenten ging die axiale Belastung anfänglich mit uniaxialer Verkürzung einher, gefolgt vom Schliessen der Poren und anschliessender radialer Extension, die in einigen Fällen in totaler Dekompaktion resultierte. Die Transformation von Illit zu Phengit und der fluid-unterstützte Massentransfer resultierten in Verformung durch Diffusionskriechen. Die mechanische Porenschliessung hingegen ist charakterisiert durch starke Kompaktionsverfestigung und teilweise Porenerholung nach der Entlastung. Die Porosität spiegelt den Prozess der Illittransformation wider, welche von erhöhter Glimmereinregelung und Neuwachstum von Quarz mit Kornformregelung begleitet wird. Das AMS-Signal der Phyllosilikate steigt linear mit zunehmender Kompaktion an, quantifiziert die Entwicklung der Struktur und gibt die Illiterhaltung wieder. Die Deformationsstrukturen entstehen als Alternative zu abgeschlossenen oder verzögerten Poren-Reduktionsprozessen.

Die kleinsten unter dem SEM erkennbaren, mit Illitplättchen assoziierten Poren verringerten sich während des Kompaktionsprozesses; grössere Poren blieben erhalten.

Die chemische Kompaktion kann im Labor unter der Voraussetzung simuliert werden, dass die Mineraltransformationsprozesse genügend beschleunigt werden. Die Anlegung einer differentiellen (tektonischen) Spannung wirkt dabei beschleunigend. Es gibt keinerlei Anzeichen dafür, dass sich davon abgesehen das Gefüge und die Porosität/Dichte unter differentieller Belastung anders entwickeln als bei isostatischer Kompaktion.

Chapter 1

Introduction

James Oppenheim once said, "The foolish man seeks happiness in the distance, the wise grows it under his feet."

Preface

This first chapter sets the stage on which this thesis is based, describing the study undertaken to better understand the compaction of illite shale, an important sedimentary rock type. I begin by providing a historical overview of past studies on this topic followed by formulation of the main questions and rationale for the designed approach. In the literature background subchapter (1.1) the reader is acquainted with the 19th century work of Sorby, the importance of multi-disciplinary collaboration and exchange of knowledge, exemplified by the application of theories developed in soil mechanics (e.g. by Terzaghi; Casagrande; Skempton and Burland) for understanding clay compaction, and the coupling between clay diagenesis and oil migration. The second subchapter (1.2) describes the problem addressed in the present study in the form of two questions that arose from the present day limitations of experimental and numerical models. Previous work has shown that the correlation between nature and laboratory analogues is generally good in the case of purely mechanical compaction. However, chemical processes, despite numerous natural studies that demonstrate their importance, are poorly known, and with few- if any laboratory controls. In a different view, numerical models that have incorporated tectonic non-vertical stresses show best correlation with nature. In particular, experimentally-derived constraints of rheological parameters routinely included in basin models are under developed. Subchapter 1.3 concludes with the rationale for the experimental set-up and chosen conditions to test gaps in the current state of knowledge. Specifically, chemical compaction within laboratory timescales is achieved by thermally accelerated clay transformation rates. The illite-phengite transition is favored as reaction of interest over the smectite-illite transformation because of the larger extent of phengite stability. The applied pressures were chosen to avoid brittle failure during compression tests and prevent unwanted slip in torsion tests. The chosen deformation styles are inspired by sandstone compaction studies and add a new approach to experimental clay compaction.

1.1: Literature background

One of the fundamental and oldest questions in geology deals with the genesis of rocks. Rocks are classified into three categories: 1) sedimentary, formed after lithification of deposited loose material, 2) igneous, formed from the cooling of magma and 3) metamorphic, sedimentary and igneous rocks modified to be adapted to altered environmental conditions. In this thesis, the kinetics and chemical processes leading to the lithification of clay-rich sedimentary rocks are addressed. Such rocks and the structures they exhibit, have inspired scientists for centuries to unravel their origin. The earliest laboratory based experiments date back to 1859, when Sorby simulated the deposition of sand and mica flakes in a jar filled with water [Sorby, 1908]. He stated that water expulsion may reduce the volume fraction by a factor of 9 for shales and slates to form, but only slightly reduce in the case of the compaction of sandstone and siltstone. He recognized that compaction of sediments is primarily due to the change in porosity and linked pressure and porosity reduction. Herein lies the key observation that founded the principles behind many laboratory and field-based studies investigating the origin of sedimentary rocks. More recently, some structures in sediments were attributed to sediment compaction [e.g. Shaw and Munn, 1911; Shaw, 1918; Blackwelder, 1920; Powers, 1920; 1922; Monnett, 1922; Teas, 1923]. Among the first to provide experimental data on factors that influence clay compaction, such as water content, permeability, shrinkage, swelling, plasticity, elasticity and compressibility was Charles Terzaghi [Terzaghi, 1925]. His experimental work [Terzaghi, 1925; 1927] and that of others [Sorby, 1908; Casagrande, 1932a; Skempton and Jones, 1944], and porosity data obtained from well log data [Hedberg, 1926; Athy, 1930] inspired the development of clay compaction models [Athy, 1930; Hedberg, 1936; Weller, 1959; Vassoevich, 1960; Aoyagi and Asakawa, 1980] and best fits mathematical compaction curves [Hedberg, 1927; Rubey, 1927; Athy, 1930]. However, the reliability of the latter was questioned due to the complex nature of compaction processes [Hedberg, 1936; Velde, 1996] and the importance of mineral composition on compaction curves in the laboratory [Skempton and Jones, 1944]. In compaction models, porosity decreases when free adsorbed water is expelled from the pore space and solid particles rearrange and pack more closely. Below approximately 10 % porosity, further compaction is required, either by solution and recrystallization [Hedberg, 1936; Aoyagi and Asakawa, 1980] or solid grain deformation of non-clay particles [Weller, 1959]. It took some decades and the advent of advanced equipment for chemical analysis before the chemical processes in Hedberg's compaction model were coupled to the smectite to illite transition and associated water release [Powers, 1967; Burst, 1969]. Poor correlation between empirical and natural compaction curves called for compaction tests at pressure conditions comparable with nature, tests on undisturbed samples rather than slurries, and technological advances in porosimetry [Jones, 1944; Skempton and Jones, 1944; Hubbert and Rubey, 1959; Rubey and Hubbert, 1959].

Previously, the Atterberg limits, named after the Swedish chemist, were introduced for the characterization of the plasticity and quantification of compositional variation among soils [Kinnison, 1915; Casagrande, 1932b]. The liquid limit (LL) is the moisture content at which the soil flows viscously when agitated. Similarly, the plastic limit (PL) defines the moisture content above which clay behaves plastically. Combining these yields the plasticity index (PI) that defines the difference between the Atterberg limits. Clays typically have PI values of 20 to > 40, whereas lower PI values are found for sands and silts [after Skempton and Jones, 1944; White, 1949]. At the time of deposition, clays are typically at, or very close to, their liquid limit [Terzaghi, 1927; Skempton and Jones, 1944]. With increasing overburden load, water is expelled and the clay becomes plastic; further pressurization causes the material to become brittle below its PL. This behavior is directly related to the porosity evolution with depth. Empirically derived compaction curves and those obtained from well logs display a first order dependence on the Atterberg limits, confirming the coupling between compaction and the clay-size fraction and clay species [e.g. Skempton and Jones, 1944; Skempton, 1953; 1970; Olson and Mitrovas, 1962]. However, Weller [1959] argued that the standardized tests for the determination of the Atterberg limits may not represent salt-water-submerged clay deposits. High-pressure clay compaction studies showed the importance of saline solution on compaction [von Engelhardt and Gaida, 1963; Warner, 1964], confirming Weller's earlier hypothesis, and revealing that the salinity of expelled fluids changes with overburden pressure [Chilingar and Knight, 1960; Chilingar et al., 1963; Rieke et al., 1964; Chilingarian and Rieke, 1968; Chilingar et al., 1969; 1973; Rosenbaum, 1976]. At about the same time, the link between fluid expulsion during compaction and petroleum migration [e.g. Chilingar, 1961; McAuliffe, 1966; Chilingarian and Rieke, 1968; Dickey, 1975] was also proposed. Two requirements for petroleum migration into reservoir rocks were identified: 1) the release of interlayer water during smectite illitization and 2) effective pressures should be high enough for fluid flow in low permeability source rock [e.g. Chilingar and Knight, 1960; Powers, 1967; Burst, 1969; Perry and Hower, 1972]. Despite this advance, however, the precise mechanism of petroleum migration out of clay-rich source rocks remained enigmatic [Aoyagi et al., 1985].

The development of physical properties during clay diagenesis remained somewhat enigmatic and further experimental clay compaction studies were undertaken, addressing not only the development of rheological, thermal and hydraulic properties [e.g. Jones and Addis, 1986; Vasseur et al., 1995; Dewhurst et al., 1998; 1999; Pouya et al., 1998; Mondol et al., 2007; Schneider et al., 2011], but also that of microstructure [Djéran-Maigre et al., 1998; Fawad et al., 2010] and texture [Baker et al., 1993; Voltolini et al., 2009]. In the meantime, chemical and physical characterization and microstructural imaging of natural mudstones and shales continued to stress the importance of the smectite-illite transformation during diagenesis of clay-rich sediments [e.g. Tribble et al., 1991; Lynch et al., 1997; Kim et al., 1999; Aplin et al., 2003; 2006; Charpentier et al., 2003; Thyberg et al., 2010; Day-Stirrat et al., 2010].

Since the mid-1980's, advances in basin modeling shifted the focus from well log and laboratory studies to computer simulations [e.g. *Bethke*, 1985; *England et al.*, 1987; *Ungerer et al.*, 1990; *Audet and Fowler*, 1992; *Audet and McConell*, 1992; *Hart et al.*, 1995; *Luo et al.*, 1998; *Pouya et al.*, 1998; *Suetnova and Vasseur*, 2000] that were primarily based on 1) mathematical relationships between porosity and effective pressure derived by *Athy*, [1930] subsequently improved by *Smith* [1971], *Shi and Wang* [1986] and *Schneider et al.* [1996], 2) soil consolidation equations and critical state theory in *Lambe and Withman* [1969], 3) Biot's theory of poro-elasto-plasticity [1941] as developed by *Coussy* [1991], 4) the Cam-Clay elasto-plastic model [*Burland*, 1990] or 5) visco-elastic rheology. *Karig and Hou* [1992], *Luo et al.* [1998] and *Pouya et al.* [1998] questioned the accuracy of these predominantly one-dimensional models, and stated the importance of non-vertical tectonic stress for accurate modeling of compaction down to a few kilometers depth (or 50 MPa effective pressure).

1.2: Problem statement

More than fifty years of experimental clay compaction has resulted in a general agreement between nature and models, regarding the mechanical aspects of compaction (i.e. up to 50 MPa effective stress or 2-3 km depth) [e.g. *Shi and Wang*, 1986; *Vasseur et al.*, 1995; *Mondol et al.*, 2007; *Peltonen et al.*, 2009]. However, processes occurring in the deeper levels of sedimentary basins are dominated by chemical processes such as illitization and dissolution/precipitation, rather than grain rearrangement and orientation (i.e. mechanical processes) [e.g. *Van der Pluijm et al.*, 1998; *Ho et al.*, 1999; *Aplin et al.*, 2006; *Day-Stirrat et al.*, 2008; *Thyberg et al.*, 2010]. To date, the problem of deep clay compaction is mostly addressed in the light of burial and vertical overburden loads. Discrepancies between nature and 1-D numerical simulations demonstrate the limits of this perhaps overly-simplistic approach [e.g. *Aplin and Vasseur*, 1998; *Luo et al.*, 1998]. *Pouya et al.* [1998] demonstrated the power of 3-D models that implement horizontal (tectonic) stress in their calculations, albeit restricted to mechanical compaction in the top 3 km of the basin infill.

These processes are clearly not well understood. However, they are crucial to improve modeling/simulation of basin development and diagenesis. As an example, the increasing awareness of the influence of illitization upon the development of physical properties and fabric during clay diagenesis emphasizes the scientific necessity for laboratory simulation of chemical compaction [*Bjørlykke and Høeg*, 1997]. It was previously believed that the reaction kinetics for clay transformation were too slow for laboratory simulations [*Nygård et al.*, 2004; *Mondol et al.*, 2007; *Fawad et al.*, 2010].

This thesis reports the first experiments designed to replicate mechanical and chemical compaction of illite-rich sediment under conditions typical of deep sedimentary systems. Two main questions are posed:

1. Can chemical compaction of clay sediments be simulated in the laboratory?
2. How does the stress regime affect clay compaction?

1.3: Rationale

Chemical compaction of clay-rich sediments is achieved by accelerating the transformation of illite to phengite. Experiments performed at conditions beyond the stability field of illite are therefore required.

Firstly, phase stability modeling of the phyllosilicates is used to select the temperature conditions during compaction tests. In the chosen temperature range (500-750 °C), stability fields for illite (< 300 °C) and phengite (< 675 °C) are traversed and partial melting is even expected (at > 710 °C). In terms of equilibrium mineral assemblages and reactions, these temperatures represent lower crustal conditions. However, as experimental compaction tests are relatively short (timescale of hours), phase equilibrium will not be achieved and several reactions are active simultaneously. The activity of chemical reactions typically increases with temperature. Hence, reactions that occur at low temperatures are more active (i.e. higher rates) and progress further than reactions that depend on high temperature. The high temperatures employed in this study, although not strictly realistic, speed up those reactions most relevant for the simulation of deep basinal processes, so that they can be studied in the laboratory. Other reactions may be triggered as well, but will be too slow to have a significant impact in the short-lived experiments.

This experimental study utilizes the illite to phengite transition over the smectite to illite transition as the reaction of interest. The temperature range for which illite and phengite are stable is much wider for phengite than for illite. For smectite illitization to proceed with laboratory time scales temperature well within the phengite stability field are deemed necessary. Simultaneous illite and phengite formation would unnecessarily complicate the analysis and interpretation of the effect of chemical processes on shale burial.

Finally, although the effective pressures applied in this study (170-300 MPa) exceed those typically associated with ~10-18 km deep basins, such pressures were needed to avoid brittle failure during deformation tests. From the Mohr-Coulomb criterion, it is generally accepted that rocks strengthen with increasing pressure. Moreover, higher pressure prevents unwanted slip between assembly spacers in torsion tests. It is justified to work with such pressures for two reasons. 1) The rate of mechanical compaction (i.e. porosity/stress) decreases logarithmically with stress [e.g. *Rieke and Chilingarian, 1974; Mondol et al., 2007*]; beyond 170 MPa, hardly any mechanical compaction is

expected. 2) Phase stability modeling revealed that the mineral reactions of interest are mostly temperature dependent. Downscaling of the experiment conditions to basin settings is therefore only needed for the temperature, and can be done in a trade-off with geological time over laboratory time. Depressurization is not expected to result in new mineral reactions. Working at higher confining pressures than 170 and 300 MPa with the available machinery is technically challenging due to an increased likelihood for jacket failure or puncture, as well as machine pressure vessel and load cell limits.

Ideally, the effect of tectonic stress on compaction is addressed by applying a true triaxial stress field ($\sigma_1 > \sigma_2 > \sigma_3 > 0$), where the overburden load is either one of the principal stress directions. Regrettably, machinery capable of such stress regime combined with a high temperature furnace is not available. Instead, different stress regimes were chosen for the compaction of illite shale. The significance of the orientation of the stress field can then be evaluated directly by comparing the end products. In analogue with sandstone compaction tests [e.g. *Wong et al.*, 1997; *Wu et al.*, 2000], compaction by isostatic stress and by confined compression was compared. Compaction by high strain twisting of the sample in confined torsion [e.g. *Paterson and Olgaard*, 2000] was attempted to address the effect of shear geometry (simple vs. pure shear).

1.4: Thesis outlook

The thesis is organized in ten chapters and includes 5 appendices. After the introduction chapter (1), an overview of the state of knowledge of sediment compaction is presented in chapter 2. The kinetics of compaction in both nature and experiments are discussed. A short description of the complexity of the Appalachian foreland basin in the U.S.A. is presented as example of a tectonic setting in which sediment compaction plays an important role. The illite shale used in this study originates from this basin. Compaction of different sedimentary rock types is separately discussed in following subchapters, focusing on shales and mudstones, and demonstrating that compaction is different for these lithologies. Other topics discussed in the background chapter are low-grade metamorphism and rock magnetism.

This study employed a range of compaction apparatus and analytical devices. Chapter 3 describes the used methods, analytical techniques, preparation procedures, and data processing calculations. In addition, the three-stage compaction procedure is described. Chapter 4 presents a paper on the precision of one of the employed instruments. The main topic of this paper is the effect of pre-existing strain on calcite flow behavior, but essentially incorporates an evaluation on machine precision.

The natural illite shale used in this study is presented in chapter 5. Argumentation is given for why Maplewood Shale was ultimately selected over two other shales. The microstructure and geological setting of Maplewood Shale is presented as example of natural shale.

The following chapter (6) deals with the chemical model that was developed to forecast the mineral reactions during the experiments. The chapter focuses on the constructed pseudosections, and discusses the role of phyllosilicate dehydration and dehydroxylation.

Chapter 7 presents the results of the compaction tests. First, porosity and density data are presented, followed by strain measurements, strength evolution and rheological data. Chemical observations are then presented, as are SEM images, microstructures and pores. Chapter 8 presents the paper that was submitted to *Geology* in October 2011. This paper deals with the development of magnetic properties during the experimental compaction of illite shale.

Chapter 9 discusses the results of the compaction experiments. In six subchapters, porosity and density, volumetric strain, deformation paths and mechanisms, chemistry and microfabric elements are discussed. The final chapter (10) concludes the thesis by providing the conclusions and by describing recommendations for further research.

In the five appendices, a list of physical quantities and constants (A) is given, as are lists of the compaction stage 3b experiments (B). Sample properties such as porosity, density, strain and water content, after various compaction stages and experiments are presented in appendices C, D and E.

Chapter 2

Sediment compaction

Gerry Spence once said, "I would rather have a mind opened by wonder than one closed by belief."

Preface

To follow a discussion on clay compaction it is imperative to understand how sediment compaction in general works. This chapter provides the required basic knowledge. Subchapter 2.1 discusses the kinetics of compaction in both nature and experiments, including those performed in this study. Compaction is inherently related to sedimentary basins and tectonics. The Appalachian Basin in New York state (USA) is a classic example of a sedimentary basin that is strongly influence by orogenies, sea level fluctuations and changes in sediment influx. The complex basin infill exemplifies the necessity for a good understanding of the diagenesis processes that affect all sorts of sediments. A summary of the state of knowledge of shale/mudstone compaction follows in subchapter 2.2, of sandstone compaction in subchapter 2.3 and of limestone compaction in subchapter 2.4. This chapter concludes with a short discussion on very low-grade metamorphism (2.5) and rock magnetism (2.6). As pressure and temperature conditions change with depth, so do minerals, especially the phyllosilicate clays. Diagenesis is typically classified in metapelitic zones, based on the progress of clay transformation reactions derived from classic sedimentary sequences. Rock magnetism provides alternative method to quantify texture development in rocks. In this study, two techniques to measure the anisotropy of magnetic susceptibility were performed. Additionally, the identification of ferrimagnetic mineral phases was attempted using techniques that measures remanence magnetization. In the final subchapter theory behind rock magnetism is presented.

2.1: Compaction kinetics in nature and experiments

Compaction affects porous materials, in particular sediments. Due to strong significance in hydrocarbon exploration and production, most studies dealing with sediment compaction are performed in, or in the context of sedimentary basins [e.g. *Rieke and Chilingarian, 1974; Lerche, 1990; Hantschel and Kauerauf, 2009*]. As such, natural compaction is typically associated with kinetics found in sedimentary basins. Compaction is more complex at active plate boundaries where crustal thickening or thinning imposes tectonic forces. In for example foreland basins compaction is expected to be controlled by both by burial-related kinetics and by active tectonics.

Nature:

Stress fields within sedimentary basins are controlled by sedimentation, erosion and tectonics. Sediments impose a gravity load on older buried deposits, represented by lithostatic pressure (p_l). With depth lithostatic pressure increases linearly following equation 2.1:

$$p_l = g \int_0^{h_w} \rho_{sea} dz + g \int_{h_w}^h \rho_b dz \quad (\text{eq. 2.1})$$

See table A1 for a description of the involved quantities. Sea level defines zero depth. As a scalar, lithostatic pressure has no direction. The stress resulting from gravity load is directed vertically (σ_v) and horizontally (σ_h), when considering fixed side boundaries to a body of compacting sediments (i.e. no free surface). The material constant Poisson ratio (ν) relates σ_h to σ_v through equation 2.2:

$$\frac{\sigma_h}{\sigma_v} = \frac{\nu}{(1-\nu)} \quad (\text{eq. 2.2})$$

Poisson ratio values for sediments range from 0.1 to 0.4, which yields a stress ratio of 0.11 to 0.67, indicating that σ_h is generally smaller than σ_v . When σ_h is equal in all horizontal directions, the stress field approximates confined compression (Fig. 2.1A), with vertically oriented maximum principal stress (σ_1) and equal intermediate and minimum principal stresses (σ_2) and (σ_3), respectively placed in the horizontal plane, parallel to σ_h .

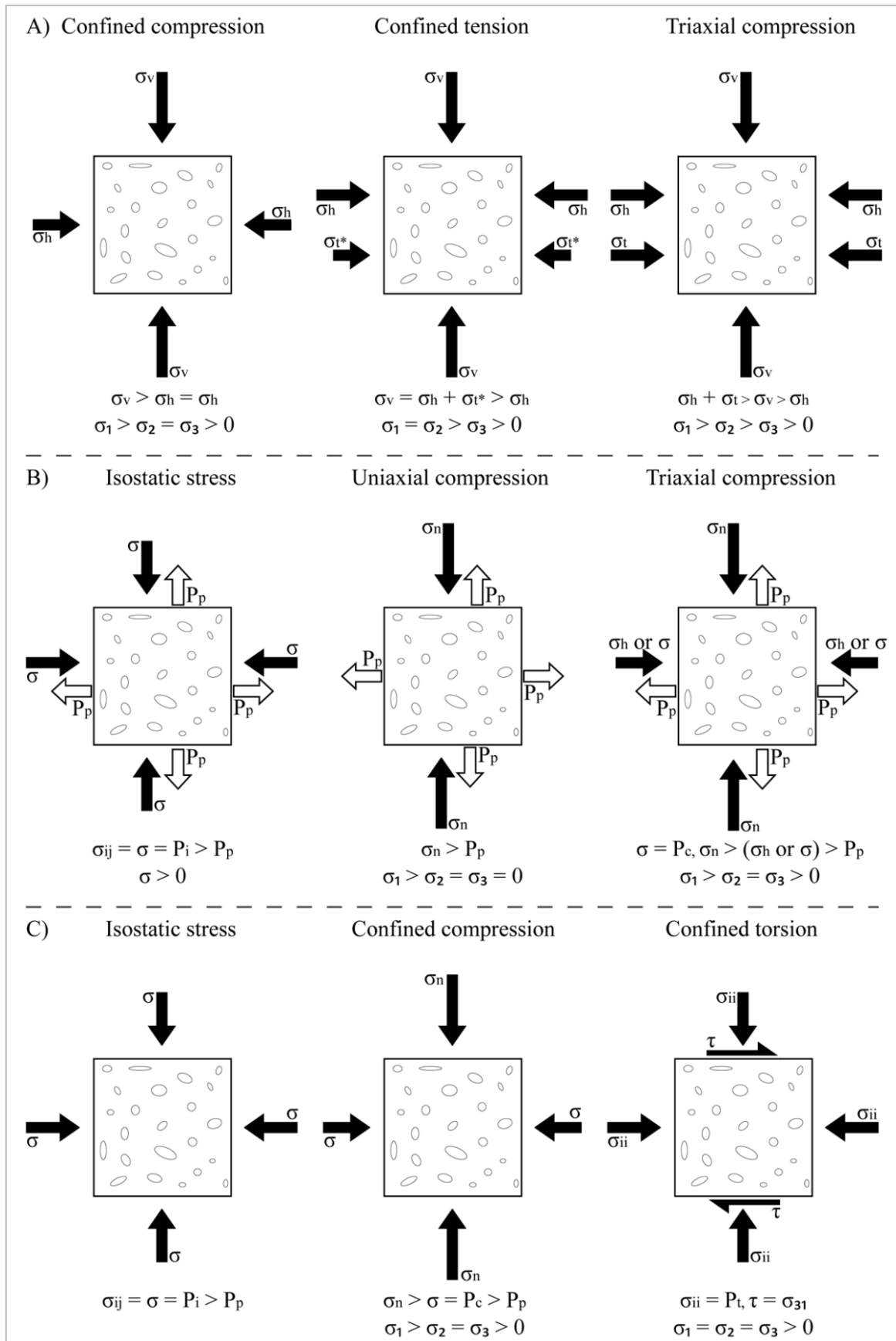


Figure 2.1: A) 2D representation of the kinetics of natural compaction in sedimentary basins. B) Typical stress field employed in experimental compaction studies. C) Three types of stress fields used in this research.

Tectonic compressive forces (F_c) impose a sub-horizontally oriented stress (σ_t) in addition to gravity load driven stress σ_h . At a certain depth (h_{ct}), σ_t may be large enough (σ_t^*) for the sum of the horizontal stresses (σ_H) to increase to a value of σ_v . In such a scenario, σ_H and σ_v are the two largest principal stresses, oriented vertically, and parallel to F_c , while σ_h is the smallest principal stress, oriented normal to F_c in the horizontal plane (Fig 2.1A). Such a stress field defines confined tension.

At shallower depth, σ_v is less than σ_H . The horizontal plane contains the minimum and maximum principal stress directions, σ_h and σ_H respectively, while σ_v is the intermediate principal stress direction parallel to gravity load or burial direction. This stress field describes a triaxial compression.

Depending on the presence of tectonic compressive forces, sedimentary basins experience stress regimes that may be best described by confined compression, confined tension, or triaxial compression with horizontal maximum principal stress direction (Fig. 2.1A).

Previous experiments:

In experimental compaction studies, attempts are made to reproduce basin kinetics. A suite of experimental equipment is available for the measurement of sample volume change with applied stress, from which rock properties (e.g. porosity and permeability) are derived. Typical kinetics employed in compaction experiments include uniaxial compression [e.g. *Chilingar and Knight*, 1960; *Karig and Hou*, 1992; *Vasseur et al.*, 1995; *Dewhurst et al.*, 1998; *Mondol et al.*, 2007; *Zhang et al.*, 2010], isostatic stress [*Zhang et al.*, 1990; *David et al.*, 1994] and triaxial compression [e.g. *Jones and Addis*, 1986; *Wong et al.*, 1997; *Baud et al.*, 2004] (Fig. 2.1B).

Research into compaction is pertinent to the energy resources industry to model sedimentary basins and improve hydrocarbon exploration and extraction. Consequently, focus in experimental compaction studies lies in simulating crustal domains where hydrocarbons are trapped and extractable (i.e. < 3-4 km depth or 100 MPa and 100 °C). In these shallow domains, sediment compaction is mostly mechanical and incomplete. Porosity and permeability remain high. Fluids are abundant and connected to the surface, making them hydrostatically pressurized. Experimental compaction studies incorporate the effect of hydrostatic fluids by impregnating or saturating the unconsolidated sample with a fluid, typically water or a brine solution. The fluid or pore pressure (P_p) affects the stress field following *Terzaghi's* [1925] principal of effective stress (σ'), equation 2.3 and table A1:

$$\sigma' = \sigma_n - P_p \quad (\text{eq. 2.3})$$

In isostatic stress tests (Fig. 2.1B), a confining medium exerts an equal pressure on the sample from all directions. No principal stress directions are identifiable and the stress tensor (σ_{ij}) can be reduced to a scalar (σ). The imposed confining pressure (P_i) is the sole driving force for σ .

Equation 2.3 can be rewritten for the case of isostatic stress resulting in equation 2.4A. To avoid hydrostatic fracturing P_i is typically greater than P_p .

In uniaxial compression tests (Fig. 2.1B), gravity load or overburden pressure is modeled with a mechanical load, resulting in a vertical normal stress (σ_n), that forces a sample to compact in the vertical direction. Low friction walls of the sample chamber inside such an oedometer, keep horizontal stresses at a minimum. Upon compression, the highly porous, fluid-filled and soft nature of the typical sample material allows fluids to extrude through a perforated cap, resulting in a volume loss proportional to compaction or porosity reduction. Imposed P_p reduces σ_n through equation 2.3, with the restriction that $P_p < \sigma_n$.

In triaxial compression tests (Fig. 2.1B), horizontal stresses result from either a vertical load (σ_n) or a pressurized confining medium (P_c). Strictly speaking, the term triaxial is misleading, since the minimum and intermediate principal stresses are equal, as for confined compression. Pore pressure reduces σ_n and σ_h to σ' . This is expressed in equation 2.4B, where σ_{ii} represents the principal stresses or diagonal components in the stress tensor matrix with i allowing values of 1, 2 or 3.

$$\sigma' = \sigma - P_p = P_i - P_p = P_{eff} \quad (\text{eq. 2.4A})$$

$$\sigma'_{ii} = \sigma_{ii} - P_p = P_{eff} \quad (\text{eq. 2.4B})$$

This study:

This experimental compaction study reports compaction tests with three distinct stress regimes: isostatic stress, confined compression and confined torsion (Fig. 2.3C). The latter regime is new compared to previous experimental compaction studies and allows simulation of simple shear deformation in a tectonically active sedimentary basin.

The kinetics of isostatic stress tests (Fig. 2.3C) in this study are comparable with previous experimental compaction studies (i.e. stress has equal magnitude in all directions and stress is a scalar). The here labeled confined compression tests (Fig. 2.3C) are essentially identical to what is commonly perceived as triaxial tests. By the addition of a mechanically induced vertical stress, the direction and magnitude of principal stress axes are defined; σ_1 is vertically oriented, while σ_2 and σ_3 act in the horizontal plane and are equal in magnitude, but greater than zero.

Confined torsion tests (Fig. 2.3C) require a more elaborate description due to their complex kinetics. Instead of a mechanical load, a torque (M) is applied to a confined sample. M acts on the horizontal plane in the sample, normal to the sample radius (r), which implies that the direction of M changes along the circle described by r . Moreover the magnitude of torque varies with r ; zero in the centre and maximum at the rim of the sample. Rheological behavior of the sample material controls the torque distribution with r . Newtonian flow yields a linear torque increase with r , whereas non-Newtonian flow yields an exponential increase of M with r [Paterson and Olgaard, 2000]. In terms of

stress, torque relates directly to shear stress (τ), which is described in matrix notation by the off-diagonal components of the stress tensor. In a 2D cross section at any value for r , M is approximately parallel to σ_{31} . The existence of a non-zero off-diagonal stress tensor component automatically sets the direction of the normal stress components (i.e. diagonal components, σ_{ii}) and principal stress axes. Values for σ_1 , σ_2 and σ_3 are equal and greater than zero, since no mechanical load as in confined compression was applied, instead samples were placed in confined medium.

Confining pressure was applied in this study to provide for σ_3 in all employed stress regimes. Practically, confining pressure is equal in these cases, yet mathematically differences exist. Unique subscripts distinguish between the different confining pressures. P_i , P_c and P_t , respectively denote confining pressure in isostatic stress, confined compression and confined torsion.

Foreland basins: Case study of the Appalachian Basin in Western New York:

This Laurentian continental foreland basin is filled with Paleozoic sediments that show a characteristic sedimentary repetition linked to several orogenic events within the Pangaea-forming Wilson-cycle such as Taconic, Acadian and Alleghenian orogenies [e.g. *Wilson*, 1966; *Fail*, 1997; *Ettensohn*, 2008]. In fact, the Appalachian Basin has formed a cornerstone for the identification and modeling of characteristic foreland basin infill dynamics. A sequence of seven characteristic stratigraphic features in such a system have been coupled to lithosphere processes such as isostatic loading and unloading, and flexural bulging [e.g. *Quinlan and Beaumont*, 1984; *Beaumont et al.*, 1988; *Ettensohn*, 2008], and are summarized here following *Ettensohn* [2008]: 1) basal unconformity due to flexural bulging of the lithosphere, 2) shallow-water transgressive deposits formed at the onset of rapid basin subsidence, comprising either transgressive carbonates or reworked shoreface sand deposits, 3) dark-mud sedimentation as a result of limited sediment influx and oxygen-deprived deepwater environments, 4) flysch-like sedimentation in deepening basin, after development of a drainage network in the sediment source following build-up of a subaerial relief (fold-thrust belt), 5) thin, regressive, shallow-water, carbonate or shale blanket, forming after the basin overflows and sediment influx ceases due to lowered source area, 6) thin, transgressive, marine, precursor sequence, formed in the anti-peripheral bulge that formed due to isostatic rebound of the eroded orogen, and 7) marginal-marine and terrestrial clastic wedge comprised of re-deposited basin sediments and material from the rebounded orogen and formed in a terrestrial delta-like environment.

Stratigraphic features of this foreland basin infill model can be identified in the Middle Ordovician to Early Silurian sediments of the Northern Central Appalachian Basin of Western New York State (Figs. 2.2 and 2-3), coupled to the Taconic orogeny. The basal unconformity is represented by the erosional contact between Trenton group platform/lagoonal carbonates and underlying crystalline basement of the Greenville craton (now exposed in the Adirondack Mountains) [*Jacobi*, 1981; *Ettensohn*, 2008]. Trenton group carbonates (Middle Ordovician) themselves represent the first deposits in shallow water in the newly formed Taconic peripheral foreland basin [*Rowley and Kidd*,

1981; *Bradley and Kidd*, 1991; *Brett and Baird*, 2002; *Ettensohn*, 2008]. Maximum burial depth estimates for Trenton group carbonates in northeastern New York State yielded values of 5.0 km [*Friedman*, 1987]. Overlying the Trenton group are siliciclastic deposits of the Late Ordovician Lorraine group, which includes the Eastern New York Utica black shales and Martinsburg slate, coupling the Lorraine group to the third characteristic foreland basin infill feature of dark-mud sedimentation [*Ettensohn*, 1991; *Lehmann et al.*, 1995]. Deposited directly above the Lorraine group are fluvio-deltaic sediments of the sandy Oswego [*Fichter and Diecchio*, 1986] and red beds of the Late Ordovician Queenston Formation [*Brogly et al.*, 1998], attributed to the final stage clastic wedge feature in the foreland basin infill model of *Ettensohn* [2008]. Late Ordovician to Early Silurian clastic wedge deposits, containing 1200-950 Ma detrital zircons, have been traced back to the Grenville craton, indicating its exposure since at least the Late Ordovician [*Gray and Zeitler*, 1997; *Park et al.*, 2010].

By Late Ordovician, the main phase of the Taconian orogeny had waned. Yet, rejuvenation of the Taconic orogeny occurred in the Early Silurian, and is visualized by the regionally extensive, low-angle Cherokee Unconformity at the Ordovician-Silurian boundary, followed by thick clastic wedge deposits of the Medina and Lower Clinton group (including Maplewood Shale) [*Brett et al.*, 1990] (Figs 2.2 and 2.3). These two groups form a sequence that onlaps on the Cherokee Unconformity in eastward direction, indicating renewed basin subsidence [*Brett et al.*, 1990].

Around the Early-Late Silurian boundary, a phase of tectonic inactivity or quiescence commenced [*Brett et al.*, 1990], which would last until the Devonian Acadian orogeny. Basin subsidence and sediment influx reached a state of equilibrium, making the depositional system most sensitive to eustatic and regional sea-level variation [*Johnson et al.*, 1985; *Cotter*, 1988; *Brett et al.*, 1990]. Basin wide repetitive contemporaneous facies of the Silurian Medina, Lower and Upper Clinton, and Lockport groups have been correlated using 3rd order (2-3 myr) and superimposed 6th order (~ 100 kyr) sea level cycles [*Johnson et al.*, 1985; *Cotter*, 1988; *Brett et al.*, 1990]. Despite ongoing subsidence, alternating shale and limestones formation in the Lower Clinton group of Western New York (Figs. 2.2 and 2.3) display 3rd order sea level cycles, which is explained by eustatic sea level fluctuations associated with Gondwana glaciation [*Johnson et al.*, 1985; *Brett et al.*, 1990].

The Paleozoic infill of the Appalachian basin in Western New York clearly demonstrates the complexity of foreland basin deposition and its sensitivity to changes in sedimentation influx and accommodation space, brought about by eustatic sea-level and tectonic activity. A third factor that controls accommodation space, especially in deep systems such as foreland basins, is sediment compaction. Space is generated when porosity is reduced. Knowledge of the compaction behavior of clay, sand and lime is essential to understand foreland basin evolution.

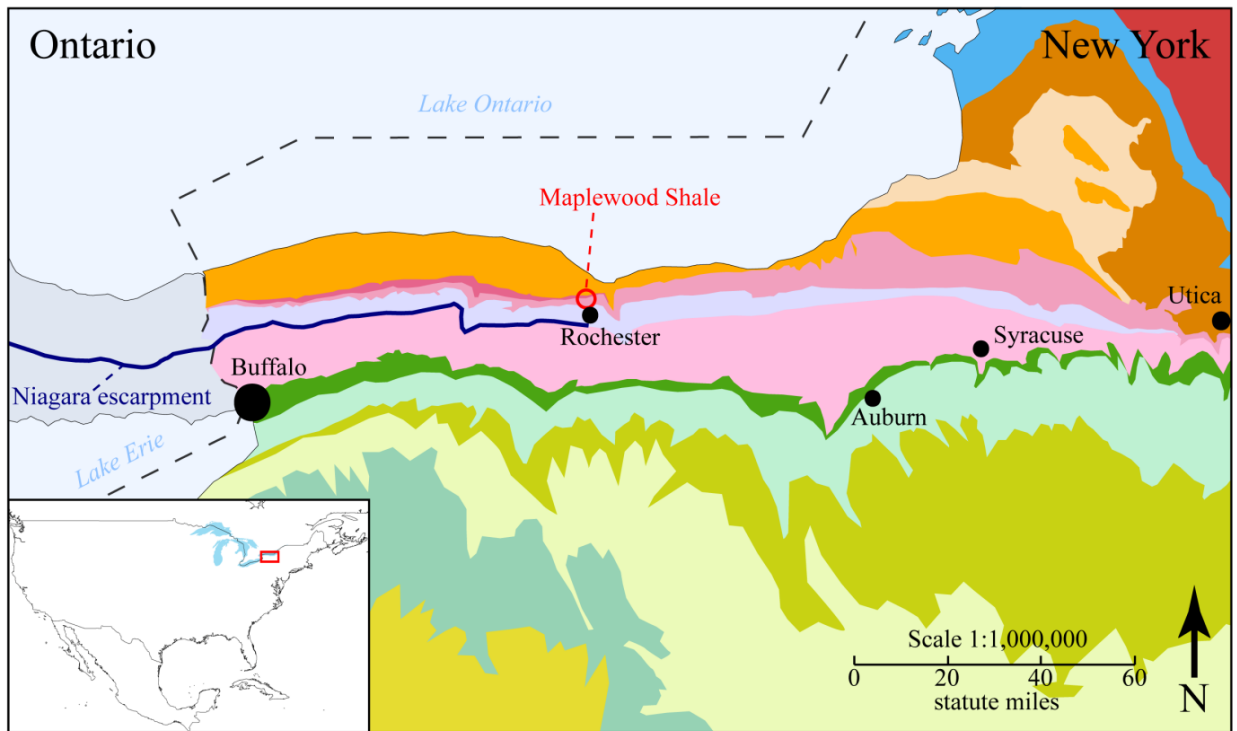


Figure 2.2: Geological map of the Northern Central Appalachian Basin of western New York State (digitized after *Rogers et al.* [1990]). The red circle highlights the type locality for the Maplewood Shale. The legend for this map is presented in figure 2.3 as a map-wide stratigraphic correlation chart.

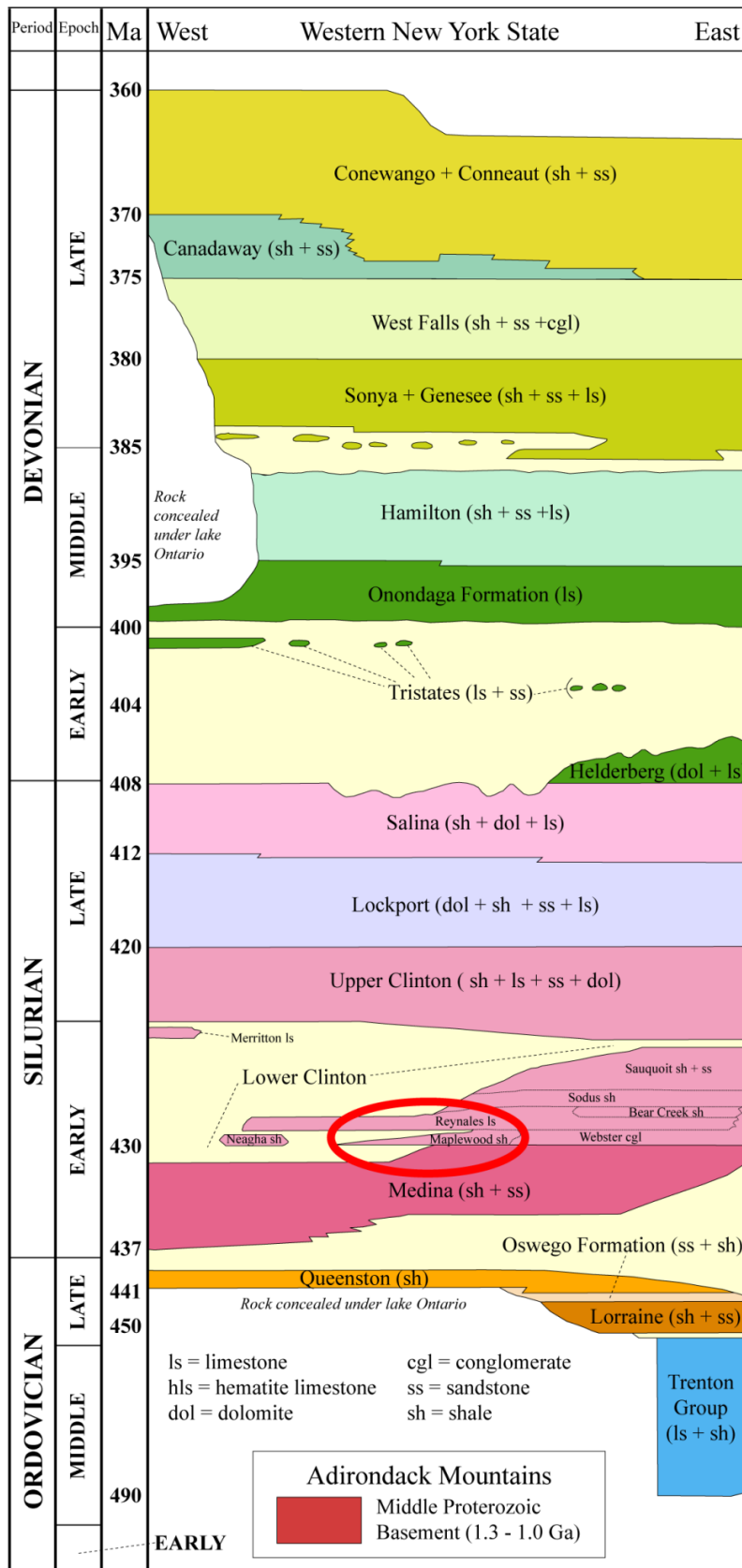


Figure 2.3: Stratigraphic correlation chart for geological map of figure 2.2 (digitized after Rogers et al. [1990]). The red ellipse highlights the stratigraphic position of Maplewood Shale. Colors and stratigraphic group names form the legend for figure 2.2. Beige colors represent periods of erosion and/or non-deposition.

2.2: Clay/mudstone compaction

Mudstones and shales are the most common sedimentary rocks [Tucker, 1981]. They are formed during the various stages of clay diagenesis, which commences immediately after deposition in low energetic marine environments. Burial initiates clay compaction by expelling free water and reducing the intergranular spacing. Rearrangement of particles and grain alignment then reduces porosity further. Increasing loads (deeper burial) forces more fluids out of the mud, thus reducing the ratio between solid grain (V_g) and liquid or pore (V_p) volume fraction (void ratio). The void ratio relates porosity and bulk volume (V_b), following equation 2.5:

$$e = \frac{V_p}{V_g} = \frac{V_p}{V_b - V_p} = \frac{\varphi}{1 - \varphi} \quad (\text{eq. 2.5})$$

Void ratio and porosity are commonly applied parameters to quantify the degree of compaction, and are frequently coupled to hydraulic and seismic properties of clay-rich sediments [e.g. Neuzil, 1994; Vasseur *et al.*, 1995; Dewhurst *et al.*, 1998; Nygård *et al.*, 2004; Mondol *et al.*, 2007; Schneider *et al.*, 2011]. The compaction behavior of argillaceous sediments in nature and laboratory is complex and controlled by both intrinsic parameters such as mineral composition, clay fraction and fluid salinity, and extrinsic parameters such as temperature, effective pressure, time and compaction rate [e.g. Rieke and Chilingarian, 1974; Bjørlykke and Høeg, 1997]. The complexities are exemplified by the spread of compaction curves (porosity/depth relationships) obtained from natural shales and argillaceous sediments (Fig. 2.4 - after Mondol *et al.* [2007]). Three general observations are made: 1) initial porosity (depth = 0) is 40-80 %, 2) rate of compaction per meter decreases with depth and 3) compaction curves converge < 2.5 km at 10-15 % porosity. In the top 2.5 km of the sedimentary column, mechanical processes such as grain rotation, alignment and close packing, are responsible for the compaction, whereas in deeper domains thermally activated mineral reactions and mass transfer dominate the compaction processes [e.g. Athy, 1930; Hedberg, 1936; Weller, 1959; Rieke and Chilingarian, 1974; Velde, 1996; Aplin *et al.*, 2003; Charpentier *et al.*, 2003; Worden *et al.*, 2005; Peltonen *et al.*, 2009; Day-Stirrat *et al.*, 2010]. Based also on microstructural observations, several conceptual compaction models have been designed, of which Hedberg's 1936 model is most elaborate (Fig. 2.5) [e.g. Athy, 1936; Hedberg, 1936; Weller, 1959; Vassoevich, 1960].

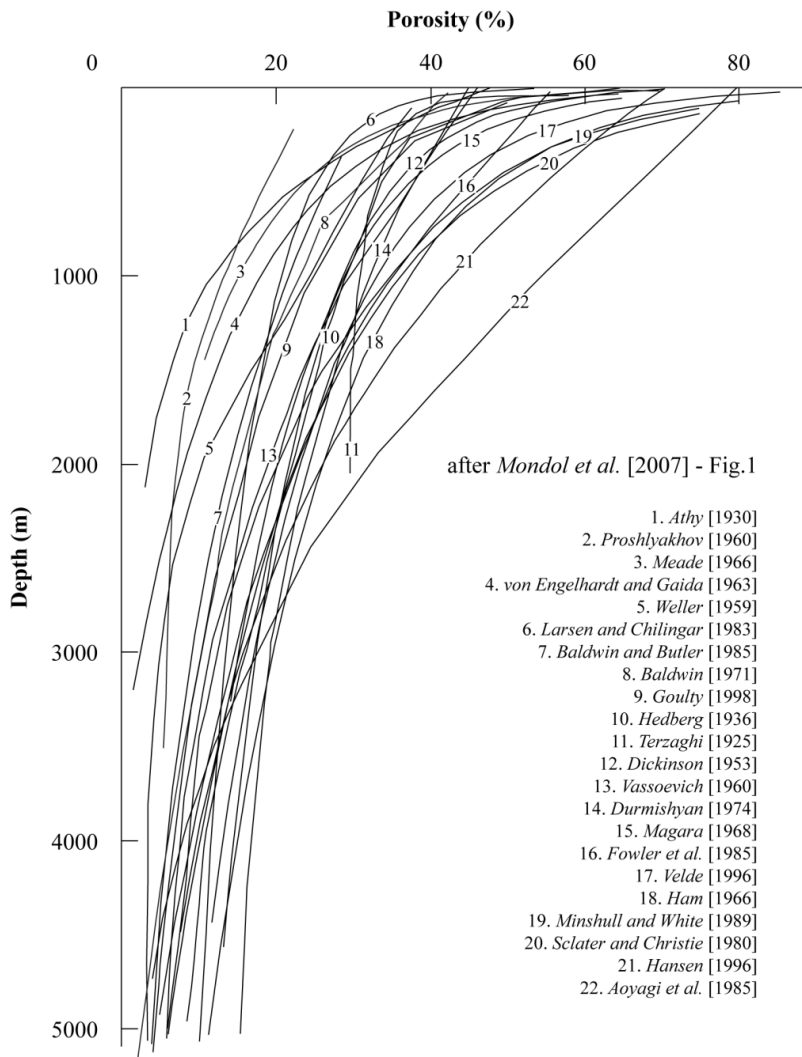


Figure 2.4: Compaction curves for natural shales and mudstones, determined predominantly from well-log measurements (after Mondol et al. [2007], Fig. 1).

				EXPULSION OF FREE WATER	LIQUID PHASE
				EXPULSION OF ADSORBED WATER	
				LOSS OF WATER THROUGH CHEMICAL COMBINATION	SOLID PHASE
				MECHANICAL REARRANGEMENT OF PARTICLES	
				MECHANICAL DEFORMATION OF PARTICLES	SOLID PHASE
				SOLUTION AND RECRYSTALLIZATION	
				ELASTICITY IN THE PRESENCE OF WATER	
0-10	10-35	35-75	75-90	PER CENT POROSITY	
RECRYSTALLIZATION	MECHANICAL DEFORMATION	DEWATERING	MECHANICAL REARRANGEMENT	STAGES	

Figure 2.5: The clay compaction model designed by Hedberg (after Hedberg, [1936], Fig. 7).

To study the effect of mechanical compaction on rock physical properties, clay compaction has frequently been simulated in the laboratory by mimicking the kinetic and chemical conditions of the shallow portions of basins (i.e. effective pressure < 50 MPa or depth < 3 km) [e.g. *Chilingarian and Knight, 1960; Rieke and Chilingarian, 1974; Vasseur et al., 1995; Dewhurst et al., 1998; Mondol et al., 2007; Voltolini et al., 2009; Schneider et al., 2011*]. Resulting compaction curves (Fig. 2.6) show a good agreement with natural curves; initial porosity is 45-80 % and compaction hardens with increasing pressure. There is however, no convergence of compaction curves observed for effective pressure ≤ 50 MPa. In fact, porosity at 50 MPa ranges from 11 to 44 %.

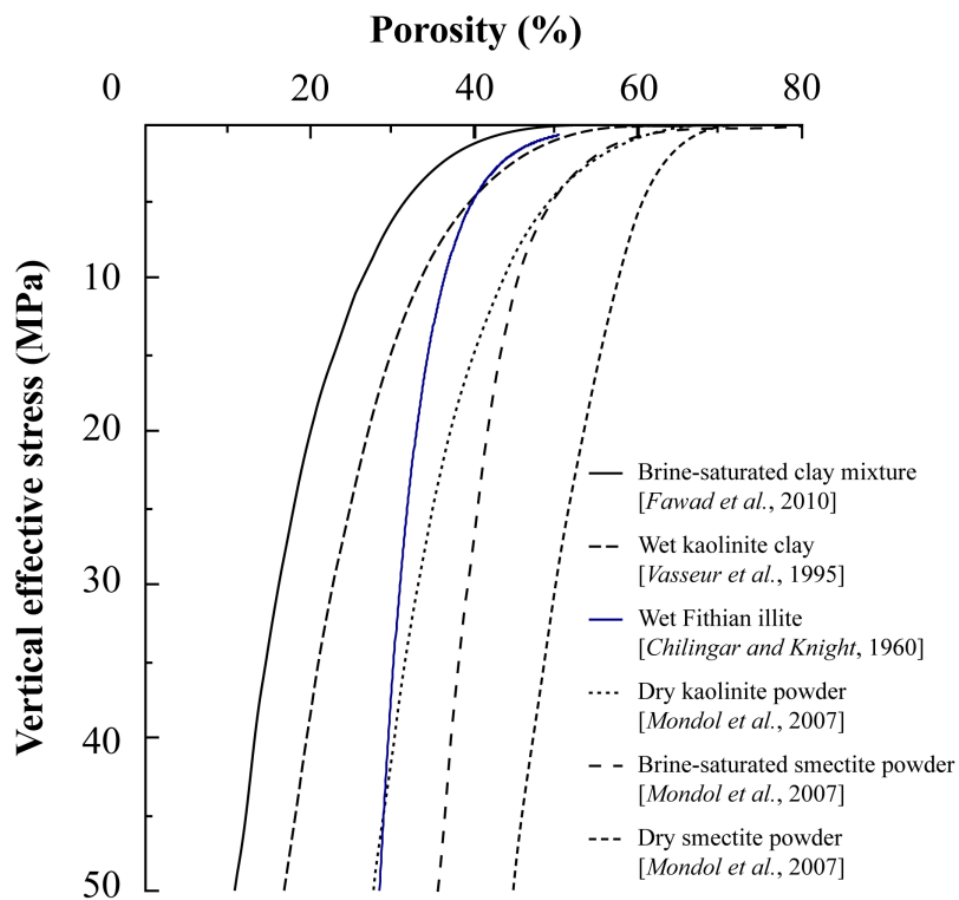


Figure 2.6: Selection of experimental clay compaction curves plotted in one figure to visualize the variation in porosity at each pressure resulting from compositional heterogeneities and saturation-state.

The transition in Hedberg's model (Fig. 2.5) from mechanical deformation ($\phi = 10-35$ %) to recrystallization ($\phi = 0-10$ %) marks the transition also from mechanical to chemical compaction. Smectite illitization occurring between 60 °C and 110 °C, is frequently associated with chemical compaction [e.g. *Towe, 1962; Perry and Hower, 1970; Hower et al., 1976; Eberl, 1993; Bjørlykke and Høeg, 1997*]. The effect of illitization on chemical and physical properties is described in numerous natural studies [e.g. *Hower et al., 1976; Ho et al., 1999; Land and Milliken, 2000; Aplin et al., 2003; 2006; Peltonen et al., 2009; Thyberg et al., 2010*], and exemplified in figure 2.7. For depth < 1700 m,

the correlation with experimental compaction curves and well-log data from natural mudstones is reasonable. However for deeper intervals, natural porosity is lower than experimental porosity (Fig. 2.7A), whereas the compression wave velocity is faster in nature than in the laboratory (Fig. 2.7B).

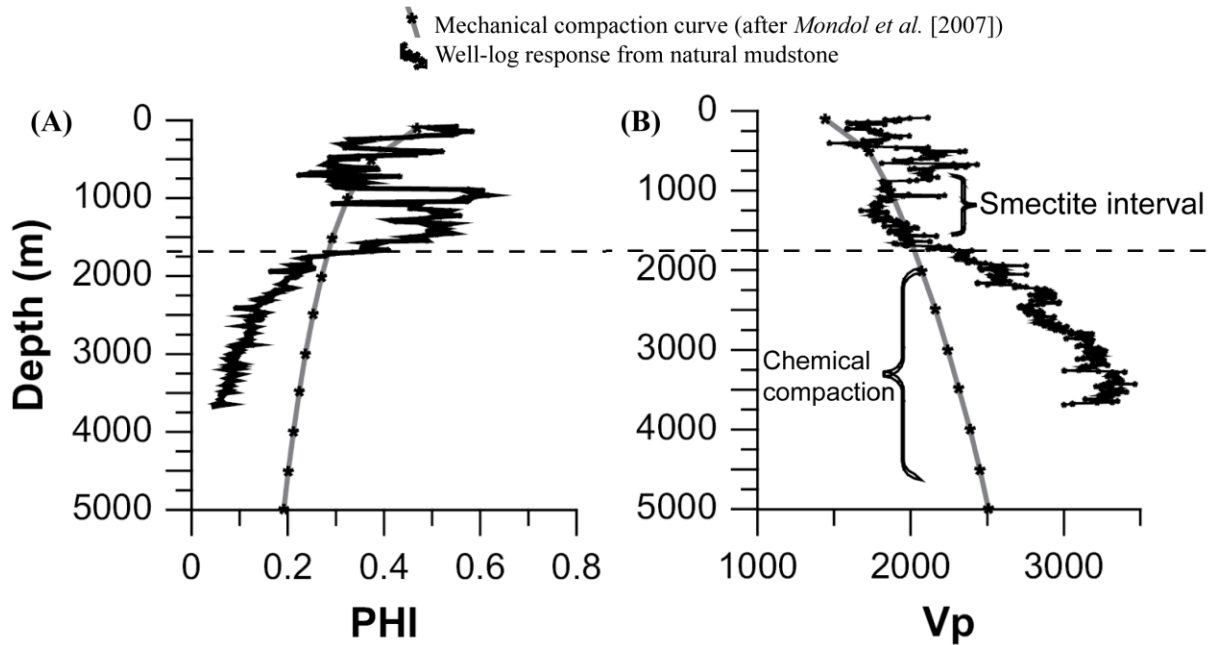


Figure 2.7: Effect of chemical compaction for A) compaction curves and B) compressional wave velocity (after Peltonen et al. [2009], Fig. 9)

Despite the complexity, clay compaction by mechanical processes is often characterized by one of two sets of parameters that are based on principles from soil mechanics. The plastic (PL) and liquid (LL) Atterberg limits [Kinnison, 1915; Casagrande, 1932b] mark the moisture content of a soil at the transition from brittle to plastic (PL) and plastic to liquid (LL) flow behavior. The range for which flow is plastic is termed the plasticity index (PI). [after Skempton and Jones, 1944; White, 1949]. Uncertainties with the validity of using reconstituted material in clay compaction experiments for the simulation of natural clay compaction led Burland [1990] to introduce alternative parameters. He introduced the void index (I_v) and intrinsic compression index (C_c) as two parameters, independent from the Atterberg limits, that can be used to express the relationship between pressure and void ratio for any reconstituted material. Equations 2.6A and 2.6B define I_v and C_c respectively.

$$I_v = (e - e_{100}) / (e_{100} - e_{1000}) \quad (\text{eq. 2.6A})$$

$$C_c = (e_{100} - e_{1000}) \quad (\text{eq. 2.6B})$$

Where e_{100} and e_{1000} are the void ratio at a specific pressure of 100 kPa and 1000 kPa, respectively.

Neither the Atterberg limits nor Burland's parameters seem suitable for the characterization of chemically compacted shales and mudstones, as they are designed and calibrated specifically for relative low-pressure mechanical compaction processes in soils (effective pressure < 10 MPa) [e.g. *Vasseur et al.*, 1995].

2.3: Sandstone compaction

Sandstones may represent a smaller fraction of sedimentary basin infill than mudstones and shales, yet they are also important for the evolution of such system. Their physical properties develop distinctively during diagenesis, which often makes them ideal reservoir rock for the storage of hydrocarbons, groundwater and CO₂. Deposited in high energetic both terrestrial and marine environments, sandstones are primarily composed of sand-size grains (typically quartz and feldspar) and contain minor amount of clays and clay minerals. Compared with mud, deposited sand is less porous [e.g. *Fraser*, 1935; *Weller*, 1959; *Bjørlykke*, 1988], volume loss during compaction is less [e.g. *Bjørlykke*, 1988], a clear relationship between porosity and pressure is absent [*Weller*, 1959] and chemical and mechanical compaction processes operate simultaneously [e.g. *Bjørlykke*, 1988]. Sands compact mechanically by grain rotation and crushing in response to increasing effective stress with burial, and compact chemically by pressure solution/precipitation processes that are controlled by effective stress, grain size distribution, temperature, and mineral and pore-water composition [e.g. *Bjørlykke*, 1988]. Mechanical compaction does not always result in total porosity reduction. Grain fracturing brought about by tectonic shear may create secondary porosity that is greater than the volume loss by shear [*Bjørlykke*, 1988]. The minimum porosity achievable by mechanical compaction of sandstone primarily depends on grain sorting [e.g. *Wong et al.*, 1997]; finer sandstone typically compact more. Cementation may reduce porosity to nearly zero, and depends mostly on the cement source and composition, and permeability of the cementing sandstone. Siliceous cement may originate from argillaceous sediments that undergo illitization [e.g. *Towe*, 1962; *Boles and Franks*, 1979; *Leder and Park*, 1986; *Land et al.*, 1997; *Lynch et al.*, 1997; *Land and Milliken*, 2000; *Van de Kamp*, 2008; *Day-Stirrat et al.*, 2010].

Experimental compaction of sandstone:

Based on the applied stress regime, experimental sandstone compaction studies are divided in two groups: 1) isostatic stress tests [e.g. *Zhang et al.*, 1990; *David et al.*, 1994; *Klein et al.*, 2001], and 2) confined compression tests [e.g. *Menéndez et al.*, 1996; *Wong et al.*, 1997; *Wu et al.*, 2000; *Klein et al.*, 2001; *Baud et al.*, 2004].

From isostatic stress tests four types of compaction behavior in volumetric strain/pressure space, known as “hydrostats”, are identified (Fig. 2.8) [*Brace*, 1978]: I) linear compaction with elastic

loading of the framework, leading to full recovery after unloading, II) non-linear compaction induced by crack closing until P^* , followed by elastic frame loading. Minor hysteresis is displayed below P^* , yielding some permanent deformation, III) continuous crack closing with major hysteresis starting immediately after unloading, reflecting pore collapse and (IV) elastic loading (type I), followed by type III non-linear loading and unloading. The inflection point is denoted as P^{**} . Porous sandstones ($\phi > 20\%$) in isostatic stress tests compact by type IV behavior. Initial porosity and grain size distribution control P^{**} . In lower porosity sandstones, compaction follows a type III behavior [Zhang *et al.*, 1990]. The commonly observed permanent deformation is typically the result of two types of cataclastic flow: 1) dilatant flow with positive pressure dependency of the yield stress for low-porosity rocks [Fredrich *et al.*, 1989; Fischer and Paterson, 1989] and 2) compactive flow with negative yield stress effective pressure dependency for high-porosity sandstones [Wong *et al.*, 1992]

In confined compression tests sandstone compact differently. In comparison with clay-rich sediments, the accommodation of axial strain in sandstone is rapidly exhausted and inelastic failure by brittle faulting or cataclastic flow, depending on effective pressure, initiated [e.g. Menéndez *et al.*, 1996; Wong *et al.*, 1997; Wu *et al.*, 2000; Klein *et al.*, 2001; Bésuelle *et al.*, 2003]. In the case of brittle faulting, total porosity may even enhance when dilative shear bands are produced (Fig. 2.9A) [e.g. Ord *et al.*, 1991; Menéndez *et al.*, 1996; Wong *et al.*, 1997; El Bied *et al.*, 2002; Sulem and Ouffroukh, 2006]. When axial strain is accommodated by cataclastic flow, a phenomenon known as “shear-enhanced compaction” occurs. Shear-enhanced compaction is defined as accelerated porosity reduction with the application of differential stress ($\sigma_{\text{diff}} = \sigma_1 - \sigma_3$) in comparison with hydrostats. [Curran and Carroll, 1979; Wong *et al.*, 1992; 1997]. With increasing effective pressure, shear-enhanced compaction commences for higher effective mean stress and greater porosity changes (Fig. 2.9B). Furthermore, the efficiency of compaction increases as well with higher effective pressure (Fig. 2.9B) [Wong *et al.*, 1997]. In the transition zone from localized brittle failure to distributed cataclastic flow a hybrid mechanism displaying both shear-enhancing compaction and localization producing high-angle shear bands and discrete low-angle compaction bands [Klein *et al.*, 2001; Wong *et al.*, 2001; Bésuelle *et al.*, 2003; Baud *et al.*, 2004].

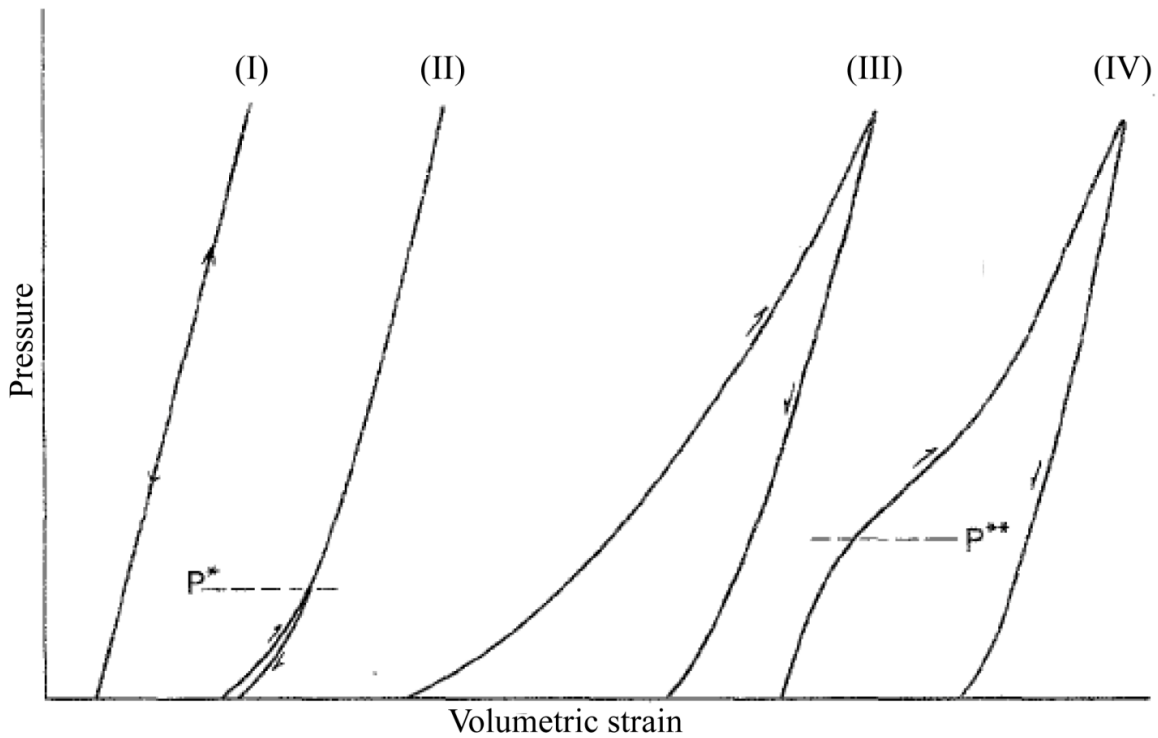


Figure 2.8: Plot of volumetric strain versus pressure showing four types of isostatic compaction behavior (after Brace, [1978], Fig. 1).

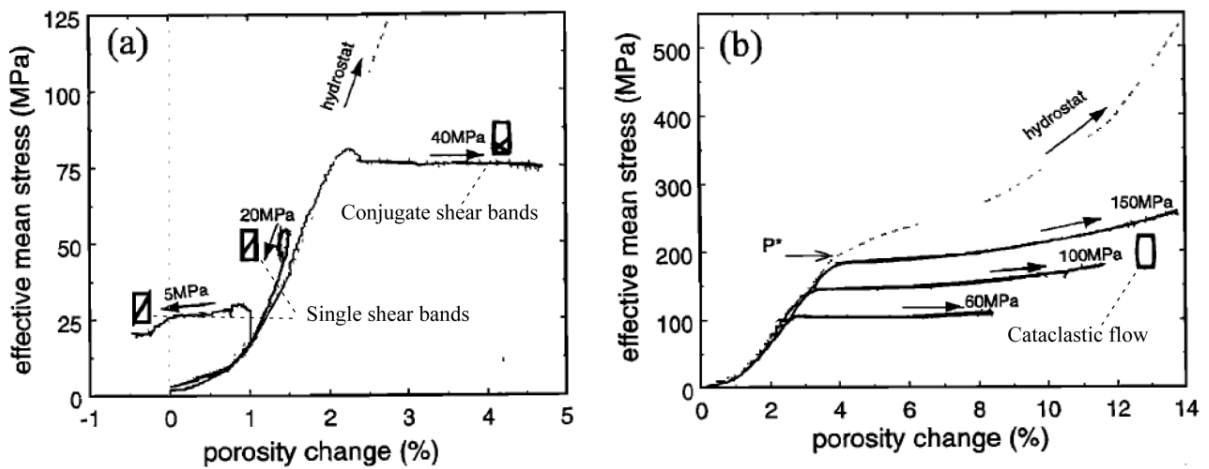


Figure 2.9: Porosity change plotted against effective mean stress for hydrostats and for confined compression tests with A) low effective pressure ($P_{\text{eff}} \leq 40$ MPa) and B) high effective pressure ($P_{\text{eff}} = 60-150$ MPa) (modified after Wong *et al.* [1997], Fig. 2).

2.4: Limestone compaction

Despite the abundance of limestone, their importance for hydrocarbon migration and maturation, and their CO_2 storage potential, the diagenesis of limestones is still poorly understood. The diversity of numerous compaction mechanisms in carbonates, often amplified by their sensitivity to compositional and structural heterogeneities, complicated porosity prediction [e.g. Ehrenberg, 2006; Croizé *et al.*, 2010], necessary for basin modeling [e.g. Sclater and Christie, 1980; Audet and Fowler,

1992]. The realization that, unlike for clays, even in shallow domains, cementation is an important compaction process is decades old [e.g. *Athy*, 1930; *Weller*, 1959; *Fruth et al.*, 1966; *Moore*, 2001; *Ehrenberg*, 2006]. Observations on natural limestone occurrences led to the conclusion that dissolution of unstable carbonate minerals, followed by precipitation of dolomite and calcite can only provide a fraction of the required cement to chemically compact a porous ($\phi = 40-70\%$) lime deposit to zero porosity limestone [e.g. *Weller*, 1959; *Bathurst*, 1971]. However, the over two decades long search for different cement sources, ironically led to the realization that, unlike commonly perceived, under certain conditions mechanical compaction of limestone can accommodate substantial volumes without completely disrupting depositional structures and fossil remains [*Shinn et al.*, 1977; *Shinn and Robbin*, 1983]. In the case of exhausted mechanical compaction, further porosity loss is accomplished by pressure solution [e.g. *Baker et al.*, 1980; *Zhang et al.*, 2010], and leads to the formation of stylolites, solution seams and fitted fabric [e.g. *Sorby*, 1908; *Stockdale*, 1943; *Dunnington*, 1954; *Wanless*, 1979; *Buxton and Sibley*, 1981].

Experiments show that in the absence of creep, shear-enhanced compaction in porous limestones occurs in a fashion comparable with sandstones [*Baud et al.*, 2000; *Vajdova et al.*, 2004]. In the presence of creep, changes in pore geometry, pore throat radius and connectivity bring about a kink (crossover porosity) in the permeability evolution with porosity loss [e.g. *Bernabé et al.*, 1982; *Zhang et al.*, 1994; *Zhu et al.*, 1999].

2.5: Very low-grade metamorphism

As sediments are buried by younger overlying deposits, surrounding pressure and temperature increase and the chemical environment alters. In response to the changed conditions notably clay phyllosilicate such as smectite, illite and kaolinite react and transform to thermodynamically stable mineral species [e.g. *Frey and Robinson*, 1998]. Two phyllosilicate reaction series involving dioctahedral and trioctahedral clays have been frequently observed in relation to diagenesis and burial [*Merriman and Peacor*, 1998]:

1. dioctahedral 2 : 1 clays

smectite \rightarrow mixed-layer illite/smectite (I/S) \rightarrow illite \rightarrow muscovite

2. trioctahedral 2 : 1 clays

Smectite \rightarrow mixed-layer chlorite/smectite (C/S) \rightarrow chlorite

Mineralogical quantification of the progress in the smectite-illite/smectite (I/S)-illite-muscovite series has led to a classification of diagenesis and very low-grade metamorphism in metapelites (Fig. 2.10, after *Merriman and Peacor*, [1998], Fig. 2.1). The Kübler index (KI) quantifies the illite crystallinity, defined as the width of the illite (001) peak in a Cu- α XRD

spectrum [Kübler, 1968]. With increasing transformation of smectite into illite and muscovite, the Kübler index decreases. In the early diagenetic zone, $KI < 1$, and the percentage of illite-muscovite in I/S is below 60 % (Fig. 2.1). The main stable clays are dioctahedral and trioctahedral smectite and kaolinite. With increasing temperature and depth, smectite transforms to illite (reaction 1), giving rise to lower KI values. The late diagenetic zone is defined for $0.42 > KI < 1$ and contains a larger illite-muscovite fraction in I/S (< 90 %). In this zone, the illite thickness, measured by transmission electron microscopy < 22 nm, and foliation is parallel to bedding (Fig. 2.1). The low anchizone is characterized by $KI = 0.30-0.42$, up to 95 % illite-muscovite fraction in I/S, and larger illite thickness. A slaty or crenulated develops in the low anchizone resulting in pencilled mudstones or slates. Furthermore, illite muscovite polytype changes from $1M_d$ to $2M_1$ (Fig. 2.1). In the high anchizone, smectite is nearly absent, with $KI = 0.25-0.30$, and over 95 % illite-muscovite in I/S. Additionally, illite flakes typically range in thickness from 38 to 52 nm and a well-developed cleavage (S_1) emerges, creating roofing-grade slates (Fig. 2.1). The high anchizone marks the boundary between sediment diagenesis and rock metamorphism. The epizone ($KI < 0.25$) metapelitic zone corresponds to lower-greenschist facies metamorphism.

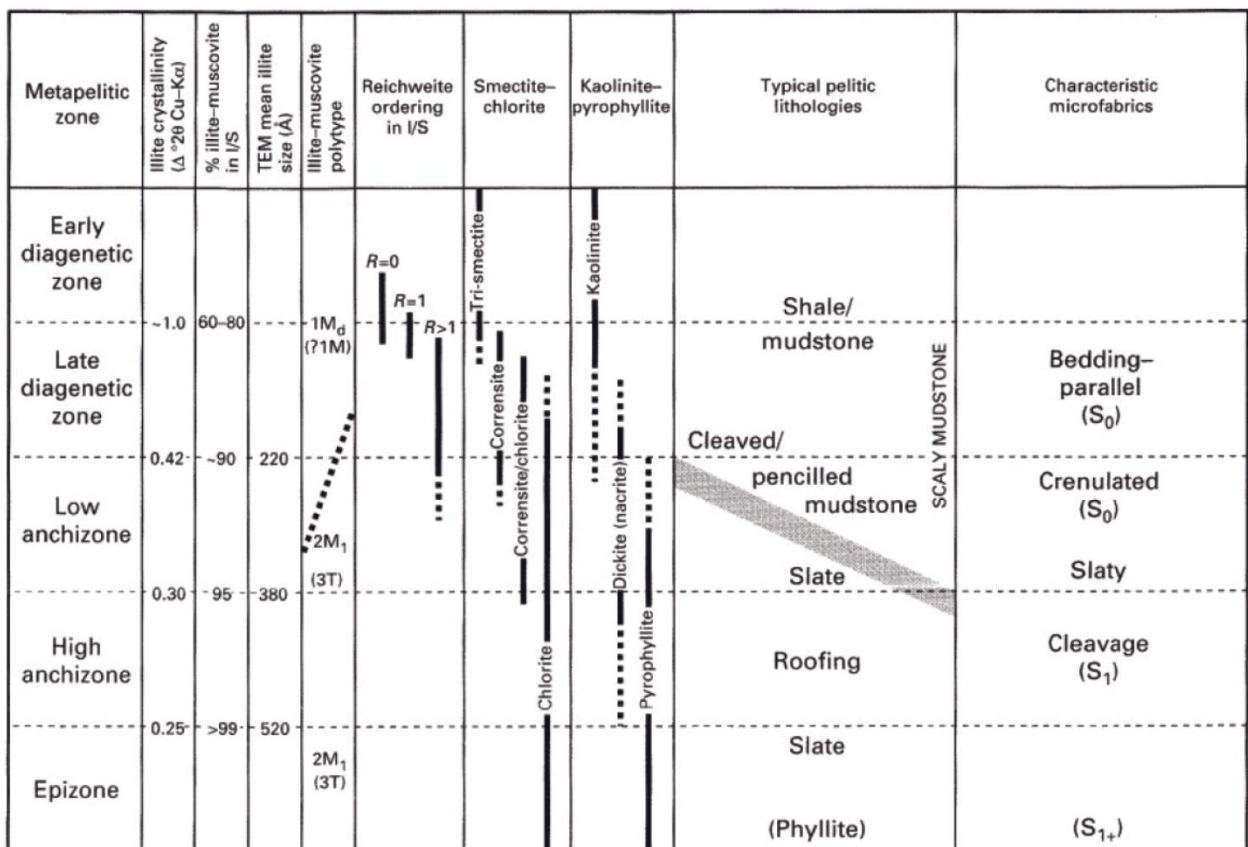


Figure 2.10: Classification for metapelitic zones in diagenetic to low-grade metamorphic argillaceous sediments, showing mineralogical and microstructural characteristics (after Merriman and Peacor, [1998], Fig. 2.1).

The full transformation of smectite through illite to muscovite is not observed in one intact sequence. In Gulf Coast sediment cores a classic and perhaps largest stretch of early diagenetic through late diagenetic to lowest anchizone grade pelites is retrieved [e.g. *Hower et al.*, 1976]. For higher anchizone and epizone grade sediment, sediment burial is typically insufficient and crustal shortening followed by uplift and erosion is required for access [e.g. *Merriman and Peacor*, 1998].

2.6: Rock magnetism

Magnetic properties are a useful parameter to quantitatively describe a rock and its development in response to stress, diagenesis and/or metamorphism.

Magnetism is exhibited by all materials. Several physical phenomena behind magnetism categorize material, including minerals, into three groups: ferromagnetic (*s.l.*), paramagnetic and diamagnetic. The fundamental phenomena are presented in numerous textbooks [e.g. *Dunlop and Özdemir*, 1997]. In brief, magnetization (M) is the sum of the induced (M_{ind}) and remanent (M_{rem}) magnetization. The first component is the magnetic response to an external magnetic field (H), whereas the latter is magnetization carried by ferromagnetic (*s.l.*) particles only, in the absence of an applied magnetic field. Because the applied field is not typically parallel to the magnetization (i.e., the magnetized material is anisotropic), a second-rank tensor, magnetic susceptibility (k), is used to couple M_{ind} and H ,

$$M_i = k_{ij}H_j \quad (\text{eq. 2.7})$$

where M_i and H_j are vectors describing M_{ind} and H respectively and in which i and j range from 1 to 3. The eigenvalues of the k_{ij} tensor geometrically describes an ellipsoid for which the principal axes follow $k_1 \geq k_2 \geq k_3$. The anisotropy of magnetic susceptibility (AMS), derived from k_{ij} , is a key parameter in the study of rock- and paleo-magnetism.

A crucial difference between ferromagnetic (*s.l.*) and para/diamagnetic materials is the response of M with increasing H . The first group of materials exhibits a non-linear magnetization with increasing H , until a critical value is reached, called magnetic saturation (M_S) at which M remains constant. The applied field at which M saturates is material specific and used to identify ferromagnetic (*s.l.*) phases in a rock sample. For para- and diamagnetic materials M_{ind} increases linearly as a function of H , with positive and negative slope (i.e. magnetic susceptibility) respectively. In low applied magnetic fields (low field), magnetic susceptibility of a granular sample is the sum of the susceptibility of all individual grains, regardless of characteristics of the magnetic response. When a high magnetic field is applied (high field), magnetic susceptibility changes linearly with H , dominantly controlled by the magnetic behavior of the para- and dia-magnetic fractions of a sample.

Similarly, low-field AMS (LF-AMS) represents the sum of AMS in all phases, whereas in high-field AMS (HF-AMS), ferrimagnetic (*s.l.*) contribution to AMS on one hand can be separated from the para- and dia-magnetic on the other hand.

As a key-parameter in rock- and paleomagnetic studies, AMS is often strongly coupled with rock fabric [e.g. *Tarling and Hrouda, 1993; Borradaile and Henry, 1997; Almqvist et al., 2009*]. The development of AMS with compaction or porosity has been described for a range of experimental clays and natural slates [e.g. *Deamer and Kodama, 1990; Kodama and Sun, 1990; Hirt et al., 1995*].

Chapter 3

Methods and analytical tools

Thomas Berry once said, "If the earth does grow inhospitable toward human presence, it is primarily because we have lost our sense of courtesy toward the earth and its inhabitants."

Preface

This chapter deals with the methods and analytical tools employed in this research. The first subchapter introduces the experimental procedure, and discusses the illite shale powder preparation procedure. It also explains the three-stage compaction procedure developed for this study. Operating conditions, such as temperature, pressure and duration are also presented. Chapter 3 focuses on a detailed description and discussion of the compaction apparatuses. The three machines are (a), a hydraulic cold press, (b) Hot Isostatic Press (HIP), and (c), a 'Paterson' apparatus; named after its developer. Subchapter 3.2 describes these machines in detail. Of the three, the Paterson apparatus is the most complex and the most widely used. A vital part of any experiment is the data recording and subsequent processing. Chosen tools and experimental procedure behind the post-experimental data calculations are presented in subchapter 3.3. In this study, a wide range of analytical tools was used to investigate the chemical and physical changes occurring in the successive compaction stages. These analytical tools are briefly described and their working conditions presented in subchapters 3.4 to 3.7. Tools for chemical analysis are discussed in section 3.4; rock properties such as density and porosity form the main topic of section 3.5. SEM imaging plays a major role in the investigation of the compacted illite shale powder. The SEM method and operating conditions are briefly discussed in subchapter 3.6. Chapter 3 concludes with a description of the tools used to investigate rock magnetic properties (subchapter 3.7). This topic includes three common methods dealing with the magnetic susceptibility and its anisotropy, and remanent magnetization for identification of remanence-carrying minerals.

3.1: Sample preparation and experiments

Powder preparation:

Illite shale fragments have been crushed in tungsten shakers. The resulting powder was oven dried at 110 °C for at least 24 hr before being sieved in two stages using 250 and 125 µm mesh sieves. The < 125 µm powder was then stored in hermetically sealed plastic canisters until usage for experimental compaction tests.

The grain size distribution of the crushed and sieved illite shale powder was determined by laser diffraction using a Malvern Mastersizer 2000. Ultrasonic agitation was applied during the analysis in order to separate flocculated (clay) particles using water as a dispersant (refractive index of 1.33). A particle refractive index of 1.52 was applied. These data, shown in subchapter 5.6, represent averaged values of three runs of grain size analysis.

Experimental procedure: 3-stage re-compaction:

Illite shale powder was compacted in three stages, utilizing three methods. In the first stage (1), powders were compacted inside a stainless steel canister (220 mm long and of 51 mm diameter) within a bolted steel housing using a hydraulic press operated at room temperature. A load of 40 tons, corresponding to ± 200 MPa was applied for about 6 s per loading step. Two spoonful amounts of Illite shale powder was added and pressed in a stepwise sequence to insure homogeneous fabric, until the canister was nearly filled. Finally, a 2-4 cm thick layer of alumina powder was placed at the bottom and top of the canisters for capturing potential water vapor released during subsequent compaction stages at elevated temperature. Due to elevated vapor pressures, canister caps may bulge and potentially rupture upon decompression. As many canisters as possible were prepared to have as much material available for later tests. It was clear from visual inspection that even after this process, powders were compacted, yet unconsolidated; care was taken not to disturb the produced fabric. The grain size of the sheet silicates was found to be too small to develop a pronounced foliation by grain alignment [Misra *et al.*, 2009]. Trace and major element contamination of the illite shale powder by the stainless steel canister was considered negligible. Filled canisters were then prepared for the next stage (HIP) via the following steps: 1) canisters were sealed by arc welding a stainless steel cap, 2) checked for punctures by submerging them in a water bath, 3) vacuum immersion, 4) sandblasted to remove surface rust and 5) stored in a 110 °C drying oven. Canisters remained there until the next compaction stage 2.

Compaction stage 2 was performed in the HIP machine. Several hermetically sealed powder-filled canisters were placed in the pressure vessel at a confining pressure of 160-170 MPa and at a temperature of 590 °C after repeated flushing sequences. The applied stress field was isostatic (Fig. 2.1B-C). Duration of this compaction stage varied between 24 and 30 hrs. The resulting powder

was consolidated and cylindrical samples could then be drilled for chemical, mechanical and magnetic analysis, and SEM imaging. These samples are referred to as HIP1 (Table 3.1). Canisters were mechanically opened by a steel saw and split into two or three pieces for ease of drilling. No visual heterogeneity was noticed between canister pieces. There is no evidence that alumina powder used to store released water during compaction stage 2 contaminated HIP1 samples. Upon opening each canister, any captured water was directly released into the atmosphere or later evaporated in a 110 °C storage oven.

In the third, and final, compaction stage, samples were compacted at temperature conditions between 480 °C and 750 °C using either the HIP machine for a second run (3a), or via the Paterson apparatus (3b). In stage 3a the procedure of stage 2 was repeated at 480 °C and P_i of 172 MPa for 15 hours. For this procedure, the stainless steel canisters were simply removed from the HIP machine after stage 2 and re-inserted in the machine for stage 3, without removing their caps or analyzing the compacted illite shale powder. Samples from the resulting powder aggregate are referred to as HIP2 (Table 3.1). As before, no evidence for alumina contamination was found.

The most challenging compaction stage, 3b, was performed in the Paterson apparatus [Paterson, 1990]. After thorough analysis, HIP1 samples were re-used for stage 3b tests. The Paterson apparatus allows compaction or deformation under three different stress regimes (subchapter 2.1): (1) isostatic stress, (2) confined compression and (3) confined torsion. Samples deformed in torsion are referred to as PAT1 (T). Confined compression and isostatic stress samples are labeled PAT1 (C) and PAT1 (I), respectively (Table 3.1). Special circumstances created two more sample groups: PAT1 (P) for stage 3b samples with induced pore pressure of 20 or 50 MPa, and PAT1 (M) for experiments run at 750 °C, in which according to modeled equilibrium phase stability (Chapter 6) should generate partial melt. For experiments run at lower temperature, approximately 700 °C, there was no evidence of partial melting or other distinguishing features and these were therefore not placed into unique sample groups. Compaction stage 3b tests were run at P_i , P_c and $P_t = 300$ MPa and temperatures of 500 °C, 650 °C, 700 °C or 750 °C. Three PAT1 (I) experiments were performed at room temperature to test the effect of high confining pressure (P_i) alone on sample compaction. As already mentioned, a pore pressure (p_p) of 20 or 50 MPa was applied during a few tests. The effective stress applied to the samples in these experiments was determined from equations 2.4A and 2.4B. Two types of sample jackets were used in compaction stage 3b, iron or copper. Samples were typically deformed in undrained conditions (not vented to the atmosphere). Few experiments were conducted under drained conditions using porous spacers to permit sample venting to atmosphere via a pore pressure system. Imposed strain rate in confined compression experiments varied between 7×10^{-6} to $1 \times 10^{-3} \text{ s}^{-1}$. The strain rate was changed during some experiments to investigate the flow behavior of the sample. Such tests are referred to as stepping strain rate tests. In confined torsion, shear strain rate was maintained at $3 \times 10^{-5} \text{ s}^{-1}$. Strain in PAT1 (C) tests was limited to 20% to avoid excessive sample bulging or buckling. Another limiting parameter was the sample strength, which often reached values close to the

maximum tolerance of the internal load cell. Sample sizes in the Paterson apparatus experiments have a length from 5.2 to 22.0 mm, and a diameter of approximately 10 mm or 15 mm. The effect of sample aspect ratio on mechanical behavior was negligible, based on repetition of experiments with sample size as only modified variable.

Table 3.1 summarizes the compaction stages and resulting sample group ID. A comprehensive table with experimental conditions for tests in compaction stage 3b is presented in Table B1.

TABLE 3.1. SUMMARY OF SAMPLE COMPACTION STAGES

Compaction stage	Compaction history	Sample group ID				
		Isostatic stress	Confined compression	Confined torsion	Pore pressure	750 °C
1	1					
2	1+2					
3a	1+2+3a					
3b	1+2+3b	PAT1 (I)	PAT1 (C)	PAT1 (T)	PAT1 (P)	PAT1 (M)

3.2: Compaction apparatus

Hydraulic cold-press:

An Enerpac-H-Frame 50 ton press was used at room temperature for powder compression in compaction stage 1 (Fig. 3.1A). An oil-driven axial motor drives a top ram into a stainless steel (inox steel EN 1.4301) canister of 220 mm length and 51 or 35 mm inner diameter. The wall thickness of these canisters is 1.5 mm. The hydraulic press can load up to 50 tons, which corresponds to 245 or 520 MPa for 51 or 35 mm diameter canisters respectively. To prevent canister blowout during loading, canisters are inserted in tightly bolted (steel 12.8) steel housing (carbon steel). Without this, the hydraulic press would be imposing a simple uniaxial stress field on the samples. However, the steel housing modifies the stress field to confined compression due to the horizontal σ_n generated in response to imposed vertical σ_n .

Sinter-HIP-Kompaktanlage (HIP machine):

The HIP machine, a shortened version for the German name Sinter-HIP-Kompaktanlage, manufactured by ABRA Fluid AG, Switzerland, is an industrial High-Press High-Temperature (HP-HT) internally heated, gas medium pressure vessel (Fig. 3.1B). It applies an isostatic stress upon internally mounted stainless steel canisters. In the rock deformation community, HIP machines are typically used for lithification of mineral powder aggregates [e.g. *Bernabé et al.*, 1982; *Zhang et al.*,

1994; Barnhoorn *et al.*, 2005b; Schmidt *et al.*, 2008; Misra *et al.*, 2009; Tumarkina *et al.*, 2011]. Isostatic stress is achieved by compressing argon gas to a confining pressure of < 200 MPa. Gas is compressed via a manually operated air-driven compressor (Schorch). Before introduction of argon gas into the pressure vessel, a vacuum pump lowers confining pressure to 4 kPa to minimize humidity and limit argon-air mixing.

A large internal furnace consisting of series of molybdenum coils was used to increase temperature up to 2000 °C, measured by a set of three W-Re thermocouples. Temperature and heating and cooling rates were both programmed using a ‘ramp-flat’ protocol and also monitored by a Eurotherm controller. A cooling water circuit prevents the pressure vessel from overheating.

Maximum pressure (P_{\max}) depends on maximum temperature (T_{\max}), following the universal gas-law that relates gas temperature and pressure and assumes argon as ideal compressible gas. Depending on the temperature desired, gas is compressed first to a pre-calculated pressure; the furnace is then used to increase the temperature, thus pressure to the eventual target pressure. During HIP experiments, pressure and temperature remain constant. Afterwards, the furnace cools down following a pre-set program. Compressed gas is vented out until room pressure is achieved. A chart recorder collects and stores data on cooling water parameters, operating pressure and pressure vessel temperatures at the sealing cap, near the bottom and at the inner hull.

The large pressure vessel (170 mm inner diameter and 500 mm length) allows space for 14 stainless steel canisters of 51 mm or 24 canisters of 35 mm inner diameter, including a 2 x 5 mm safety margin for protecting the furnace windings and thermocouples.

HPT gas-medium testing machine (Paterson apparatus):

The rock deformation Paterson apparatus (designed by Prof. Mervyn Paterson at Australia Scientific Instruments Pty Ltd) uses compressed argon gas as confining medium (Fig. 3.1C) [Paterson, 1990]. Confining pressures up to 500 MPa are achievable. Pressure is usually increased over several stages by manually operating a series of valves connected to a gas plumbing system: 1) equilibration up to ~40 MPa of argon bottle pressure and pressurized argon gas in the secondary pressure vessel or intensifier with the cylindrical main pressure vessel, 2) gas booster pump (Haskel) increases confining pressure up to ~ 105 MPa and 3) intensifier oil-pump further increases pressure to 300-400 MPa. Re-stroking of the intensifier pump is required to reach higher pressures at room temperature. Otherwise, gas pressure can be further increased by thermal expansion following temperature rise. A stabilization time of at least 10 minutes is often required to cool-down pressurized argon gas back to room temperature.



Figure 3.1: A) Hydraulic cold-press used during compaction stage 1. B) HIP machine, with extruded pressure vessel, casing and control panel, used for compaction stages 2 and 3a. C) Compaction stage 3b Paterson rig pressure vessel with cooling water tubes inside protective steel casing. This picture shows the machine set-up for a confined compression or furnace calibration test.

Typically, confining pressure is increased using the intensifier pump until 230-240 MPa, after which confining pressure is increased to 300 MPa via heating. In practice, higher pressures are only occasionally applied, since the risk of leaks associated with the assembly jackets and load cell o-rings increases substantially above ~ 320 MPa. Gas leaks are prevented by a series of o-rings and copper-beryllium mitre rings. A system of nine leak detectors or ‘bubblers’ allows locating potential leaks. The leak detectors are a set of plastic tubes that connect parts of the pressure vessel with a transparent oil-filled tube placed in front of the machine in the main operation panel. Confining pressure is measured by a well-calibrated pressure transducer connected to the pressure vessel feeder pipe. The plumbing system in the Paterson apparatus is comprised of high-pressure stainless steel couplings and pipes manufactured by SwissNova and Sitec and designed for gas pressures up to 700 MPa. Grease-covered blowout holes in the couplings indicate possible gas leaks from the plumbing system. Three rupture discs are placed in the plumbing system to protect critical equipment (gas bottle, gas booster and pressure vessel) from over pressurization and damage. Digital alarms are set to shut down the intensifier pump or bleed the intensifier vessel when pre-determined critical pressures are reached. Finally, the apparatus is surrounded by a 1” thick steel casing designed to stop shrapnel in the event of a high-pressure explosion. Two slide doors and a hatch allow access to the pressure vessel from the lower side and top, respectively. An automatic lock prevents opening of any of these doors when the pressure vessel is pressurized above 30 MPa. Additionally, the gas booster is blocked when the doors are opened and confining pressure is higher than 30 MPa. The Paterson apparatus is operated fully from one side of the casing where displays indicate and regulate load cell parameters (Amalgamated instruments and Eurotherm) and temperature (Eurotherm).

A furnace and load-cell are placed inside the pressure vessel leaving a free volume of 0.21 l for the sample assembly. Maximum achievable temperature in the Paterson apparatus is ~ 1600 K (1327 °C). Furnaces are cylindrically shaped alumina tubes with an inner diameter of 21 mm.

Molybdenum windings are wound around the top, center and bottom of the core insulated with sheets of hot isostatically pressed alumina paper around the windings. A metallic casing holds the components in place. Temperature in the three-zone furnace is monitored by three R-type thermocouples; each one situated a few mm away from the corresponding winding. Inside the pressure vessel, the furnace is placed on top of the internal load cell. Power is supplied to each winding via a sealed plug-head positioned on the top of the furnace. A pressure of at least 50 MPa is required before power supply to the furnace can be applied. Furnace design is optimized for high-pressure (> 100 MPa) operation.

By adjusting the relative power sent to each of the three coils, a stable temperature profile is set. Specifically a thermal plateau where temperature varies by less than 2 °C is desired. Such a plateau represents the constant temperature hot spot where the sample is positioned. The location of the plateau within the furnace is recorded by a travelling K-type (chromel-alumel) thermocouple through a furnace ‘calibration assembly’ where temperature can be measured at intervals of typically 1 cm over an 8 cm range.

Calibrations were regularly performed to verify furnace performance and maintain optimal temperature conditions. Calibration settings are controlled by three parameters: 1) temperature, 2) confining pressure, 3) type of metallic calibration assembly sleeve or jacket. Usually, relatively more power is required from center and top windings if temperature is increased. Furnace calibration changes noticeably when confining pressure is changed by more than 100 MPa; a few percent less power is required for furnace calibration at lower confining pressure. Comparing iron and copper jacket furnace calibration reveals a prominent difference in plateau length; ~ 2 cm for copper and 4-5 cm for iron. The difference in thermal conductivity between iron (at 27 °C: 80 W m⁻¹ K⁻¹) and copper (at 27 °C: 401 Wm⁻¹K⁻¹) explains the recorded behavior.

The heart of the Paterson apparatus is the load cell at the bottom of the pressure vessel. It is enclosed in a protective casing and rests on a 6 cm thick nut. The internal load cell contains a set of linear variable differential transducers (LVDT) used to record axial displacement over a range of 3 cm. The internal load cell also contains an elastic element with a capacitance displacement transducer attached to it and electric resistance strain gauges for monitoring axial force (kN). The maximum force that can be applied in both extension and compression is 100 kN. An internal capacitor-type torque cell is used for recording internal torque (Nm). Between the pressure vessel and axial actuator an external load cell is situated to record external force (kN), which encompasses load cell internal force and friction. The pre-calibrated external load cell is used as reference for internal force calibration. A spring with known elasticity is axially compressed under confined conditions to load both load cells. Friction caused by the internal load cell results in a nearly constant offset between linearly increasing internal and external force. After friction correction, internal load cell settings are fine-tuned to match external force data. Axial displacement readings are calibrated by comparing

them with an external displacement gauge mounted to the top of the axial actuator, and adjusting the load cell settings accordingly.

In confined experiments with the Paterson apparatus, compression is achieved by driving a piston upwards from below the pressure vessel, using an axial actuator powered by a Printed Motors Works Ltd servomotor through reduction gearing. The actuator is operated and monitored through a Eurotherm type 2604 controller. The piston can travel over 50 mm at maximum displacement rates of 0.55 mm s^{-1} . A stirrup connects the external axial actuator piston with the internal compensating piston, located inside the load cell casing, below the actual core of the load cell. The sample assembly is inserted inside the furnace and pressure vessel, with its bottom anvil mounted inside the load cell. Upwards movement of the axial actuator piston forces the sample assembly to move up towards the fixed closure nut for the pressure vessel. The axial position and internal and external force data recorded at the moment of touch between sample assembly and the closure nut (a.k.a. 'touch point' or 'hit point') make zero-reference values to correct the subsequently collected data. Experiments carried out in isostatic stress mode require that the sample remains continuously at touch point conditions to ensure isostatic stress. The same applies to confined torsion tests. Combining compression and torsion yields unreliable load cell data because zero-reference data for internal torque drift significantly with internal force, and vice versa.

In confined torsion tests, the torque is generated by rotating or twisting the sample assembly in a clock- or counterclockwise direction. A Berger Lahr servomotor provides the rotation through a belt and gearbox system (54600 : 1), which is mounted on top of the pressure vessel as part of a specially designed torsion module for the Paterson apparatus [*Paterson and Olgaard, 2000*]. A rotating member transmits the rotation from the gearbox to the assembly. A Schaevitz rotary variable differential transducer (RVDT) records angular displacement of the rotating member. The servomotor is operated through a Berghof control panel. It can be operated up to 1000 Nm at velocities from 1 to 2000 rpm, which corresponds to a twist rate range of 3×10^{-7} to $6 \times 10^{-4} \text{ rev s}^{-1}$. The torque value at the equivalent torsion touch-point is used for zeroing torque data recorded in the subsequent experiment. The RVDT is manually reset to zero angular displacement at the start of an experiment.

A standard Paterson apparatus sample assembly consists of cylindrical 15 mm diameter ceramic rods with a 2 mm diameter through-going hole (1), and intact 3 mm thick ceramic spacers (2) that sandwich a rock specimen (3). Ceramic rods and spacers are made of either partially stabilized zirconia (PSZ) (dark) or alumina (Al_2O_3) (beige), and have characteristic low thermal conductivity (Fig. 3.2A-D). This, and their high strength and toughness, make them ideal assembly material for high temperature experiments. A specially designed anvil, situated at the base of the column, fits inside the internal load cell. Depending on the choice of experiment kinetics, an anvil for transmitting torsion (5) or axial force (6) is placed on top of the assembly column. Both top and bottom anvils have an axial hole. In the top part of the assembly, the holes align to form a channel used to place the tip of a k-type thermocouple 3 mm above the specimen. A similarly connected channel in the bottom

part of the assembly is aligned with a tube that goes through the internal load cell casing and forms the load cell pipe. In standard Paterson apparatus tests, these assembly channels are vented to the atmosphere. A copper or iron jacket (7) in combination with a set of nitrile rubber o-rings (8) is used to separate the pressure vessel argon gas from the vented assembly channels. At room temperature, high-pressure experiments employing polyolefin shrink tubes as jacketing material have been successful. The compression anvil (6) has a concealed o-ring that prevents gas from escaping the pressure vessel. The asymmetric assembly column of ceramic rods and spacers places the specimen about 5 mm above the center of the furnace such that the specimen in the sample assembly matches the furnace temperature 'plateau' inside the pressure vessel. Typically, the temperature plateau is offset to the top by 5-10 mm with respect to the furnace center. Alumina rods can be modified to accommodate 10 mm diameter specimens (10).

The Paterson apparatus is also equipped with a pore pressure system comprised of two reservoirs connected to the top and bottom ends of the sample assembly. The sample assembly used for pore pressure experiments is characterized by a feed through pipe (12) attached to a modified top anvil (9) and by ceramic spacers (11) having five holes to allow an even distribution of the pore medium into the specimen. Figure 3.2C shows the pore pressure top anvil and a small part of the feed through pipe. The top pore pressure or upstream reservoir consists of a volumometer, high-pressure pipe and a tee-piece above the pressure vessel that serves as a connection between the top anvil feed through pipe and the volumometer pipe. The volumometer is a small pressure vessel with 7 mm diameter piston that can move over 50 mm. The maximum volumometer volume is $\sim 1900 \text{ mm}^3$. The piston is driven by a Printed Motor Works Ltd GM9 servomotor and its position monitored by a Schaevitz LVDT. Directly connected to the volumometer is a Stellar Technology Inc. pressure transducer. The tee-piece allows a thin k-type thermocouple to be positioned inside the top anvil feed through pipe. The bottom pore pressure or downstream reservoir is comprised of the assembly channel, a pore pressure pipe inside the load cell casing and the load cell pipe that runs through the compensating piston and exits the load cell casing. A pressure transducer and tee-piece close the reservoir. A high-pressure pipe and valve connect the intensifier pressure vessel with the volumometer. The pore pressure system is designed to withstand pressures of 500 MPa and to use both liquids and gas as pore medium.



Figure 3.2A-D: Typical sample assemblies and parts for Paterson apparatus experiments in confined compression and isostatic stress mode (A), confined torsion mode (B) and confined compression or isostatic stress mode with imposed pore pressure (C). D Alumina rods used for 10 mm samples (10) and alumina spacer with five pore-pressure holes (11) used in pore pressure assembly.

3.3: Data recording and processing for compaction stage 3b

The Paterson apparatus is equipped with various sensors to monitor and record sample displacement, applied forces, temperature and pressure. The calibrated and amplified signals are collected in an 18-channel Eurotherm Chessel 6100A chart recorder. Care was taken to ensure that recorded values match those shown by respective panels and displays. The chart recorder is connected to a Eurotherm developed data collection software called iTools OPC scope, version 7.60. This software writes recorded data to an ASCII based text file, which can be imported by spreadsheet software for processing and visualization. The following quantities are logged in order of their channel input: assembly temperature (in °C), confining pressure (in MPa), internal force (in kN),

torque position (in rad), internal torque (in Nm), internal position (in mm), external force (in kN), downstream pressure (in MPa), volumometer position (in mm) and upstream pressure (in MPa). A selection out of these ten quantities is usually made, based on experimental set-up and specific needs. Sampling rate is selectable, but varies from every 3 s for short experiment and dynamic scenarios to every 5 mn for steady state sample behavior. Absolute time is always logged.

Post-experimental data processing includes the calculations and corrections that are now discussed. In confined compression experiments, sample cylinder length (L) at any point in time during the experiment is derived from the displacement of the load cell with respect to its initial position at ‘touch-point’, eq. 3.1A:

$$L = l - (D - D_0) \quad (\text{eq. 3.1A})$$

$$\varepsilon_{tot} = \frac{(L-l)}{l} = \frac{(d-d_0)}{l} \quad (\text{eq. 3.1B})$$

Where l is the original sample length (in mm), D and D_0 are the internal position (in mm) of the load cell during an experiment and at the start of the experiment (touch-point), respectively. Normalization over original length gives the total axial strain (ε_{tot}) in % (eq. 3.1b), and includes elastic (recoverable) strain.

Similarly, recorded internal or external force data are corrected for initial values at the start of the experiment and converted to σ_{diff} using equation 3.2A, representing sample strength (S):

$$S = \sigma_{diff} = 0.001 \frac{F_i - F_0}{A} \quad (\text{eq. 3.2A})$$

$$A = A_0 + \left[\frac{(A_f - A_0)}{(t_f - t_0)} \right] (t - t_0) \quad (\text{eq. 3.2B})$$

Where A is the linearly corrected sample cross-sectional area in m^2 , F_i is internal force (in kN), F_0 is internal force at ‘touch-point’ (in kN). The multiplication factor 0.001 converts the unit kPa to MPa. A_0 and A_f are the initial and final cross section area of the sample, respectively. A_f represents the area change following permanent deformation only. Elastic strain is neglected. Consequently, the rate of area change is underestimated. The term $(t_f - t_0)$ represents the duration of the experiment, where t_f and t_0 are the absolute time (in s) at the end and the beginning of the experiment, respectively. The absolute time during an experiment is expressed by t . Table A1 summarizes the terms used in equations 3.2A and 3.2B.

As data quality check, corrected internal force is compared with external force. On average, external force is 3 % higher than internal. Among experiments, the average external over internal force ratio ranges between 0.97 and 1.08, with periods of better and poorer agreement. Since there is

no systematic deviation between internal and external force data, no further corrections to internal force data, for example for machine compliance, were applied.

The load borne by the iron or copper jacket was not corrected for. At 500 °C for a strain rate of $1 \times 10^{-4} \text{ s}^{-1}$, a 250 μm wall thickness iron jacket with 15 mm inner diameter contributes ~ 13 MPa. At 750 °C the contribution is reduced to ~ 3 MPa. For copper the jacket load at 500 °C and 700 °C, for a strain rate of $1 \times 10^{-4} \text{ s}^{-1}$ is ~ 8 and ~ 2 MPa. Calculations were based on rheological and thermodynamical data from *Frost and Ashby* [1982] and are in agreement with jacket load values reported by *Chopra and Paterson* [1981] and *Chopra* [1997].

No displacement data was recorded during isostatic stress tests. Instead, axial, radial and volumetric finite strain was derived from the sample geometry by comparing data before and after experiments.

After confined torsion experiments, acquired raw torque data was corrected for the ‘touch point’ value at the onset of the experiment. The conversion from torque (M) to shear stress (τ) is given by *Paterson and Olgaard* [2000], equation 10, which after rearranging gives:

$$\tau = \frac{4(3+n^{-1})M}{\pi d^3} \quad (\text{eq. 3.3})$$

Table A1 describes the quantities used. The stress exponent characterizes the rheological behavior of stressed material and is 1 for Newtonian fluids, > 1 for non-Newtonian fluids, with values for rocks of 1-3 for flow by diffusion creep and 4-10 for flow by dislocation creep processes. The slope of a best-fit line in a log stress vs. log strain rate plot gives the value of n . Equation 3.3 is valid for power-law creep (i.e. $1 < n < 10$). Calculated values for τ only have meaning within the sample group. However, torque values are normalized for sample diameter, which allows comparison of different samples. A value of 1 is assumed for n .

Shear strain (γ) is the product of experiment time (in s) and the applied strain rate (in s^{-1}), which is derived from sample geometry and rotary motor speed (v), eq. 3.4:

$$\dot{\gamma} = 54600 \frac{\pi d l}{v} 60 \quad (\text{eq. 3.4})$$

The multiplication factors of 54600 and 60 convert v (in RPM) to sample twist rate (v) in rev s^{-1} .

After experiments, shear strain is verified from the shear angle (ψ) described by strain markers grooved in the jacket before the experiment. Shear strain is calculated from ψ (in rad) using equation 3.5:

$$\gamma = \tan(\psi) \quad (\text{eq. 3.5})$$

3.4: Methods for chemical analysis

To monitor compositional and mineral phase changes a suite of qualitative and quantitative chemical analysis techniques was applied. Thermogravimetry (TGA) and Karl Fischer Titration (KFT) analysis gave insight into the dehydration and dehydroxylation processes. X-ray fluorescence (XRF) analysis was performed to investigate major element behavior. Mineral phases were monitored with X-ray diffraction (XRD) analysis. General advantages of the chosen analytical methods include the bulk sample nature of the analysis and relative ease of the sample preparation.

Thermogravimetry:

During thermogravimetry analysis, mass loss is continuously measured. A wide range of chemical processes, such as dehydration, decomposition and oxidation are identified in a material characteristic 'TGA curve' in which mass losses at process-specific temperature intervals are identified. For geological materials, mineral reactions and transformations are normally too slow to be captured in TGA curves. However, dehydration reactions, and reactions producing for example, CO or CO₂ gas are faster and clearly identifiable. In this study, phyllosilicate dehydration is considered to be the only source for mass loss.

TGA has been applied to several pelitic samples and post compaction stage 2 HIP1 synthetic metapelites. Their comparison provides a quantitative measure for the effect of hot isostatic pressing in compaction stage 2 on water content and further dehydration behavior. TGA of other shales mostly reflects variation in clay content.

A Netzsch STA 409 C/CD thermobalance, with top-loaded samples and digital balance, was used for the TGA. A linear heating program with a rate of 10 K/min from room temperature to 1500 °C was applied. Sample powders were placed in alumina crucibles of known mass. Simultaneously, a reference alumina crucible (1400 mg) with 50 mg alumina powder was measured to obtain sample holder correction values. Initial mass of sample powders varied between 50 and 230 mg. Resolution of the mass balance system is 2 µg. To avoid reactions between sample and air, analyses were performed in an inert argon-gas atmosphere, maintained with an input flow rate of 40 ml/min. Data were collected and processed using proprietary Proteus® software.

X-ray powder diffraction:

XRD is a family of non-destructive analytical techniques that yield information about the crystallographic structures of minerals. An X-ray detector records the scattered intensity of X-rays as a function of incident angle (θ). Results are displayed in a diffractograph with 2θ versus intensity. Crystallographic planes of minerals peak at a characteristic 2θ angle, which allows their identification using the database of diffraction data maintained by the International Centre for Diffraction Data.

XRD measurements were performed on a range of natural shales to identify mineral content and clay crystallinity. Maplewood Shale samples after compaction stages 2, 3a and a selection of 3b were analyzed to identify any growth of new mineral phases.

The employed diffractometer is a Bruker AXS D8 Advance, equipped with a Lynxeye superspeed detector and automatic 9-slot sample changer. Powder samples were measured between 4 and 89.9° 2 θ angle, with 0.025° step size per second. Glass discs were used to hold a few milligram of sample material. Scans were performed in locked coupled mode with a divergence and antiscattering slit of 20 mm, while rotating samples. Position of the Lynx-iris was at 12 mm. Scan settings were set and adjusted using templates constructed with Bruker AXS XRD Wizard version 2.4.3 software. Scans were performed using Bruker AXS DIFFRAC plus XRD Commander 2.4.3. The proprietary software package ‘EVA 2’ (developed by SOCABIM, now Bruker AXS), version 11.0.03 was used to correct XRD diffractographs for background noise and to apply curve smoothing as well as establishing a link to the database.

X-ray fluorescence:

Bulk major element composition of several natural shales including Maplewood Shale was determined using XRF. Upon excitement from high-energy X-ray bombardment, sample material emits a characteristic X-rays spectrum, which is detected by a photomultiplier that counts the number of photons passing through as a measure of element quantity.

XRF analysis was performed using a wavelength dispersive X-ray fluorescence spectrometer (Axios PANanalytical) equipped with five diffraction crystals. Analysis was performed on fused glass beads prepared from sample powder mixed with dilithium-tetroborate in a 1:5 ratio using a Claisse M4® fluxer. Glass bead preparation includes loss on ignition (LOI) measurements calculated from the weight loss of a ~ 2 g powder during a 2 hr exposure to 1050 °C. The calculated LOI should be similar to the TGA weight loss up to 1050 °C. Like in the interpretation of TGA curves, water content in a sample is assumed to be equal to the LOI value.

Karl Fischer Titration:

Water content was determined using KFT [e.g. *Behrens et al.*, 1996]. The advantages of this technique include high accuracy and precision, selectivity for water, small sample quantity requirement, short analysis duration and easy sample preparation. Unlike water content determination by TGA or loss on ignition calculations, KFT directly measures bulk sample water loss. No assumption about the contribution of dehydration to total mass loss has to be made. KFT works on the basis that water released from the sample upon heating is captured and diverted to a reagent. This reagent is designed to have all reaction species in excess, water excepted. The rate of the reaction is monitored by a voltmeter; voltage is a function of reaction products.

After each compaction stage, except stage 1, a representative part of a sample was removed, crushed and ground into a powder. About 30 to 40 mg of powder was then placed in a platinum capsule and heated in a platinum furnace following a fixed program called ‘mica-test’. This program controls an initial 2 minute of heating period to 300 °C. After 60 seconds, the software starts recording titration values. This one-minute delay is designed to allow free water to be released before it is included in the total water content analysis. Temperature is held at 300 °C for 3 minutes and followed by 8 minutes of further heating. Temperature is increased to a constant value of 1200 °C is reached. Typically, water release starts at ~ 700 °C and continues until the maximum temperature has been established. Titration recording is aborted when the rate of water release decreases to 0.40 mg/s or less. Background values for water release (i.e. < 0.40 mg/s) are subtracted from the total water release value. Water content is the sum of the water release rate at each time step. Normalization over sample mass gives water content. Before each batch of KFT samples was analyzed, blanks were measured to ensure the absence of free water inside the KFT set-up. KFT calibration and reliability were checked using single crystal muscovite with known water content. Samples were analyzed two or three times when sufficient sample powder was available to get insight in reproducibility and errors. Resolution of the KFT method is within 0.01 wt %, but precision is estimated at 0.2 wt. %.

3.5: Porosity and density measurements

Porosity and density are key parameters describing the compaction grade of buried sediments. Numerous studies have been devoted to the relationship between porosity and fluid- or heat-flow parameters like permeability and thermal conductivity. In this study, a helium pycnometer was employed to measure grain density and porosity after each step of the experimental compaction procedure, except for step 1.

Helium pycnometer:

Connected porosity and grain density were measured indirectly by a Micromeritics AccuPyc 1330 helium pycnometer. The pycnometer uses pressurized (~ 1.44 MPa) helium gas to determine the grain volume of the solid material that occupies one of two chambers of calibrated space. Connected porosity (φ_c) is calculated using equation 3.6:

$$\varphi_c = \frac{V_p}{V_b} = \frac{V_b - V_g}{V_b} \quad (\text{eq. 3.6})$$

Similarly, grain density is defined as the ratio of mass (m) over V_g in g cm^{-3} or kg m^{-3} . Bulk density was calculated as the ratio of mass over bulk volume (V_b) in g cm^{-3} or kg m^{-3} . V_b was determined from 10-micrometer resolution caliper measurements of cylinder diameter and length.

The pycnometer chambers were calibrated with industry-certified standards. Detailed analysis of pycnometer accuracy, precision and resolution yielded working values of 0.01 %, 0.20 % and 0.001 cm³ respectively, for the smallest and the most commonly used calibrated chamber of 10 cm³, using an iron cylinder of known grain volume. The offset caused by accuracy is manually corrected by applying a multiplication factor of 0.993 to grain volume determinations. Room temperature variations have a noticeable effect on volume estimates. Error analysis on an iron cylinder of known volume and zero porosity revealed a slope of 0.0017 cm³/°C. Sample volume estimates were corrected linearly for temperature effects using this slope value and a reference temperature of 29.0 °C. The pycnometer was set to automatically repeat volume measurements seven times to improve statistics and to rule out gas pressure effects on the sample's pore structure. Data were accepted only when two requirements were met: 1) a robust difference between minimum and maximum values within seven runs of less than 0.01 cm³, and 2) volume estimates 1 to 7 that do not describe a systematically increasing or decreasing volume, which would indicate an unstable pore structure. Corrected average grain volume values (V_g) were used to determine sample porosity following equation 3.5. Volume correction habitually decreases porosity estimates by 0.6-7 %, while temperature corrections can yield a 1 % porosity estimation adjustment. Before pycnometer analysis, samples were oven dried at 110 °C for at least 1 hour to remove free water from the pores.

3.6: SEM imaging

Microstructural analysis provides key insight into compaction processes. The study of shales mostly involves material (clay and fine silt) that is very fine-grained, such that optical light microscopy is ineffective. Scanning Electron Microscopy (SEM) permits a magnification of over 100,000 and to sub-micron resolution. In this study, microstructural visualization is performed by SEM and is undertaken to inspect the behavior of fabric and mineral phases during compaction. Emphasis was placed upon microstructural parameters such as foliation, grain shape and size, mineral phase transformation, pore structure, deformation structures (e.g. micro-fractures and cracks, micro-folds, recrystallization, and signs of crystal lattice defects) and melt. SEM analysis was performed on both polished and broken surface samples, employing backscatter electron (BSE) and secondary electron (SE) detecting techniques. Mineral phases were identified using their grayscale contrast in BSE images and their major element distribution obtained from the semi-quantitative energy dispersive X-ray (EDX) technique.

The SEM used for this study is a FEI Quanta 200 FEG. FEG stands for field emission gun, a specialist electron gun that generates an electron beam by using emitters of zirconium oxide; known as Schottky type FEG. Employed SEM settings are highly variable and depend on sample type and coating conditions in terms of quality, polish grade and cleanliness, purpose (semi-quantitative

chemical analysis versus, high-resolution imaging). The SEM is operated at high vacuum ($< 10^{-4}$ Pa) but low vacuum (30-100 Pa) was applied for samples with a particular poor electron conduction due to, for instance, damaged or thin coating. The electron beam is usually operated with a high voltage of 10 kV, but deflections to 5 kV to avoid sample charging, or 20 kV to improve particle emission from the sample were used as required. Beam spot size varied between 4 and 6 units and beam aperture was set at 30 μm for high vacuum or 40 μm for EDX analysis. Working distance (i.e. distance between objective lens and sample surface) was maintained around 10 mm.

Samples in this study are mostly cylindrical. Sample surfaces created for SEM analysis generally originate from cutting the cylindrical sample parallel to the axis at distance R' (2-3 mm) away from the sample periphery or distance R away from the axis (Fig. 3.3A). This cut produced two surfaces, an inner cut plane and outer cut plane. Inner cut planes are vertically mirrored copies of the outer cut planes (Fig. 3.3B-C). Large samples ($l > 10$ mm) are cut normal to the cylinder axis at length L to minimize SEM sample size and preserve sample material for further analysis.

Polished surface BSE imaging and EDX analysis:

Polished surface samples are obtained from the exterior plane of a sample cut (Fig. 3.3C). To avoid loss of quartz grains during fine-polishing, samples were impregnated with cold mounting epoxy resin (Struers) to close pore space and support soft clay/mica matrix. The resin was prepared by mixing EpoFix resin and hardener (25:3). A desiccator with vacuum pump was used to force the EpoFix resin mixture into sample pore space, followed by > 6 hr drying in a 60 $^{\circ}\text{C}$ oven. Samples were then included in a transparent epoxy (Struers) using SpeciFast acrylic hot mounting resin and a Struers LaboPress-3 with 5-minute heating time at 180 $^{\circ}\text{C}$ and force of 15 kN and 8-minutes cooling. Resulting samples were subsequently polished using wet abrasive papers with increasing grits until the original sample was exposed again. Then diamond paste (Struers) polishing was applied to remove scratches generated during the wet abrasive paper polishing, employing decreasing particle sizes (6, 3 and 1 μm).

After thorough cleaning with alcohol, a carbon coating of 15-20 nm thickness was applied using a self-made graphite-electrode coating machine, which uses Edwards vacuum pumps and a Bal-tec QSG 060 quartz thickness and rate monitor. The sample was then mounted on an aluminum SEM stage holder and silver-painted to improve electric conductivity of the sample. Inside the SEM sample chamber, sample cylinder planes or their parallel equivalents were rotated to a horizontal orientation.

Samples were particularly well observed in BSE mode, which yields an atomic number- or Z-contrast imaging. Back-scattered electrons are beam electrons that have been reflected back from the sample by elastic scattering (i.e. no energy exchange between electron and atom). As the primary electron beam scans the sample surface, heavier elements, backscatter more electrons and thus appear brighter.

BSE images were primarily used to distinguish mineral phases, though sample topography at irregularities like pores and grain boundaries is also imaged due to electron beam shadow effects. An EDAX Pegasus detector was used to perform energy-dispersive X-ray spectroscopy (EDX) on selected sample sites. The detector measures the energy of element-specific X-rays emitted from the sample after interaction with the high-voltage electron beam. EDX spectra plot X-ray energy versus intensity. Peaks correspond with element orbitals from where the X-rays originated.

Broken surface SE imaging:

Broken surface samples were obtained by fracturing the sample near its periphery (Fig. 3.3A). In most cases, the interior plane is used for broken surface imaging (Fig. 3.3B). No polish or epoxy impregnation was required. A flat base was created by either fast polish on low-grit abrasive paper or automated diamond saw cutting. Loose material on the surface was removed by blowing compressed air before coating sample with gold, using a Bal-tec SCD 500 sputter instrument equipped with Bal-tec QSG 100 Quartz film thickness monitor. Gold coating was 8-10 nm thick. The coated samples were then attached to an aluminum SEM stage holder and their sides were silver painted for better electric conductivity. Once inside the SEM sample chamber, samples were rotated to ensure optimum image quality. This implies that fabric elements are not imaged in a consistent framework.

The preferred SEM detection mode to image broken surfaces records the current of incoming secondary electrons (SE). The SE detector (a scintillator-photomultiplier) collects low-energy (< 50 eV) secondary electrons that originate from the k-orbitals of atoms through inelastic scattering processes as the primary electron beam passes. Because of their low energy, secondary electrons originate from the top few nm of the sample. This allows high resolution. SE intensity strongly depends on surface topography and slope angles. Grayscale contrast in SE images thus represents mostly grain and pore shapes. Broken surface SE imaging allows the visualization of intact grains, voids and apparent 3D fabric elements for the evaluation of the dependence of varying experimental conditions on compaction processes.

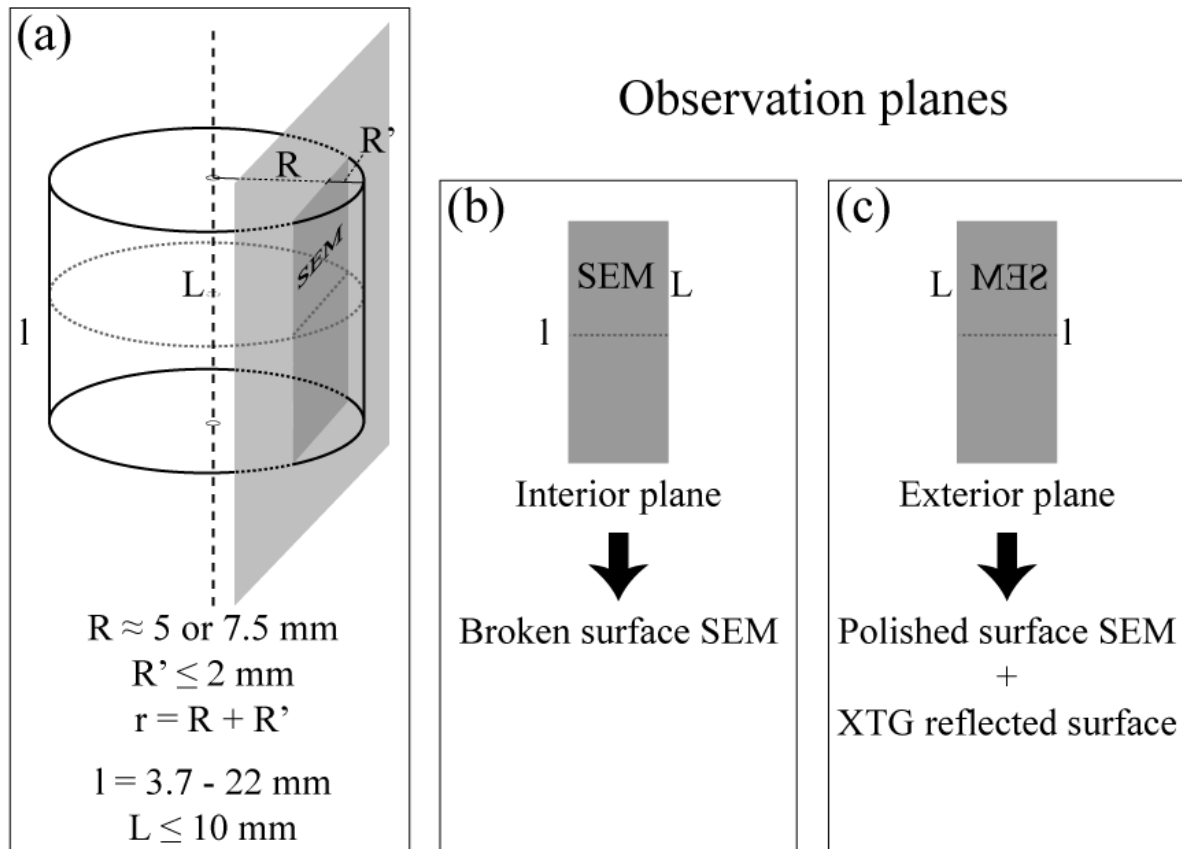


Figure 3.3: SEM sample surfaces of observation and analysis. A) Sample cut parallel to the cylinder axis at distance R from the axis or distance r from the periphery. Large samples ($l > 10 \text{ mm}$) are typically cut to length L . B) Interior plane mostly used for broken surface observation. C) Exterior plane mostly used for polished surface SEM and XTG reflection mode analysis. Note that images are vertically mirrored between interior and exterior planes.

3.7: Magnetic properties

In this study, both low- and high-field susceptibility measurements were performed to quantify AMS during compaction, expressed in porosity, as a measure of texture. Isothermal remanent magnetization (IRM) acquisition curves were constructed for the identification of the ferromagnetic minerals in illite shale.

Bulk susceptibility and low-field AMS:

Absolute or bulk magnetic susceptibility (K_m) was determined with an AGICO KLY-2 Kappabridge. Since ferromagnetic minerals intrinsically have a strong magnetic susceptibility, K_m is proportional to their quantity. Strong variation in K_m between compaction stages indicates chemical alteration by e.g. contamination or heterogeneous powder mixing, and/or phase transformation of ferromagnetic phases due to heating and/or fluid release.

AMS was determined with low applied field using an AGICO KLY-2 Kappabridge susceptibility meter. Susceptibility data were corrected by subtracting sample holder susceptibility.

Sensitivity of the susceptibility bridge is 4×10^{-8} (S.I.). The full susceptibility tensor was defined using a fifteen-step orientation scheme [Jelínek, 1978]. Average susceptibility values have been calculated and normalized for sample grain volume (V_g). The degree of low-field AMS is commonly expressed by the ratio of maximum over minimum principal susceptibility (P), eq. 3.7A.

$$P = \frac{k_1}{k_3} \approx P_j \quad (\text{eq. 3.7A})$$

An alternative expression for AMS that also includes k_2 has been proposed by Jelínek [1981],

$$P_j = \exp\sqrt{\{2[(\eta_1 - \eta)^2 + (\eta_2 - \eta)^2 + (\eta_3 - \eta)^2]\}} \quad (\text{eq. 3.7B})$$

where, η_i are the natural logarithms of the principal axes for k_{ij} (k_i), so P_j expresses anisotropy in terms of scatter of the logarithms of the principal magnetic susceptibilities and η is the average of η_i .

High-field AMS:

AMS was also determined in high field using magnetic torque measurements with a torque magnetometer [Bergmüller *et al.*, 1994], following the method proposed by Martín-Hernández and Hirt [2001]. Sample torque (in J m^{-3}) was measured over 360° in 30° steps around three orthogonal axes, for six fields ranging between 0.5 and 1.5 T and in the absence of an applied field. Applied magnetic fields are above the saturation field for magnetite. Hence, increasing torque is solely attributed to the linearly increasing magnetization signal from the paramagnetic and diamagnetic minerals (Fig. 3.4A). The different contribution of paramagnetic and ferrimagnetic minerals to torque at different fields is exploited in order to separate the two magnetic sub-fabrics. The absolute contribution to torque from ferrimagnetic minerals in their magnetically saturated state is given by the intercept of the linear regression line and is equal for all values of H . The paramagnetic torque is then derived from the total measured torque. Data processing to determine the susceptibility tensor from torque data includes corrections for sample holder and zero-field torque values. Torque-derived AMS is quantitatively expressed as the grain volume-normalized difference between maximum and minimum principal axis ($\Delta k = k_1 - k_3$). Direct comparison with eigenvalues of the low field susceptibility tensor is however not straight forward. Torque is measured at a range of applied fields. Torque differences between applied fields yield the deviatoric susceptibility tensor (i.e. deviations from isotropy), from which high field AMS is derived. The relative contribution of the paramagnetic and ferrimagnetic sub-fabric to total AMS was also determined. The contribution to paramagnetic AMS of diamagnetic quartz, is negligible, since its magnetic susceptibility is more than one order of magnitude lower than that of illite and mica. Furthermore, quartz AMS is considered very weak based

on its stiffness and shape preferred orientation in Maplewood Shale (quartz aspect ratio \ll clay and mica aspect ratio), which makes it magnetically nearly isotropic.

Samples were prepared from natural illite shale (NAT), HIP1, HIP2 and PAT1 sample groups (Table 3.1). Some ferrimagnetic phases such as hematite and iron-sulphides, are notoriously difficult to separate with the high field method because their saturation magnetization is very high ($H > 1$ T). They cause deviations from linearity, which affect the error of the intercept determination. These phases were not accounted for in the AMS separation (Fig. 3.4A). The validity of this omission depends largely on which ferrimagnetic minerals are preserved or formed.

Isothermal Remanent Magnetization:

Isothermal remanent magnetization (IRM) curves were acquired to identify which ferromagnetic (*s.l.*) mineral phases occur. IRM acquisition was imparted either in a random direction for compacted samples or on a powder, using a vibrating sample magnetometer (VSM). IRM acquisition curves show the measured magnetic remanence (M_r) of the sample, carried by the ferromagnetic (*s.l.*) fraction of the minerals, at increasing applied magnetic field (0 to 1000 mT) and normalized over the saturation remanence (M_s). The average of three runs was used. Saturation remanent magnetization occurs at mineral specific values for H . IRM provides further quantitative data on remanent coercivity (H_{cr}) (Fig. 3.4B-C). Preceding IRM acquisition, hysteresis loops of M_r as a function of H were performed using the same VSM. From such loops, characteristic parameters such as initial slope (K_M), magnetization saturation (M_s), remanence (M_r) and coercivity (H_c) were determined (Fig. 3.4B). The ratios M_r/M_s and H_{cr}/H_c are useful material characteristic parameters.

One sample at each compaction stage, except after stage 1, was analyzed using IRM acquisition and hysteresis loops. Differences in shape and rate of saturation of the acquisition curves indicate that the magnetic remanence carrying minerals in the sample underwent alteration, which gives insight in the chemical processes occurring during individual compaction stages.

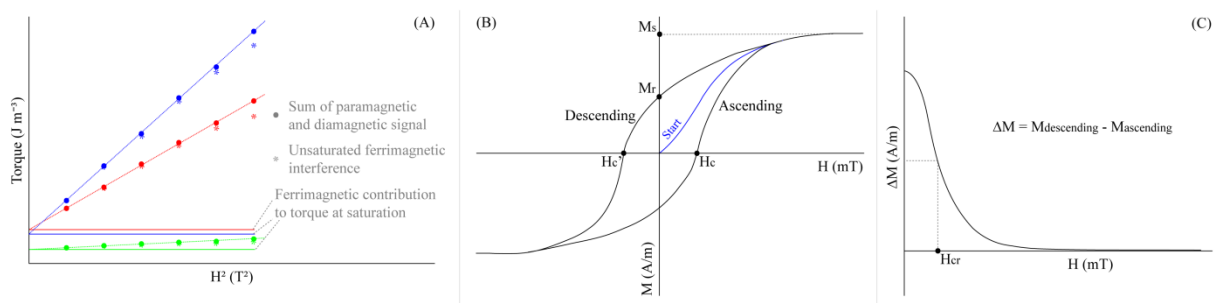


Figure 3.4: A) Magnetic field versus torque-plot, showing the linear increase of torque used in high field AMS. Three lines comprised of six data points correspond to orthogonal sample orientations. B) Magnetic hysteresis loop comprised of ascending and descending magnetization curves. Specific magnetic properties such as remanence (M_r), saturation (M_s) and coercivity (H_c and H_c') are displayed [Tauxe, 2010]. C) ΔM curve gives remanent coercivity (H_{cr}) at half the maximum value for ΔM [Tauxe, 2010].

Chapter 4

Evaluation of instrumentation precision

Glenn Turner once said, "Worrying is like a rocking chair, it gives you something to do, but it gets you nowhere."

Preface

The Paterson apparatus is well-known and widely applied by the experimental rock deformation community to solve a range of geological problems. In fact, it is one of the few types of high pressure and temperature deformation machines that are commercially sold to several rock physics labs worldwide. Furthermore, since the first model Paterson apparatus was made available in the late nineteen eighties, its designer and his support team at Australian Scientific Instruments Pty Ltd in Canberra (Australia) have always been deeply involved in machine maintenance and revisions, and have been available for troubleshooting on any technical level. One of the advantages of the Paterson apparatus over other deformation machines is the high sensitivity and accuracy of the load-cell, provided sample material is rheologically homogeneous and sensor and furnace calibration was performed sensibly. To scientifically verify and quantify the load-cell performance in terms of data reproducibility a series of repeated-torsion tests on pure calcite Carrara marble was performed in the first year of my PhD (2008). This small project served secondly as the tutorial on how to operate and maintain the Paterson apparatus. The rheological flow behavior of Carrara marble has been investigated earlier in previous PhD studies at the rock deformation laboratory of the Geological Institute at ETH Zurich. Findings from these studies served as basis for this 2008 follow-up study with a tutorial character. In April 2011 the results were published in the special volume of the peer-reviewed journal *Tectonophysics*, on the thermo-hydro-chemo-mechanical couplings in rock physics and rock mechanics. This volume was dedicated to the late Dr. Luigi Burlini, at the time lab manager and supervisor for my PhD project. The text, tables and figures in this chapter are directly taken from the original manuscript of the published paper, minor lay-out and formatting modifications to ensure homogeneity in this thesis.

Bruijn, R. H. C., K. Kunze, D. Mainprice, and L. Burlini (2011), Mechanical and microstructural development of Carrara marble with pre-existing strain variation, *Tectonophysics*, 503, 75-91, doi:10.1016/j.tecto.2010.09.029.

Mechanical and microstructural development of Carrara marble with pre-existing strain variation

Rolf H.C. Bruijn^{1*}, Karsten Kunze², David Mainprice³ and Luigi Burlini

¹ Geological Institute, ETH Zurich, Sonneggstrasse 5, CH-8092 Zurich Switzerland

² Electron Microscopy, ETH Zurich, Wolfgang-Pauli-Strasse 16, CH-8093 Zurich Switzerland

³ Géosciences Montpellier, CNRS and Université Montpellier 2, Place Eugène Bataillon, 34095 Montpellier, France

* Corresponding author: rolf.bruijn@erdw.ethz.ch

Abstract

A series of two-stage torsion experiments on Carrara marble were conducted to constrain the influence of known prior deformation on rheological response and microstructural evolution. Comparison with previous experimental data on Carrara marble flow and fabric evolution during single-stage torsion deformation experiments provided direct insights into the significance of initial deformation at various conditions. Our experiments were conducted at 727 °C temperature and 300 MPa confining pressure, while maintaining a constant strain rate of $3 \times 10^{-4} \text{ s}^{-1}$ on the periphery of the cylindrical samples. Under these conditions, the marble is known to deform in power-law ($n = 6-10$) ductile flow. All torsion experiments were performed with a Paterson type gas-medium testing machine equipped with a torsion actuator module.

Prior (D1) and subsequent (D2) deformation are accomplished by two torsion experiments in sequence on same sample segments. The effect of D1 strain history is investigated during D2 by applying counter-clockwise torsion to a sandwich sample consisting of three segments with different D1 rotation sense. D2 samples experienced continued, first and reversed shearing deformation in top, centre and bottom segments, respectively. D2 bulk strain was chosen equal to D1 strain in top and bottom segments.

D1 experiments followed the typical single-stage deformation behaviour of Carrara marble under the applied experimental conditions. Yielding was followed by strain hardening until a peak stress was reached at a shear strain around 1, after which work softening occurred. Weakening gradually evolved into a constant stress regime. During hardening, a shear microstructure and crystallographic preferred orientation (CPO) developed. Afterwards the volume fraction of smaller dynamic recrystallised grains increased continuously, resulting in a recrystallisation microstructure and CPO at shear strains of 5 and higher. The new D2 experiments displayed a strain variation between homogeneously deformed sample segments that increased with increasing D1 strain. The stress-strain behaviour of the D2 bulk sandwich samples showed less pronounced work -hardening and -softening when compared with single-stage deformation experiments. Furthermore, constant flow stress was attained at increasingly lower strain with increasing D1 strain. In most D2 segments, fabric development is equivalent to single-stage experiments at corresponding absolute strain. The fabrics differed markedly from those in single-stage experiments in the case of reversed two-stage deformation at moderate strain (D1 shear strain 1 and 2.6). Experiments show that grain shape by shearing of relict grains is defined by finite strain and thus affected by strain reversal. Recrystallisation is controlled by absolute strain and not influenced by strain reversal.

4.1: Introduction

Modeling of lithosphere strength is based on the observed flow behaviour of rock-forming minerals in lab experiments extrapolated to natural geological conditions [e.g. Kirby, 1983; Carter and Tsenn, 1987; Kohlstedt et al., 1995]. The aim of most rock deformation studies is to find parameters that describe the flow behaviour of samples under steady state conditions (i.e. constant stress and strain rate, and completed microstructure and texture development). It is common belief that most significant lithosphere deformation is accommodated by high strain shear zones that have reached such steady state.

Calcite single crystals, limestones and marbles are at present, and have been historically, among the most commonly studied rock type in experimental deformation studies [e.g. Adams and Nicolson, 1901; Griggs, 1936; Griggs and Miller, 1951; Rutter, 1974; 1995; 1998; Schmid et al., 1977; 1980; 1987; Walker et al., 1990; De Bresser and Spiers, 1993; Covey-Crump, 1998; Pieri et al., 2001a; b; Barnhoorn et al., 2004; Barber et al., 2007]. Their widespread appearance, low stress plastic flow behaviour at low temperature and lab strain rates, monomineralic composition make them ideal for rock deformation studies. In addition, limestones and marbles are frequently associated with upper crustal shear zones [e.g. Schmid, 1975; Pfiffner, 1982; Bestmann et al., 2000; Herwegh and Kunze, 2002; Austin et al., 2008].

High temperature ($T \geq 500^\circ\text{C}$) and pressure ($P_{\text{conf}} \geq 200 \text{ MPa}$) pure shear tests on Solnhofen limestone, Yule Marble, Carrara marble and synthetic calcite aggregates revealed three distinct plastic flow regimes separated by differential stress: 1) At high stresses, flow is best described by an exponential law, while deformation is accommodated primarily by e-twinning and intracrystalline slip [Turner et al., 1954; Heard, 1963; Heard and Raleigh, 1972; Rutter, 1974; Schmid, 1976; Schmid et al., 1977; 1980]. 2) At intermediate stresses, power law flow behaviour with stress exponent $n \geq 4$, associated with dislocation creep processes and dynamic recrystallisation by subgrain rotation and grain bulging dominates [Heard and Raleigh, 1972; Schmid, 1976; Schmid et al., 1977; 1980; Walker et al., 1990; Rutter, 1995]. 3) At low stresses, observed flow behaviour is strongly grain size dependent. For fine grained limestone flow is best characterised by a power law with $n \leq 2$, related to grain boundary sliding aided by diffusion creep processes [Schmid, 1976; Schmid et al., 1977; Walker et al., 1990]. Whereas, for coarse-grained Carrara marble flow behaviour follows a power law with $n \leq 4$ associated with dislocation creep processes and dynamic recrystallisation by grain boundary migration [Schmid et al., 1980; Rutter, 1995].

These pure shear experiments are limited in strain and reliable for $\epsilon < 25\%$. Their validity became questionable when simple shear experiments to initially $\gamma = 2.5$ and later $\gamma > 5$ revealed work softening in Carrara marble deforming in the dislocation creep field, related to dynamic recrystallisation [Schmid et al., 1987; Paterson and Olgaard, 2000; Pieri et al., 2001a; Barnhoorn et al., 2004]. New notion of steady state in calcite was established when constant strain rate torsion

experiments revealed a constant flow stress without discernable fabric changes for shear strain > 5 . This strain value, though, decreases with increasing temperature and lower strain rates [Casey *et al.*, 1998; Paterson and Olgaard, 2000; Pieri *et al.*, 2001a; Barnhoorn *et al.*, 2004]. Three explanations for work softening related to dynamic recrystallisation have been proposed: 1) grain refinement leading to an increased contribution of grain size sensitive flow (diffusion creep controlled) at the cost of grain size insensitive flow (dislocation creep controlled) [e.g. Poirier, 1980; De Bresser *et al.*, 2001; Ter Heege *et al.*, 2002], provided grain growth is suppressed [Olgaard, 1990], 2) geometrical or fabric softening (i.e. crystal preferred orientation (CPO) development leading to crystal alignment in easy slip orientations) [e.g. Poirier, 1980; Rutter, 1998; Pieri *et al.*, 2001a; b] and 3) grain boundary migration recrystallisation replacing grains with high dislocation density [Poirier, 1985; Rutter, 1998]. Although the latter was disputed by Ter Heege *et al.* [2002] for Carrara marble.

In parallel, Covey-Crump [1998] evaluated the alleged low strain steady state and concluded that the associated microstructural development, unlike previously considered, had not completed yet. A different train of thought was followed by a group of researchers that continued to investigate flow behaviour of calcite aggregates, limestone and marble in uniaxial compression. Intrigued by observed work softening in Carrara marble simple shear experiments, Rutter [1999] proposed a modification of the power law equation by adding a strain exponent term. In comparison with dislocation climb controlled creep in other rock-forming minerals [e.g. Evans and Kohlstedt, 1995] extraordinary high values for stress exponent n are reported for marble (i.e. $n \geq 7$, [Schmid *et al.*, 1980; 1987; Pieri *et al.*, 2001a]). De Bresser [2002] proposed dislocation cross-slip as dominant recovery mechanism for regime 2 instead of classic dislocation climb controlled recovery mechanism. Renner *et al.* [2002] concluded that a Peierls relation [e.g. Weertman, 1957; Frost and Ashby, 1982] better described their data on dislocation creep flow in calcite. The apparent power law parameters (stress exponent and activation energy) were found to be stress, grain size and temperature dependent [Renner *et al.*, 2002]. Rybacki *et al.* [2003] also found a stress dependence of n in Solnhofen limestone torsion experiments where dislocation creep dominated. While most of these proposed model flow laws match approximately with the available experimental data, which are restricted to a small range in strain rate, their prediction very largely when extrapolated to natural strain rates [Barnhoorn *et al.*, 2004].

Rock deformation studies are not limited to supplying lithosphere models the appropriate flow parameters. Fabrics in natural mylonitic shear zones are commonly interpreted in terms of shear sense and strain magnitude based on experimentally derived microstructures and textures [e.g. Ramsay and Huber, 1983]. In doing so geologists typically assume that strain features observed in natural rock represent the latest deformation phase. Inferences about earlier deformation phases are often unavailable due to thermal or tectonic overprint of the fabric. Experimental studies focussing on fabric overprint primarily investigated grain growth dynamics [e.g. Covey-Crump, 1997; Barnhoorn *et al.*, 2005a] and fabric development with strain during constant experimental conditions. However, natural deformation is typically more complex with multiple deformation phases under variable conditions.

Consequently, the role of tectonic overprint in nature from an experimental point of view is poorly constrained.

A series of specially designed torsion experiments on Carrara marble was developed with the aim to understand the rheological and microstructural consequences of multi-stage deformation. By deforming a sandwich sample consisting of three Carrara marble segments with different deformation history and shear sense, complexities like interruption of deformation, strain reversal, and pre-existing strain gradient were investigated. Bulk flow behaviour was simultaneously recorded, allowing the investigation of rheological consequences. This study extended primarily on the work of *Delle Piane and Burlini* [2008], but also built on the already extensive database of single-stage Carrara marble torsion experiments [*Pieri et al.*, 2001a; b; *Barnhoorn et al.*, 2004; 2005a]. Some researchers reported two-stage or multiple stage uniaxial compression tests on Carrara marble [*Rutter and Rusbridge*, 1977; *Covey-Crump* 1994; 1998], and calcite aggregates [*Renner et al.*, 2002]. In these studies, samples were re-loaded under identical kinematics and strain magnitude was small compared to the high strains possible in torsion tests. Strain reversal in torsion tests have also been performed by *Rybacki et al.* [2008], who used hot-pressed anorthite glass powder as sample material.

4.2: Method

Starting material and sample preparation:

Sample material was drilled from the same block of Carrara marble (type Lorrano Bianco) as described and used by *Pieri et al.*, [2001a; b] and *Barnhoorn et al.* [2004; 2005a]. Drilling direction was arbitrarily chosen but consistent for all cores. Carrara marble is a well-investigated natural marble from Tuscany (Italy) with an isotropic fabric, nearly pure calcite composition (98% calcite, and traces of quartz, mica and dolomite). Grain size has a nearly normal distribution with an arithmetic mean 2D grain size of 150 μm . Any shape (SPO) or crystal preferred orientation (CPO) is very weak [*Pieri et al.*, 2001a, b].

Drilled cylindrically shaped cores were sawed and polished and then oven dried at approximately 110 °C for at least 24 h. Together with alumina spacers and partially stabilized zirconia pistons, they were placed inside a polished and cleaned iron jacket with a wall thickness of 0.25 mm. The jacket separated samples from the confining gas inside the pressure vessel. Straight and parallel grooves were scratched gently into the exterior of the iron jackets to record strain development at the periphery of the sample. In addition, the grooves allowed for checking whether slip along sample, segments, or spacer interfaces occurred.

Experiments:

Multi-stage deformation was achieved by exposing Carrara marble samples to two torsion tests. During the second test, the sample was comprised of three segments with different deformation

history. For the first deformation event (D1), six sample cylinders were twisted either clockwise or counter-clockwise to reach a shear strain at the sample periphery of $\gamma = 1, 2.6$ or 5 (Fig. 4.1A). These samples were then cut, and ends polished parallel to create cylindrical segments with a length of 5 mm that would be used as samples for the second deformation event (D2) (Fig. 4.1B). After D1 no surface irregularities or deviations from cylindrical symmetry related to volumetric strain or strain localisation were observed. Some surface damage related to jacket peel-off occurred. Zones with the least surface damage were selected for re-sampling, without re-machining the cylindrical sample periphery (Fig. 4.2A).

Re -sampling and -jacketing has been shown to have no effect on subsequent deformation behaviour. From our experience, we infer that the mechanical and microstructural state of the samples was hardly altered during this pause between experiments. The time during which annealing could potentially alter the fabric was limited to 20 minutes. This annealing time is derived from furnace heating and cooling rates (20 and $>30^\circ\text{C}/\text{min}$, respectively, and minimum temperature for annealing of 600°C) as well as furnace stabilization time. Grain growth due to annealing is time, pressure and temperature dependent and becomes noticeable after 1 hour at our deformation conditions [Covey-Crump, 1997; Barnhoorn *et al.*, 2005a], whereas mechanical strength is not affected by annealing until 75 minutes [personal communication De Raadt, 2009].

D2 sample assemblies consisted of three polished cylindrical segments each with a different D1 history, placed on top of each other like a sandwich (Figs. 4.1C and 2A). The total length of these assemblies was 15 mm and their diameter was approximately 15 mm. D2 was imposed by a counter-clockwise torsion, producing top to the right shear. The amount of imposed bulk shear during D2 was always equal to that in D1, meaning when $\gamma_{D1} = 1$, then $\gamma_{D2} = 1$, when $\gamma_{D1} = 2.6$, then $\gamma_{D2} = 2.6$ and when $\gamma_{D1} = 5$, then $\gamma_{D2} = 5$. Consequently, during D2 tests top and bottom segments were deforming in a continued and reversed sense of shear, respectively, while the centre segment was deforming for the first time. It has been shown before that friction between segments exceeds flow strength [Delle Piane and Burlini, 2008].

Data acquisition and processing:

All experiments were conducted with an internally heated Paterson gas-medium testing machine equipped with an external torsion actuator [Paterson and Olgaard, 2000], in the rock deformation laboratory at ETH Zurich. Pure inert argon gas was used as a confining medium. During experiments, confining pressure was maintained within 1% variation around 300 MPa. Temperature distribution within the furnace was set-up in such a way that around the sample a constant temperature profile within 2 K accuracy existed. A K-type thermocouple was used to measure the temperature at 3 mm above the sample, but within the constant temperature profile. All samples were deformed at 1000 K (727°C). Experimental conditions (Table 4.1) were chosen in such a way that they correspond with previous constant twist-rate torsion experiments on Carrara marble, comprised of one

deformation event, performed by *Pieri et al.* [2001a; b], *Barnhoorn et al.* [2004] and *Delle Piane and Burlini* [2008]. This type of experiments will be referred to from here on as single-stage torsion experiments.

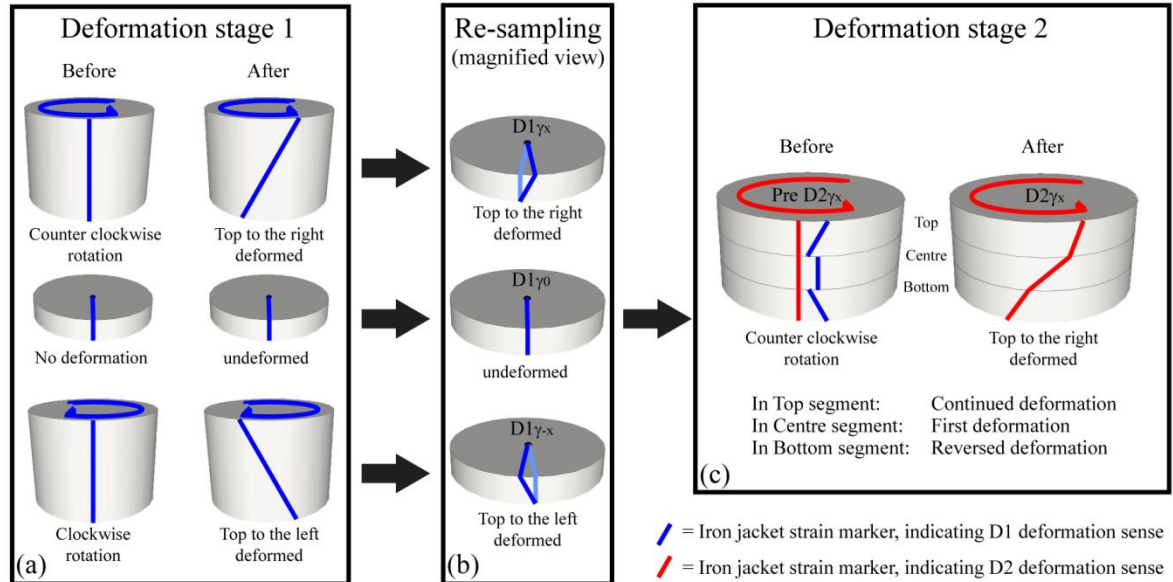


Figure 4.1: A-C) Carrara marble sample set-up for deformation stages 1 (D1) and 2 (D2). D2 sandwich samples are comprised of segments with different D1 history in terms of strain or rotation sense. Shear angles in C reflect arbitrary strain values.

Deformation stage	Experiment number	radius (mm)	length (mm)	Twist rate (rad s^{-1})	Imposed shear strain	Designation
1	P1086	7.5	22.0	8.8×10^{-4}	+ 1.0	$D1_{\gamma_1}$
1	P1119	7.5	21.4	-8.6×10^{-4}	- 1.0	$D1_{\gamma-1}$
1	P1087	7.5	22.1	8.9×10^{-4}	+ 2.6	$D1_{\gamma_{2.6}}$
1	P1116	7.4	21.9	-8.9×10^{-4}	- 2.6	$D1_{\gamma-2.6}$
1	P1130	7.4	22.1	9.0×10^{-4}	+ 5.0	$D1_{\gamma_5}$
1	P1128	7.5	21.5	-8.6×10^{-4}	- 5.0	$D1_{\gamma-5}$
2	P1127	7.4	15.0	6.1×10^{-4}	+ 1.0	$D2_{\gamma_1}$
2	P1120	7.5	15.0	6.0×10^{-4}	+ 2.6	$D2_{\gamma_{2.6}}$
2	P1138	7.4	15.0	6.1×10^{-4}	+ 5.0	$D2_{\gamma_5}$

Table 4.1: D1 and D2 torsion experiment characteristics. For all experiments, confining pressure and temperature were held constant at 300 MPa and 727 °C, respectively. Variation in sample geometry is compensated by adjusted twist rate, to allow a constant peripheral bulk shear strain rate of $3 \times 10^{-4} \text{ s}^{-1}$. Positive twist rate corresponds to counter-clockwise rotation and results in negative strain.

An internal load cell measured torque during experiments with an accuracy of 0.2 Nm. Torque corrections include compensation for confining pressure changes and for initial internal torque. Torque drift was not investigated, since sample re-loading was performed in two separate torsion experiments and no anomalous mechanical behaviour was recorded during D1 tests. No corrections for iron-jacket

were applied, since this would only offset torque values slightly (< 2.5%) at these experimental conditions. Resulting torque values (M) were then converted to shear stress (τ) using [Paterson and Olgaard, 2000]

$$\tau = \frac{\left(3 + \frac{1}{n}\right)}{2\pi r^3} M \quad (\text{eq. 4.1})$$

for power-law creep, where, r is sample radius and n is the stress exponent. For all conversions using equation 4.1, n is assumed 10, following *Barnhoorn et al.* [2004] and *Delle Piane and Burlini* [2008]. From equation 4.1 it is clear that the calculated shear stress is quite insensitive (<2 %) to the exact value of n for $n > 4$. Previous studies on Carrara marble have shown that the stress exponent n varies with deformation conditions and finite strain between 6 and 10 [e.g. *Schmid et al.*, 1980; 1987; *Rutter*, 1995; *Pieri et al.*, 2001a; *De Bresser*, 2002; *Barnhoorn et al.*, 2004]. Depending on sample dimensions twist rate during D1 and D2 experiments was adjusted between 6.0×10^{-4} and 9.0×10^{-4} rad s^{-1} , corresponding to a shear strain rate of $3.0 \times 10^{-4} s^{-1}$ at the sample periphery. Positive and negative twist rate values during a torsion test lead to top to the right and left shearing, respectively. From the imposed strain rate, time was transformed into bulk shear strain values. The shear strain in the sample segments after experiments is calculated from the tangent of the shear angle ψ , which is recorded by the strain markers in the assembly jacket. The resulting shear strain gives the shear strain rate when divided by the duration of the experiment in seconds.

We benefited from the pre-existing database on Carrara marble torsion tests by comparing D2 mechanical data and fabric with the typical behaviour found in single-stage torsion experiments under nominally identical conditions. All mechanical data presented in this paper, including those from *Delle Piane and Burlini* [2008], *Pieri et al.* [2001a] and *Barnhoorn et al.* [2004] were treated equally with regard to torque corrections. Since raw data from *Pieri et al.* [2001a] was not numerically available, we took strain/stress curves directly from the paper and added the strength contribution of the iron-jacket.

D2 Microstructural analysis:

After D2 experiments, deformed samples were retrieved from their iron jackets. A $< 10 \mu\text{m}$ thin section was prepared from a slice cut close to the periphery and parallel to the cylindrical axis (Fig. 4.2B). Although derived near sample periphery, thin section cuts represent lower (-10%) than maximum shear strain. Photographs were taken with a Jenoptic C5 camera attached to a NIKON Optiphot polarisation microscope.

For electron backscatter diffraction (EBSD) analysis, another tangential surface of the remaining samples was first mechanically polished with fine-grained abrasive paper until sufficiently large surface, but still close to the rim, was exposed. Then diamante paste was used for fine polishing.

Finally, the exposed surfaces were polished for one to two hours using an alkaline colloidal silica suspension (25 nm particle size). Texture analysis was performed on a FEI Quanta 200F scanning electron microscope (SEM) equipped with a Hikari EBSD module made by EDAX. SEM working conditions were 20 kV acceleration voltage, 15 mm working distance, 40 μm aperture and a spot size of 5, resulting in a nominal beam current of 7 nA, at a chamber pressure of 50 Pa (water vapour). The tilt angle of the sample inside the SEM chamber was 70°. EDAX/TSL software package OIM 5.2 was used to collect and index EBSD patterns. Texture index J was determined to quantify CPO strength. Contoured pole figures were calculated from collected orientation data using harmonic series expansion to a series rank of 28 and Gaussian smoothing of 10° (following Bunge [1982]) as used in OIM 5.2, which is equivalent to 16.65° Gaussian smoothing in Berkeley Texture Package (Beartex) (following *Wenk et al.* [1998]). Ambiguous indexing points (confidence index <0.1) were disregarded for pole figure calculations.

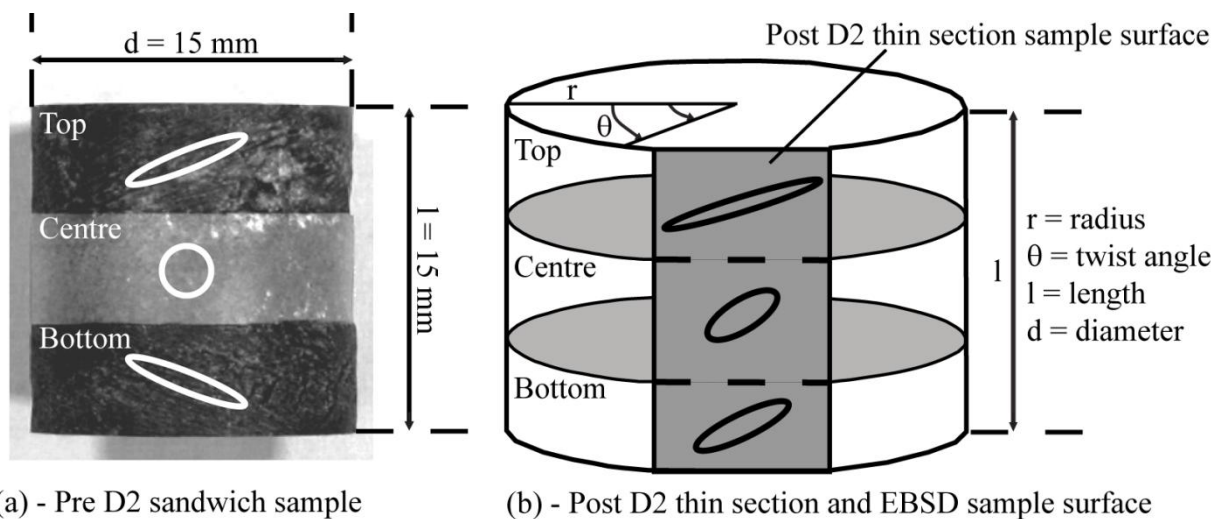


Figure 4.2: A) Pre-D2 sample with equally deformed, but opposing sense top and bottom segments and undeformed centre segment. B) Post-D2 sample with plane of thin section cut indicated (modified after *Pieri et al.* [2001a and b]). Strain ellipses in panels A (D1) and B (D1 + D2), indicate correct shear sense, but not necessarily correct ratios.

4.3: Results

Now we present data of D2 experiments in a framework set by single-stage torsion experiments on Carrara marble provided by *Pieri et al.* [2001a; b], *Barnhoorn et al.* [2004; 2005a] and *Delle Piane and Burlini* [2008] and from D1 experiments in this study. Experimental results after D2 comprise of several types of data: strain variation, shear stress/shear strain curves, thin section microstructures, foliation orientation, and CPO pole figures.

D2 Strain variation:

Strain markers on the iron jacket indicate for all D2 experiments an extraordinary variation in strain between the different segments, while strain is homogeneous along the axis of each individual segment (Fig. 4.3). Table 4.2 lists the measured and calculated data derived from figure 4.3.

Quantitative analysis of the observed strain variation is presented in table 4.2 as well. Strain markers show no offset across the boundaries between ceramic segments and sample or between the sample segments, indicating that no slip occurred during the experiments. Experiment P0772 by *Delle Piane and Burlini* [2008] also resulted in strain variation across sample segments with initial deformation contrast, which is added here for reference.

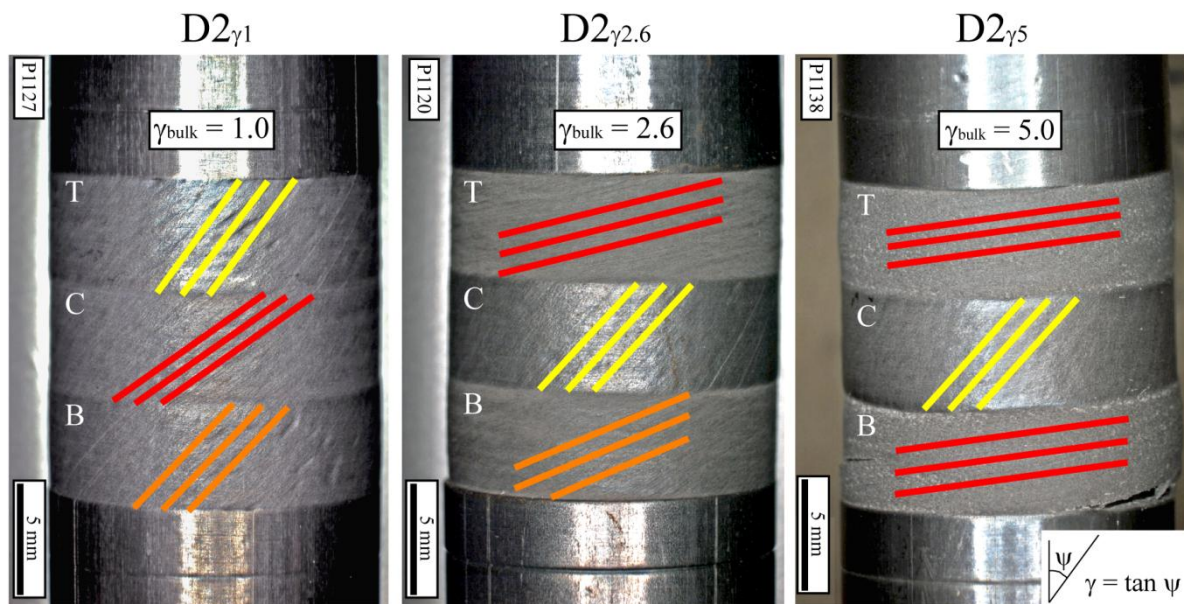


Figure 4.3: Strain markers, acting as passive lines, after D2 experiments indicate homogeneous strain within each segment, but strain variation between the individual segments of the sandwich samples. Solid parallel lines, black, grey and white for maximum, intermediate and minimum strain, respectively, highlight the strain ratios.

For the $D2_{\gamma 1}$ experiment, maximum and minimum strain are recorded by the centre and top segment respectively. For higher strain D2 experiments, maximum and minimum strains are accommodated oppositely in the top and centre segments, respectively (Fig. 4.3).

In the D2 experiments, the mean between the three segments of shear strain and shear strain rate are equal to bulk shear strain and imposed shear strain rate. This confirms once more that slip between samples was prevented.

To characterise the strain variation independently of different bulk shear strain reached in D2 experiments, parameters for shear strain -contribution, -factor and -rate ratio are introduced. Shear strain contribution is defined as the percentage of shear in a sample segment relative to the total shear of the bulk sample. In the case of homogeneous deformation, each of the three equal length sample segments should have a shear strain contribution of 33%, making a sum of 100%. A deviation from 33% in the case of three equally sized segments implies strain variation. The shear strain factor λ is a

strain independent measure for the strain variation applicable to three equally sized-segmented samples following:

$$\lambda = \frac{\gamma_2^2}{\gamma_1\gamma_3} = \frac{\gamma_2/\gamma_1}{\gamma_3/\gamma_2} \quad (\text{eq. 4.2})$$

where, $\gamma_1 > \gamma_2 > \gamma_3$. The expression is derived as a dimensionless parameter, in analogy to the k-parameters for characterisation of strain ellipsoids in a Flinn-diagram [Ramsay and Huber, 1983]. Since λ is calculated from strain ratios, and therefore dimensionless, it applies to shear strain -rate and -contribution as well. For $\lambda = 1$, no strain variation exists. For $\lambda < 1$, lowest and intermediate strain are more similar than intermediate and highest strain. The opposite is true for $\lambda > 1$.

It is more appropriate to use the shear strain rate ratio, γ_1/γ_2 , in the case of two-segmented samples, for example, P0772 in *Delle Piane and Burlini* [2008].

		Shear strain					
	Segment	Angle (°)	Value	Mean rate (s ⁻¹)	Contribution	Factor	Rate ratio (max/min)
D2 _{γ1} (P1127)	Top	36.6 ± 0.7	0.74 ± 0.02	2.2x10 ⁻⁴	24 %	0.9	1.9
	Centre	54.8 ± 0.3	1.42 ± 0.02	4.1x10 ⁻⁴	45 %		
	Bottom	44.1 ± 1.2	0.97 ± 0.04	2.8x10 ⁻⁴	31 %		
	<i>Bulk</i>		1.04	3.0x10 ⁻⁴	100 %		
D2 _{γ2,6} (P1120)	Top	76.9 ± 1.3	4.46 ± 0.5	5.1x10 ⁻⁴	58 %	1.3	4.7
	Centre	42.7 ± 0.4	0.92 ± 0.01	1.1x10 ⁻⁴	12 %		
	Bottom	66.2 ± 0.6	2.28 ± 0.07	2.6x10 ⁻⁴	30 %		
	<i>Bulk</i>		2.56	3.0x10 ⁻⁴	100 %		
D2 _{γ5} (P1138)	Top	81.9 ± 0.4	6.99 ± 0.3	4.2x10 ⁻⁴	47 %	8.0	7.9
	Centre	41.5 ± 0.5	0.89 ± 0.02	5.3x10 ⁻⁵	6 %		
	Bottom	81.9 ± 0.5	7.02 ± 0.5	4.2x10 ⁻⁴	47 %		
	<i>Bulk</i>		4.97	3.0x10 ⁻⁴	100 %		
P0772 [Delle Piane and Burlini, 2008]	Top	61.3 ± 1.1	1.83 ± 0.09	1.8x10 ⁻⁴	88 %	N.A.	7.2
	Bottom	14.1 ± 0.4	0.26 ± 0.01	2.6x10 ⁻⁵	12 %		
	<i>Bulk</i>		1.04	1.0x10 ⁻⁴	100 %		

Table 4.2: Quantitative description of strain variation after D2. Errors in shear angle estimates are propagated to errors in shear strain, but subsequent errors are omitted for all the other entities for reasons of simplification. Shear strain factor (λ) cannot be calculated for two segmented samples.

D1 and D2 mechanical behaviour:

Figure 4.4A shows a diagram with shear stress plotted against shear strain for all D1 experiments that yielded reliable mechanical data. Additionally, results from single-stage torsion experiments, equal in principal and experimental conditions to D1 tests, on Carrara marble using the same deformation apparatus are plotted. D1 curves, despite of considerable scattering between the experiments, follow a similar behaviour as in previous studies and fit within the general trend.

This trend is summarized by a rather wide envelope of stress-strain curves, related to experiment reproducibility and sample variability. What remains clear is the typical hardening behaviour after yielding up to $\gamma = 0.5-0.8$. Peak stresses are maintained until $\gamma = 1$, after which work softening initiates. By $\gamma = 5$, most curves have reach steady state flow conditions. The envelope of curves is transferred to figure 4.4B as best representative of general D1 stress behaviour with strain. Regrettably, individual D1 curves show a considerable variability within the envelope. This is one reason why we did not attempt to follow individual runs from D1 to D2 in their stress-strain curves. The other reason for this lies in the nature of D2 sandwich samples, which originate from three different D1 experiments and not just one.

The $D2_{\gamma 1}$ experiment (P1127) shows a slightly different mechanical behaviour than the range of single-stage torsion experiments for Carrara marble. The yield stress falls well within that broad range, but the peak stress is relatively low, thereby indicating limited work hardening. Both peak stresses are recorded at similar shear strain values ($\gamma = 0.8$). Strain softening initiated quickly after peak stress, but as the experiment was stopped shortly afterwards at $\gamma = 1$, it could not be decided whether constant stress condition was reached.

The $D2_{\gamma 2.6}$ experiment (P1120) initially shows a very similar mechanical behaviour compared with $D2_{\gamma 1}$. Peak stress however, is reached earlier at $\gamma = 0.6$. Work softening persists until $\gamma = 1.5$, where constant stress condition is reached at a flow stress of 45 MPa.

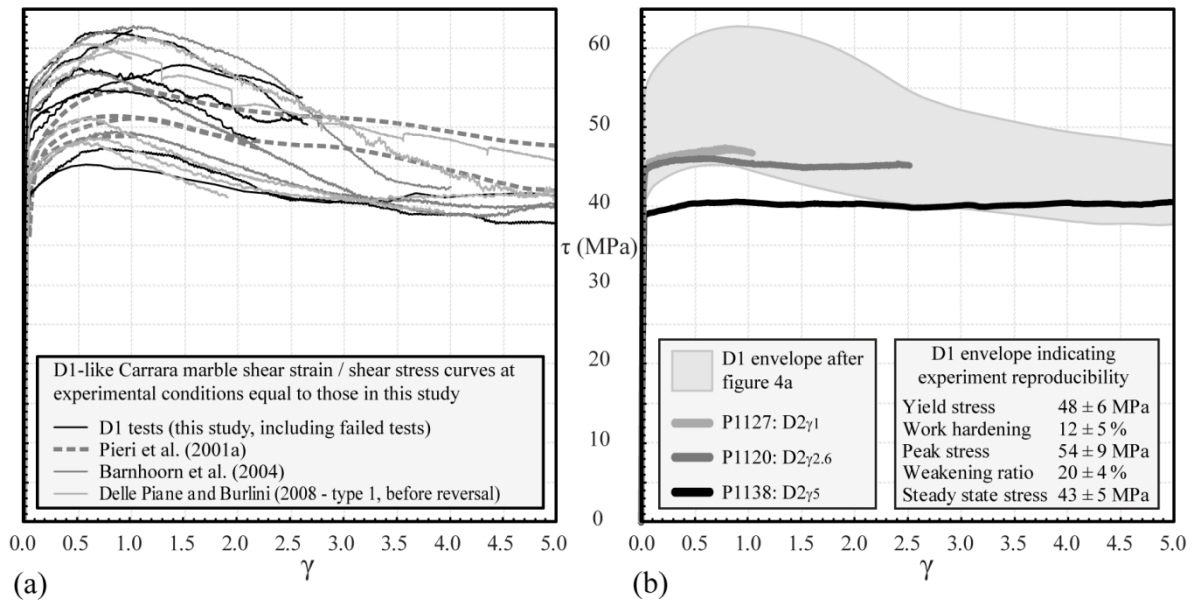


Figure 4.4: A) Collection of shear stress-shear strain curves for single-stage torsion deformation tests, including D1, with identical experimental conditions as in this study. B) Curves of figure 4.4A represented by light grey band in comparison with bulk D2 sample stress-strain behaviour. Experimental reproducibility for D1-like curves is expressed by the width of the light grey band and error of values in the table.

The high strain D2 experiment, D2 $_{\gamma 5}$ (P1138) yields at a significantly lower flow stress and work hardens 4-8 %. From $\gamma = 0.5$, peak stress was reached and flow continued at little over 40 MPa without significant work softening.

D1 Microstructures:

Figure 4.5 displays cross-polarized light micrographs of Carrara marble at different stages of shear deformation, corresponding to the amount of deformation produced during D1 experiments in this study. In the figure, micrographs are placed in such a format that they schematically represent the starting set-up for D2 experiments. Bottom segment micrographs are flipped versions of the top, and for the three centre segments the same micrograph is used repeatedly. Sources for the micrographs were previously prepared thin sections from experiments P089 ($\gamma = 1$) and P143 ($\gamma = 2.3$) performed by *Pieri et al.* [2001a] and P267 ($\gamma = 5.3$) performed by *Barnhoorn et al.* [2004]. In figure 4.5, from left to right in both top and bottom segments shear strain changes from 1.0 to 2.3 to 5.3. The micrographs are oriented in such a way that the shear zone boundary is horizontal. Centre images represent a piece of undeformed Carrara marble and lack any reference orientation. D1 samples were not always available for thin sectioning as most of the material was used for D2 experiments. Experimental conditions in P089, P143 and P267 were nominally identical to ours, such that their fabric is equivalent to respective D1 fabric, as was the mechanical behaviour.

Solid white lines and ellipses in figure 4.5 represent the shear angle and strain ellipse, respectively, corresponding to the finite shear strain in the respective segment. Strain ellipses are constructed by graphically shearing a circle to the shear of the related segment. Dashed and dotted white lines represent the visually estimated traces of foliation S_a and S_b , respectively, defined by grain

stretching, alignment of grain boundaries and/or aggregates of recrystallised grains. Similar, but coloured lines are used in figure 4.6, for microstructures after D2 experiments. The foliation subscripts a and b are chosen instead of the more common use of 1 and 2 to avoid confusion regarding relative timing of the two deformation stages. S_a and S_b are believed to have developed simultaneously and are therefore not necessarily associated with either D1 or D2. All mentioned foliation orientations are measured with respect to the normal of the shear zone boundary (SZB) and thus directly comparable with the shear angle ψ .

Past studies described the progressive change of microstructure in Carrara marble deformed to high strains in detail already [*Pieri et al.*, 2001a; *Barnhoorn et al.*, 2004]. At low strain, grains are dominantly deforming by twinning and dislocation creep processes, producing rather homogeneously stretched elongate grains with twins and patchy extinction patterns in the form of undulose extinction and deformation bands. Subgrains and later recrystallised grains can be identified, especially near grain rims, producing a core-mantle like structure. Above a shear strain of around 1, recrystallisation becomes more dominant with strain. Relict grains continue stretching, but the amount of subgrains and recrystallised grains is increasing rapidly. Hardly any new twins are recognizable. The amount of elongated primary grains decreases with increasing strain. At the strain where constant stress is reached ($\gamma \approx 5$), elongated relict grains are barely visible and the sample appears pervasively recrystallised. Details on grain size distribution, orientation angle of SPO and foliation, grain aspect ratios and recrystallisation fractions are presented by *Pieri et al.* [2001a], *Ter Heege et al.* [2002] and *Barnhoorn et al.* [2004].

D2 Microstructures:

After the D2 experiments, the sandwich samples experienced two deformation stages in the top and bottom segments and one deformation stage in the centre segment. The developed microstructure is different for nearly each segment and experiment.

Figure 4.6 displays micrographs of the characteristic microstructure in each sample segment after D2 experiments. White lines and ellipses indicate shear angle and maximum principal axes, associated with the finite shear strain of the respective segment. Red and green lines represent traces of S_a and S_b foliation, respectively, defined by grain stretching, grain boundary alignment and/or aggregates of recrystallised grains, as in figure 4.5.

The microstructure for the top segment of the $D2_{\gamma 1}$ experiment ($\gamma = 1.7$) is characterized by a bi-modal grain size distribution with large, elongated and internally deformed old grains, and very fine and less deformed recrystallised grains. The stretched old grains display thin twins, undulose extinction, deformation bands and subgrains. The recrystallised grains make up about 10 vol. %, and dominate along former grain boundaries at the rims of the stretched old grains, producing an elongated core and mantle structure. Traces of the e-twinning planes appear preferentially sub-parallel to the

stretching direction of the grain. Grain stretching defines a continuous foliation (S_a) at flat angle with respect to the shear zone boundary.

The centre segment experienced a lower finite shear strain ($\gamma = 1.4$) than in the top. Still, a bi-modal grain size distribution is produced by fine recrystallised grains and big stretched old grains. Volumetrically, less recrystallised grains appear, about 5%. The centre segment shows twinned grains and grains with undulose extinction. Twin planes are parallel to the stretching direction of grains. In comparison with the top segment, foliation S_a is 6° steeper with respect to the SZB.

Remarkably different is the microstructure in the bottom segment in $D2_{\gamma 1}$ ($\gamma = 0$). Relict grains lost the typical stretching related SPO, but a core- and rim-like microstructure is clearly present. Relict grain shape is equant with serrated grain boundaries. Recrystallised fine grains make up 5 vol.%. Evidence for internal deformation includes high concentration of thin twins and presence of some lensoidal twins, undulose extinction and deformation bands. Occasionally, multiple sets of twins are recognizable, and two orientations dominate. Often, bends in twins correlate with crosscutting deformation bands. No foliation plane could be identified, due to lack of SPO.

Top segment of the $D2_{\gamma 2.6}$ sample ($\gamma = 6.9$) is characterized by a microstructure best described as a highly stretched and recrystallised calcite aggregate. Former grains are faintly recognizable by zones with similar extinction colour. Within these former grains, small differences in extinction colour indicate recrystallised grains with an average size of 5 to 10 μm . The former grains are strongly stretched, but with lobate to serrated boundaries, whereas the fine recrystallised grains are equant and their boundaries are smooth. Rare twin traces appear parallel to the long axis of the former grain relicts. Two foliation planes are recognized, a high-angle S_a and low-angle S_b , separated by about 43° .

The centre segment realized the least shear strain during $D2_{\gamma 2.6}$ ($\gamma = 0.9$). Old grains are slightly stretched, intensely twinned and occasionally contain deformation bands and undulose extinction. Some of the twins are bent. Rarely, grains are surrounded by a thin layer of fine-grained recrystallised calcite, forming a core-mantle like structure and serrated grain boundaries. The recrystallised grains make up for around 2 vol.%. The trace of the twins is often parallel to the direction of maximum stretching of the grain. A near 45° S_a foliation is marked by weak grain SPO.

The bottom segment for the $D2_{\gamma 2.6}$ ($\gamma = -0.3$) experiment has a distinctive microstructure. Two deformation stages of roughly equal shear strain magnitude, but opposite sense produced a well-developed bi-modal grain size distribution. The volume percentage of large relict grains (70-120 μm) and recrystallised grains (3-10 μm) is about equal. Nearly all large grains are stretched in the direction of D2 shearing. Grain boundaries of large grains are serrated. Stretched grains display the highest abundance of twinning and undulose extinction. Twins are occasionally bent, but primarily oriented towards the direction of maximum D2 strain. In some large grains, a second set of twins is present. S_a foliation is recognizable from grain SPO of stretched grains. A weak S_b foliation with low-angle orientation is identifiable as well. The angle between S_a and S_b is around 34° .

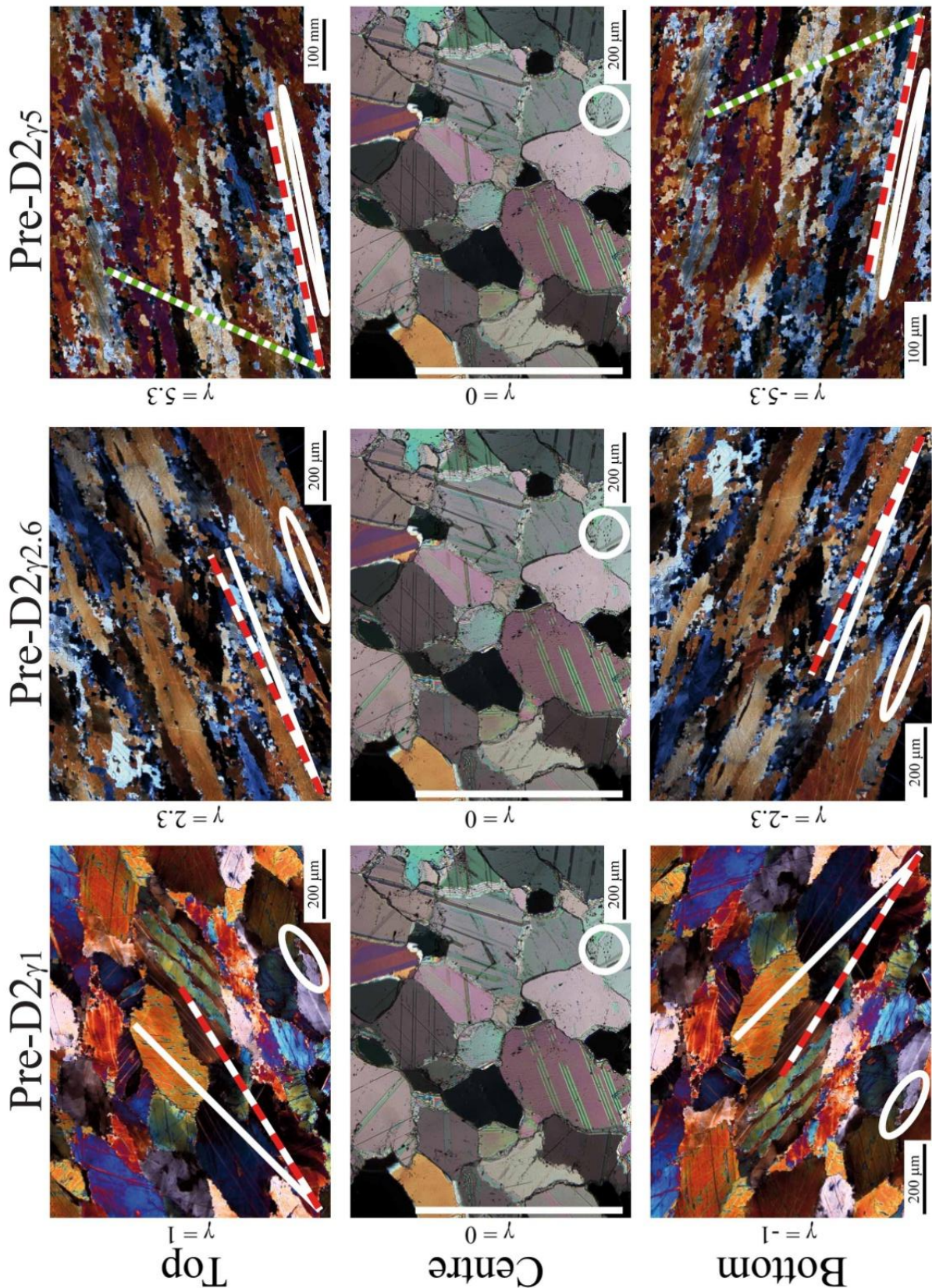


Figure 4.5: Starting material microstructure of D2 sandwich samples. The cross-polarized light micrographs originate from thin sections from torsion tests by *Pieri et al.* [2001a] and *Barnhoorn et al.* [2004]. Thin sections that best represent D1 microstructure (i.e. experimental conditions were identical to those used in this study) were chosen. Top segment images were artificially mirrored to represent D2 bottom segment starting fabric. For all centre segments, one micrograph representing undeformed Carrara marble was used. Note the change of magnification for micrographs that display a dominantly recrystallised microstructure.

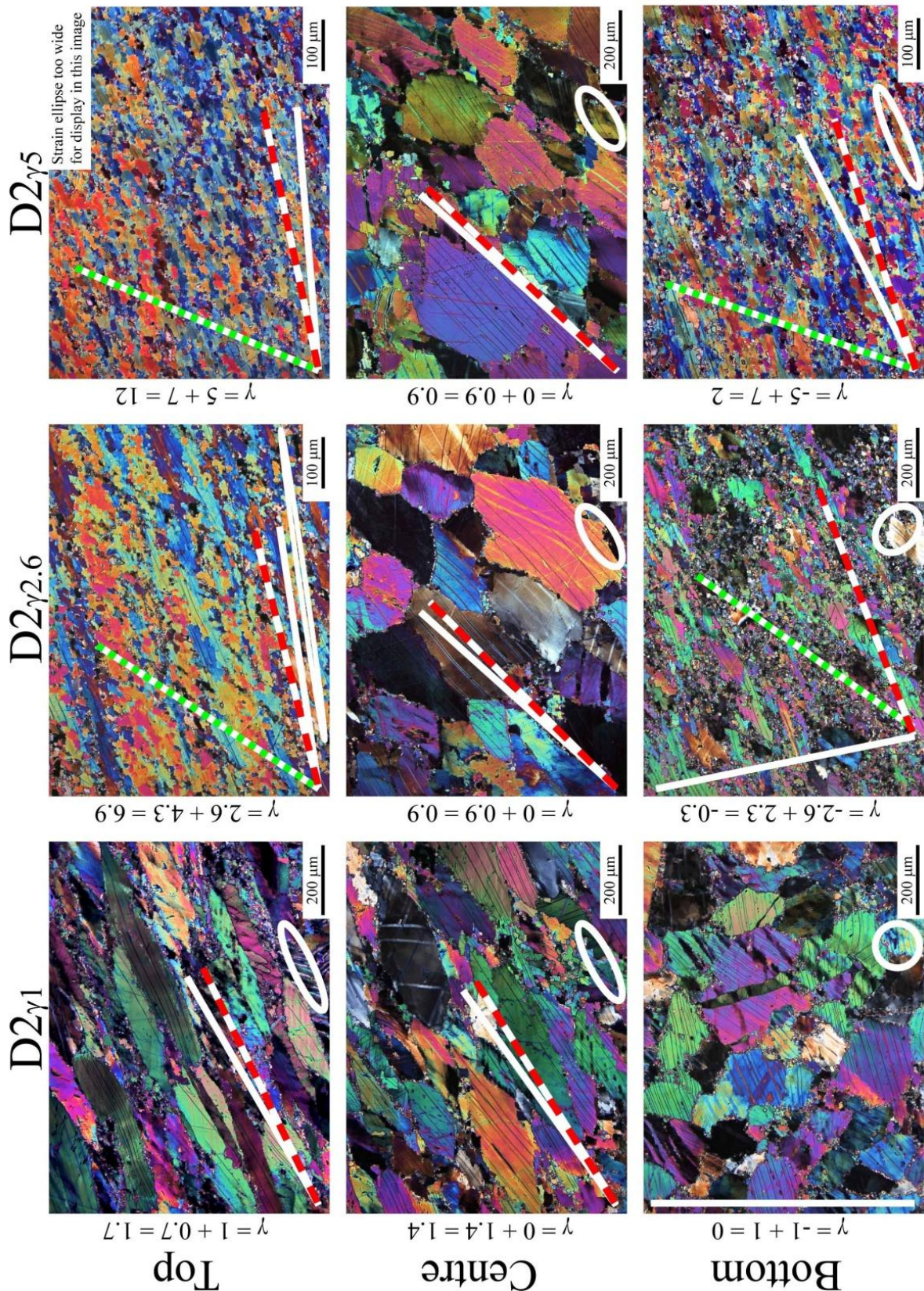


Figure 4.6: Cross-polarized light micrographs of thin sections from the rim of D2 sandwich segments, after D2. The ellipse for top segment of D2 γ_5 is too stretched for display. D2 shear strain values displayed in this figure are rounded up in comparison with the associated values in table 2. For each micrograph finite strain (calculated as sum of γ_{D1} and γ_{D2} , with top to the right shearing taken as positive strain) is indicated. Note the change of magnification for micrographs that display a dominantly recrystallised microstructure.

The microstructure of the top segment in the D2_{γ5} experiment ($\gamma = 12$), is characterized by a completely dynamically recrystallised microstructure. New grains are small and nearly equant. They show little sign for internal deformation and contain few twins. Hardly any traces from relict grains survived. Two foliation planes are apparent: 1) an almost flat primary foliation S_a, defined by SPO of clusters of recrystallised grains with similar crystal orientation, inherited from former relict grains. 2) A poorly developed steep secondary foliation S_b, defined by trails of recrystallised grains and subgrain boundaries. The angle between S_a and S_b is around 55°.

The centre segments for both the D2_{γ5} and D2_{γ2.6} experiments were deformed to equally small shear strain, $\gamma = 0.9$, although at different strain rates. Grain size and shape is similar and both segments show the same evidence for internal deformation, without significant contributions from dynamic recrystallisation.

In the bottom segment for the D2_{γ5} experiment ($\gamma = 2.0$), microstructure appears strongly deformed with nearly pervasive recrystallisation to fine grains. In fact, the microstructure is similar to that of the top segments of the D2_{γ5} and D2_{γ2.6} experiments. The matrix of fine-grained recrystallised grains contains irregularly shaped and strongly stretched clusters of similarly oriented recrystallised grains that represent former relict grains. However, S_a and S_b orientation angles are smaller (72° vs. 78°), and (19° vs. 24°), respectively.

Foliation development:

Microstructural development is quantified by measuring foliation orientation with respect to the normal to the SZB, changing with strain. Undeformed Carrara marble lacks any foliation. At the onset of torsion deformation, grain shape changes according to the simple shear strain ellipse, with the infinitesimal principal strain axes at 45°, producing a SPO defined foliation.

The reference for foliation orientations after D2 is provided by single-stage torsion experiments on Carrara marble, including *Pieri et al.* [2001a], *Barnhoorn et al.* [2004] and *Delle Piane and Burlini* [2008] and D2 centre segments from this study. Figure 4.7 plots S_a (circles) and S_b (triangles) orientations from single-stage (black), continued (grey) and reversed (open) torsion tests, as a function of (finite) shear strain. Also included are theoretical curves for passive line rotation (ψ , solid line, after *Ramsay* [1967], Eq. 3.71) and principal axis of strain ellipse rotation ($\beta = 90 - \theta'$, dashed, after *Ramsay and Huber* [1983], Eq. 2.4), in simple shear.

Data points from single-stage torsion experiments indicate a rapid increase in S_a orientation with strain from 45° onwards. As strain increases S_a rotates gradually towards the SZB. The reproducibility associated with this trend is expressed by a light grey band. Initially this band includes both theoretical curves. At larger strain, S_a-orientation increases more slowly with strain in comparison with the curves. For $\gamma > 7$, inclination of main foliation is systematically lower than of

theoretical curves. However, foliation orientation is more difficult to determine at high strain, since elongated relict grains are removed by dynamic recrystallisation.

S_a orientation in continued torsion experiments plots without exception within the trend for single-stage experiments. Whereas S_a orientations from reversed torsion tests are systematically below that trend.

The angle of S_b foliation develops in strongly recrystallised Carrara marble (i.e. $\gamma > 5$) [Pieri *et al.*, 2001a; Barnhoorn *et al.*, 2004; Delle Piane and Burlini, 2008] and Solnhofen limestone [Rybacki *et al.*, 2003; Barnhoorn *et al.*, 2005a]. S_b orientation data from this study alone (i.e. open and grey triangles in figure 4.7) suggest a gradually decreasing angle with strain between $\gamma = 5$ and 12. This trend is highlighted by a grey envelope. Data from single-stage torsion tests by Pieri *et al.* [2001a], Barnhoorn *et al.* [2004] and Delle Piane and Burlini [2008] partly fit this trend. A data point at $\gamma = 10.5$ clearly plots outside the envisaged trend.

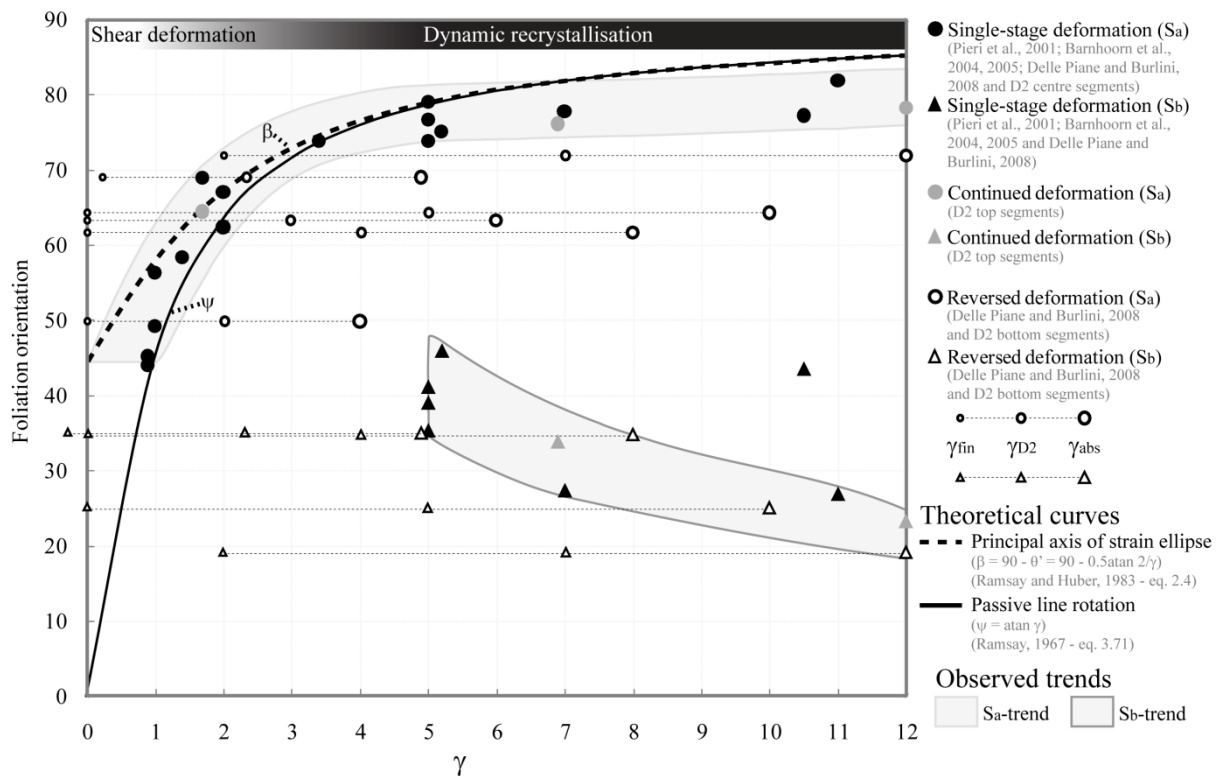


Figure 4.7: S_a - and S_b -orientation development with shear strain. S_a foliation development with strain from single-stage torsion experiments is represented by the light grey bounded grey band. S_b -orientation data suggest, a trend, which is highlighted by a dark grey bounded grey band.

CPO development:

The CPO development in single-stage torsion experiments is well known for the experimental conditions of this study [Pieri *et al.*, 2001a; b; Barnhoorn *et al.*, 2004], and thus suitable as reference for the textural data from D2 experiments in this study. The left part of figure 4.8 displays that texture evolution in basal and r-plane pole figures with grey-level contours.

No CPO is observed in undeformed Carrara marble. With increasing strain, texture with monoclinic symmetry develops, often referred to as shearing CPO [Pieri *et al.*, 2001a; b; Barnhoorn *et al.*, 2004]. Shearing CPO is best explained by intracrystalline slip with $r\{10\bar{1}4\}$, $f\{01\bar{1}2\}$ and $c\{0001\}$ slip systems activated in different degree [Pieri *et al.*, 2001b]. The c-axes are distributed into two maxima, one perpendicular to the SZB (trace of SZB is horizontal in the pole figures), and one oblique to the shear plane (40-45°) and against the shear sense. Until a shear strain of around 2, shearing CPO dominates. At higher strains, with increasing dynamic recrystallisation, texture changes as dynamic recrystallisation comes into play. This recrystallisation CPO is characterized by well-developed c-axis maxima with 60-85° degrees dip and orientation normal to the shear direction, and r-poles maxima in orthorhombic symmetry with one of them nearly perpendicular to the SZB. To explain this recrystallisation CPO, according to models based on self-consistent polycrystal plasticity theory, dominating contribution by the $r\{10\bar{1}4\}a < \bar{1}2\bar{1}0 >$ slip system is required [Pieri *et al.*, 2001b; Barber *et al.*, 2007].

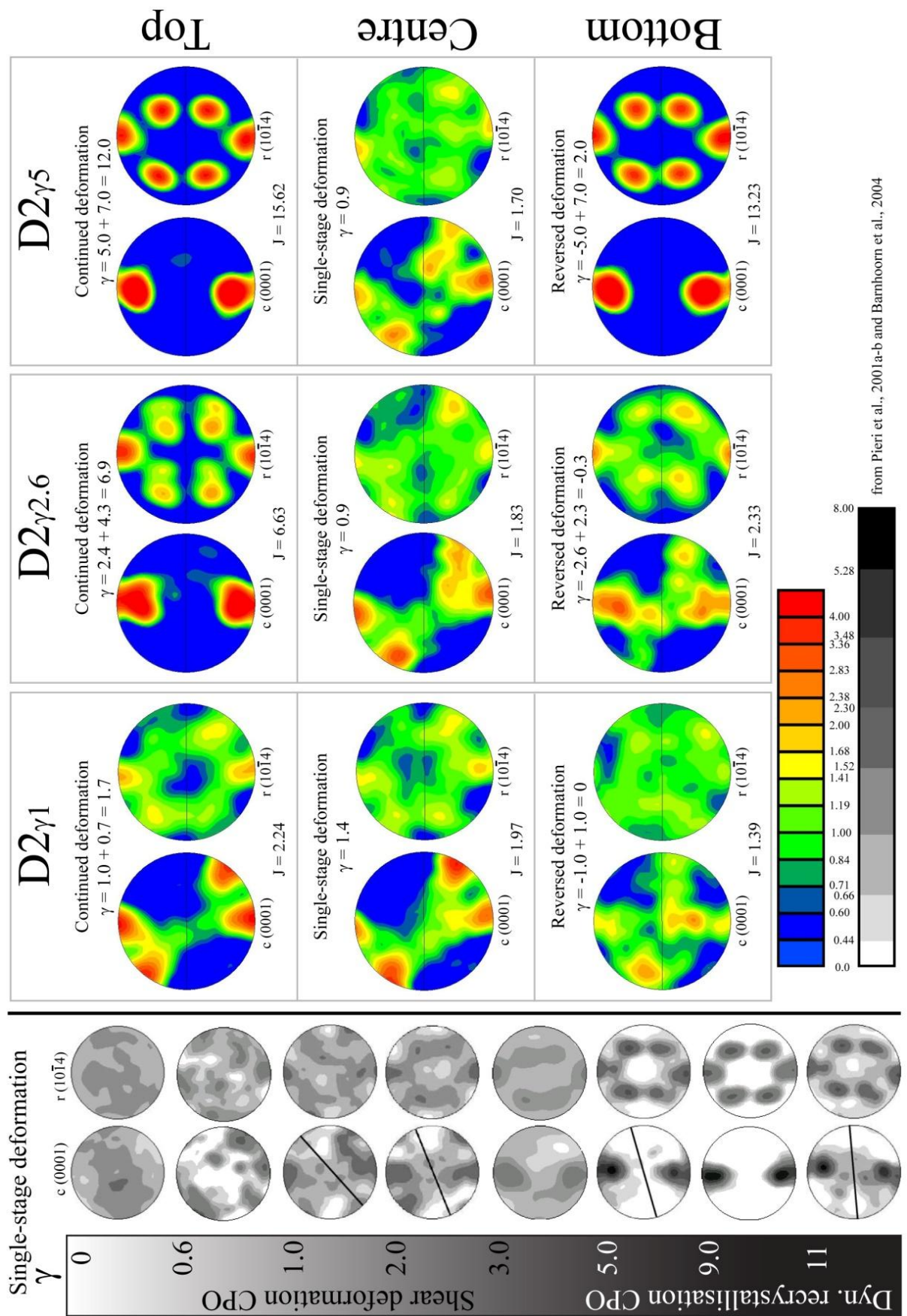
D2 Carrara marble samples show various CPO developments during single-stage, continued and reversed deformation in the centre, top and bottom segments, respectively (right part of figure 4.8). The top segment after $D2_{\gamma_1}$ ($\gamma = 1.7$) displays a strongly developed shear deformation CPO that implies a top to the right shear sense. The texture of the centre segment after $D2_{\gamma_1}$ ($\gamma = 1.4$) is similar in type to that of the top segment, but lesser developed.

In the bottom $D2_{\gamma_1}$ segment ($\gamma = 0$), CPO is weakly developed. Both shear deformation and recrystallisation texture components can be recognized. Although, the c-axis maxima associated with shearing deformation are rotated about $15 \pm 14^\circ$ towards the SZB, in comparison with typical shearing CPO. The bottom segment basal plane pole figure indicates a top to the right shearing. Pole figures of the top segment of $D2_{\gamma_2.6}$ ($\gamma = 6.9$) show a well-developed recrystallisation CPO. No shear sense could be inferred from the pole figures, due to orthorhombic symmetry of the dynamic recrystallisation texture.

The centre segment of the same experiment ($\gamma = 0.9$) established a shearing deformation texture with maxima positions that indicate apparent top to the right shearing.

In the bottom segment of the $D2_{\gamma_1}$ experiment ($\gamma = -0.3$) the CPO developed into a combination of shearing deformation and dynamic recrystallisation texture. Strongest maxima are associated with a recrystallisation CPO, although remnants of the characteristic girdle for the shearing CPO are also apparent. The shearing CPO girdle infers a top to the right sense of shear.

The top and bottom segments of $D2_{\gamma_5}$ have almost identical pole figures. In both segments, despite the large difference in finite shear strain, a very strongly developed dynamic recrystallisation texture is recorded. The J-index values for both segments indicates that CPO in the top segment is slightly more developed ($J = 15.62$ vs. 13.23). The centre segment in $D2_{\gamma_5}$ has a shearing texture that is similar in both type and magnitude to that of the centre segment in the $D2_{\gamma_2.6}$ experiment.



from Pieri et al., 2001a-b and Barnhoorn et al., 2004

Figure 4.8: Pole figures (lower hemisphere, equal area projection) for single-stage deformation (left) and D2 (right) experiments. Legends for grey scale, and coloured pole figures are aligned for quick comparison. Grey scale pole figures originate from Pieri et al. [2001a]; Barnhoorn et al. [2004] and represent deformation experiments run under similar conditions as in this study.

4.4: Discussion

We followed up on and extended work by *Delle Piane and Burlini* [2008], who first explored rheological and microstructural consequences of complex deformation history in Carrara marble. Our observations after two-stage torsion experiments are discussed in light of results from single-stage torsion experiments under nominally identical experimental conditions. A rheological interpretation for observed D2 strain variation is given, followed by a discussion on developed fabrics. We conclude with a discussion on geological implications.

Strain variation:

Single-stage torsion experiments [*Pieri et al.*, 2001a; *Barnhoorn et al.*, 2004; 2005a] always resulted in strain distributions that are homogeneous along any profiles parallel to the cylinder axis. Iron jacket strain markers for D2 experiments in this study clearly show that the strain is homogeneous within, but variable between sample segments. Such a variation was expected to occur during D2, in a way similar to the type 2 experiment P0772 by *Delle Piane and Burlini* [2008]. Type 2 refers to a special torsion experiment on Carrara marble, with a sample comprised of two segments, one with pre-existing strain of $\gamma = 5$ and one undeformed. Strain variation was observed after the torsion experiment, with the highest strain achieved in the previously deformed segment [*Delle Piane and Burlini*, 2008].

The observed strain variation in this study is not to be confused with strain localisation or strain partitioning; terms that are commonly used in relationship with heterogeneous strain. Strain localisation refers to a zone of higher strain in otherwise homogeneous material. Strain partitioning is often linked with compositional variation within a deforming sample [e.g. *Ji et al.*, 2004; *Bystricky et al.*, 2006; *Holtzman and Kohlstedt*, 2007]. Strain partitioning has been defined before as the scheme of partition of finite bulk strain into components based on different deformation mechanisms [*Mitra*, 1976]. Neither strain terms apply to the strain variation observed in this study. Sample scale strain variation in solid rock experimental deformation is typically associated with rheological variation induced by compositional differences [e.g. *Bons and Urai*, 1996; *Barnhoorn et al.*, 2005b; *Bystricky et al.*, 2006; *Holtzman and Kohlstedt*, 2007; *Delle Piane et al.*, 2009a; 2009b]. Macro-scale strain variation in torsion experiments is reported for synthesized quartz and anorthite [*Ji et al.*, 2004], and diopside and anorthite layers [*Rybacki and Dresen*, 2006], and composite segments of Carrara marble [*Delle Piane and Burlini*, 2008]. For the first two, strain variation was caused by rheological segregation related to the compositional layering [*Ji et al.*, 2004; *Rybacki and Dresen*, 2006].

In our D2 experiments, samples contained microstructural heterogeneity related to variation in deformation history from undeformed to steady state strains. Our results show that strain variation within a sample expresses a rheological contrast for non-steady state strains. The individual D1

deformation history of each D2 segment, reflected in a specific mechanical and microstructural state, is primarily responsible for the variation in rheological response and the microstructure produced by D2. In torsion experiments, torque is equal for any circular plane of the cylinder. This applies to shear stress as well, under the reasonable assumption, that the conversion from torque to shear stress following equation 4.1 can be based on the same rheology, without major switches in deformation mechanism throughout the segments. Therefore, when considering that the D2 bulk samples experienced relatively homogeneous stress, the observed strain (rate) variability between segments can only be explained by different flow strength in each segment. At each increment of time, the weaker sample segments deformed at higher strain rate and vice versa. With ongoing deformation, the relative strength ratios changed. Consequently, strain (rate) was different between, but homogeneous in each segment during a D2 experiment.

As there is no record of segment strain rate during D2 experiments, the reported strain rates are averages derived from strain markers and run times. To understand the observed strain variation during D2 experiments, we need to know the strength (i.e. strain rate) evolution with strain of each sample segment individually. There are two approaches to estimate the required stress-strain behaviour: 1) borrow stress-strain behaviour from single-stage torsion experiments at similar experimental conditions or 2) apply relevant flow laws for coarse-grained calcite using bulk sample flow stress. The first method has the advantage that a rich database of stress-strain curves is directly available (Fig. 4.4A-B); even for the case of strain reversal in the bottom segments of D2 samples [Delle Piane and Burlini, 2008]. The disadvantage is the inability of quantifying strain rates for the individual segments, as the borrowed stress-strain curves apply to a fixed strain rate only. In D2 segments, strain rates are changing continuously as relative strength between sample segments evolves with strain until all segments have reached mechanical steady state. The second method has the advantage that strain rates are quantitatively determined. The accuracy of the modelled strain rates is easily tested by taking the average of the three sample segments at a given D2 strain. This average strain rate should be equal to the bulk sample or imposed strain rate. A major disadvantage is the lack of accurate strain dependency term(s), which incorporate both low-strain hardening and higher-strain weakening. Furthermore, to our knowledge strain reversal effects have never been incorporated in flow laws. The essence of flow laws is usually to model strain rate-stress relationships at steady state conditions for arbitrary strains. Steady state implies an independency of strain history and deformation path. Strain reversal should therefore have no effect.

We chose to follow the first method, primarily because it accounts to some degree for the mechanical effect of strain reversal. However regrettably, at best a qualitative description of strength and strain rate evolution with D2 strain of the individual segments can be inferred from that method.

Strain rate evolution in D2 sample segments:

The stress-strain curve from single-stage torsion experiments are used to predict the strength evolution during D2 of individual D2-sample segments under the following necessary assumptions:

1. Strain interruption and reversal have no influence on flow strength evolution with strain. As such, total shear strain in each segment defines the momentary flow strength and consequently strain rate.
2. Within the range of strain rates covered in D2 tests, shape of stress-strain curves remains similar. In other words, regime 2 of *Schmid et al.* [1980] with dislocation creep flow is the only regime addressed.

Since microstructure and texture development are strongly linked with finite strain, fabric analysis adds further evidence to justify the above assumptions.

Stress-strain curves for single-stage torsion experiments cover a range in flow stress (Fig. 4.4A-B) due to sample variability and experiment reproducibility. The common trend of these curves is generalized by an envelope. A schematic strain rate-strain plot for constant stress was derived from this trend and extended to $\gamma = 10$ (Fig. 4.9C) using the assumption that for $\gamma > 5$ no mechanical changes occurred. For each D2 experiment, such a strain rate-strain curve is used as template for strain rate evolution with strain for each D2 sample segment.

In the top part of figure 4.9A, the suspected strain rate evolution for individual $D2_{\gamma 1}$ segments is shown.

At the onset of $D2_{\gamma 1}$, the top and bottom segments were already deformed to $\gamma = 1$ and remained close to their peak shear stress state. The still undeformed centre segment started at lower strength. Consequently, top and bottom segments start D2 deformation at a much lower strain rate than the centre segment. As the centre segment was work hardening and the others were work softening with strain, flow strength contrast was reducing and thus strain rates homogenized, as is conceptually illustrated in the top part of the diagram. Total work hardening requires four times less strain than total work softening (Fig. 4.9C). The top and bottom segments thus remained harder than the centre segment during most of the $D2_{\gamma 1}$ experiment. Hence, most shear strain was accommodated by the centre segment.

A small difference in D2 strain exists between top and bottom $D2_{\gamma 1}$ segments. Apparently, total flow strength between $\gamma = 1$ and 1.7 is lower for reversed than for continued strain. This observation will be discussed later in section 4.4.

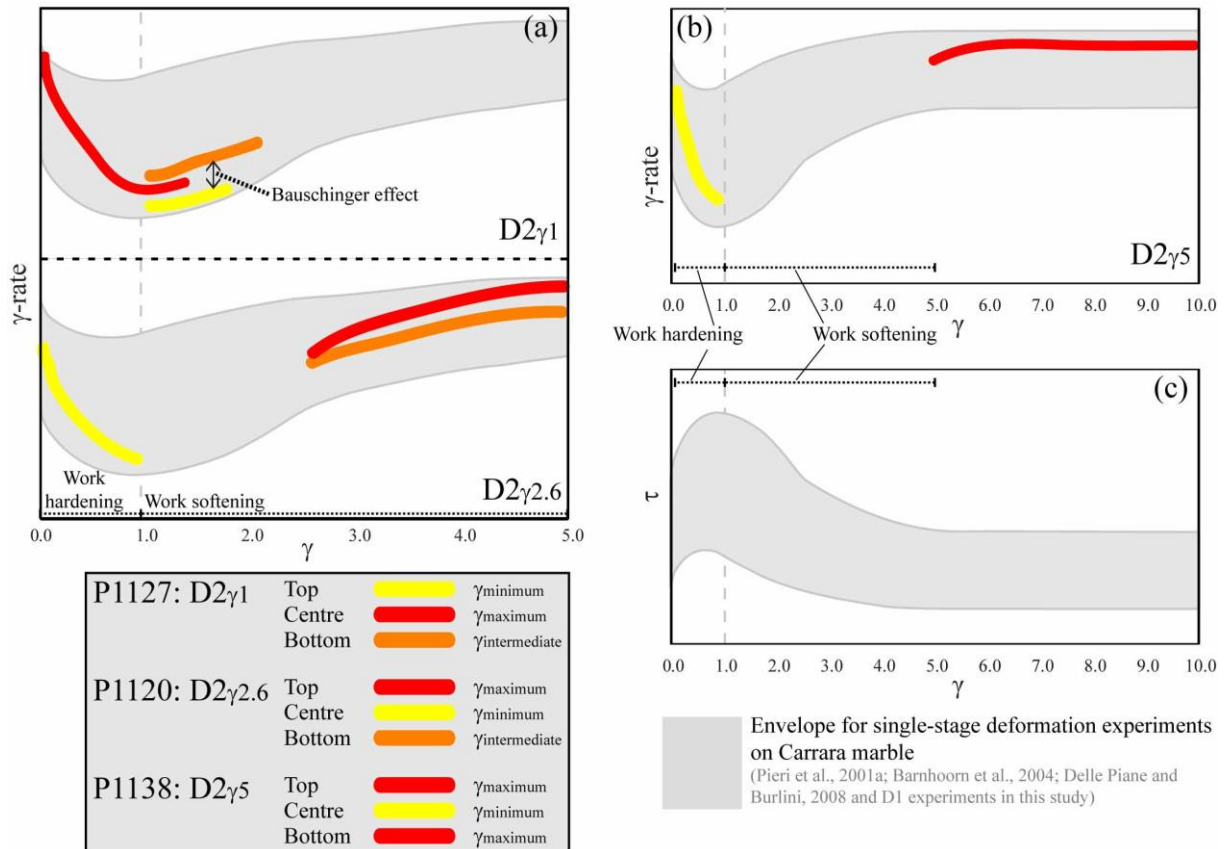


Figure 4.9: A-B) Strain rate segmentation for D2 experiments. Single-stage deformation flow behaviour conceptually predicts strain rate development for each segment during D2. C) Extended strain-stress envelope for single-stage deformation experiments. Beyond $\gamma = 5$, mechanical steady state is considered.

D1 $\gamma_{2.6}$ and D1 $\gamma_{2.6}$ experiments finished midway during the softening phase of Carrara marble. At the onset of D2 $\gamma_{2.6}$, flow strength contrast between the three segments was negligible. Right from the start of the D2 event, relatively rapid work -hardening in the centre and -softening in the top and bottom segments, changed strain rate proportions in the bulk sample (lower half figure 4.9A). Deformation quickly became more favoured in the top and to a lesser extent the bottom segments. In the end, minimum and maximum D2 strain was recorded in the centre and top segments, respectively. The bottom segment turned out to be harder than the top segment, unlike for D2 γ_1 .

During D1 γ_5 and D1 $\gamma_{5.5}$, the samples reached already a shear strain where mechanical constant flow stress (steady state) is achieved and the material was completely recrystallised to a fine-grained mylonite. The flow stress became lower than the yield stress of undeformed Carrara marble (48 vs. 43 MPa). In the D2 γ_5 experiment, sample strength was initially favouring the top and bottom segments for shearing. With strain, the centre segment work hardened and its strain rate dropped quickly. Strain rate in the top and bottom segments increased to maintain the bulk sample shear strain rate at $3 \times 10^{-4} \text{ s}^{-1}$, resulting in increasing strain rate contrast between the segments (Fig. 4.9B). Up to the end of D2 γ_5 , strain rate for the centre segment was reducing and always lower than that of the other segments. Top and bottom D2 γ_5 segments have similar γ_{D2} . No flow strength contrast between them existed.

Bulk sample D2 flow behaviour:

The D2 stress/strain curves show markedly different flow behaviour compared with single-stage deformation experiments (Fig. 4.4A-B). Hardening after yielding is less pronounced and with the exception of D2_{γ1}, peak stress is reached at lower strain ($\gamma = 0.5-0.6$, vs. $\gamma = 0.8-1.0$). Work softening after peak stress is nearly negligible and constant stress flow is reached at lower strain ($\gamma = 1-1.5$). Apparently, pre-existing strain variation within the D2 samples results in stress-strain curve levelling during subsequent deformation. This phenomenon becomes more apparent with greater D1 strain. We believe that the strain rate ratio or strength contrast between the individual segments controls the bulk sample flow stress. Soft segments deform at relatively fast strain rate and therefore accommodate most of the strain.

In D2_{γ1}, the centre segment had the highest shear strain contribution (Table 4.2). This relates well with the observed bulk sample hardening and peak stress at $\gamma = 0.8$. The limited hardening is then explained by the slowly recrystallising top and bottom segments, which gradually become weaker due to the increasing appearance of dislocation free recrystallised grains. Since these sample segments overall had a smaller shear strain contribution their influence was only minor.

Due to negligible strength contrast at the onset of D2_{γ2.6}, the bulk sample behaved as a mechanically uniform specimen. Yield stress was then comparable with the trend from single-stage torsion experiments. As the strength contrast between the individual segments increased with strain, flow became more dominated by the recrystallising, and thus work softening, top and bottom segments (Fig. 4.9A). Bulk sample hardening is minimized and peak stress reached at slightly lower strain than typical ($\gamma = 0.6$ vs. $0.8-1.0$). Recrystallisation in the top and bottom D2 segments continued, while the centre hardened due to dislocation entanglement, allowing the bulk sample to soften. The relatively elevated bulk sample steady state stress is explained by cancelling out effects of the weakening bottom and hardening centre segment, weighted by the shear strain contribution (Table 4.2). At this bulk D2 strain, complete recrystallisation is achieved within the top segment alone.

The strength contrast between top and bottom on one side, and centre segment on the other in the D2_{γ5} experiment lowered the bulk sample yield stress and reduced hardening considerably. The steady state flow in fully recrystallised top and bottom segments clearly dominated the bulk sample flow behaviour. The bulk sample steady state flow stress matches well with that associated with single-stage torsion experiments (Fig. 4.4A-B).

Mechanical effect of strain reversal:

The relative strength contrast between top and bottom segments is different in all three D2 experiments. In D2_{γ1}, the bottom segment is slightly softer. Unlike in D2_{γ2.6}, where the bottom segment is clearly harder. However, in D2_{γ5}, the top and bottom segments appear equally strong. In metallurgy, the behaviour in D2_{γ1} is known as the Bauschinger effect [*Bauschinger*, 1881], which has been topic of much follow up research [e.g. *Abel and Muir*, 1972; *Stoltz and Pelloux*, 1976; *Bate*

and Wilson, 1986; Stout and Rollett, 1990]. The Bauschinger effect refers to commonly observed behaviour of polycrystalline metals and alloys upon stress reversal in the plastic range. After re-loading up to tens of percentages of straining, yield stress and work hardening are reduced over an amount of strain one to two times that of pre-straining, in comparison with the forward loading behaviour. Deformation in that kind of material is accommodated by movement of dislocations, creating dislocation density heterogeneities. During work hardening, dislocations develop and migrate until they encounter obstacles, like grain boundaries or precipitates, and create tangles, which in the third dimension results into tangled walls. Although, tangled walls and cells are the pre-cursors for subgrain walls and subgrains, respectively, they are metastable and less sharply bounded. With reverted loading, these tangled walls disintegrate and new dislocations are formed in the low dislocation density cells [e.g. Hasegawa *et al.*, 1986]. The relatively 'fresh' start for the deforming material explains the lower yield and flow stresses observed even though the average dislocation density might have been nearly constant.

In rocks, the Bauschinger effect has been proposed by *Delle Piane and Burlini* [2008] to understand yield strength reduction in reversed deformation of Carrara marble. Similarly, the observation of the higher strain in the bottom compared with the top sample in the D2_{γ1} experiment is explained by the Bauschinger effect. At the onset of D2_{γ1}, the bottom and top segments are both at peak stress conditions (Figs. 4.4A-B and 4.9), indicating high dislocation entanglement.

Alternatively, anisotropic slip in calcite might explain the higher strain in the D2_{γ1} bottom segment. However, critical resolved shear stress (CRSS) estimations by *De Bresser and Spiers* [1997] show no evidence for glide sense anisotropy along $r < \bar{2}021 >$ and $f < 10\bar{1}1 >$ slip systems. Basal plane slip system $c < a >$ has been postulated and confirmed as important for the experimental conditions of this study [*De Bresser and Spiers*, 1993; 1997; *Barber et al.*, 2007]. By definition though [*Turner et al.*, 1954], the basal slip systems are symmetric with respect to glide sense.

On the other hand, the pole figures for bottom segments in D2_{γ1} and D2_{γ2.6} indicate slightly rotated shear texture maxima, which suggests some contribution by geometric (CPO induced) weakening.

For D2_{γ2.6} the Bauschinger effect clearly does not hold anymore. Instead, we observe that dynamic recrystallisation proceeded faster in the top than bottom segment (Fig. 4.6). As work softening is correlated with increasing recrystallisation [*Schmid et al.*, 1987; *Pieri et al.*, 2001a; *Barnhoorn et al.*, 2004], delay in the bottom segment lead to relative hardening compared with the top segment.

Strain reversal does not affect recrystallisation rates directly. In D2_{γ5}, fabric and strength of top and bottom segments are similar again. We relate the delayed progress of recrystallisation in the D2_{γ2.6} bottom segment to the shape recovery of stretched relict grains. Apparently, because of Bauschinger effect it was energetically favoured to restore their shape than to pursue dynamic

recrystallisation. Actual recrystallisation leads however to more weakening than the Bauschinger effect does. Hence, D2_{γ2.6} bottom segment was relatively harder than the top.

Microstructural consequences of deformation history:

Microstructure analysis in this study serves four purposes: 1) to verify the assumption that total strain in each segment defines the momentary flow strength or strain rate (all D2 segments), 2) to investigate the effect of the interruption of deformation (D2 top segments), 3) to detect possibly changes in deformation mechanism due to segment strain rate deviation from the bulk strain rate (D2 centre segments), and 4) to reveal the microstructural consequences of shear sense reversal (D2 bottom segments).

In continued shearing (top segments, Fig. 4.6), microstructure development is similar to that for single-stage deformation (top segments, Fig. 4.5). In addition, S_a-orientation data from top segments (grey circles Fig. 4.7) plots into the trend set by S_a-foliation obtained from single-stage deformation experiments. Interruption of deformation without change of shear sense at comparable stress but slightly altered strain rates ($2.5 \times 10^{-4} \text{ s}^{-1}$) has no major effect on microstructural development of Carrara marble.

In the centre segments, low strain microstructures that developed during D2 show no evidence for other deformation mechanisms than dislocation creep and e-twinning. Despite a strain rate ratio of 5 between D2_{γ2.6} and D2_{γ5} centre segments, fabrics, including S_a foliation angles, are similar. In general, almost one order of magnitude strain rate difference ($5 \times 10^{-5} - 4 \times 10^{-4} \text{ s}^{-1}$) did not affect shearing microstructure development.

The microstructural effect of strain reversal can be studied in the three bottom segments of the D2 experiments. The microstructures of D2_{γ1} and D2_{γ2.6} bottom segments are markedly different from any other D2 segment or single-stage deformation experiment. The presence of fine recrystallised grains, twin planes, undulose extinction and deformation bands indicates that also in these segments dislocation creep is accompanied by dynamic recrystallisation. From comparison between top and bottom segments, which were deformed to almost the same absolute strain, it is obvious again that the presence of large stretched relict grains has a retarding effect on the progress of dynamic recrystallisation upon strain reversal.

In the bottom segment of D2_{γ1} initially strongly elongated grains are recovered in shape and appear equant and similar to grains in undeformed Carrara marble. The strain history is still recognizable, though, by a high concentration of twins, undulose extinction and deformation bands. Furthermore, the large grains have a weakly developed rim of small recrystallised grains, a feature that is associated with an absolute strain of $\gamma = 1.5-2$. Similar behaviour is reported by *Delle Piane and Burlini* [2008] for torsion tests on Carrara marble with strain reversal ($\gamma = 1 + -1$).

The bottom segment of D2_{γ2.6} is strongly recrystallised, but also contains sheared relict grains. The amount of recrystallisation is comparable with that in single-stage deformation experiments to

$\gamma = 4-5$. The absolute shear strain of the bottom segment of D2 $_{\gamma 2.6}$ is 4.9. The progress of recrystallisation appears to be merely depending on γ_{abs} , meaning plastic work in the segment, rather than finite strain. We interpret this observation in terms of total strain energy (being about proportional to absolute strain as long as stress remains in the same magnitude) which is recorded in the defect structure of the material and which is primarily driving recrystallisation.

Two observations regarding the relict grains in bottom segment of D2 $_{\gamma 2.6}$ are noteworthy: 1) they have a strong elongation, which forms a SPO-derived S_a foliation, but despite $\gamma_{D2} < \gamma_{D1}$, foliation indicates top to the right shear. 2) Comparison with sheared grains in single-stage deformation experiment to $\gamma = 2.3$ (Fig. 4.5) reveals that grain size is 2-4 times smaller. Points 1 and 2 are linked by the grain size reducing effect of recrystallisation. Relict grain aspect ratio is a function of strain. Non-isotropic recrystallisation of rims of sheared relict grains reduces grain size and aspect ratio. The resulting grain shapes are typically associated with lower shear strain. Consequently, during strain reversal and with dynamic recrystallisation, less strain is required to recover a strongly sheared relict grain back to spherical shape. When excess strain is available during the reversal, grain shearing can continue into the direction of the reversed strain, as is the case for the bottom segment of D2 $_{\gamma 2.6}$.

The type 1 strain reversal experiment on Carrara marble reported by *Delle Piane and Burlini* [2008] where the sample was deforming first to $\gamma = 2$ and secondly to $\gamma = -2$, also shows a weak SPO indicating the shear sense of the last deformation.

The microstructures for the top and bottom segment of D2 $_{\gamma 5}$ are identical, with the exception of the S_a and S_b orientations, which are 6° and respectively 4° steeper in the bottom. For both segments, the microstructure is completely reworked to a fine-grained matrix by dynamic recrystallisation. Strain reversal and interruption of deformation have no visible microstructural effect on this recrystallisation process.

Foliation development:

Figure 4.7 shows that, 1) S_a -orientation follows similar development in continued deformation and single-stage deformation, 2) the range of strain rates in D2 centre segments has no influence on S_a -orientation development, and 3) S_a orientation with respect to SZB is systematically steeper in reversed deformation than in equivalent single-stage deformation.

In the D2 segments in this study ($\gamma_{\text{abs}} < 12$), S_a is primarily defined by SPO of relict grains. Clearly, the pre-existing relict grain SPO in opposite orientation retards the development of the final foliation in reversed deformation. Aspect ratio reduction in relict grains by dynamic recrystallisation, however, counteracts the retardation effect of pre-existing SPO. The decreasing difference between reversed and single-stage S_a orientations reduces with strain (Fig. 4.7, open circles in comparison with general trend).

S_b foliation is primarily caused by grain boundary alignment of fine recrystallising grains [*Pieri et al.*, 2001a; *Barnhoorn et al.*, 2004] and reported constant with strain up to $\gamma = 50$ [*Barnhoorn*

et al., 2004]. In similarly fine-grained carbonates (Solnhofen limestone), S_b inclination angle increased between $\gamma = 15$ and 19 from 18 to 31° [Rybacki *et al.*, 2003: their figure 16A]. Constant orientation with strain is explained by cyclic recrystallisation, resetting foliation planes and keeping S_b steep with respect to SZB. Temperature strongly controls recycle frequency and thus the angle or steepness. With decreasing temperature, recrystallisation is slower and S_b -orientation on average becomes flatter [Barnhoorn *et al.*, 2004].

Based on new data from this study and Della Piane and Burlini [2008], between $\gamma = 5$ and 12, S_b -orientation appears to have steepened. Though we interpreted the rock to be almost completely recrystallised at $\gamma = 5$, here we have to consider that a few highly sheared relict grains are still present at much larger strain. The observed non-equilibrium of the recrystallisation process is explained by incomplete recrystallisation of the sample. This implies that microstructural steady state is not reached before $\gamma = 12$ under the experimental conditions of this study.

Texture development:

Single-stage deformation experiments on Carrara marble in regime 2 [Schmid *et al.*, 1980] develop initially a shearing and later a recrystallisation CPO [Pieri *et al.*, 2001a; b; Barnhoorn *et al.*, 2004]. Texture consequences of deformation interruption, strain rate changes and deformation reversal are discussed here.

The pole figures for D2 experiments (Fig. 4.8) indicate that continued deformation develops texture similarly as single-stage deformation. Low strain CPO development in D2 centre segments is insensitive of strain rate within nearly one order of magnitude difference. Similar conclusions were drawn from microstructural observations.

All three D2 bottom segments have some degree of texture. In the D2 $_{\gamma 1}$ bottom segment, a slightly modified shearing deformation CPO is easily recognized, despite the nearly zero finite shear strain. CPO in the bottom segment of D2 $_{\gamma 2.6}$ resembles the transition to the recrystallisation texture known from the intermediate strain samples (left part Fig. 4.8). The sense of shear derived from the associated pole figures indicates for both segments, top to the right (i.e. D2) shearing. Despite a clear SPO, CPO identifies the latest deformation stage. SPO follows more strictly the finite shear strain. CPO is easier to overprint and develop during strain reversal than SPO is.

In comparison with texture derived from single-stage torsion tests, c-axes are slightly rotated towards the SZB in reversed segments of D2 $_{\gamma 1}$ and D2 $_{\gamma 2.6}$ (Fig. 4.8). Low strain reversal tests by Della Piane and Burlini [2008, their figure 7A] shows similar behaviour.

The well-developed recrystallisation texture of top and bottom segments in D2 $_{\gamma 5}$ are nearly indistinguishable. This implies that recrystallisation has completely overprinted the shearing texture, independent of shear sense, as was previously concluded based on microstructural observations. The previously discussed delay of dynamic recrystallisation on shear reversal is reflected here in slightly lower texture strength in the bottom compared to the top segment.

Justification of earlier assumptions:

To understand qualitatively the observed D2 strain variation, we used stress-strain curves from single-stage torsion tests. Two assumptions were made (section 4.2). Now, we justify using these assumptions.

No fabric element seems to have been affected by strain interruption. There is no evidence for deformation outside regime 2 of *Schmid et al.* [1980], despite a strain rate range of more than one order of magnitude. Strain variation data shows that for $D2_{\gamma 1}$ and $D2_{\gamma 2.6}$ strain reversal has a significant effect. For $D2_{\gamma 5}$ there is no effect. Therefore, only for low to intermediate strain reversed deformation the use of stress-strain curves from single-stage torsion tests is not justified. Hence, alternative curves for that situation are required.

Delle Piane and Burlini [2008] reported Carrara marble strain reversal experiments in torsion (their results are reproduced in modified form in figure 4.10). For comparison, the envelope for stress development with strain from single-stage experiments is plotted there as well. In P0577 ($\gamma = 1 + -1$), flow stress upon reversal remained similar and work softening occurred at similar rate. In experiments P0583 ($\gamma = 2 + -2$) and P0638 ($\gamma = 4 + -4$), strain reversed samples weakened at similar rate, but overall 5-7 MPa higher flow stress. In experiment P0586 ($\gamma = 5 + -5$), the deformation progressed upon reversal at nearly constant, but 3 MPa higher flow stress.

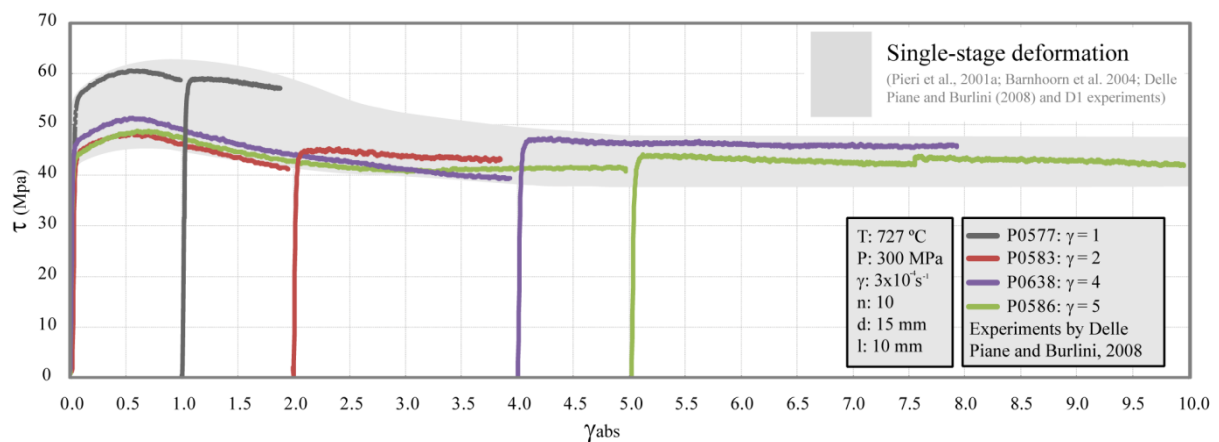


Figure 4.10: *Delle Piane and Burlini* [2008], Fig. 2A-B, modified to show the mechanical effect of strain reversal at strains between $\gamma = 1$ and 5.

None of the curves by *Delle Piane and Burlini* [2008] displayed a lowered flow stress upon shear reversal, meaning no indication for Bauschinger effect at shear strain of 1 to 5. However, the curves plotted in figure 4.10 were not corrected for torque drift during the tests. Recent re-loading tests under similar conditions with Carrara marble by De Raadt [pers. comm. *De Raadt*, 2009], revealed a torque drift upon re-loading of ± 3 Nm, which is equivalent to ± 2.5 -3.6 MPa. Only in P0583 and P0638 of *Delle Piane and Burlini* [2008] re-loaded shear stresses were greater than potential drift.

The effect of torque drift might also be larger than the Bauschinger effect. We can estimate the Bauschinger effect by comparing $D2_{\gamma 1}$ top and bottom segments. The observed strain rate ratio of 1.3

correlates to a flow stress ratio between 1.04 and 1.02 for $n = 6$ to 10, respectively. For an absolute flow stress of 45 MPa this ratio yields a flow stress difference of 1 to 2 MPa. The Bauschinger effect is thus smaller than the variability of torque due to drift.

By first approximation, hardening upon reversal for intermediate strain in *Delle Piane and Burlini* [2008] is in agreement with the strain reversal behaviour recorded by the $D2_{\gamma 2.6}$ bottom segment in this study. The strain/stress curves from *Delle Piane and Burlini* [2008] can thus at least be used as support for the slightly larger flow stress in the $D2_{\gamma 2.6}$ bottom segment. For understanding the slightly weaker $D2_{\gamma 1}$ bottom segment, new strain reversal tests with accurate torque drift corrections are required.

Geological consequences:

Deformed coarse-grained marble that has not yet reached steady state flow conditions shows clear evidence for strain reversal. Grain shearing is reversible, but recrystallisation continues at seemingly comparable rate after strain reversal, resulting in unique microstructures of equant relict grains within a fine-grained matrix. Texture is unique in having a slightly offset shearing texture. Sense of shear from this texture relates to the latest deformation stage, even when magnitude of strain during the last stage are equal ($D2_{\gamma 1}$) or less ($D2_{\gamma 2.6}$).

Calcite twinning is used for paleostress [e.g. *Jamison and Spang*, 1976; *Rowe and Rutter*, 1990; *Ferrill*, 1998] and paleostrain estimates [e.g. *Groshong et al.*, 1984 and references therein; *González-Casado et al.*, 2003]. Strain reversal in principle allows more twins to be activated compared to continued deformation, as is demonstrated by $D2_{\gamma 1}$ and $D2_{\gamma 2.6}$ top and bottom segments (Fig. 4.6). Simply speaking, finite strain will be overestimated when reverted strain is not considered. Paleostress estimates using twins are for example based on twin density [*Rowe and Rutter*, 1990; *Ferrill*, 1998]. In $D2$ experiments stress is considered similar for any circular plane of the cylinder. Despite comparable absolute strain in $D2_{\gamma 1}$ and $D2_{\gamma 2.6}$ top and bottom segments twin density is different. Strain reversal clearly affects twin density.

Texture of (ultra-)mylonitic marble (i.e. steady state conditions) develops with absolute strain, regardless of shear sense. Sense of shear cannot be derived from such recrystallised material and no evidence for strain reversal is visible. No effect of strain reversal on mechanical strength in well-developed mylonite marbles is observed.

Crustal domains with a homogeneous lithology, but heterogeneous strain history, develop strain variation when fabric heterogeneities result in rheological contrast (e.g. shear zone reactivation). $D2$ experiments show that an initial small rheological contrast leads to large strain variation when segments develop differently (i.e. hardening vs. softening or constant flow stress) during subsequent deformation.

4.5: Conclusions

High temperature and pressure torsion experiments on sandwich Carrara marble samples with pre-existing strain variation were performed to study the rheological, microstructural and textural consequences of multi-stage deformation. Complexities like strain interruption, reversal and pre-existing strain variation have been investigated. Strain history was produced by torsion experiments, representing deformation stage 1 (D1). Sandwich samples are then deformed by counter-clockwise torsion during deformation stage 2 (D2).

The rheological consequences are summarized as follows:

- In all D2 experiments, shear strain is homogeneous within, but variable between sample segments. Pre-existing strain variation has a significant effect on strength and rate of subsequent deformation.
- Bulk D2 sample flow stress is more constant compared with single-stage deformation experiments. Work hardening and work softening cancel each other mostly and apparent steady state stress is achieved at increasingly lower strain with increasing D1 strain, i.e. increasing variation in strength and fabric.
- Bulk D2 sample flow behaviour is mostly defined by the softest D2 segment. This phenomenon becomes the more pronounced the larger the D1 strain (i.e. the larger the strength contrast between segments).
- Flow strength contrast is responsible for the observed strain rate variation. A small variation in flow stress varies strain rate by magnitudes, as would be expected for power law flow behaviour with high stress exponent n between 6 and 10.
- Total strain in each segment defines the momentary flow strength only for, 1) continued deformation (i.e. strain interruption has no effect on flow stress behaviour with strain) and 2) high strain deformation with complete recrystallisation, when flow stress is independent on shear sense.
- Strain reversal leads to modified flow stress behaviour when relict grains are still present in the sample after the first deformation stage (i.e. $\gamma < 5$ for the conditions in this study).

The microstructural and textural consequences are summarized as follows:

- Finite strain relates to the grain shape of relict grains, if still existing. Shearing of grains is complemented by grain size reduction due to dynamic recrystallisation leading to aspect ratio equilibration.
- Total or absolute strain controls the amount of recrystallisation and strength of recrystallisation CPO, which are independent of shear sense, but represent total amount of work and strain energy in the material.
- Compared with SPO, CPO requires less strain to be overprinted on reversal.

- Reversed deformation is recognized at low strain in microstructural characteristics like SPO and CPO, and orientation of foliation planes. At high strain, where dynamic recrystallisation dominates, the indications of pre-strain in reversed sense become much more subtle and fade out eventually. Those indicators are S_a foliation angle, CPO strength, and degree of recrystallisation.
- In the absence of recrystallisation ($\gamma < 1$), flow stress is lower for reversed than for continued deformation (Bauschinger effect). Delayed recrystallisation during strain reversal at intermediate strains ($1 < \gamma < 5$) reduces work softening. Consequently, in this strain range reversed deformation is harder than continued. Full recrystallisation ($\gamma > 5$) leads to a CPO without shear sense sensitivity and flow stress for reversed deformation is similar to that for continued deformation.
- Between $\gamma_{abs} = 5$ and 12, orientation of S_b is steepening with respect to the SZB. Consequently, microstructural steady state is not reached before $\gamma_{abs} = 12$.

4.6: Acknowledgements

This research was financially supported by ETH grant: TH 1/03-3/2704.5 as part of the PhD project of R.H.C. Bruijn. We greatly appreciate the technical and educational support from R. Hoffmann, S. Misra and F. Ornelas Marques in the laboratory and with servicing the experimental apparatus. F. Pirovino is thanked for preparing $<10 \mu\text{m}$ thin sections. We were please to have valuable discussions with N. Mancktelow, J-P. Burg, W.S. de Raadt, C. Delle Piane, B.S.G. Almqvist and N. Tisato. The Centre of Electron Microscopy ETH Zürich (EMEZ) is gratefully acknowledged for providing the EBSD-SEM facility. Thanks to insightful commentary from reviewers Eric Rybacki and Alexandre Dimanov, the manuscript could be greatly improved.

Chapter 5

Material: illite shale

Oscar Wilde once said, "We live in an age when unnecessary things are our only necessities."

Preface

This chapter deals with two linked topics, 1) rationale for the choice of source material and 2) presentation of the naturally compacted Maplewood Shale. To understand the selection of Maplewood Shale, a detailed description in terms of mineral and chemical composition is required. The first subchapter introduces the illite shale model and explains why clays used in previous experiments are unsuitable. The chapter then continues with a detailed description of Maplewood Shale. Sample fragments are described in subchapter 5.2, followed by a discussion on microstructure and mineral composition as determined by SEM BSE imaging and XRD analysis. Then, physical properties are discussed and a description of the pore types is presented in subchapter 5.4. After that, a new subchapter discusses bulk composition of three pre-selected shales (Maplewood Shale, Argiletz shale (France) and Silver Hill shale (Montana)) as determined by XRF and places them in the context of geochemical shale standards. The overall description is concluded by a subchapter on the grain size distribution of Maplewood and Silver Hill shales. The physical and chemical rationales for ultimately choosing Maplewood Shale as best source for illite clay are then presented (subchapter 5.7). The chapter concludes with the geological history of the Early Silurian Maplewood Shale. Its stratigraphic position in the Paleozoic sediments of the Appalachian foreland basin and regional evidence for deformation are the topic of the concluding subchapter.

5.1: Illite shale selection

Shales are notorious for their wide range of composition and fabric. Resulting physical properties are highly scattered, often because of a complex diagenetic history. In the simplest configuration, a model for shale is a mixture of clast-forming silt and matrix-forming clay. To address the problems in this study, silty quartz clasts in clay-matrix of pure illite should be used. Although monophasic silty quartz is commercially available, clay-sized pure illite is not. A compromise was therefore needed for the matrix-forming fraction of a simulated illite shale powder. Previous clay and shale compaction and resedimentation experiments have used natural shale [Nygård *et al.*, 2004], commercially available silt and clays such as quartz, kaolinite and smectite [Vasseur *et al.*, 1995; Mondol *et al.*, 2007; Fawad *et al.*, 2010] or worked with a mixture of natural clay and commercial silt [Schneider *et al.*, 2011]. Though illite is present, none of the previously used clay-rich materials are suitable as matrix-forming illite clay, due to their high smectite and/or illite-smectite content. Alternative natural illite-rich shales were thus required.

Natural occurrence of illite shale is common and well documented. Three illite shales have been pre-selected based on direct availability: Maplewood Shale, Argiletz shale and Silver Hill shale. Maplewood Shale was ultimately selected as most suitable. Reasons for this choice follow description of Maplewood Shale fragments, microstructure and mineral composition, bulk rock composition and grain size distribution. Simultaneously, its fabric is given as an example of the type of fabric produced by natural (chemical) compaction of clay-rich sediments. The physical state of Argiletz shale (powder) and Silver Hill (< 1mm thin rock fragments) did not allow conventional preparation of a SEM sample. Consequently, as a shale reference Argiletz shale is only included in the discussion of Maplewood Shale bulk rock composition, whereas Silver Hill shale is only part of the discussion of bulk rock composition and grain size distribution.

5.2: Physical state of the shales

Maplewood Shale:

Fragments of Maplewood Shale have been donated by WARD's natural science, in Rochester (NY), United States of America. The rock type is otherwise sold as hand specimen #52 in a rock collection kit marketed for teaching purposes. The olive green to greenish-gray fragments range in size from 3 to 10 cm with thickness of less than 3 cm (Fig. 5.1A). Color variation within and between fragments is minimal and no veins or lenses of coarser particles are visible by the unaided eye, indicating rather homogeneous composition and fabric.

Well-developed cleavage resulted in platy and fissile fragments. Bedding and cleavage are (sub)parallel, therefore no intersection lineation is perceptible. Larger fragments exhibit irregular

bedding planes. No sedimentary features or fossil remains are visible. Other larger samples show evidence of exposure; millimeter sized lichens or fungi, and discoloration due to weathering reactions. Weathered surfaces display a more brownish color.

The fissile nature of the fragments complicates drilling of cylindrical samples that would have been useful for analysis or deformation experiments. When wet, the fragments easily split along their cleavage plane. Samples are very soft and easy to polish on high-grit abrasive paper. Dry polishing leaves a white-to- greenish-white residue, characteristic of illite.

Argiletz shale:

Argiletz shale (also known as French green clay) is supplied by the French company Laboratoire ARGILETZ S.A. It is sold as illite shale powder, although advertized as finely ground green clay. The creamy light-green powder (Fig. 5.1B) is mostly sandy and originates from the Paris Basin (France).

Silver Hill shale:

Olive-green thin (< 2 mm) rock slices of Silver Hill shale (Silver Hill Formation) were collected from a small outcrop in the Flint Creek Range of Granite County, Montana (USA). High fissility reflects cleavage development. Color of the shale fragments is consistent, indicating homogeneous composition and no weathering-related alteration. Fragments are too thin for drilling or surface polishing.

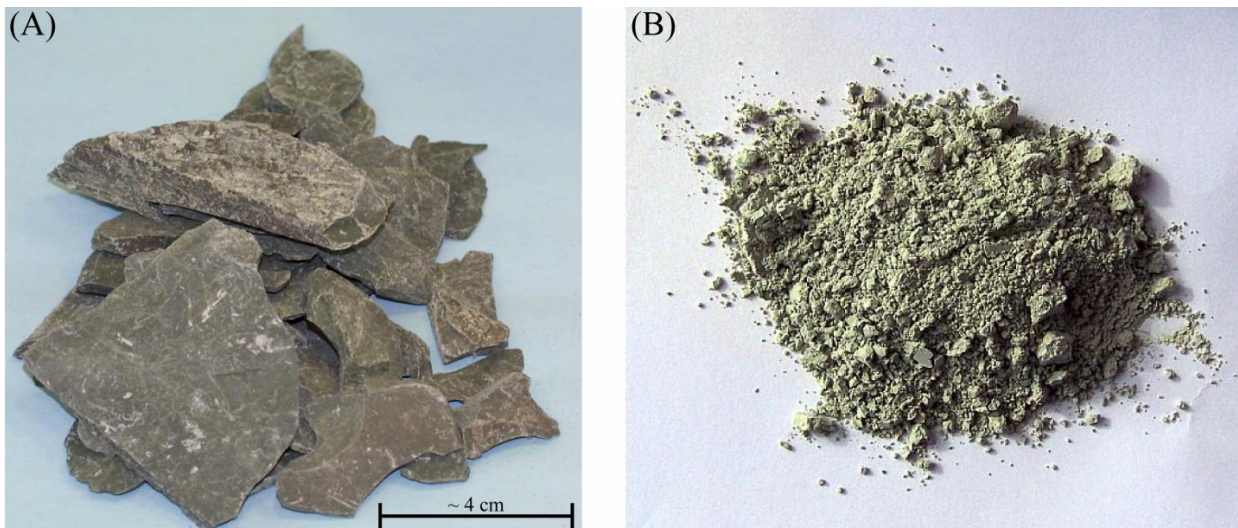


Figure 5.1: pre-selected illite shales. A) Small pile of Maplewood Shale fragments. B) Small pile of Argiletz shale powder.

5.3: Mineral phases and microstructure

Maplewood Shale:

SEM BSE imaging and EDX analysis of Maplewood Shale fragments revealed that the main mineral phases are illite, phengite, clinocllore and quartz (Fig. 5.2A-F). The phyllosilicates and quartz represent roughly 60-75 % and 20-30 % of image area, respectively, based on grid-point analysis. Quartz distribution is heterogeneous within a cm-sized sample, thereby defining high and low clay-content zones or alternatively matrix and grain-supported zones (Fig. 5.2A-B). Quartz distribution is homogeneous in such zone of few mm².

Secondary phases, with on average less than 2 area %, include coarse detrital biotite, pyrite, apatite, rutile and K-feldspar. Distribution of some of these secondary phases is heterogeneous; within a SEM-prepared sample, zones enriched (> 5 area %) in biotite, rutile or apatite may exist.

Minerals are very fine-grained matrix particles, rigid clasts (sub-micron to > 100 µm in size), or both. Regardless of clay amount, the matrix is primarily comprised of clay-sized flakes with aspect ratio (i.e. $\lambda = \text{length}/\text{width}$) ≥ 2 , such as the clays and some of the finest grains of secondary phases. Most rigid clasts in both low and high clay-content zones are detrital quartz. Those clasts have irregular and angular grain boundaries. Quartz is visually coarser in clay-poor than clay-rich zones (Fig 5.2A-B), possibly reflecting variations in water-current energy during deposition. The aspect ratio of quartz clasts is variable ($1 < \lambda < 5$). Occasionally, quartz grains are irregularly surrounded by an apatite-rim (red-ellipse Fig. 5.2A). No authigenic quartz that may have formed during smectite to illite transformation [Peltonen *et al.*, 2009; Thyberg *et al.*, 2010] has been identified, suggesting an open system during burial [Day-Stirrat *et al.*, 2010]. Detrital biotite and phengite (silt-size) in the matrix have very high aspect ratios ($\lambda > 5$). Equant and non-equant secondary phase particles > 2 µm form rigid clasts in the clay-dominated matrix, with pyrite occurring also in framboidal configuration, sized 40-60 µm (Fig. 5.2B).

The degree of alignment of clays and high λ secondary minerals between low and high clay-content matrices is markedly different. Matrix-supported parts of the sample, with high clay-content, exhibit up to two foliations (Fig. 5.2A, E-F), both of which are interpreted to be of diagenetic origin. In fact, also $\lambda > 1$ quartz clasts are frequently aligned to one of the matrix foliations. In grain-supported parts of Maplewood Shale, where quartz content is markedly higher (> 40 area %), the clay matrix displays no foliation (Fig. 5.2B-C).

Inspired by a recent clay-silt compaction studies by Schneider *et al.* [2011] and Fawad *et al.* [2010] a conceptual model is designed that describes the origin of both strongly foliated matrix-supported domains and grain-supported domains without clay alignment (Fig. 5.3). Before natural (mechanical) compaction of matrix-supported zones, when porosity was high and fluids abundant, clays were likely randomly oriented and together with dispersed rigid clasts were not displaying a

foliation (Fig. 5.3 high porosity state). During diagenesis, as fluids are expelled from the pores, represented in figure 5.3 by 20 % vertical shortening, floating clay particles align to the flow direction. Rigid silt clasts force fluid flow around the clasts. After fluid expulsion, clay particles wrapped around silt clasts indicate the previous flow pattern.

In 2D, assuming fluid flow in a horizontal direction, the appearance of one or two clay-matrix foliations depends on the amount of silt clasts. In the absence of clasts, horizontal foliation develops upon gravity-driven compaction. With increasing amount of rigid particles, clay wrapping becomes more dominant. For a certain amount of silt clast, the two dominant orientations, equally tilted with respect to the loading direction, resulting from clay wrapping, dominate the overall microstructure as is evident from figure 5.2A.

For grain-supported quartz-rich domains of Maplewood Shale, it is inferred from the lack of foliation that the matrix experienced a lesser degree of (mechanical) compaction. Pressure shadowing by the abundant and touching quartz clasts could then explain the limited compaction (Fig. 5.3). In a high porosity state before compaction and fluid expulsion, it is likely that silty clasts were randomly distributed, floating in a matrix of saturated mud. During compaction, as fluids are expelled, rigid clasts move closer. Upon touching of rigid clasts (green ellipses), provided sufficient clasts are present, pressure shadows are formed and fluids become trapped and create an overpressure. Nearby clays are then protected from diagenesis by surrounding rigid particles and the local overpressure. Porosity remains high in these areas as compaction is prohibited. Clay foliation does develop as fluid flow is absent and clays are not aligning to flow (Fig. 5.3 red ellipses). In this conceptual model for grain-supported domains, a local clay alignment may develop between rigid clasts when spacing is wide (Fig. 5.3 blue ellipse). Such alignment, however, rarely extends to neighboring grains and is not necessarily oriented normal to the burial direction. Local clay alignment in grain-supported domains thus seldom qualifies as foliation. In quartz-rich parts of Maplewood Shale, matrix foliation is lacking, even though locally, on the scale of 3-6 μm , pockets of illite flake appear aligned (Fig. 5.2C orange circles).

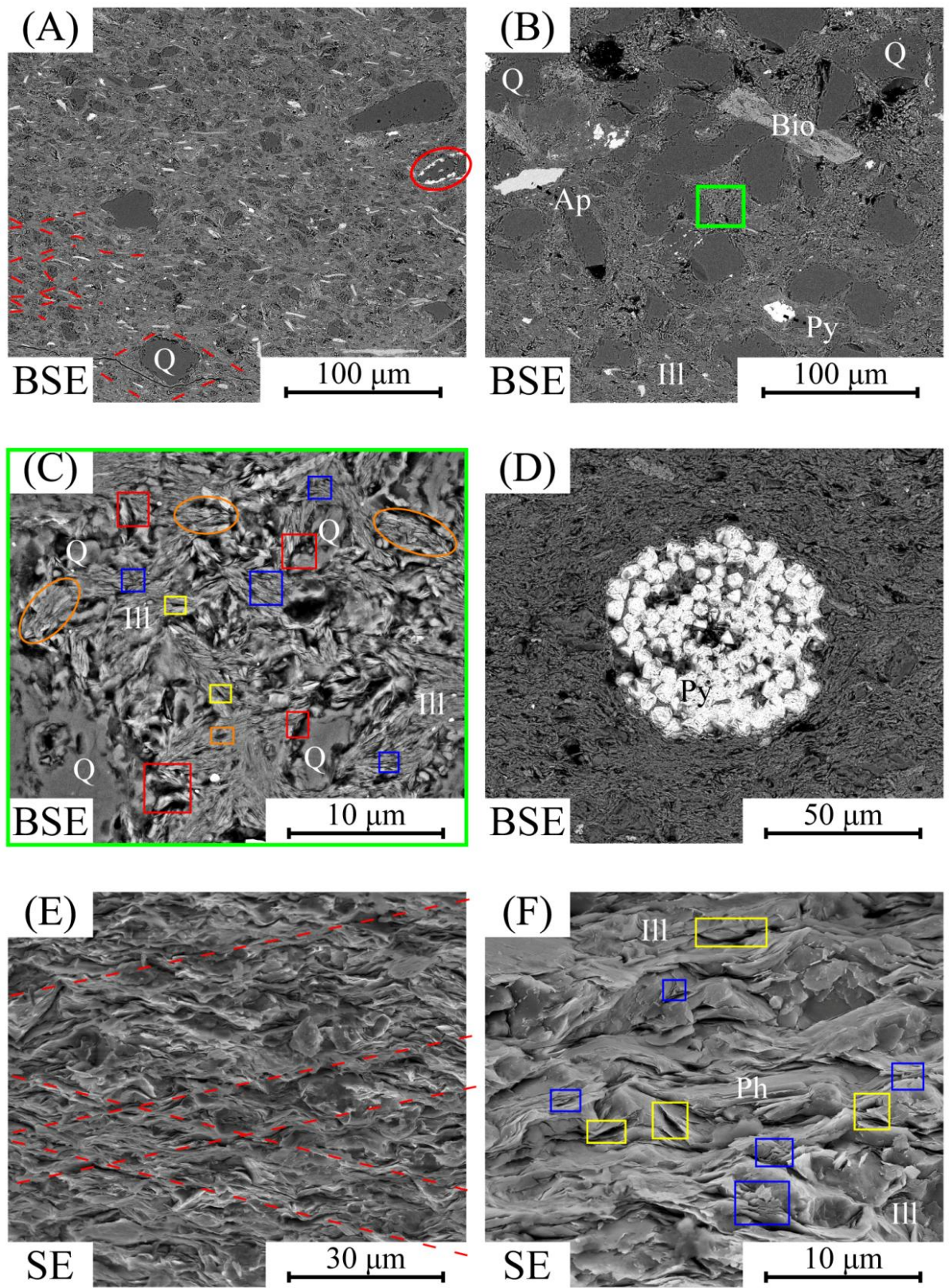


Figure 5.2: Micrographs of Maplewood Shale. Q = quartz, Ill = illite, Py = pyrite, Ap = apatite, Bio = biotite, Ph = phengite. A) BSE image of high clay-content zone with mica-dominated matrix and apatite-rimmed quartz. B-C) overview and zoomed BSE image of low clay-content zone and poorly aligned clay clusters (red ellipses). E-F) SE micrograph of broken surface natural Maplewood Shale. All image planes are normal to bedding.

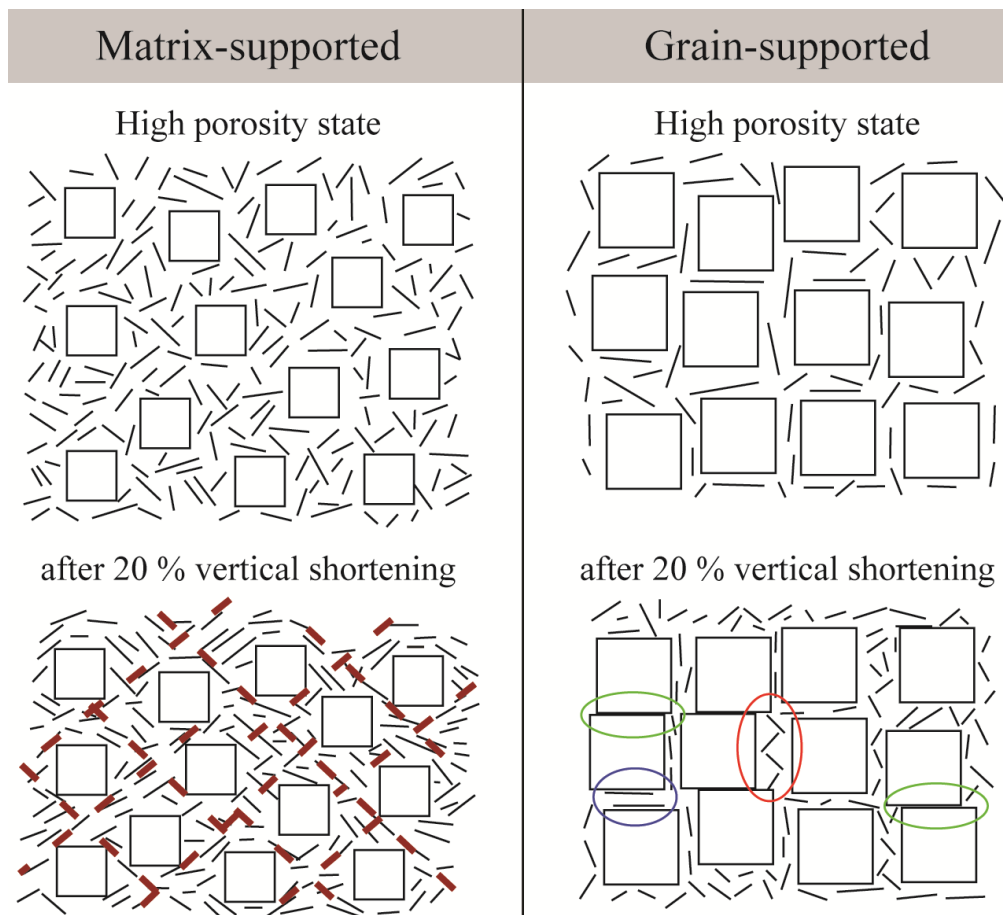


Figure 5.3: Conceptual model for matrix and grain-supported foliation development in Maplewood Shale. Dark red lines highlight matrix-supported foliation after vertical shortening by compaction and fluid expulsion. In grain-supported domains, foliation does not develop because pressure shadows created by immobile clasts (green ellipses) prevent clays from compacting (red ellipse). Clay alignment between rigid clasts is non-penetrative (blue ellipse).

XRD analysis Maplewood Shale:

XRD analysis on Maplewood Shale powder revealed the presence of the primary minerals quartz, the dioctahedral micas and trioctahedral clinocllore (Fig. 5.4A). The small peak at $\sim 8.2\theta$ suggests the presence of a smectite-group mineral. The narrow width of the illite basal plane (001) peak at $\sim 8.9\theta$ indicates that sediment burial reached anchizone conditions, where the illite/smectite ratio > 9 [Merriman and Frey, 1998]. Smectite is indistinguishable from illite in BSE images due to similar average atomic numbers and grain shapes. The XRD detection limit is too high to recognize 2θ peaks for the secondary phases identified by SEM, except for apatite.

XRD analysis Argiletz shale:

Mineral phases detected by XRD analysis in Argiletz shale are quartz and clays, such as illite and kaolinite (Fig. 5.4B). Other prominent peaks indicate calcite and dolomite. Compared to Maplewood Shale, the illite basal plane peak ($\sim 8.9^\circ 2\theta$) is relatively low and wide, indicating lower illite content and poorer crystallinity (i.e. maximum burial to late diagenetic zone) [Merriman and

Frey, 1998]. Smectite group minerals are not directly recognized, but can be inferred from the illite basal plane peak. Smectite in the form of illite-smectite is likely present.

XRD analysis Silver Hill shale:

XRD analysis of Silver Hill shale (Fig. 5.4C) shows that the primary mineral phases are quartz, phengite, illite, kaolinite and biotite. High counts for the basal plane of the illite, phengite and biotite at around $2\theta = 9^\circ$ indicate a relative higher clay/mica content than Maplewood Shale. The crystallinity of illite, especially, is poorly developed, as indicated by the peak width [Merriman and Frey, 1998]. As burial to late diagenetic zone does not result in biotite or phengite crystallization, these mineral in Silver Hill shale are detrital.

5.4: Porosity/density and pores

Maplewood Shale:

The connected helium porosity for Maplewood Shale is 2.7 ± 0.2 %. Bulk and grain density are 2.60 ± 0.02 and 2.68 ± 0.02 g cm⁻³, respectively. Based on grain density of the primary mineral phases, quartz (2.62 ± 0.02 g cm⁻³), clinocllore (2.65 ± 0.1 g cm⁻³), illite (2.75 ± 0.15 g cm⁻³) and phengite (2.82 ± 0.05 g cm⁻³), the phengite fraction is estimated ≤ 10 wt. %, the quartz + clinocllore fraction combined is estimated 20-30 wt. % and the illite fraction is estimated 60-70 wt.%.

Several pore types have been identified in mudstones and shales using recently developed focus ion beam SEM (FIB-SEM) [Desbois *et al.*, 2009; Heath *et al.*, 2011] and Ar-ion-beam- milling SEM [Loucks *et al.*, 2009] imaging techniques.

Based on SEM broken and polished surface imaging, pores in Maplewood Shale are categorized into four generic types: 1) fractures, 2) matrix-clast-voids, 3) clay-micropores and 4) matrix-pores. Fractures form thin tabular planes, usually parallel to foliation (Fig 5.2A bottom left). No distinction was possible between natural and unloading fractures. Matrix-clast-voids are pores at the contact between matrix material and coarser clasts and originate from geometrical misfits between different mineral shapes (Fig. 5.2C red boxes). Typically, their 2D cross section is triangular or elongated, with size usually < 2 μm . Clay-micropores exist within stacked illite flakes and represent planar, slit-like voids between irregular clay surfaces (Fig. 5.2C, F blue boxes). The thickness of these micro voids is usually < 100 nm. Matrix-pores are 1-3 μm sized voids inside the matrix, which originate from geometric misfits between matrix-forming minerals (Fig. 5.2C, F yellow boxes). Matrix pores are differently shaped, i.e. tabular, pyramidal or spherical and are sometimes geometrically similar to clay micropores or matrix-clast-voids.

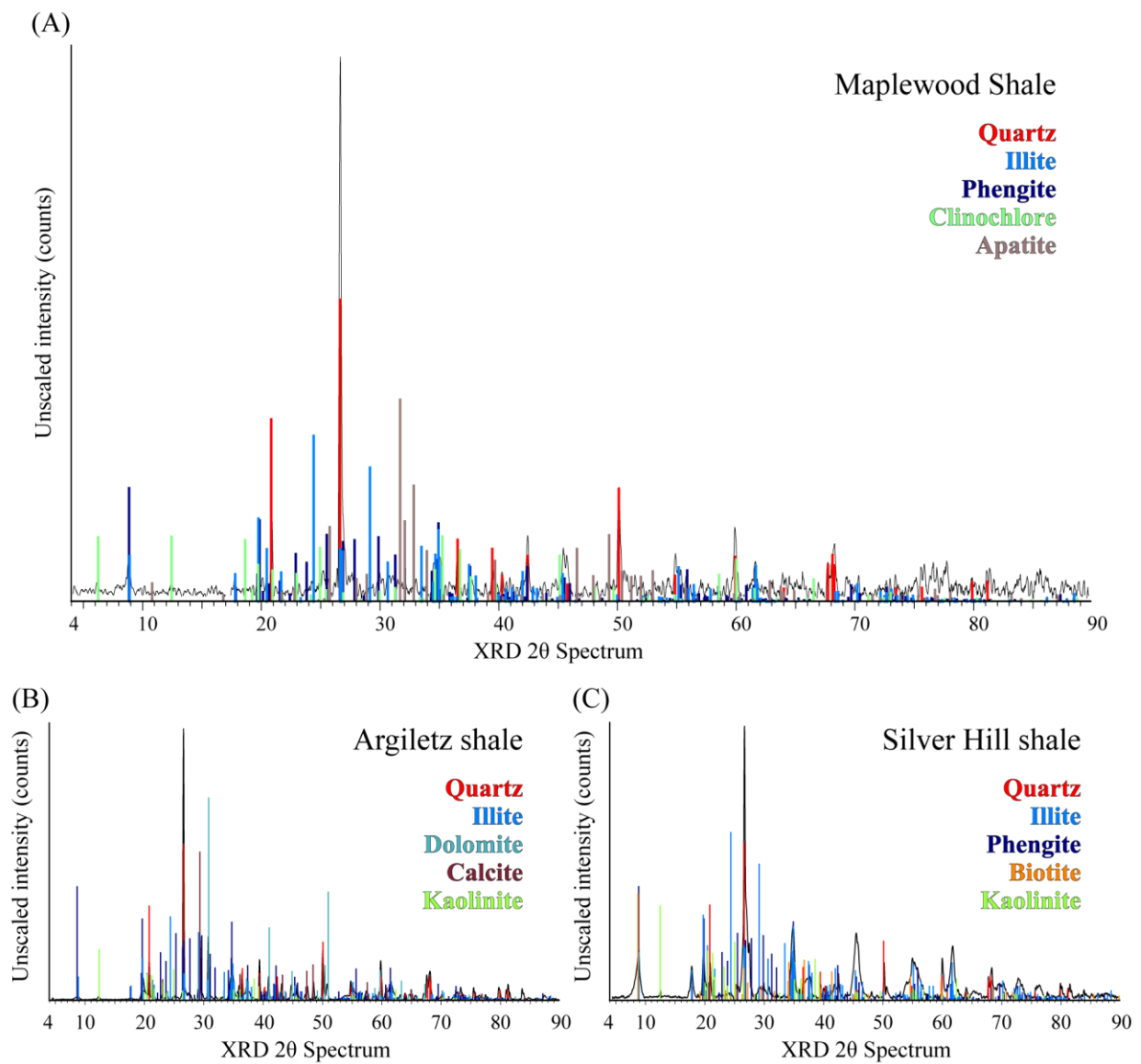


Figure 5.4: XRD spectra for A) Maplewood Shale, B) Argiletz shale and C) Silver Hill shale with interpreted mineral phases after 2θ peaks. XRD quartz pattern after Antao *et al.* [2008], illite after Drits *et al.* [2010], phengite after Pavese *et al.* [1999], clinochlore after Welch and Marshall [2001], apatite after Hughes *et al.* [1989], dolomite after Ross and Reeder [1992], calcite after Antao and Hassan [2010], kaolinite after Bish and Von Dreele [1989], and biotite after Bohlen *et al.* [1980].

Fractures in Maplewood Shale relate to pore-types VI of Heath *et al.* [2011]. Kwon *et al.* [2004] pore-types I and II, and Desbois *et al.* [2009] and Heath *et al.* [2011] pore-type I show strong correlation with Maplewood Shale clay-micropores. Matrix-clast-voids relate to type III pores of Desbois *et al.* [2009] and type V pores of Kwon *et al.*, [2004]. Matrix-pores show the best morphological correlation with Kwon *et al.* [2004] types III and IV, Heath *et al.* [2011] types II and III, and Desbois *et al.* [2009] type II pores.

5.5: Major element composition

Maplewood Shale:

Bulk major element composition of Maplewood Shale is presented in table 5.1. The principal sources for SiO₂ are quartz, mica, clay minerals and K-feldspar. TiO₂ occurs primarily in rutile. The sources for Al₂O₃, K₂O and likely Na₂O are the phyllosilicates and K-feldspar. Iron originates from the phyllosilicates and pyrite, whereas MgO is found only in clinocllore, illite and phengite. Apatite is the principal mineral that contains P₂O₅ and CaO. The origin of MnO is undetermined. Loss of ignition (LOI in table 5.1) is attributed solely to dehydration, dehydroxylation and melting of smectite, illite, phengite and clinocllore during heat treatment up to 1000 °C.

Argiletz shale:

Bulk composition of Argiletz shale (Table 5.1) is comparable to that of Maplewood Shale for SiO₂, Fe₂O₃ + FeO, TiO₂ and MnO. CaO, Al₂O₃, K₂O and MgO concentrations are noticeably different, reflecting higher carbonate and lower clay content in Argiletz shale than in Maplewood Shale. More striking is the high value for LOI, which probably represent the combination of dehydration and dehydroxylation of clays and degassing of carbonate minerals.

TABLE 5.1: MAJOR ELEMENT COMPOSITION OF ILLITE-RICH SHALES

Oxide ¹	Maplewood Shale	Argiletz shale	Silver Hill shale
SiO ₂	63.549	61.086	55.798
Al ₂ O ₃	19.609	16.155	23.372
K ₂ O	6.333	3.507	9.524
Fe ₂ O ₃ + FeO	5.300	5.399	6.643
MgO	2.537	4.345	1.671
TiO ₂	0.930	0.865	0.815
P ₂ O ₅	0.253	0.144	0.140
Na ₂ O	0.236	0.175	0.120
CaO	1.275	8.294	1.572
MnO	0.041	0.047	0.045
Total	100.070	100.017	99.700
LOI	5.439	17.050	5.200

¹All values in wt. %.

Silver Hill shale:

Compared to Maplewood Shale, Silver Hill shale is enriched in Al₂O₃, K₂O, Fe₂O₃ + FeO, and CaO (Table 5.1). In combination with lower SiO₂ concentration, the enriched oxides indicate

lower quartz and higher phyllosilicate content. Lower P_2O_5 concentrations suggest a low apatite presence. Water content in Silver Hill shale is consistent with illite-rich shales.

Comparison with geochemical standards:

Maplewood Shale bulk composition is used as input for the chemical model discussed in chapter 6 and as a representative shale type. For the latter purpose, the bulk composition is compared with that of commonly used geochemical standard for shale (Table 5.2) and Argiletz and Silver Hill shales (Fig. 5.5). Oxide concentrations are normalized over the average value of 11 geochemical shale standards (Table 5.2). Oxides in both tables 5.1 and 5.2 and figure 5.5 are sorted by increasing variation in concentration among the geochemical standards (i.e. increasing range of occurrence). The concentration of SiO_2 , $Fe_2O_3 + FeO$, MgO , TiO_2 and P_2O_5 in Maplewood Shale plots within the range of the geochemical shale standards and also within 20 % of their average (Fig. 5.5). The concentration of Al_2O_3 (1.10) is also close to the standards' average, but outside their range (0.93-1.09). K_2O concentration (1.71) is markedly higher than the average and normalized maximum concentration (1.35) of the standards. Conversely, Na_2O and MnO concentrations (0.14 and 0.25, respectively) are significantly lower than both the average and normalized minimum values (0.51 and 0.46, respectively) for the shale standards. Finally, while CaO concentration in Maplewood Shale (0.22) is noticeably lower than the average, it is still higher than the normalized minimum value (0.14) of standards.

For nearly all oxides, Argiletz shale fits within the general range of geochemical shale standards. One low-importance oxide, Na_2O is severely depleted. Other more important oxides, such as SiO_2 , Al_2O_3 and K_2O are below average. These oxides are important for shale composition, roughly representing quartz and clay content. Argiletz shale therefore represents a rather exotic shale composition, one that makes its use as illite shale source particularly impractical.

Silver Hill shale represents a different shale composition. It is enriched in Al_2O_3 , K_2O , $Fe_2O_3 + FeO$ and CaO compared to the average composition of the geochemical shale standards. On the other hand, Silver Hill shale is depleted in SiO_2 , MgO , Na_2O , CaO and MnO . The overall composition and pattern hints at a phyllosilicate-richer type of shale than on average. Based on its composition, Silver Hill shale is a suitable candidate to provide illite clay for the modeled illite-quartz shale.

TABLE 5.2: MAJOR ELEMENT COMPOSITION OF GEOCHEMICAL SHALE STANDARDS AND THEIR AVERAGES

Oxide ¹	PAAS ²	NASC ³	AS ⁴	ANAPS ⁵	ARPS ⁶	ANAMCS ⁷	ARMCS ⁸	ACPS ⁹	ARPS ¹⁰	ACAS ¹¹	AAS ¹²	Average
SiO ₂	62.8	64.80	64.21	59.75	56.78	67.78	64.09	66.90	63.04	62.13	65.47	63.43
Al ₂ O ₃	18.90	16.90	17.02	17.79	16.89	16.59	16.65	16.67	18.63	18.11	16.11	17.30
K ₂ O	3.70	3.99	3.58	4.82	4.38	2.44	2.73	4.97	4.57	2.92	2.37	3.68
Fe ₂ O ₃ or FeO	6.50	5.66	6.71	5.59	6.56	4.11	6.03	5.87	7.66	7.33	5.85	6.17
MgO	2.20	2.86	2.70	4.02	4.56	3.38	2.54	2.59	2.60	3.57	2.50	3.05
TiO ₂	1.00	0.70	0.72	0.98	0.92	0.70	0.82	0.78	0.94	0.78	0.49	0.80
P ₂ O ₅	0.16	0.13	0.19	0.12	0.13	0.10	0.12	0.14	0.10	0.17	0.14	0.14
Na ₂ O	1.20	1.14	1.44	0.72	0.77	0.98	1.27	1.50	1.02	2.68	2.80	1.41
CaO	1.30	3.63	3.44	6.10	8.91	3.91	5.65	0.53	1.31	2.22	4.10	3.74
MnO	0.11	0.06	0.50		0.08		0.07	0.06	0.12	0.10	0.07	0.13
Total	97.87	99.87	100.51	99.89	99.98	99.99	99.97	100.01	99.99	100.01	99.90	99.84

¹All values in wt. %.

² PAAS = Post-Archean Australian Shale [Taylor and McLennan, 1985]

³ NASC = North America shale composite [Gromet et al., 1984]

⁴ AS = Average shale [Clarke, 1924]

⁵ ANAPS = Average North American Paleozoic shale [Ronov and Migdisov, 1971]

⁶ ARPS = Average Russian Paleozoic shale [Ronov and Migdisov, 1971]

⁷ ANAMCS = Average North American Mesozoic/Cenozoic shale [Ronov and Migdisov, 1971]

⁸ ARMCS = Average Russian Mesozoic/Cenozoic shale [Ronov and Migdisov, 1971]

⁹ ACPS = Average Canadian Proterozoic shale [Cameron and Garrels, 1980]

¹⁰ ARPS = Average Russian Proterozoic shale [Ronov and Migdisov, 1971]

¹¹ ACAS = Average Canadian Archean shale [Cameron and Garrels, 1980]

¹² AAS = Average Archean shale [Ronov and Migdisov, 1971]

Figure 5.5 shows the relative bulk composition of Maplewood Shale after compaction stage 2 (HIP1). The oxide pattern is identical to natural Maplewood Shale, except for P₂O₅. No contamination or depletion of elements occurred during sample preparation or compaction stage 2. Major element concentration in Maplewood Shale determined by Kaszuba et al., [2005] is identical, except for slightly lower P₂O₅ and CaO values. The fact that different studies, samples and measurement techniques detected no variation in composition for Maplewood Shale, except for P₂O₅, suggests that apatite distribution is heterogeneous.

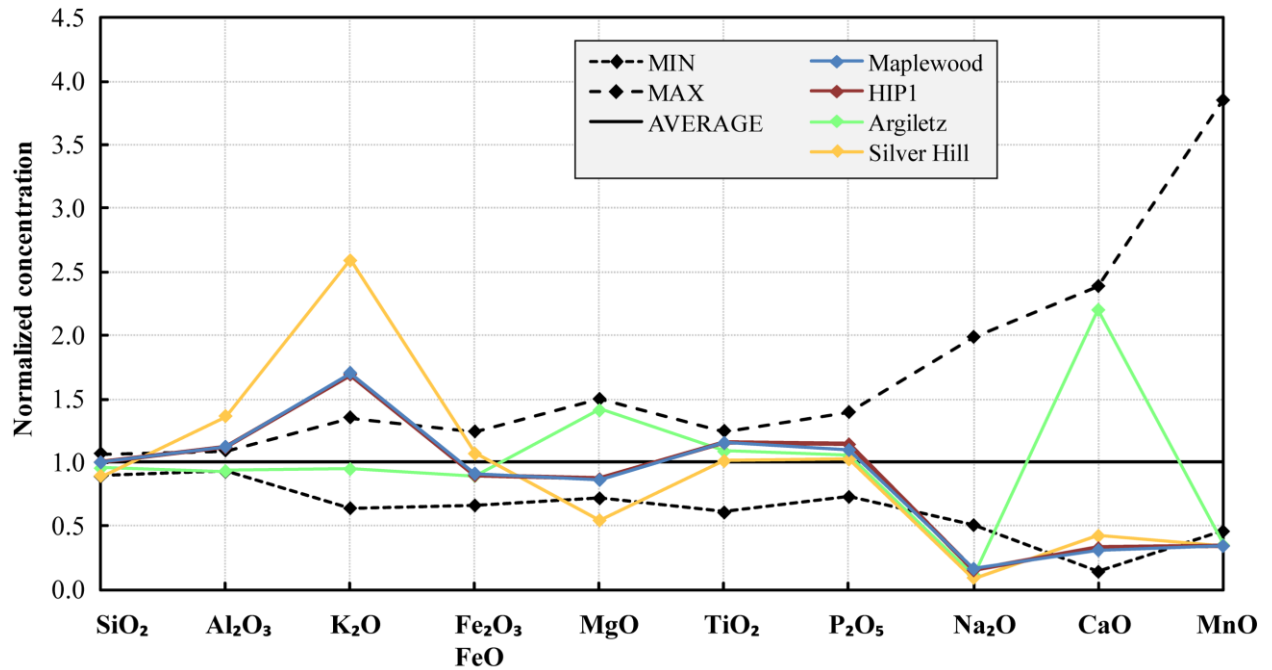


Figure 5.5: Major element concentrations of Maplewood Shale, Argiletz and Silver Hill shales normalized over the average of geochemical shale standards listed in Table 5.2. Dashed MAX and MIN lines represent normalized maximum and minimum values among the shale standards of Table 5.2, respectively.

5.6: Powder grain size

Maplewood Shale:

Maplewood Shale powder used for experimental re-compaction tests has a mean grain size of 21.1 μm , and contains 15.1 vol. % clay (< 2 μm), 79.5 vol. % silt (2-63 μm) and 5.4 vol. % sand (> 63 μm) (Table 5.3). Grain size distribution is visualized in figure 5.6 (MwS<125), together with the result of grain size analysis of coarser Maplewood Shale powders. The grain size distributions of crushed Silver Hill Shale powders, which have received identical crushing and sieving treatment, are plotted for comparison.

Despite sieving, Maplewood Shale (MwS) powders show similar grain size distributions. This was found to be the result of the initial crushed material containing only a relatively small grain fraction > 100 μm , rendering sieving unnecessary. Grain flocculation explains why 125 and 250 μm mesh sieves filtered apparent coarse grains. Electrostatic forces act to cluster fine clay and quartz particles, resulting in coarse-grained aggregates. Ultrasonic agitation during the grain size analysis disintegrated these aggregates.

TABLE 5.3: GRAIN SIZE DATA FOR MAPLEWOOD SHALE AND SILVER HILL SHALE

Powder ID	Mean grain size (μm)	Clay vol. %	Silt vol. %	Sand vol. %
Maplewood Shale				
MwS<125	19.9	15.1	79.5	5.4
MwS<250	14.0	15.6	81.9	2.4
MwS>250	18.1	15.6	81.5	2.9
MwSunsieved	19.9	13.3	83.2	3.5
Silver Hill shale				
SH<125	43.0	7.4	73.1	19.5
SH125-250	100.0	5.6	38.0	56.4

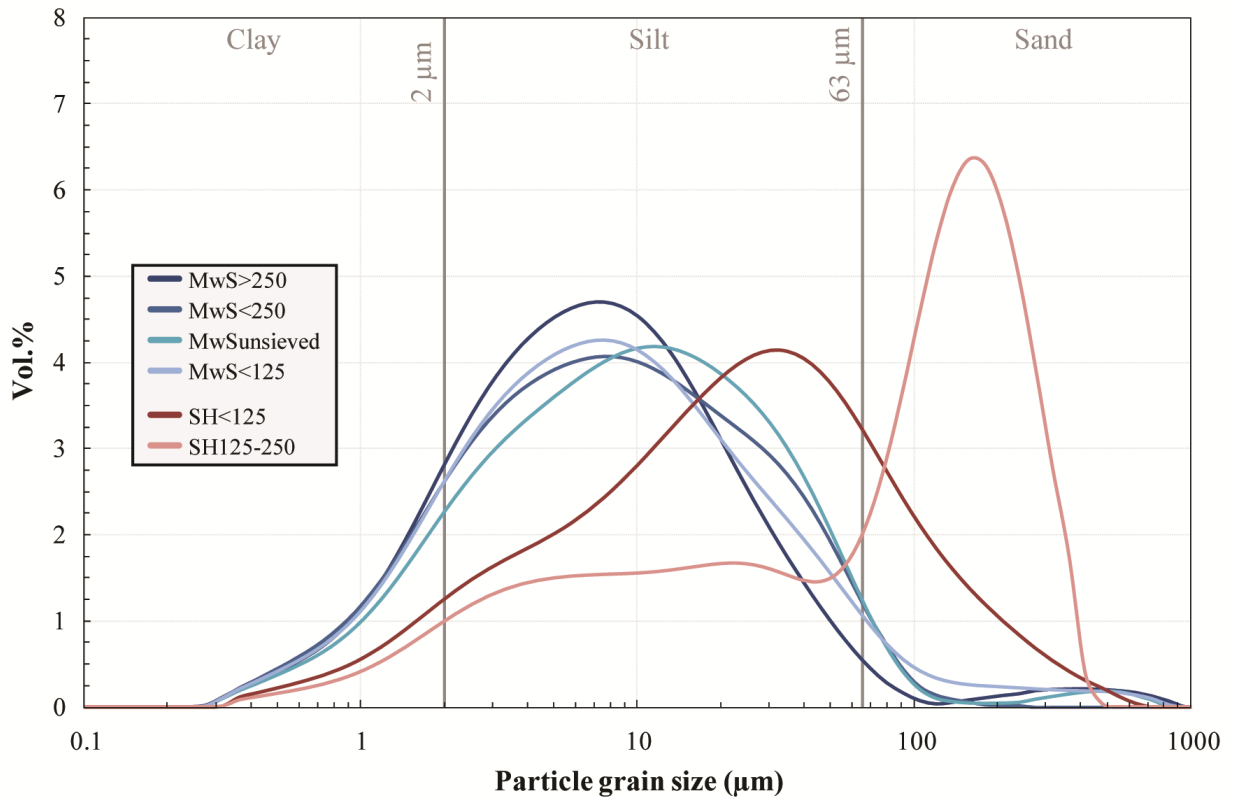


Figure 5.6: Grain size distribution plots for Maplewood Shale (MwS sample set) and Silver Hill shale (SH sample set) powders after grain crushing and sieving. Particles smaller than 2 μm are considered clay, between 2 and 63 μm silt; coarser material is considered to be sand.

Silver Hill shale:

Sieving of crushed Silver Hill shale resulted in grain separation. The sieved fraction < 125 μm has a dominant grain size of $\pm 40 \mu\text{m}$. The residue (SH125-250) has a prominent peak in vol. % at 170-180 μm , which fits in the sieve threshold. The larger minimum grain size is likely to have prevented grain flocculation.

5.7: Choice of Maplewood Shale

This chapter started with the dilemma which of three natural illite shale, Maplewood Shale, Argiletz shale and Silver Hill shale, to select as most appropriate source for illite clay. Now follows the explanation why Maplewood Shale was ultimately selected.

Maplewood Shale:

Maplewood Shale contains impurities such as smectite, phengite, clinochlore, non-silicates and K-feldspar. These impurities are however not conflicting with illite and quartz as explained below.

XRD analysis (Fig. 5.4A) revealed that smectite content is low, which confirms estimated burial conditions of late diagenetic zone to anchizone [Friedman, 1987]. The smectite to illite transformation during compaction stages 2 and 3 plays a marginal role in the total chemical compaction process. All chemical activity in high-temperature compaction tests could be attributed to the illite to phengite transformation. Detrital phengite is thermodynamically stable during all experiments, except those at 750 °C (Chapter 6), and will not interfere with the formation of authigenic phengite. The presence of clinochlore in Maplewood Shale is in fact beneficial because it facilitates tracing the progress of mineral reactions during the high temperature compaction tests. The stability field of chlorite extends to higher temperature than that of illite (Chapter 6). Secondary phases such as biotite and K-feldspar represent a negligible fraction in terms of chemistry and mechanics. Biotite is morphologically and mechanically similar to phengite, while K-feldspar behaves like quartz. Moreover, both biotite and K-feldspar are stable throughout the full range of experiments (Chapter 6). Other secondary phases such as the non-silicates represent such a small fraction, as illustrated by the TiO_2 and P_2O_5 normalized concentrations in figure 5.5 that their chemical and mechanical effects are negligible. No chemical reaction involving pyrite, apatite and rutile is expected and, in terms of mechanics, they will act as rigid clasts. In summary, albeit an impure illite shale, Maplewood Shale is a suitable candidate for representing the illite-fraction in the modeled illite shale. In fact, since the silt fraction of Maplewood Shale is dominantly quartz only crushing of rock fragments and subsequent powder mixing is required to eliminate microstructural and chemical heterogeneities.

Argiletz shale:

With Argiletz shale, which is available as powder, a chemical treatment and probable subsequent clay filtering are required to eliminate carbonates. The bulk rock composition and XRD analysis further hint at relatively low clay and mica content (Fig. 5.4B and 5.5). For these reasons, Argiletz shale was found less suitable as source for illite clay than Maplewood Shale.

Silver Hill shale:

Silver Hill shale is dissimilar in mineral and major element composition to Maplewood Shale. Higher Al_2O_3 and K_2O , but lower SiO_2 concentrations (Fig. 5.5) as well as the XRD spectrum (Fig. 5.4C) suggest higher phyllosilicate and lower quartz content. Carbonates are also absent. As for Maplewood Shale, other non-silicate impurities in Silver Hill shale can be ignored. The reason that Maplewood Shale was preferred to Silver Hill shale is based primarily on grain size distribution (Fig. 5.6). The clay content is much lower and the dominant grain size much coarser than for Maplewood Shale. The fact that sieving affects grain size distribution in Silver Hill shale suggests that clay flocculation did not occur, reflecting higher mica content and smaller amount of clay compared with Maplewood Shale.

5.8: Geological setting of Maplewood Shale

Stratigraphy:

Maplewood Shale is an Early Silurian (Llandoveryan, ~ 430 Ma) green shale unit in the Northern Central Appalachian Basin, exposed in Western New York State (Fig. 2.2). In Rochester (NY), the Genesee river gorge provided Maplewood Shale exposure of 7 m thickness [Chadwick, 1918]. Together with the Neagha Shale that outcrops northeast of Buffalo (NY) and Webster conglomerate Bed that outcrops east of Rochester (NY), Maplewood Shale forms the base of the Lower Clinton Group (Fig. 2.3). The westward thinning Lower Clinton Group unconformably overlies the Medina Group clastic wedge shales and sandstones and represents a tectonically controlled fluctuating eastward transgression across the basin. The onset of a transgression cycle is marked by hematitic, phosphatic beds: 1) Densmore Creek beds and Webster conglomerates at the Medina-Lower Clinton contact [LoDuca and Brett, 1994; Brett *et al.*, 1990] and 2) Budd Road Phosphate Bed (or Furnaceville Member) of the Reynales Limestone Formation that overlies Maplewood Shale [LoDuca and Brett, 1994; Brett *et al.*, 1995]. Regional relative sea-level fluctuation is expressed also by repetition of lithologies (e.g. shales of the Bear Creek and Sodus Formation, and limestones of the Wolcott Formation as well as coarser clastic wedge deposits of the Sauquoit Formation (Fig. 2.2). A widespread, angular unconformity attributed to global sea level low defines the contact with the overlying Upper Clinton group [Johnson *et al.*, 1985].

Structures:

Deformation structures are scarce throughout most of the Paleozoic sediments in the Northern Appalachian Basin. The Ordovician and Silurian sediments form a gently southward dipping sequence of weakly deformed rocks, exposing underlying rocks. Deformation is manifested in residual elastic

strain, elastic anisotropy, mechanical twinning and cleavage formation associated with pressure solution [Engelder, 1979]. Minor folds and stylolites have been identified in the Onondaga Formation in the eastern margin of the geological map of figure 2.2 [Groshong, 1975]. 30-40 km west of Rochester (NY), in Silurian and Late Ordovician sediments, the Clarendon-Lindin fault system forms a N-S striking monocline with 3° dip to the west [Engelder, 1979]. Systematic deformation structures are found more to the south in Middle to Late Devonian sediments, and form the outermost major folds of the Appalachian fold and thrust belt [Engelder, 1979].

Chapter 6

Chemical model

The fiction character Kelvin R. Throop once said, “Isn’t it interesting that the same people who laugh at science fiction listen to weather forecasts and economists?”

Preface

This chapter presents a model that describes the equilibrium mineral phase stability at the experimental conditions for Maplewood Shale. The chapter commences with explaining why such a chemical model is required to understand compaction processes occurring during experiments, and introduces a number of commercially available software packages for numerically simulating mineral phase stability. The results of the thermodynamic phase equilibrium modeling are discussed in subchapter 6.2. The importance of water content is discussed, ultimately leading to the construction of an x_{H_2O}/T diagram in subchapter 6.3. Such a diagram visualizes the water dependency of the modeled equilibrium mineral assemblages. The chapter then discusses in subchapter 6.4 the results of thermogravimetry analysis. Obtained data are used to compare modeled dehydration and dehydroxylation reactions with observed water loss during room pressure heating of sample material. The chapter concludes with a short summary on the findings and conclusions from the performed petrological analysis.

6.1: Phase stability modeling

Illite shale powder is subjected to temperature conditions higher than those marking the stability field of illite (80 - 200 °C), during compaction stages 2 and 3. Although, the durations of these stages are hours to days, which is some orders of magnitude shorter than in a natural setting, the mineral assemblage of the illite shale samples are affected. Chemical equilibrium cannot be assumed, due to the very short duration of the exposure to elevated temperatures. Chemical models that predict non-equilibrium mineral assemblages are up to date unavailable. Predictions of mineral reactions progress were attempted here using equilibrium phase stability modeling. Out of four well-known and applied software packages, Perple_X [Connolly, 1990], THERMOCALC [Powell and Holland, 1988; Powell *et al.*, 1998], Theriak-Domino [de Capitani and Brown, 1987; de Capitani and Petrakakis, 2010] and TWQ [Berman, 1991; 2007] Perple_X version 6.5.0 [Connolly, 2009] was ultimately selected. The choice for Perple_X is explained now. In terms of thermodynamic calculation and input database, the four thermodynamic calculation packages are principally identical, and resulting pseudosections are similar. The key advantage of Perple_X over THERMOCALC is the shorter calculation time and limited required input data. THERMOCALC requires pre-existing knowledge of expected mineral reactions for backward phase equilibrium modeling. In this study, such knowledge is missing because the illite shale powder has not experienced metamorphism.

For the Perple_X modeling, the 2002 update of the thermodynamic dataset of *Holland and Powell* [1998] was used together with the NCFKMASH system (i.e. Na₂O, CaO, FeO/Fe₂O₃, K₂O, MgO, Al₂O₃, SiO₂ weight percent composition data obtained by XRF analysis (Table 5.1)). Titanium and manganese were found to have no visible effect on location of phase stability fields in the modeled pseudosection. Solid solution calculations were calculated for phengite, staurolite, chlorite, chloritoid, K-feldspar, biotite, garnet and melt. No phases were excluded from thermodynamic minimum Gibb's free energy calculations. Input values for major element concentrations are reported in table 5.1, although for water a value of 5.18 wt. % was used.

6.2: Pseudosection

A simplified pseudosection based on Maplewood Shale composition is shown in figure 6.1. For purpose of clarity, small fields were merged and reactions that do not involve mica or clay were omitted. Ultimately, five principal equilibrium stability fields were identified, based chiefly on phyllosilicate content. The fields, labeled I-V, are dominantly temperature controlled, especially above 50 MPa. Differing confining pressure between compaction stages 2 and 3a, and 3b thus has little effect on mineral reactions and stability. Quartz is stable in fields I to IV whereas water is in excess.

Illite, chlorite and phengite are stable in field I bounded at about 350 °C by the disappearance of illite and introduction of biotite as a stable mineral phase. Based on maximum burial depth estimates of 5 km for New York Trenton Group carbonates that underlies the Maplewood Shale [Friedman, 1987], peak equilibrium conditions for illite shale powder before experimental compaction tests are estimated at 125-145 MPa and 145-180 °C. These conditions plot outside the pseudosection of figure 6.1, but agree with field I mineral phases. Compaction experiments performed under the operating conditions of field I are unlikely to trigger clay mineral reactions and will therefore only activate mechanical compaction.

Chlorite, biotite and phengite are stable in field II whose upper boundary at 450 to 550 °C is the disappearance of chlorite. Compaction tests of stage 3a as well as stage 3b performed at 500 °C both plot in this field. Equilibrium phyllosilicate assemblage in HIP2 and a selection of PAT1 (CIP) samples is expected to be chlorite, biotite and phengite. If in these samples illite is present or authigenic biotite absent, then equilibrium was not achieved.

Biotite and phengite are stable in field III, which includes the operating conditions of compaction stage 2 (HIP1 samples) and 650 °C compaction stage 3b tests (some PAT1 CIP samples). No chlorite or illite is thus expected in equilibrium mineral assemblage of these samples. The phengite dehydroxylation reaction (phengite + quartz → K-feldspar + Al-silicate + H₂O) marks the boundary between field III and IV.

Stable mineral phases in Field IV are the reaction products of the phengite dehydroxylation reaction and biotite. 700 °C experiments in compaction stage 3b are performed at operating conditions of field IV. Equilibrium mineral assemblages in associated PAT1 (CIPT) samples contain only K-feldspar, an aluminosilicate (most probably sillimanite), and biotite. The presence of phengite, chlorite or illite, or absence of authigenic feldspar and sillimanite indicates non-equilibrium mineral assemblages. The transition from field IV to V is the wet-solidus.

In field V, partial melt is generated at the expense of quartz, biotite and water. Sillimanite also contributes to melt at higher temperature. Absence of melt (glass after quenching) is indicative for non-equilibrium, as is the occurrence of phengite, biotite, quartz, chlorite, or illite.

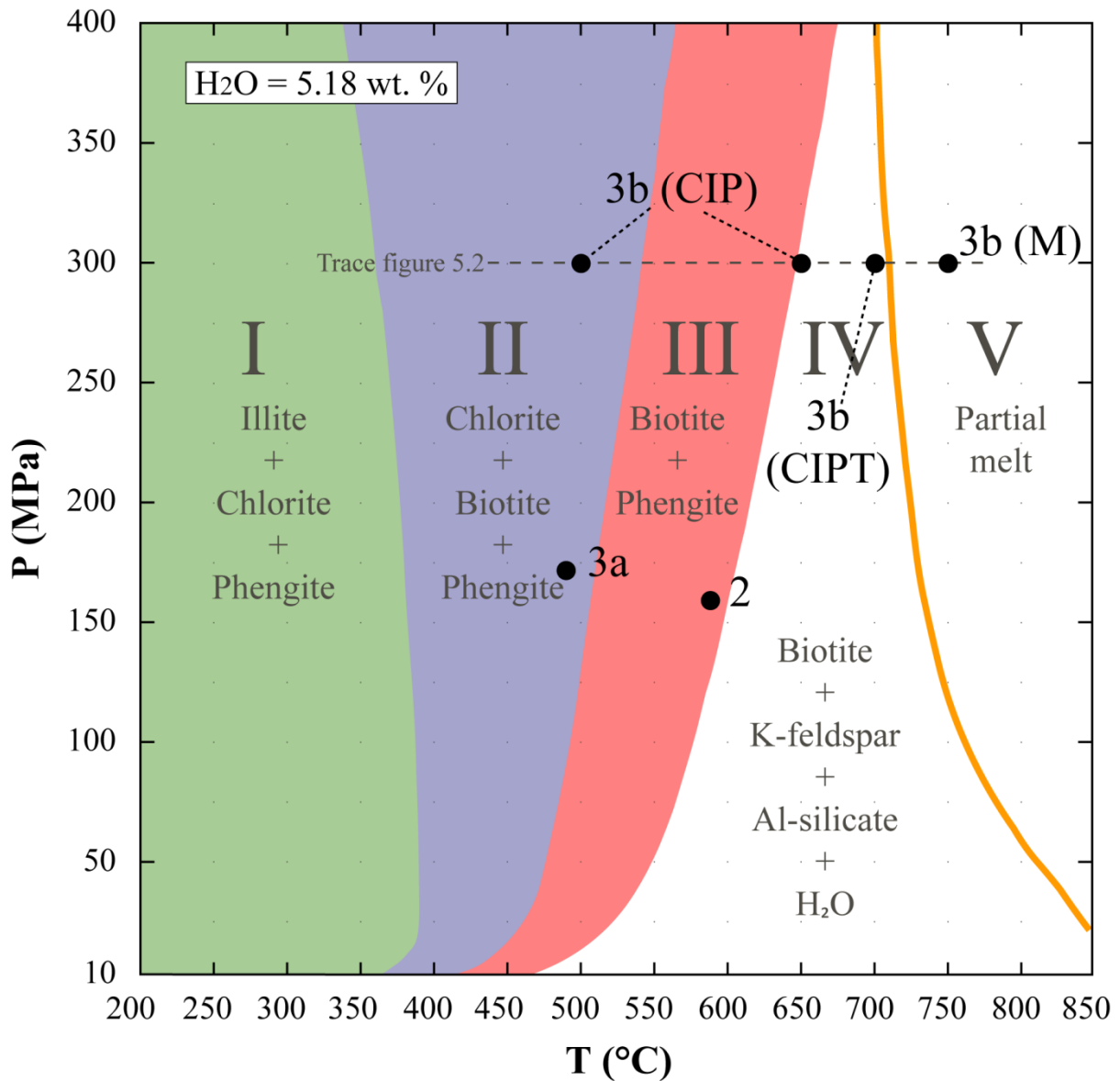


Figure 6.1: Simplified *Perple_X* pseudosection for Maplewood Shale major element composition. Labeled black dots indicate operating conditions of respective compaction stages. Bracketed letters I, C, P and M refer to sample subgroup ID of compaction stage 3b (Table 3.1). Dotted horizontal line indicates the temperature range of diagram in figure 6.2.

6.3: Water dependency

Since bulk rock composition before and after compaction stage 2 is identical for major elements (subchapter 5.5), one can consider the chemical system to be closed. This, however, does not apply to water. Water content is much lower after compaction stage 2 than before (4.0-5.5 wt. % vs. 2.6-3.1 wt.%) and maintained (KFT H_2O = 2.71 wt. %) after compaction stage 3a (i.e. second hot isostatic pressing event). Lower temperature conditions during compaction stage 3a restricted mica dehydroxylation. The minimum water content required to maintain the equilibrium phase stability fields II to V (Fig. 6.1) can be read off a T/xH_2O diagram. Fields I to V are constructed by *Perple_X*

using a water content of 5.18 wt. % as input value. Fields of equilibrium mineral assemblages at $x_{H_2O} = 5.18$, and variable T in the T/x_{H_2O} diagram correspond to fields I to V. Such diagram (Fig. 6.2) was calculated using the same input parameters as for the pseudosection (Fig. 6.1) at a confining pressure of 300 MPa.

Coupling between a pseudosection and T/x_{H_2O} diagram is done via the input value for the H_2O concentration in the simulation of the pseudosection and the fixed value for pressure in the T/x_{H_2O} diagram. The trace line (dashed grey line) in one figure, display the conditions for which the other figure is constructed. Along these trace lines, equilibrium assemblage fields are matching in both types of figures. From this, it can be seen that field I occurs below the minimum temperature depicted in figure 6.2. The extent of fields II and III is marked by total water content and temperature. Those fields characteristically have excess water, meaning that the amount of water in hydrous mineral less than the total water content. Excess water exists for $T < 640$ °C, for H_2O values > 2.2 wt. %. Field II equilibrium mineral assemblage exists below 510 °C, and that of field III exists below 640 °C. Field IV extends to lower water content values (minimum $H_2O = 1.0$ wt. %). Between 640 °C and ~700 °C, in field IV, excess water is present above ~ 1.0 H_2O wt. %.

The boundary between field IV and V is identified by the wet solidus at 700 °C. Below 1.0 wt. % H_2O , the solidus shifts to higher temperature (> 750 °C).

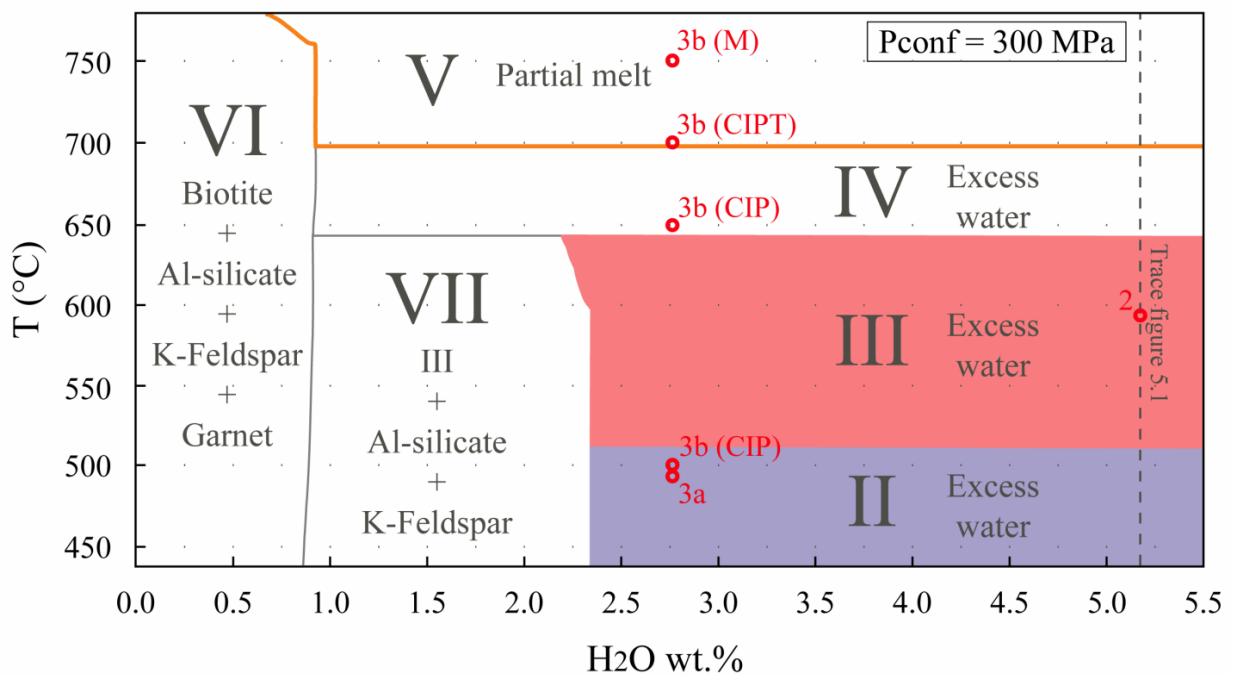


Figure 6.2: Simplified T/x_{H_2O} diagram for Maplewood Shale major element composition. Labeled red circles indicate operating conditions of respective compaction stages. I, C, P and M letters in parentheses refer to sample subgroup ID of compaction stage 3b (Table 3.1). Dotted vertical line indicates the temperature range of the pseudosection in figure 6.1.

Besides fields I to V, two additional fields are identified, at low H₂O values (< 2.2-2.3 wt. %). Field VI exists below 0.9-1.0 wt. % H₂O. Total water content is too low to maintain phengite as a stable phase. Instead, the mineral assemblage in equilibrium consists of biotite, an aluminosilicate (andalusite or sillimanite), K-feldspar and garnet. At higher water contents, between 0.9 and 2.3 wt. % H₂O but below 650 °C, field VII accepts the stable mineral assemblage of biotite, phengite, andalusite or sillimanite and K-feldspar; quartz is also stable in this field. Water in fields VI and VII is incorporated in the phyllosilicates; no excess free water exists.

It is important to note that water loss during compaction stage 2 has no consequence for mineral stability. During compaction stage 3, water loss is most crucial for experiments performed at temperature < 650 °C, as the transition from field II and III to field VII occurs at H₂O wt. % of 2.3. However, since phyllosilicates dehydroxylated to 590 °C during compaction stage 2, subsequent heating below that temperature yields no further dehydroxylation. Dehydroxylation is expected for compaction stage 3b experiments (temperature ≥ 650 °C). But the transition from field IV and V to VI occurs at much lower water content (1.0 wt. H₂O). Hence there is a substantial margin until equilibrium mineral assemblages move outside the pseudosection of figure 6.1.

6.4: Dehydration and dehydroxylation

Thermogravimetry (TGA) analysis of illite shale powder before compaction stage 1 and after compaction stage 2 are presented in figure 6.3. Data from NAT (P) TGA shows the anticipated smectite dehydration at low temperatures (50-150 °C), as well as illite and phengite dehydroxylation at intermediate temperature (450-750 °C). The TGA curve for HIP1 indicates the onset of dehydroxylation at 550 °C, which is complete by 1000 °C. For reference, mineral characteristic curves for illite, Clay Mineral Society illite specimen from Silver Hill, Montana by *Earnest* [1991], and muscovite by *Mariani et al.* [2006] were added. Considering only the dehydration and dehydroxylation behavior, NAT (P) best compares with Silver Hill-illite. The higher water content of Silver Hill-illite is explained by its larger smectite and illite fraction than in Maplewood Shale. The onset of dehydroxylation in HIP1 is thus comparable with that of muscovite. Prolonged dehydroxylation until 1000 °C is more compatible with Silver Hill-illite, indicating the presence of illite in HIP1 samples. Different TGA behavior for NAT (P) and HIP1 is explained by complete smectite to illite transformation and partial illite to phengite transformation during hot isostatic pressing in compaction stage 2.

The thermogravimetry analysis is also a test for the accuracy of the pseudosection. For correlation between TG curves (Fig. 6.3) and the pseudosection mineral assemblage fields (Fig. 6.1), pressure sensitivity of phyllosilicate reactions at low pressure should be taken into consideration. Equilibrium mineral assemblage fields I to III in the pseudosection are predominantly temperature

controlled, except at low pressure. With pressure below 50 MPa, boundaries for fields I to III shift to lower temperatures. Field I is barely affected; its boundary is situated at ~ 370 °C at 10 MPa. The transition from field II to III at 10 MPa occurs at ~ 420 °C, instead of > 500 °C at $P = 300$ MPa. The phengite dehydroxylation boundary of field III is most pressure sensitive. At 10 MPa, field III is bounded at ~ 470 °C. The wet solidus shows opposite behavior. The boundary from field IV to V shifts to higher temperature at low pressure (> 850 °C at 10 MPa).

Correlation between TGA and mineral reactions is best performed using the phengite dehydroxylation reaction. This marks the boundary between fields III and IV and is identified in the TGA curve for NAT (P) at 450-500 °C. This temperature range coincides with the boundary between fields III and IV in the pseudosection at low pressure. On the other hand, onset of the phengite dehydroxylation reaction for HIP1 samples is identified in the TGA curve at 550 °C. When extrapolated from 170 to 300 MPa this reaction is expected between 650 and 700 °C. The *Perple_X* pseudosection (Fig. 6.1) is most accurate for compaction stage 2 modeling of mineral assemblages. Despite closed system chemistry and water loss without chemical consequences, the pseudosection is less accurate for compaction stage 3 tests, as at least the phengite dehydroxylation reactions seems to occur at 50-100 °C higher temperature.

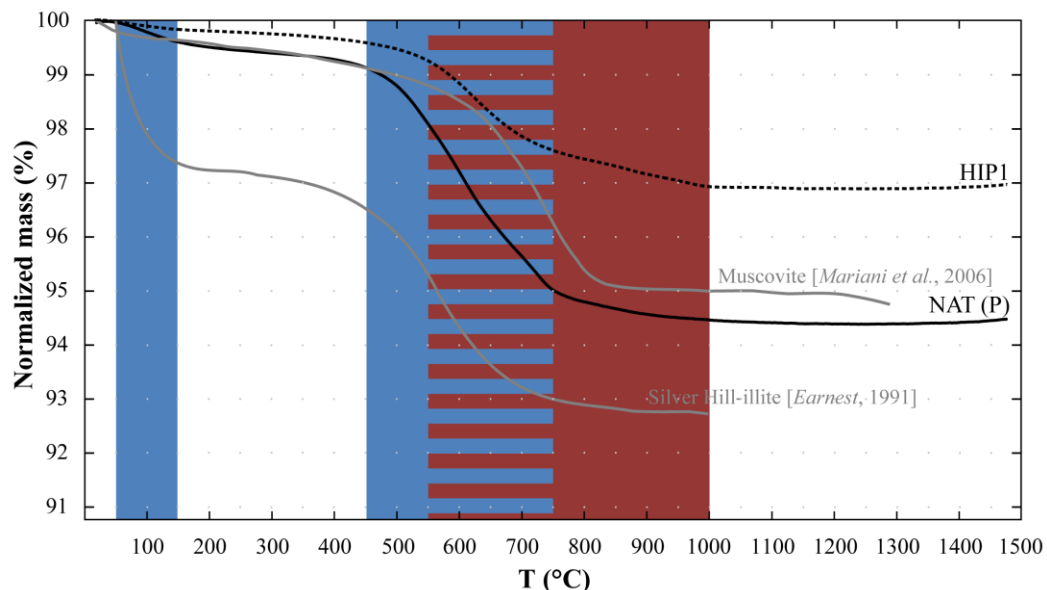


Figure 6.3: Thermogravimetry curves for illite shale powder before compaction stage 1 (NAT (P)) and after compaction stage 2 (HIP1). Blue and red areas denote NAT (P) and HIP1 dehydration, respectively. For comparison, mineral characteristic TG curves for illite and muscovite were added.

6.5: Summary

In summary, the chemical model, as visualized by a pseudosection, xH_2O/T diagram, and TGA curves constrains the uncertainties associated with compaction tests performed at pelite disequilibrium experimental conditions. The pseudosections identified five fields of equilibrium

mineral assemblages. Field I represents the illite shale stability. Other fields are addressed in one or more compaction stages. As the targeted mineral assemblages are known for each experiment, the progress of mineral reactions towards equilibrium can be monitored. Mica dehydration and dehydroxylation affects the position of the fields. So caution is required when water content decreases below threshold values and one of two additional fields, characterized by the absent or low amount of hydrous minerals, is addressed instead. TGA curves provided information on the actual water loss expected with heating. However, KFT H₂O measurements will be pivotal to verify precisely which field of equilibrium mineral assemblages was in fact addressed during notably compaction stage 3b tests.

Chapter 7

Results

Harry S. Truman once said, “It is amazing what you can accomplish if you do not care who gets the credit.”

Preface

This chapter presents the products of the experimental high temperature and pressure compaction of illite shale powder and the mechanical and rheological data from compaction stage 3b tests in the Paterson apparatus. The synthetic metapelites are characterized by porosity, bulk density and strain behavior (subchapter 7.1), which provided important information for the quantification and understanding of compaction mechanisms. Two sample subsets are identified based on density development. Strain was found to be primarily accommodated by porosity reduction, with temperature playing a key role in the amount of compaction. Mechanical data represent the sample strength evolution with strain (subchapter 7.2). In 500 °C, 650 °C and some 700 °C tests, samples experienced rapid hardening, without reaching steady state flow, whereas at higher temperatures steady state flow is achieved. Rheological data obtained during steady state flow is then used to characterize the flow (subchapter 7.2).

Chemical changes during compaction are monitored using XRD analysis and water content measurements based on KFT analysis (subchapter 7.3). Phengite crystallinity enhanced and biotite content grew at the expense of the clay minerals originally present in the illite shale powder. Furthermore, water loss is used to compare and contrast the modeled mineral assemblage fields during the compaction stages (subchapter 7.3). High-magnification SEM BSE and SE images were used to visualize the development of mineral content, microstructure and pores, confirming the findings from XRD analysis (subchapter 7.4). Microstructures revealed that porous domains are illite-rich and display no foliation, whereas crystalline domains are illite-poor and exhibit a strong foliation (subchapter 7.5). Also, quartz grains were found to be affected by compaction and authigenic grains were formed. A new generic pore-type, associated with fractured quartz grains, is identified (subchapter 7.6); clay micropores are identified as the principal pore type that accommodates compaction.

7.1: Porosity and density

Two of the most fundamental and basic rock parameters are porosity and bulk density. The properties of argillaceous sediments, such as those of interest, are likewise related to porosity and bulk density [e.g. *Rieke and Chilingarian, 1974; Vasseur et al., 1995; Mondol et al., 2007*]. In general, natural shales and mudstones with porosity < 15 % exhibit evidence for illitization of smectite and silica cementation and/or texture enhancement [e.g. *Kim et al., 1999; Aplin et al., 2003; 2006; Worden et al., 2005; Peltonen et al., 2009; Thyberg et al., 2010; Day-Stirrat et al., 2010*]. Porosity and bulk density are parameters controlling the dominant mode of compaction in compaction stages 2 and 3. In addition, the effect of stress field on compaction processes is potentially expressed by density development, through the consideration of the effect of different mineral reactions or reaction rates.

The two- and three-stage compaction of illite shale powder resulted in lithified aggregates with connected porosity ranging from 1 to 17 % and bulk density ranging from 2.35 g cm⁻³ to 2.69 g cm⁻³ (Fig. 7.1AB and Appendices C-D). Based on the density-porosity data two sample subsets can be identified (Fig. 7.1A). The synthetic metapelites in both subsets represent a linear density increase with porosity reduction. Assuming all porosity is connected, extrapolation of the best fit curves for the subsets to zero porosity gives the average grain density. For subsets 1 and 2 grain density is estimated at 2.73 g cm⁻³ and 2.63 g cm⁻³, respectively. Each of two Maplewood Shale measurements fit with one subset (Fig. 7.1A).

Repetition of hot isostatic pressing (HIP2) and Paterson apparatus tests (PAT1) reduced porosity to the measured minimum value of ~ 1 %, corresponding to maximum bulk density of 2.69 g cm⁻³ (Fig. 7.1B). Subset 2 is mostly comprised of HIP2 samples (Fig. 7.1AB). PAT1 (C) and (I) exhibit comparable trends, in which other PAT1 samples also plot. To a degree, the trend from PAT1 samples overlaps with HIP1 samples, but is denser than HIP2 samples (Fig. 7.1B). A small number of PAT1 samples are noticeably more porous than HIP1 samples, but have similar density (Fig. 7.1B).

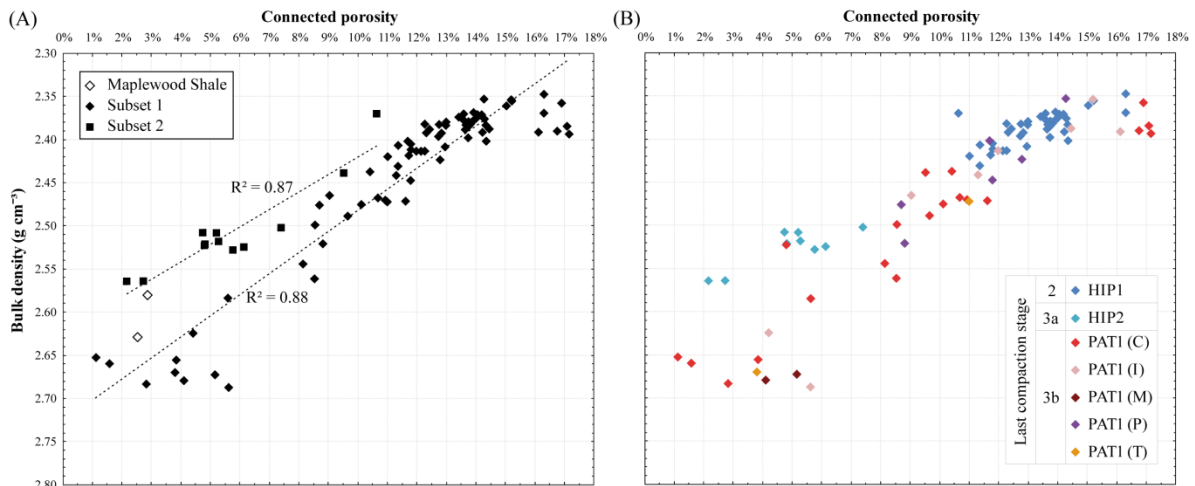


Figure 7.1: A) Bulk density of synthetic metapelites, split in two subsets, and Maplewood Shale as a function of porosity. B) Figure 7.1A color coded according to compaction stage history (Table 3.1).

7.2: Finite volumetric strain

Compaction may be described as the accommodation of strain by pore closing, regardless of the mechanism. For compaction to be the principal mechanism of strain accommodation, volumetric strain and porosity reduction are required to be identical. To test which samples exhibited compaction only, and which additionally deformed by brittle or ductile processes, porosity reduction is plotted against volumetric strain (Fig. 7.2). Density increase due to phase transformation is ignored and mass balance is assumed. The expected illite (average density = 2.75 g cm^{-3}) to phengite (average density = 2.83 g cm^{-3}) transformation for example will not result in significant density increase. In the first quadrant of the plot, the line finite volumetric strain = porosity reduction describes strain accommodation solely by pore collapse. Excessive strain requires brittle deformation of the solid framework. Excessive porosity reduction occurs when the pore network decreases connectivity without closing all pores. Porosity increase or delayed reduction during deformation is explained by 1) pore network enhancement as strain improves the connectivity of pores through e.g. grain refinement or cracking, or 2) the formation of secondary porosity by mechanical or chemical processes such as dissolution in combination with fluid dissipation.

Porosity reduction during compaction stage 3b was found to increase with finite volumetric strain along the pore space collapse line, regardless of stress field orientation (Fig. 7.2A and Table D1). Lowering the effective confining pressure was found to limit the maximum finite volumetric strain and porosity reduction (PAT1 (P) samples), whereas experiments at higher temperature yielded higher volumetric strain and porosity reduction (Fig. 7.2B and Table D1). Three $700 \text{ }^\circ\text{C}$ PAT1 metapelites, compacted in different stress fields, extend the most in the solid grain deformation field. Room temperature isostatic stress tests increased porosity without significantly dilating the sample. Three PAT1 (C) $500 \text{ }^\circ\text{C}$ samples simultaneously decompact and contracted.

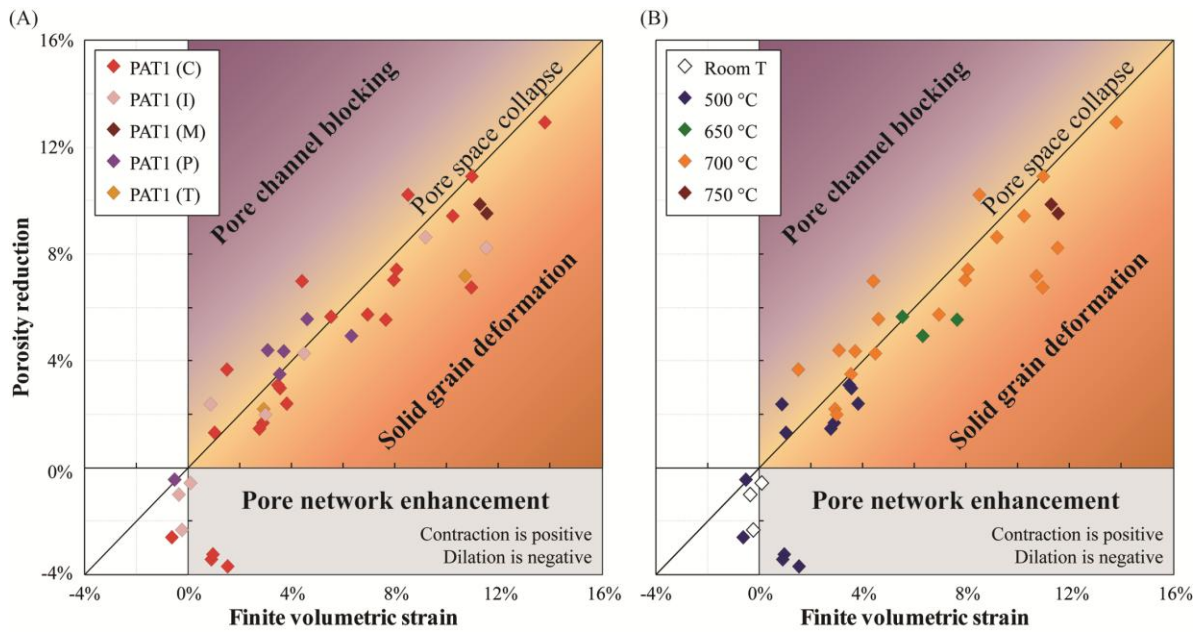


Figure 7.2: Porosity reduction plotted against finite volumetric strain for PAT1 samples, color coded according to A) compaction stage history (Table 3.1) or B) temperature. Both horizontal and vertical error bars (estimated in both cases at 0.2-3 %) are comparable in size with the data point symbols.

7.3: Finite sample deformation

Further compaction of porous synthetic metapelites (HIP1) in the Paterson apparatus is achieved by applying deformation in different stress regimes and under varying pressure and temperature conditions. The permanent deformation of the sample is described by finite axial (ϵ_{ax}) and radial axial (ϵ_{rd}) strain. In an $\epsilon_{ax}/\epsilon_{rd}$ diagram (Fig. 7.3), fields and lines define characteristic strain modes such as simple flattening, uniform and non-uniform contraction, pure shear and uniaxial strain. In the field of non-uniform contraction (including the uniform contraction line) the volumetric strain is seen to be contractive. The field of simple flattening is separated in a contractive (upper) and dilative (lower) part by the line for pure shear (no volume change).

Plotting ϵ_{ax} and ϵ_{rd} for PAT1 samples gives insight in the strain development during the compaction tests. Within a sample group and for each unique temperature, ϵ_{ax} - ϵ_{rd} data points describe a sample deformation path. When finite and total axial strain compare, these paths may be coupled to sample strength development during confined compression tests. Using this method, nearly all PAT1 samples plot between the lines for pure shear and uniform contraction (Fig. 7.3A). In fact, most metapelites experienced biaxial strain, so that volumetric strain and axial strain are not necessarily related. PAT1 (I) and PAT1 (T) samples plot nearest to the uniform dilation line (Fig. 7.3A). Scattering between non-uniform contraction and pure shear occurs for PAT1 (P) and PAT1 (C) samples. Nearly half of the PAT1 (C) samples show an overall uniaxial straining, whereas both PAT1 (M) samples exhibit simple flattening.

Finally, within this spread, especially of PAT1 (C) samples, a thermal gradient is seen (Fig. 7.3B). Samples compacted at room temperature and 500 °C are closest to the line of pure shear. Higher temperature samples plot away from pure shear and towards uniaxial strain. For finite axial strain < 13 %, some 700 °C PAT1 (C) samples entered the field of non-uniform dilation (Fig. 7.3B). Construction of the deformation paths for PAT1 (C) and PAT1 (P) samples at 500 °C, 650 °C and 700 °C and PAT1 (M) samples is discussed in subchapter 9.3.

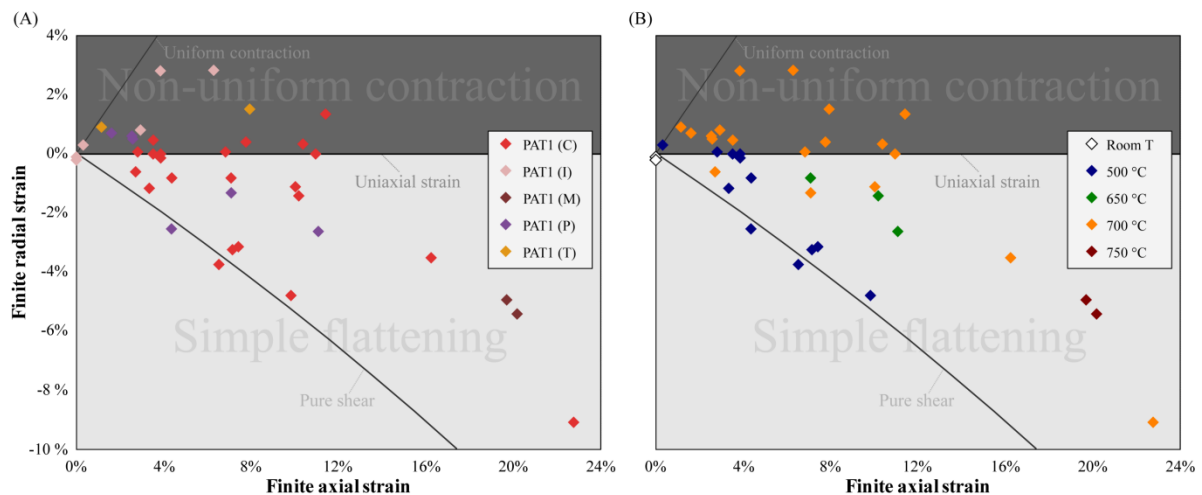


Figure 7.3: Finite axial strain/finite radial strain diagrams for PAT1 samples, color coded according to A) compaction stage history (Table 3.1) and B) temperature. Data is also presented in Table D1.

7.4: Mechanical data and rheology

During the compaction stage 3b confined compression and torsion tests, the strength evolution with strain was recorded in the usual way. For most rock types, this depends on several factors such as the microfabric elements, mineral composition, pressure, temperature, strain rate and water availability. In compaction stage 3b tests, controlled changes in temperature, strain rate, water content and effective pressure were applied to elucidate the factors controlling the of sample strength development with total strain. A list of experiments and their operation conditions is presented in table B1. For 700 and 750 °C confined compression the stress exponent, n , could be determined. Too few data points existed to determine the activation enthalpy of the flow.

Confined compression (500-650 °C):

In confined compression experiments at 500 °C and 650 °C, rapid and linear sample hardening is observed immediately upon application of strain (Fig. 7.4A). At 4 % axial strain, sample strength in most experiments exceeds the 300 MPa effective confining pressure. Hardening continues in an approximately linear (experiment # P1242, P1282, P1284, P1307, P1313, P1331, P1332) or slowly decreasing fashion (experiment # P1336, P1337 and P1472) until load cell limits were

approached at ~550 MPa for 15 mm, and ~1200 MPa for 10 mm diameter samples. Consequently, 10 mm diameter samples could be deformed to a maximum strain of 13-14 %, whereas 15 mm diameter samples only to a maximum strain of 7-8 %. Copper jacketed samples were found to strain-harden at a marginally lower rate than iron jacketed samples. No consistent strain rate effect is observed. For example, samples P1336 and P1337 behave similarly to at least 10 % axial strain, despite one order of magnitude strain rate difference (Table B1). Sample strength development in 500 °C and 650 °C tests is indistinguishable.

Confined compression (700 °C):

The strength evolution of confined compression tests at 700 °C differs from that in the lower temperature experiments (Fig. 7.4B). In all tests, differential stress increases linearly immediately after the onset of straining, until at least 4 % strain. In most of the 700 °C confined compression tests no mechanical steady state is reached within the strength limits of the load cell. A maximum axial strain of 15 % is achieved by experiment P1346. Unlike for 500 °C tests, at comparable strain rate, iron jacketed samples harden at a lower rate than copper jacketed samples (P1243 vs. P1305 and P1330). A drained sample hardens faster than an undrained sample (P1339 vs. P1328). For undrained iron jacketed samples, hardening rate varies. At 7 % axial strain sample strength ranges from 305 to 585 MPa. No explicit correlation was found between strain rate and hardening rate (Figs. 7.4B and 7.5A). In tests P1345 and P1347, initial linear hardening continues at decreasing rate until 7 % and 9 % total axial strain, respectively, where mechanical steady state is achieved. During test P1345, strain rate was repeatedly altered to perform stepping strain rate tests and determine the stress exponent of the steady state flow (Fig. 7.5B and Table 7.1). Mechanical steady state in P1347 is briefly maintained and at 10 % axial strain weakening is initiated.

Pore pressure:

Confined compression tests with applied pore pressure of 50 MPa (PAT1 (P)), resulted in comparable stress/strain curves despite different ambient temperatures (Fig. 7.4C). Steep linear hardening initiates immediately after sample loading. At 1.5-2.0 % axial strain, hardening becomes nonlinear and slowly declines. Sample strength exceeds the confining pressure of 300 MPa at 3.0-3.5 % axial strain; similarities with the 500 °C and 650 °C stress-strain curves are evident. Experiments were aborted after 12-13 % axial strain was reached, reading differential stress values of 700-750 MPa.

Confined compression (750 °C):

The weakest samples were recorded during two separate confined compression tests at 750 °C (Fig. 7.4C). In tests P1469 and P1471, relatively small initial hardening was followed by mechanical

steady state flow at 2.5 % and ~4 % axial strain respectively. To determine the stress exponent of the flow, steady state stress levels were recorded at different strain rates (Fig. 7.5C and Table 3.1).

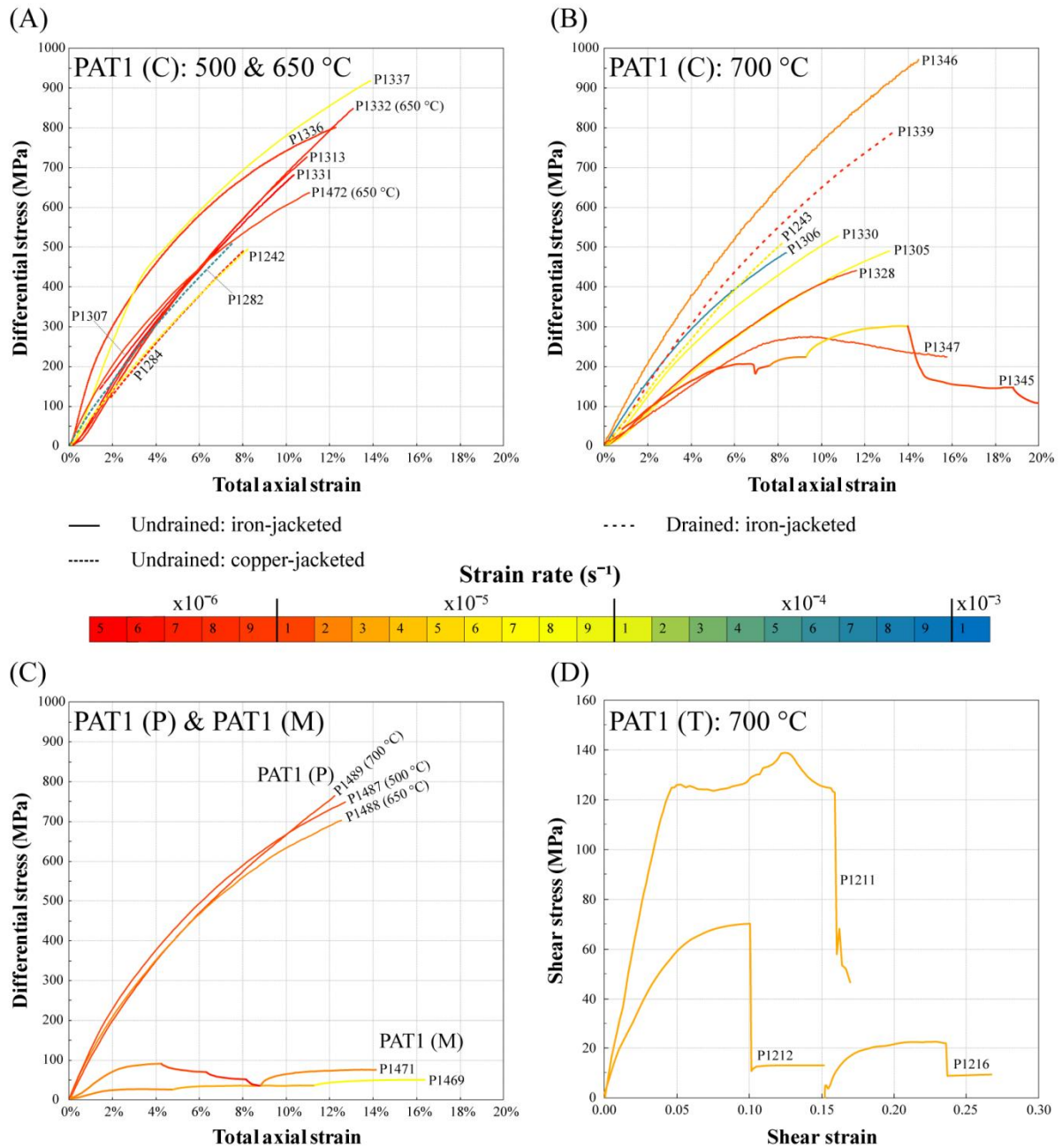


Figure 7.4: Stress/strain curves for compaction stage 3b tests. Colors of the curves represent strain rate. A) Confined compression tests performed at 500 °C and 650 °C. B) Confined compression tests performed at 700 °C. C) Confined compression tests performed at 750 °C and 500 to 650 °C with pore pressure tests. D) Confined torsion tests performed at 700 °C.

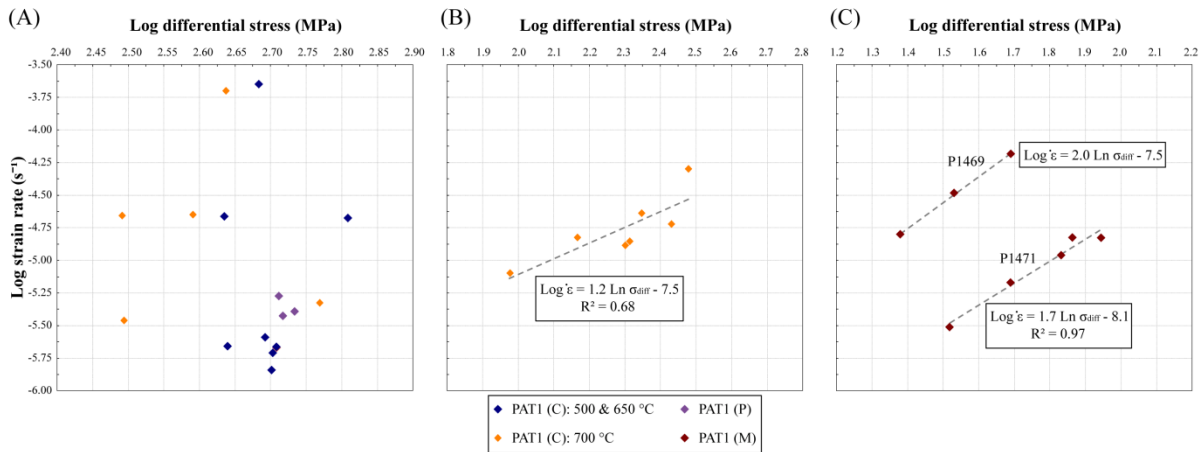


Figure 7.5: Logarithm plots of stress versus strain rate showing strain rate dependency of sample strength, measured A) at 7 % axial strain for hardening samples, and B-C) at mechanical steady state in B) 700 °C and C) 750 °C confined compression tests. The linear correlations found in B and C, are evaluated with the coefficient of determination (R^2).

TABLE 7.1. STRESS EXPONENT DATA FROM STEPPING STRAIN RATE TESTS

Experiment	Group	Temperature	Stress exponent	number of data points	R^2
P1345	PAT1 (C)	700 °C	1.2	7	0.68
P1469	PAT1 (M)	750 °C	2.0	3	-
P1471	PAT1 (M)	750 °C	1.7	5	0.97

Confined torsion (700 °C):

Nearly linear hardening is different for confined torsion tests, P1211, P1212 and P1216 (Fig. 7.4D). Constant sample strength commences for P1211 at $\gamma = 0.05$ and continues until $\gamma \approx 0.07$. Steady hardening follows, until peak strength is reached at $\gamma = 0.12$ where weakening initiates. At $\gamma = 0.16$, the confining pressure and shear stress suddenly decreased, indicating sample slip and jacket failure. No strain was visible on the jacket strain markers. Slip occurred along assembly spacers and pistons (Fig. 7.6). In the case of experiment P1212, steady state was reached at $\gamma = 0.10$, but slipped immediately after without rupturing the assembly jacket and continued with resistant slip along assembly interfaces. During test P1216 the re-jacketed P1212 sample deformed by a further $\gamma = 0.08$ before failure occurred and resistant slip was subsequently recorded (Figs. 7.4D and 7.6). No jacket failure occurred. Due to repeated slip along assembly interfaces at relatively low strain, no more confined torsion tests were attempted.

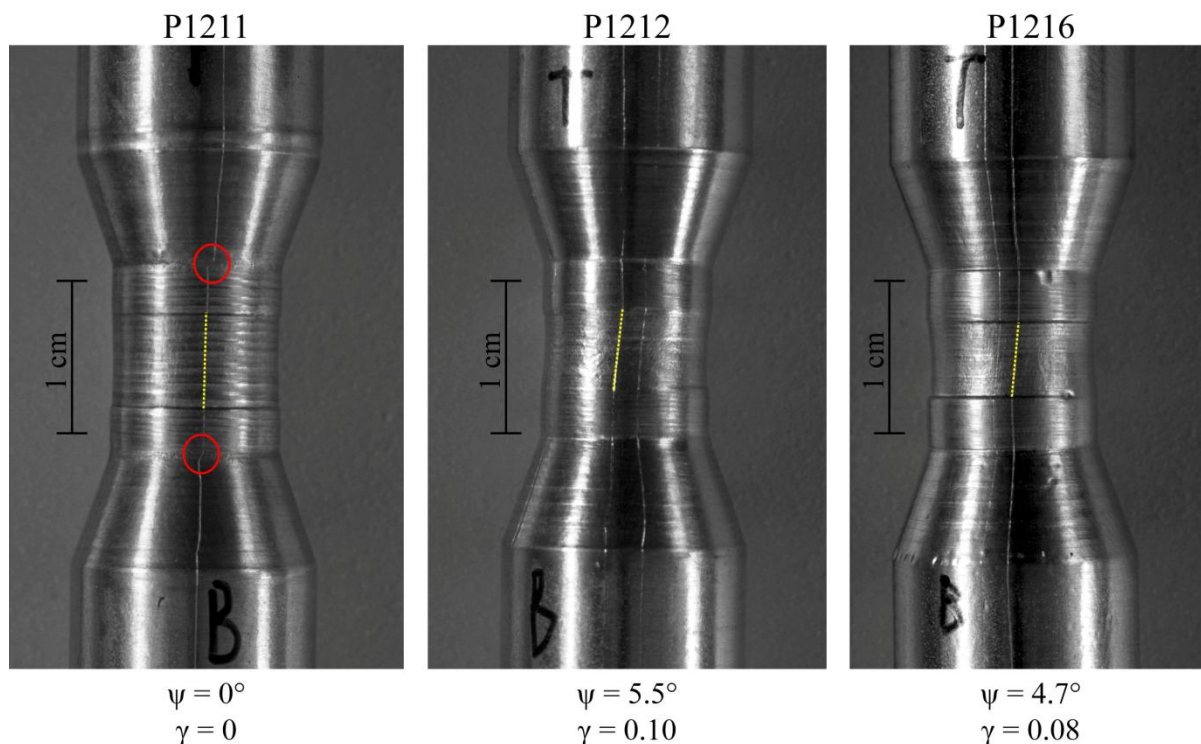


Figure 7.6: Assembly pictures showing the copper jacket strain markers after confined torsion tests. Red circles indicate slip along assembly spacer and piston interfaces. Yellow dotted lines highlight the strain markers used to determine the shear angle.

7.5: Chemistry

Mineral composition of synthetic metapelites is in non-equilibrium during compaction stage 2 and 3 (Chapter 5). The progress of activated mineral reactions transforming illite assemblages to targeted equilibrium metapelitic assemblages was monitored by XRD analysis. Mineral identification is essential for evaluating the compaction processes that created the synthetic metapelites. In particular, water content of samples after compaction stage 3b was measured to verify whether or not reactions towards stability fields VI and VII (Fig. 5.2) were activated.

XRD spectra:

XRD spectra from all synthetic metapelite groups show a transformation of the original illite assemblage (NAT) into a more crystalline phengite, biotite and quartz dominated assemblage (Fig. 7.7). The synthetic metapelites show no characteristic peaks for clinocllore basal (001) and (002) planes, smectite basal (001) and apatite (144) and (414) planes anymore. Instead, sharp peaks associated with the phengite (114) planes and biotite (020) and (110), and (131) and $(\bar{2}02)$ planes are observed. Additionally, copper jacketed samples yield copper oxide peaks at $2\theta = 43.4^\circ$ (Fig. 7.7), indicating some jacket contamination. Other peaks in the metapelite spectra are comparable with Maplewood Shale and represent quartz and detrital phyllosilicates. Overall, a variation in peak height associated with mica and quartz crystal planes is observed. Noticeable compositional heterogeneities

exist among the metapelite samples. The selected HIP2, PAT1 (P), and PAT1 (T) sample material is relatively mica poor, whereas the analyzed PAT1 (I) sample is relatively richer in phyllosilicates.

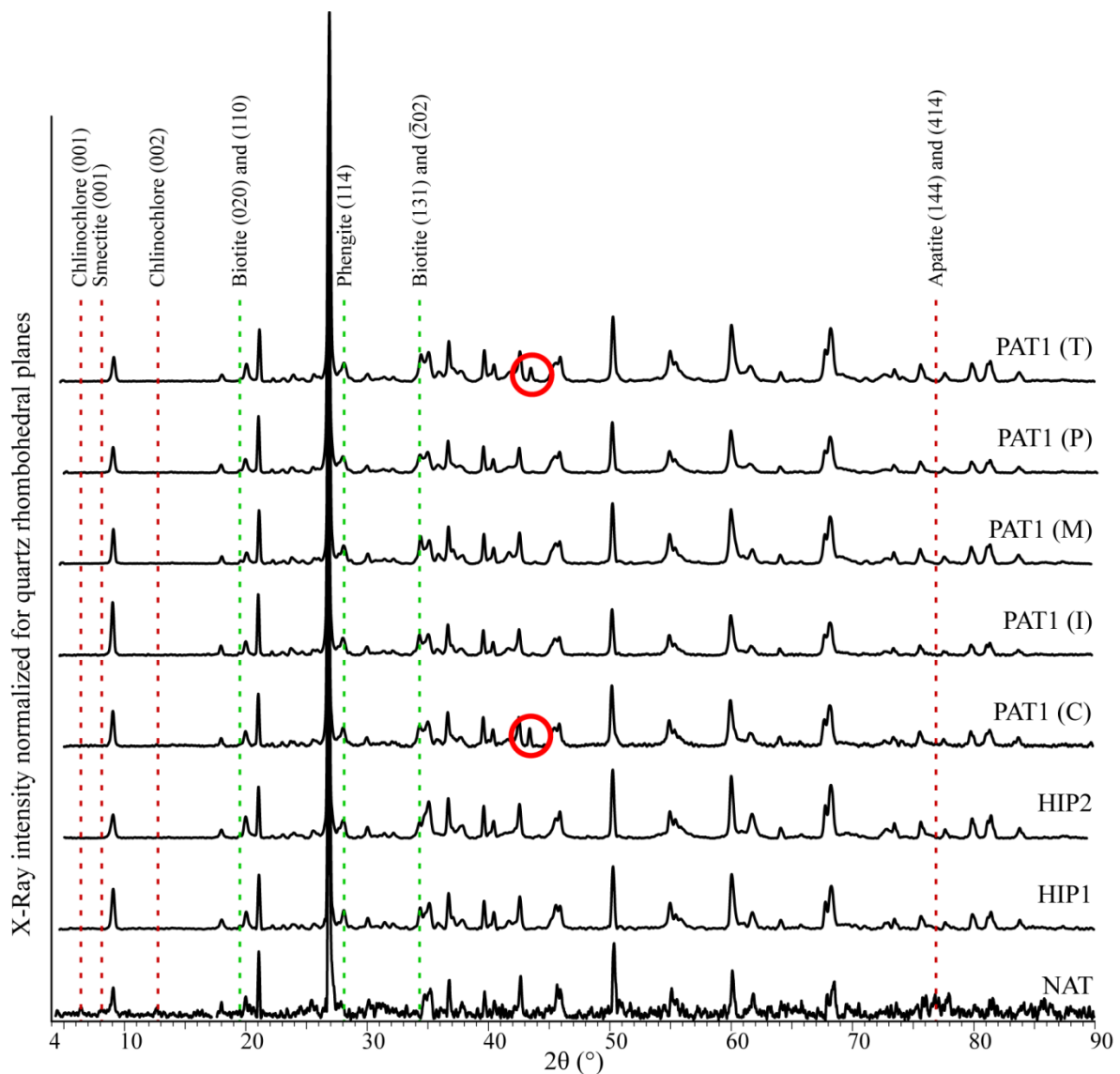


Figure 7.7: Selection of XRD spectra from each compaction sample group as defined by their compaction history (Table 3.1). Dotted red and green lines indicate disappearance and appearance, respectively, compared to the Maplewood Shale (NAT) 2θ pattern of mineral phases. Associated mineral crystal planes are identified. Red circles highlight copper oxide peaks.

Water content:

A controlling factor for the mineral equilibrium reactions in the synthesized metapelites is the amount of water. Mineral stability fields are bounded by temperature, pressure and water content (Chapter 6). Monitoring the water content of compacting metapelites provides insight in the possible chemical reactions during the high temperature and pressure experiments. In the original illite shale (NAT), KFT-measured water content is 3.7 ± 0.3 wt. % (Fig. 7.8A and Table E1). During compaction stages 2 and 3a, the only mineral reactions were those towards stability fields II and III, because water content in HIP1 and HIP2 samples is greater than 2.4 wt. % (Figs. 6.2 and 7.8A, and Table E1). In the

Paterson apparatus experiments, synthetic metapelites experienced various water loss (0.6-2.9 remaining H₂O wt. %) (Table E1 and Fig. 7.8A-B).

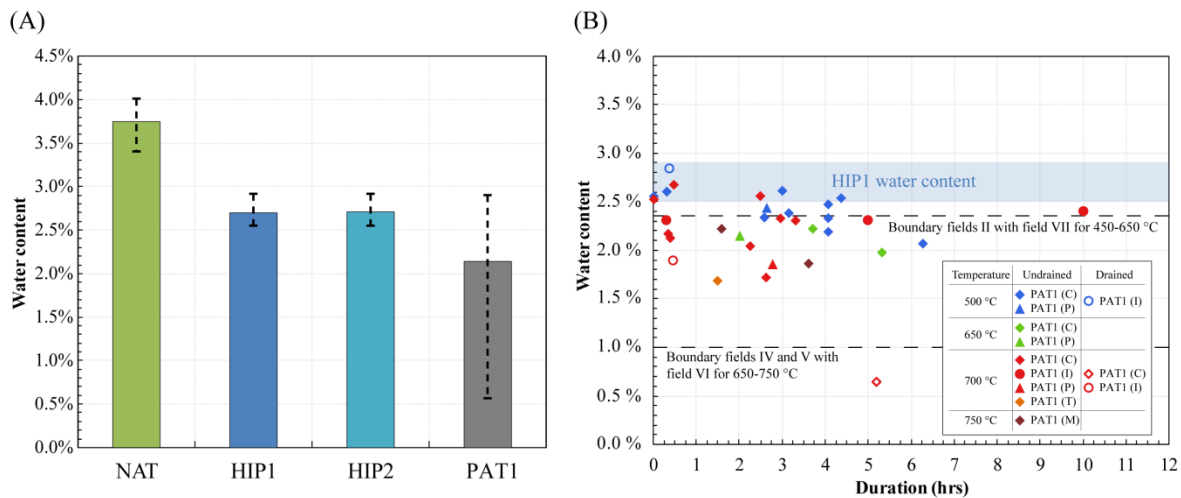


Figure 7.8: A) Column graph showing KFT water content data for synthetic metapelites and Maplewood Shale (summary of Table E1). B) Water content as a function of compaction stage 3b duration. Labels are differentiated according to experiment operating parameters temperature, drainage system and stress regime.

Temperature, drainage conditions and duration are controlling parameters (Fig. 7.8B). The water content of half of the 500 °C PAT1 metapelites lowered below the boundary of stability fields II and VII at 2.4 wt. % (Figs. 6.2 and 7.8B, and Table E1). For 650 °C, 700 °C and 750 °C PAT1 samples, the boundary between mineral stability fields IV and V, and field VI occurs at 1.0 H₂O wt. %. All of these samples, except for the drained 700 °C PAT1 (C) sample, have higher water content (Figs. 6.2 and 7.8B, and Table E1). No reaction that would produce field VI minerals is therefore expected for these samples.

7.6: SEM mineral phase characterization

As an alternative to XRD analysis, BSE images of polished surfaces permits the identification of mineral phases. Contrary to XRD, authigenic minerals can be distinguished from detrital minerals, and low-volume-percentage phases are visualized in BSE images. These advantages allow easier distinction between compaction by isostatic stress and by differential stress. Synthetic metapelites are divided into three porosity groups: 1) high porosity ($\phi > 10\%$), 2) intermediate porosity ($\phi = 5-10\%$) and 3) low porosity ($\phi < 5\%$).

Isostatic compaction:

In high porosity metapelites, the primary mineral phases are detrital illite (III), detrital quartz (dQ), and transition illite-phengite material (I/Ph) (Fig. 7.9A). Illite occurs as submicron flaky

minerals whereas quartz grains are silty and have angular grain boundaries. The transitional illite-phengite material is characterized by diffusive compositional variation and poorly developed grain boundaries.

In low porosity metapelites, the main phases are quartz, phengite and biotite (Fig. 7.9C). Quartz is present as silty detrital and clayey authigenic grains. Authigenic grains (aQ) are not only finer, but also more elongated and rounded than detrital grains. Detrital micas are silty flakes, whereas both authigenic phengite (aPh) and biotite (aBt) are clayey flakes. Transitional illite-phengite material is also present, albeit in lower quantity than in higher porosity metapelites (Fig. 7.9C).

Intermediate porosity metapelites contain domains of relatively high and low porosity (Fig. 7.9D). In porous domains, illite is preserved in flocculated clusters. In compacted domains, nearly all illite is replaced by phengite and biotite. Both angular detrital and rounded authigenic quartz are recognized. The boundary between these domains is sharp (Fig. 7.9D).

Deformation-induced compaction:

Compaction by confined compression or torsion was performed on samples that previously experienced isostatic compaction to 13 ± 3 % porosity. If present, the effect of deformation-induced compaction on mineral phases is probably most pronounced in low-porosity metapelites. High-porosity samples ($\phi > 10$ %) are similarly abundant in illite and transitional illite-phengite material (Fig. 7.10A-B) compared with HIP1 samples. Micas and quartz are present only as detrital material. The presence of some fractured detrital quartz grains is the only compositional difference.

In samples with an intermediate porosity, clayey authigenic biotite, phengite and quartz are present and more detrital quartz grains are fractured (Fig. 7.10D). Illite is predominantly present in relatively porous and clast-rich domains.

In low-porosity metapelites authigenic biotite, phengite and quartz and their detrital equivalents are abundant (Fig. 7.9E). Silty quartz grains are angular, but display more rounding than in porous metapelites and detrital K-feldspar (dKfs) (Fig. 7.9E). Clayey quartz are rounded and elongated.

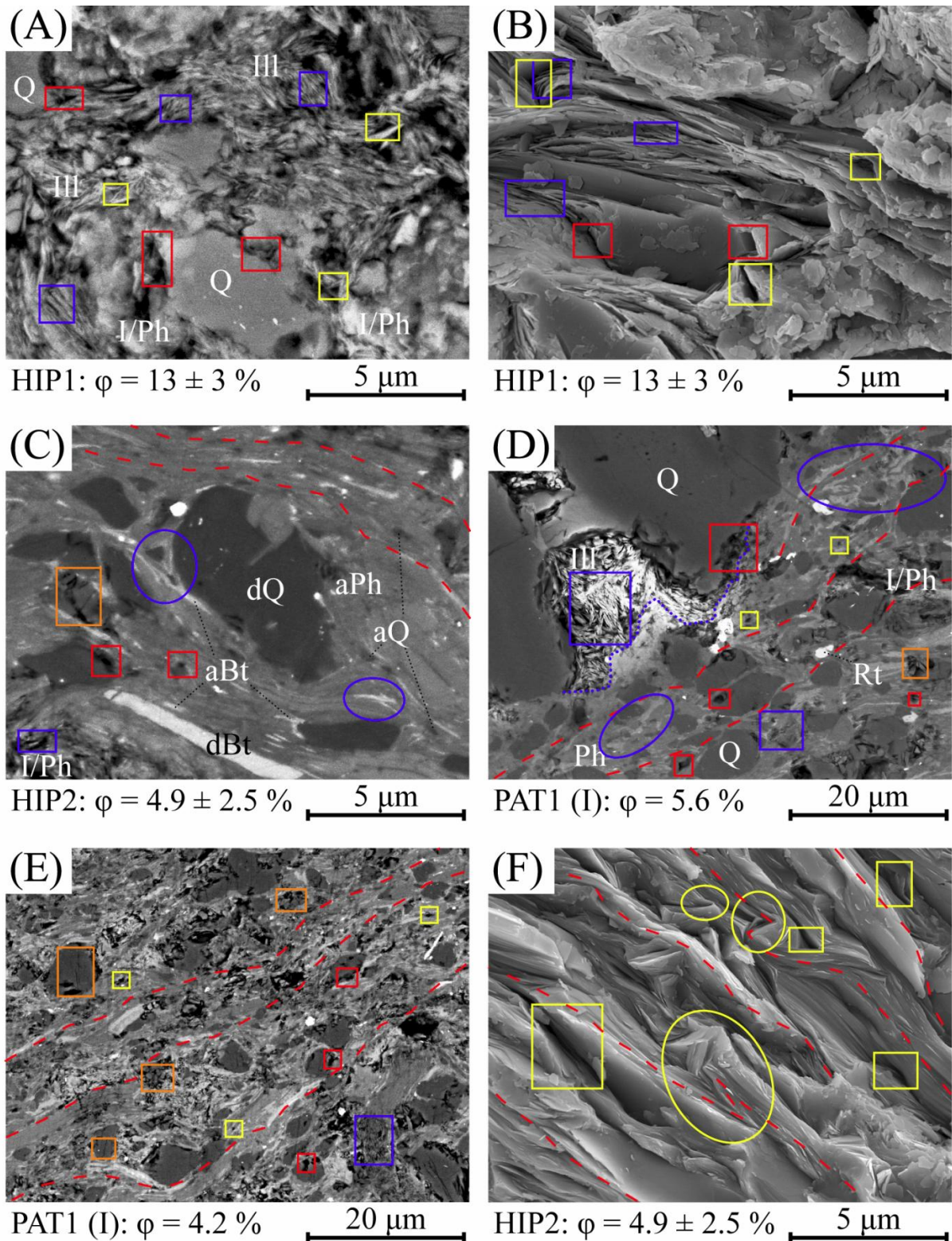


Figure 7.9: BSE and SE images of isostatically compacted metapelites. Sample cylinder axis is vertical for all images. Colored boxes highlight examples of pore types (red = matrix-clast voids, blue = clay micropores, yellow = matrix pores and orange = intragranular fractures). Colored ellipses exemplify structural features (blue = complex authigenic biotite clusters, red = authigenic quartz aligned to foliation, and yellow = mica-kinks or microfolds). Dashed red lines denote traces of the foliation and dotted blue line highlight the boundary between different porosity domains. A-B) High-porosity HIP1 samples. C and F) Low-porosity HIP2 samples. D) Intermediate porosity PAT1 (I) sample. E) Low-porosity PAT1 (I) sample.

7.7: Microstructures

Microstructural elements such as foliation, microfolds and fractures are commonly used to characterize deformation phases in rocks [e.g. *Passchier and Trouw*, 1996]. In this study, microstructures are used to compare metapelites compacted by isostatic and by differential stress. SEM imaging in BSE and SE modes allow visualizing the interaction of the clay-silt particles. As in subchapter 7.4, the synthetic metapelites are divided in three groups of different porosity domains. The synthetic metapelites are composed of predominantly clayey to fine silty matrix minerals, typically with elongated shapes, and more equant silty to sandy clasts (Figs. 7.9-10).

Isostatic compaction:

In high-porosity samples, randomly oriented illite flakes and unorganized illite-phengite transitional material make up most of the matrix (Fig. 7.9A). Illite flakes are aligned in micro-clusters of 1-3 μm size. These flocculated clays have a random orientation. Quartz clasts are unaffected by the compaction processes. Non-equant clasts are common, yet no persistent shape preferred orientation (SPO) is identifiable (Fig. 7.9A) and no sample-scale penetrative structures were identified.

In intermediate porosity metapelites, the porous domains display a microstructure that is comparable to that of high-porosity samples (Fig. 7.9D). A relatively higher content of clasts is observed in porous domains. In more crystalline domains, porosity is lower and alignment of clayey and silty mica gives rise to a weak foliation, consistent over at least 100 μm (Fig. 7.9D). The foliation is irregular due to mica-wrapping around clasts, and is frequently interrupted or diverted by patches of complexly shaped submicron biotite grains (Fig. 7.9D). Quartz SPO is weak in silty particles, but stronger in clay-sized particles.

In metapelites with low porosity ($\phi < 5\%$), compacted phengite-biotite matrix dominates (Fig. 7.9C, E-F). The foliation is more pronounced and continuous, than in higher porosity samples. Mica-wrapping around quartz clasts is common. Open and isoclinal micro-folds (1-3 μm) and mica kinks fold the foliation (Fig. 7.9F). The SPO of detrital quartz is weak but aligned with the matrix foliation (Fig. 7.9E).

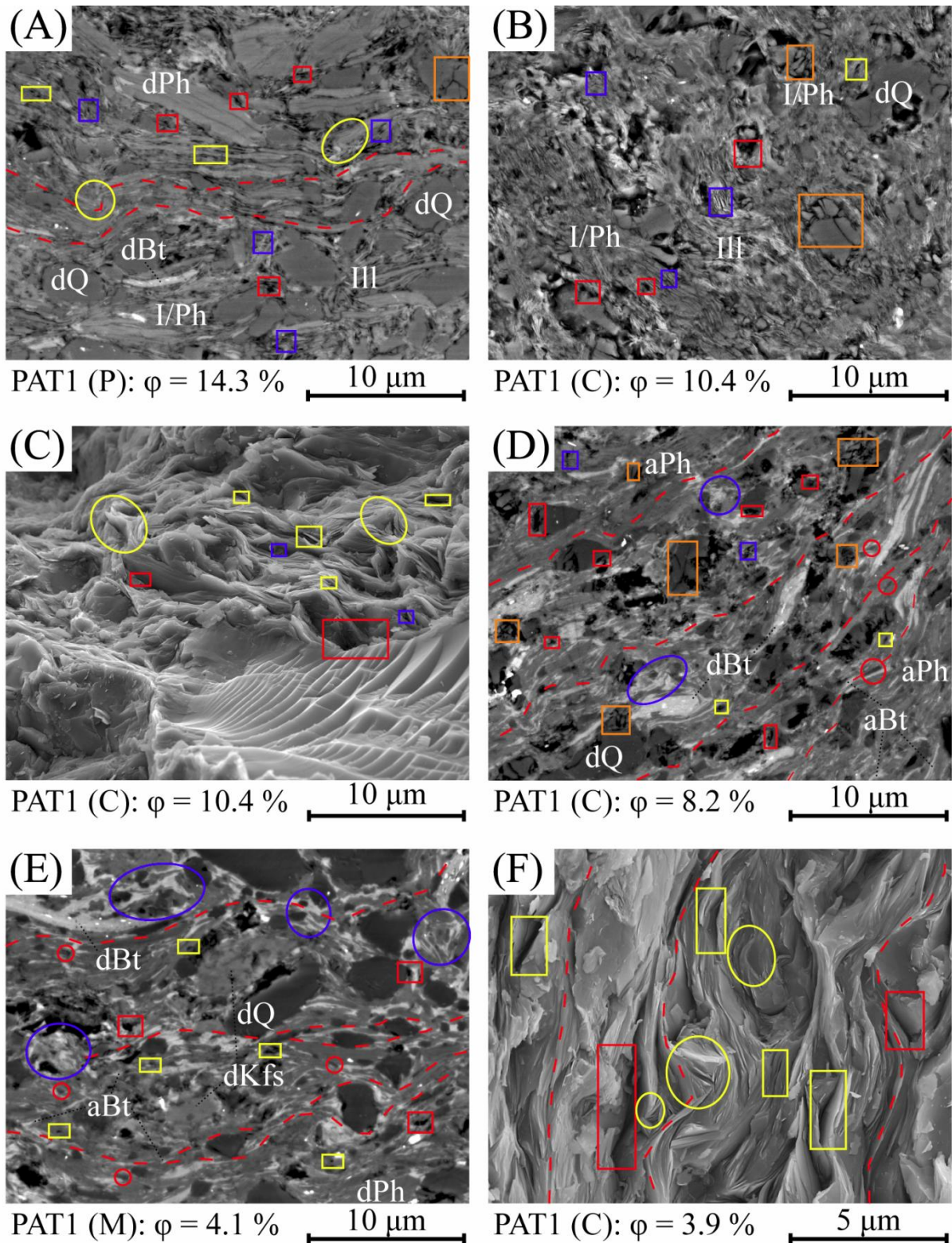


Figure 7.10: BSE and SE images of metapelites after compaction by confined compression. Sample cylinder axis is vertical for all images. Colored boxes and ellipses as in figure 7.9. A) High-porosity PAT1 (P) sample. B-C) High-porosity PAT1 (C) sample. D) Intermediate porosity PAT1 (C) sample. E) Low-porosity PAT1 (M) sample. F) Low-porosity PAT1 (C) sample.

Deformation-induced compaction:

Detrital micas in high-porosity metapelites that experienced confined compression possess a weak, irregular and folded foliation (Fig. 7.10A). Micro-folds and kinks are occasionally observed in detrital and authigenic micas (Fig. 7.10A, C). Illite-rich patches in the matrix are not foliated (Fig. 7.10B), and the silty quartz grains in the matrix do not display a SPO.

Intermediate porosity metapelites have a more pronounced foliation, defined by detrital and authigenic micas (Fig. 7.10D). The foliation is diverted by micas wrapping around clasts and is interrupted by patches of complexly organized authigenic biotite (Fig. 7.10D) or underdeveloped phengite. Both detrital and authigenic quartz grains are frequently aligned to the foliation (Fig. 7.10D).

In low-porosity synthetic metapelites, few illite-rich patches remain. The foliation is well-developed (Fig. 7.10E-F), but occasionally interrupted by patches of distorted ultrafine biotite (Fig. 7.10E). Micas display 1-3 μm open and isoclinal folds or kinks (Fig. 7.10F). Micro-folds and mica-wrapping fold the main foliation. Quartz has a weak SPO for detrital grains and strong SPO for authigenic grains (Fig. 7.10E). Both SPO types are aligned to the local foliation.

7.8: Pores

Pores are a key feature in rocks, coupling microstructural observations to quantifiable flow-related properties. The development of pores in the synthetic metapelites is recorded by BSE and SE imaging. As compaction progresses pores are deformed and ultimately closed. Information on the type, shape, size and distribution of remaining pores gives insight in compaction processes. Some of the pore types found in Maplewood Shale (section 5.4), clay-micropores, matrix-clast-voids and matrix-pores are observed in the synthetic metapelites (Figs. 7.9-10). Intragranular fractures (pore-type VI in *Kwon et al.* [2004]) form an additional generic pore type.

The submicron clay micropores separate illite flakes, and allow recognition of individual clay particles (Figs. 7.9 and 7.10). Clay-micropores are typically parallel to illite flakes. As porosity decreases illite becomes less abundant (Section 7.4). Consequently, the amount of clay-micropores decreases with porosity, regardless of the stress field during compaction. Phengites in both fully and partially crystallized state are pore-free to at least 500 nm resolution (Figs. 7.9F and 7.10F). Ultimately, phengite is distinguished in broken surface SE images from illite by tight stacking of ultrathin mineral sheets. Clay micropores identified may also be used to distinguish illite from phengite in polished surfaces.

Matrix-clast-voids and matrix-pores represent open spaces generated by geometric misfits between angular clasts and fine-grained matrix material and among matrix-forming minerals (Figs. 7.9 and 7.10). Both pore-types range in length from submicron to 2-3 μm . Matrix-clast-voids

and matrix-pores are frequently found in high-porosity metapelites (Figs. 7.9A-B and 7.10A-C). Importantly, however, compaction does not eliminate them. The two pore types are frequently observed in both the isostatically compacted HIP2 and PAT1 (I) metapelites (Fig. 7.9C-F), and high-strain PAT1 (C) and PAT1 (M) samples (Fig. 7.10E-F).

Intragranular fractures represent the openings created by the fracturing of rigid (quartz) clasts (Figs. 7.9 and 7.10). These fractures either transect or die out within quartz grains. Consequently, a range of shapes from slit-like to tabular to irregular pyramidal and semi-spherical is observed. Intragranular fractures are frequent in PAT1 (C) and PAT1 (P) samples of diverse porosities (Fig. 7.10A-B, D), but rare to absent in PAT1 (M) samples (Fig. 7.10E). In isostatically compacted metapelites, intragranular fractures first appear in intermediate porosity samples (Fig. 7.9D) and are more frequent in low porosity samples (Fig. 7.9E). There is no evidence for healing of intragranular fractures or filling in with authigenic minerals.

Chapter 8

Magnetism

Richard Bach once said, "The more I want to get something done, the less I call it work."

Preface

In the previous chapter, the magnetic properties of the synthetic metapelites were not mentioned. The reason for this is that the acquired magnetic data deserve an entire chapter devoted to them. The complexity of the magnetic development is such that it does not directly provide an answer to the main problem addressed in this thesis. Therefore, magnetic properties are not primarily considered a useful tool to describe compacting shale. Instead, the roles are reversed and chemical compaction of illite shale powder in the laboratory is considered a useful tool for the simulation of rock magnetic processes. In this view a manuscript for a letter-format paper was prepared. On October 26th 2011 this manuscript was submitted to the peer-reviewed journal *Geology*. The text, tables and figures in this chapter are directly taken from the submitted manuscript, minor lay-out and formatting modifications to ensure homogeneity in this thesis.

Chemical compaction of shales: clay transformation recorded by magnetic fabric

Rolf H.C. Bruijn^{1*}, Bjarne S.G. Almqvist¹, Ann M. Hirt² and Philip M. Benson¹

¹ Geological Institute, ETH Zurich, Sonneggstrasse 5, CH-8092 Zurich Switzerland

² Geophysical Institute, ETH Zurich, Sonneggstrasse 5, CH-8092 Zurich Switzerland

* Corresponding author: rolf.bruijn@erdw.ethz.ch

Bruijn, R. H. C., B. S. G. Almqvist, A. M. Hirt, and P. M. Benson (2011), Chemical compaction shale: clay transformation recorded by magnetic fabric, *Geology*, submitted October 26th 2011.

Abstract

Understanding the compaction of clay rich sediments is fundamental for exploring how key diagenetic processes and other rock physical parameters influence the deposition and burial of basin sediments. Natural observation of chemical compaction, following mineral transformation and dissolution/precipitation processes is rarely addressed in experiments. Here we report, for the first time, on the development of magnetic susceptibility in a chemically compacted illite shale powder of natural origin that was experimentally subjected to temperatures of 500 to 750 °C and confining pressure of 170 or 300 MPa. The experimental procedure comprised of three compaction stages, involving dry triaxial compression (resembling mechanical compaction), hot isostatic pressing (chemical compaction by burial), and Paterson apparatus compaction in confined compression, torsion or isostatic stress (chemical compaction by deformation or burial). Magnetic properties were characterized by magnetic susceptibility and its anisotropy (AMS) in both high- and low-applied field. Isothermal remanent magnetization and first-order reversal curves were used to characterize the remanence-bearing minerals. Results suggest that during hot isostatic pressing ferrimagnetic iron-sulfides form after reduction of magnetite and detrital pyrite in combination with lower sulfur fugacity. The degree of low-field AMS is unaffected by porosity reduction from 15 to ~1 %, regardless of operating conditions and compaction history. High-field paramagnetic AMS increases with compaction, for all employed stress regimes and conditions, and is attributed to clay transformation to iron-bearing mica. AMS of authigenic iron-sulfide minerals remains constant during compaction, indicating non-dependence on clay transformation.

8.1: Introduction

Experimental compaction of argillaceous material provides key insights into the development of geophysical parameters important for basin exploration, nuclear waste repositories, CO₂ sequestration and seismic modeling [e.g. *Vasseur et al.*, 1995; *Nygård et al.*, 2004; *Mondol et al.*, 2007; *Voltolini et al.*, 2009; *Fawad et al.*, 2010; *Schneider et al.*, in press]. Additionally, in paleomagnetism such experiments have proved to be essential for better understanding inclination shallowing recorded in deep marine sedimentary sections [*Blow and Hamilton*, 1978; *Anson and Kodama*, 1987; *Arason and Levi*, 1990; *Deamer and Kodama*, 1990; *Lu et al.*, 1990; *Jackson et al.*, 1991; *Sun and Kodama*, 1992]. Nonetheless, clay compaction experiments have mostly addressed mechanical compaction processes under operating conditions that suppress clay transformation, thus avoiding chemical compaction, which is an important aspect of diagenesis in deep basins. Compaction by mechanical processes alone results in porosity > 15 %. This threshold marks the onset of divergence from natural compaction trends where chemical compaction is evident [*Mondol et al.*, 2007; *Crawford et al.*, 2008].

Here we report on the evolution of magnetic fabrics in an experimentally compacted illite shale powder under operating conditions favoring mica formation and phyllosilicate dehydroxylation. Samples are characterized by their bulk magnetic susceptibility (K_m), and anisotropy of magnetic susceptibility (AMS) in both low- and high-fields. Additionally, magnetic remanence is described using acquisition of isothermal remanent magnetization (IRM) and construction of first-order reversal curves (FORC) diagrams [*Pike et al.*, 1999; *Roberts et al.*, 2000]. We place particular emphasis upon defining subfabrics of the paramagnetic (phyllosilicates) and ferromagnetic (*s.l.*) phases, to define how these develop in response to chemical compaction by clay transformation.

8.2: Method

Source material:

Source material is Maplewood Shale from the Lower Clinton Group (Llandoveryan) in the Appalachian basin of Western New York, supplied by Ward's Natural Science®. The mineral composition consists of illite, clinocllore, quartz, and phengite as primary phases (> 5 vol. %) with smectite, pyrite, rutile, apatite and biotite as secondary phases (< 5 vol. %). For our experiments, illite shale powder was produced by crushing fragments of Maplewood Shale using a high power tungsten 'shaker'. Resulting powder has 15 vol. % clay, 80 vol. % silt and 5 vol. % sand by size fraction, and an average grain size of 20 µm, as determined by laser diffraction using a Malvern Mastersizer 2000 with ultrasonic agitation.

Compaction stages:

Illite shale powder was compacted in three stages: 1, 2, and either 3a or 3b. For stage 1 compaction, dry powder was compressed inside stainless steel canisters enclosed within a heavy steel casing using a ram to provide ~200 MPa of vertical stress. In this stage, compaction is solely mechanical without lithification. In stage 2, illite shale powders are further compacted isostatically for 24 hrs inside the canisters by pressurized argon gas (170 MPa and 590 °C), using a hot isostatic press (HIP) apparatus. Stage 2 lithifies the illite shale powder into a porous (porosity 11-15 %) synthetic metapelite. The resulting canisters are then split into two groups. The first of which is further compacted in the HIP to yield compaction stage 3a. From the second group cylindrical samples are prepared for stage 3b, by drilling with a hollow diamond coring drill to yield samples of 10 mm or 15 mm diameter and of 5-20 mm length via wet abrasive paper polishing.

In stage 3b, further compaction was achieved using a Paterson-type HPT gas-medium testing machine equipped with axial and torsion actuators and pore-pressure system [Paterson, 1990; Paterson and Olgaard, 2000]. A constant confining pressure of 300 MPa was applied, while temperatures were fixed at 500, 650, 700 or 750 °C. Stage 3b tests were performed in isostatic stress, confined compression or confined torsion. The range of applied constant strain rate in both torsion and compression was 10^{-6} - 10^{-4} s⁻¹. A maximum axial strain and shear strain of 20% and respectively 0.3 was achieved. A selection of confined compression tests at each temperature was performed (with the exception of 750 °C) using either 20 or 50 MPa pore pressure (argon gas). Samples are labeled according to their compaction stage history (Table 8.1-2).

TABLE 8.1. SAMPLE GROUPS ACCORDING TO COMPACTION HISTORY

Compaction stage	Compaction	
	history	Sample group ID
1	1	None
2	1+2	HIP1
3a	1+2+3a	HIP2
3b	1+2+3b	PAT1*

*Further subdivision is given in Table 8.2.

TABLE 8.2. SAMPLE SUBGROUPS FOR COMPACTION STAGE 3B TESTS

Confined compression	Isostatic stress	confined torsion	Pore pressure	750 °C
PAT1 (C)	PAT1 (I)	PAT1 (T)	PAT1 (P)	PAT1 (M)

Sample analysis:

The degree of compaction is evaluated by porosity, measured with a Micromeritics AccuPyc 1330 helium pycnometer; to ensure accuracy the calculations are based on an average of seven volume determinations of cylindrical samples.

Bulk magnetic susceptibility was determined with a low-field AGICO KLY-2 kappabridge (300 Am^{-1} applied field at 875 Hz frequency). Degree of low-field AMS is expressed by P_j [Jelínek, 1981], which was derived from the eigenvalues ($k_1 \geq k_2 \geq k_3$) of the symmetric second rank magnetic susceptibility tensor. High-field AMS, expressed by Δk (i.e. $k_1 - k_3$), was measured using a torque magnetometer [Bergmüller *et al.*, 1994], following the method proposed by Martín-Hernández and Hirt [2001]. Sample torque was measured over 360° in 30° steps about three orthogonal axes, for six fields ranging between 0.5 and 1.5 T, as well as in the absence of an applied field. IRM and FORC data were acquired to characterize the ferromagnetic (*s.l.*) mineral phases present during various stages of the compaction procedure. IRM acquisition was imparted with a Princeton Measurements Corporation Vibrating Sample Magnetometer (VSM) (Model 3900). The FORC measurements used a saturating field of 1.0 T, with 100 ms averaging time and 130 reversal curves. A FORC diagram is a contour plot of the FORC distribution with coercive force (H_c) on the horizontal axis and interaction field (H_u) on the vertical axis [e.g. Pike *et al.*, 1999].

8.3: Results

The three-stage compaction of illite shale powder resulted in synthetic metapelites with a porosity range from 16 to 1 %. For Maplewood Shale, the mean K_m increases by one order of magnitude subsequent to crushing (NAT (P)); however, variation exists among batches of the powder (Table 8.3). The highest susceptibility is recorded in illite shale powder that were compacted into HIP2 synthetic metapelites. During compaction stage 2 and 3a, susceptibility decreased. PAT1 sampled display smaller values for K_m in comparison with HIP1 samples. K_m for crushed Silver Hill shale (SH-NAT) is at least 973 μSI lower than for crushed Maplewood Shale.

IRM for powdered Maplewood Shale (NAT (P)) closely resembles the typical behavior of magnetite/maghemite (Fig. 8.1). The synthetic metapelites of HIP1, HIP2 and PAT1 (C) sample groups, however, have different IRM acquisition with an unsaturated component. Minimal variation in IRM acquisition is observed among the synthetic metapelites (Fig. 8.1).

Two distinct FORC distribution types emerged from the analysis of HIP1, PAT1 (C) and HIP2 samples (Fig. 8.2). Type 1 shows a broad coercivity distribution between 20 and 90 mT with a maximum between 40 to 55 mT, and a distribution in interaction fields that centers around -6 mT (Fig. 8.2A). This FORC distribution is typical for greigite (Fe_3S_4) [Roberts *et al.*, 2006; 2011]. Type 2 also shows a broad coercivity distribution up to 150 mT, with a peak distribution between 25 and 35

mT. The distribution in interaction fields is narrower and centered around $H_c = 0$ (Fig. 8.2B). This FORC distribution is more difficult to ascribe simply to a single phase. The tail in the distribution suggests the presence of a higher coercivity phase, such as pyrrhotite (Fe_7S_8) or possibly hematite ($\alpha-Fe_2O_3$) [Roberts *et al.*, 2006]. The high susceptibility, IRM acquisition curve, and FORC behavior are more compatible with an iron sulfide.

TABLE 8.3. BULK SUSCEPTIBILITY VALUES

Sample group	Mean K_m (μSI)	Min K_m (μSI)	Max K_m (μSI)	n [*]	Standard error [†]
<u>Maplewood Shale</u>					
NAT	223	200	266	11	7.5
NAT (P) [§]	2516	1341	3938	13	323.4
<u>Synthetic metapelites</u>					
HIP1	497	473	547	10	7.6
HIP2	967	559	1122	10	70.2
PAT1 (C)	421	209	709	21	31.2
PAT1 (I)	367	234	469	4	58.6
PAT1 (M)	455	442	469	2	13.5
PAT1 (P)	333	255	408	5	24.2
PAT1 (T)	846	262	1430	2	584.1
<u>Silver Hill shale</u>					
SH-NAT (P) [#]	359	347	368	6	2.8

* n = number of measurements.

† Standard error = $(\sigma n^{-1})^{0.5}$, where σ is standard deviation

§ (P) refers to crushed shale (i.e. illite shale powder before compaction stage 1)

SH = Silver Hill

Low-field AMS values for P_j vary in the range of 1.05 to 1.14, with an average value of 1.09, regardless of porosity and compaction history (Fig. 8.3).

High-field AMS measurements permit the separation of ferrimagnetic AMS from paramagnetic and diamagnetic AMS [Martín-Hernández and Hirt, 2001]. Ferrimagnetic AMS (Δk_f) is systematically smaller than paramagnetic AMS (Δk_p). All sample groups except HIP2 exhibit comparable Δk_f (trend (1) in figure 8.4A). HIP2 samples have relatively higher ferrimagnetic AMS (Fig. 8.4A). Lack of data points, permits correlation between porosity and HIP2 Δk_f . With the exception of the one PAT1 (T) outlier data point, all metapelites plot in a trend of increasing AMS as function of K_m (Fig. 8.4B). The trend is adequately described by a linear regression with a coefficient of determination (R^2) of 0.91.

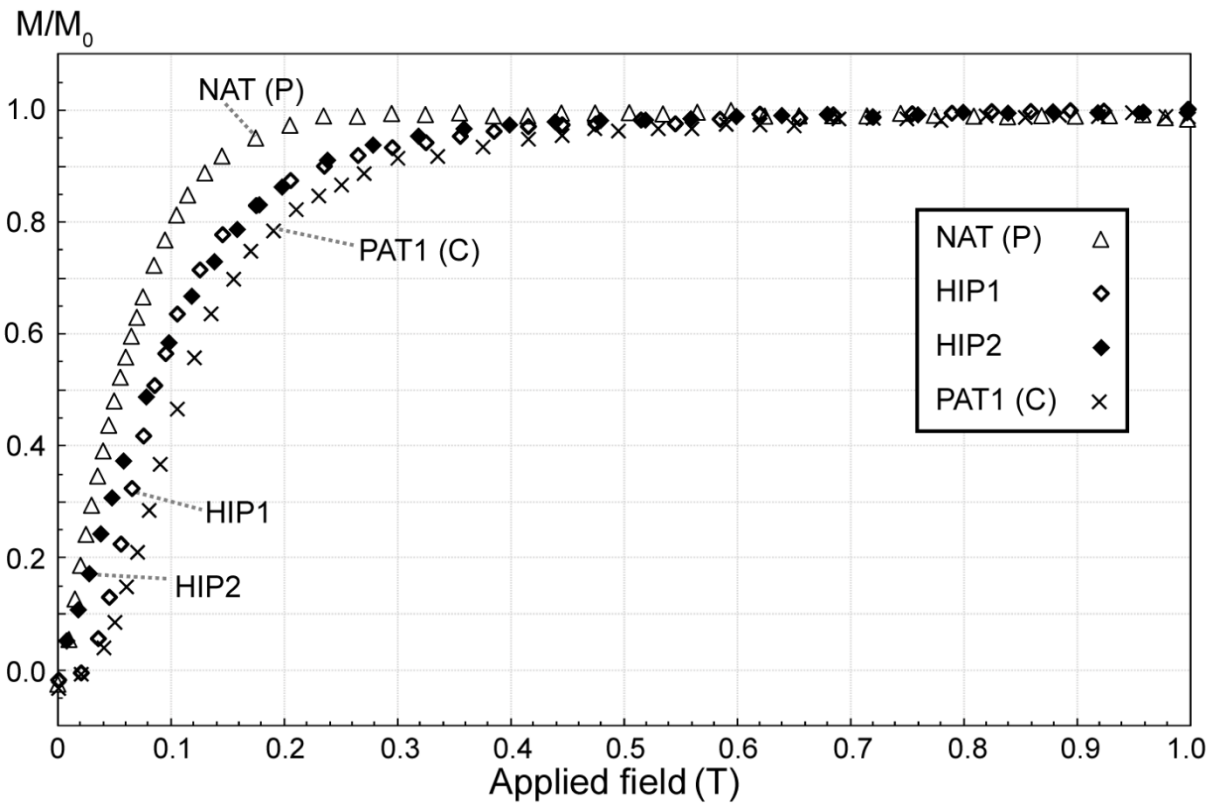


Figure 8.1. Isothermal remanence magnetization (IRM) acquisition curves for samples of crushed Maplewood Shale powder (NAT (P)), and synthetic metapelites (HIP1, HIP2 and PAT1 (C)). M_0 is the value for M at an applied field of 1.0 T.

Δk_p values display a different behavior as a function of porosity than Δk_f values (Fig. 8.4A). HIP1, HIP2 and PAT1 (C-I-T) samples combined describe increasing anisotropy with decreasing porosity (trend (2) in figure 8.4A). The slope of the best-fit linear regression shows a positive trend. The linear trend is significant at 99 % confidence, using $n = 16$ and standard error = 9.0×10^{-6} . Both PAT1 (M) and PAT1 (P) data Δk_p values plot systematically above data cloud (2). The minimum principal axis (k_3) of the synthetic metapelites shows a gradual inclination steepening (trend (3) in figure 8.4C). The other principal axes (k_1 and k_2) remain shallow ($< 25^\circ$ inclination), regardless of porosity and compaction history. In an equal area plot, k_3 is centered, without preferred declination, around 90° dip, while k_1 and k_2 plot at low dip with scattered declination (Fig. 8.4D).

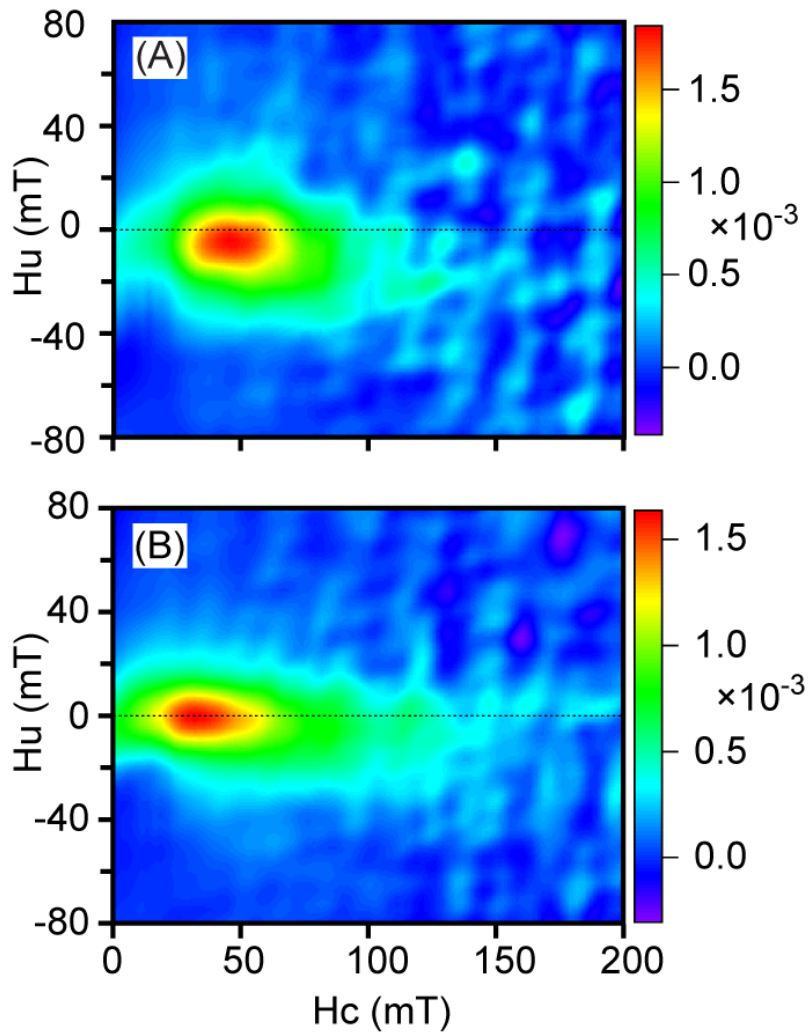


Figure 8.2. First-order reversal curves (FORC) diagrams computed with FORCinel v.1.17 [Harrison and Feinberg, 2008] obtained from a HIP1, HIP2 and PAT1 (C) sample showing A) FORC distribution type 1 and B) FORC distribution type 2.

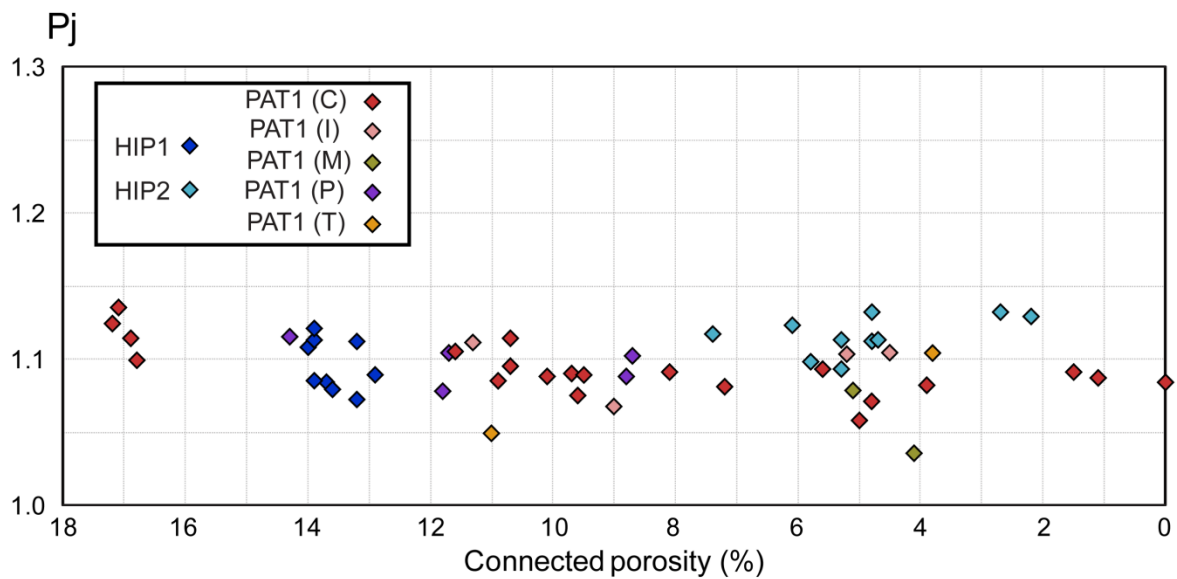


Figure 8.3. Low-field anisotropy of magnetic susceptibility (AMS) as a function of porosity of synthetic metapelites, color-coded according to compaction history (Table 8.1-2).

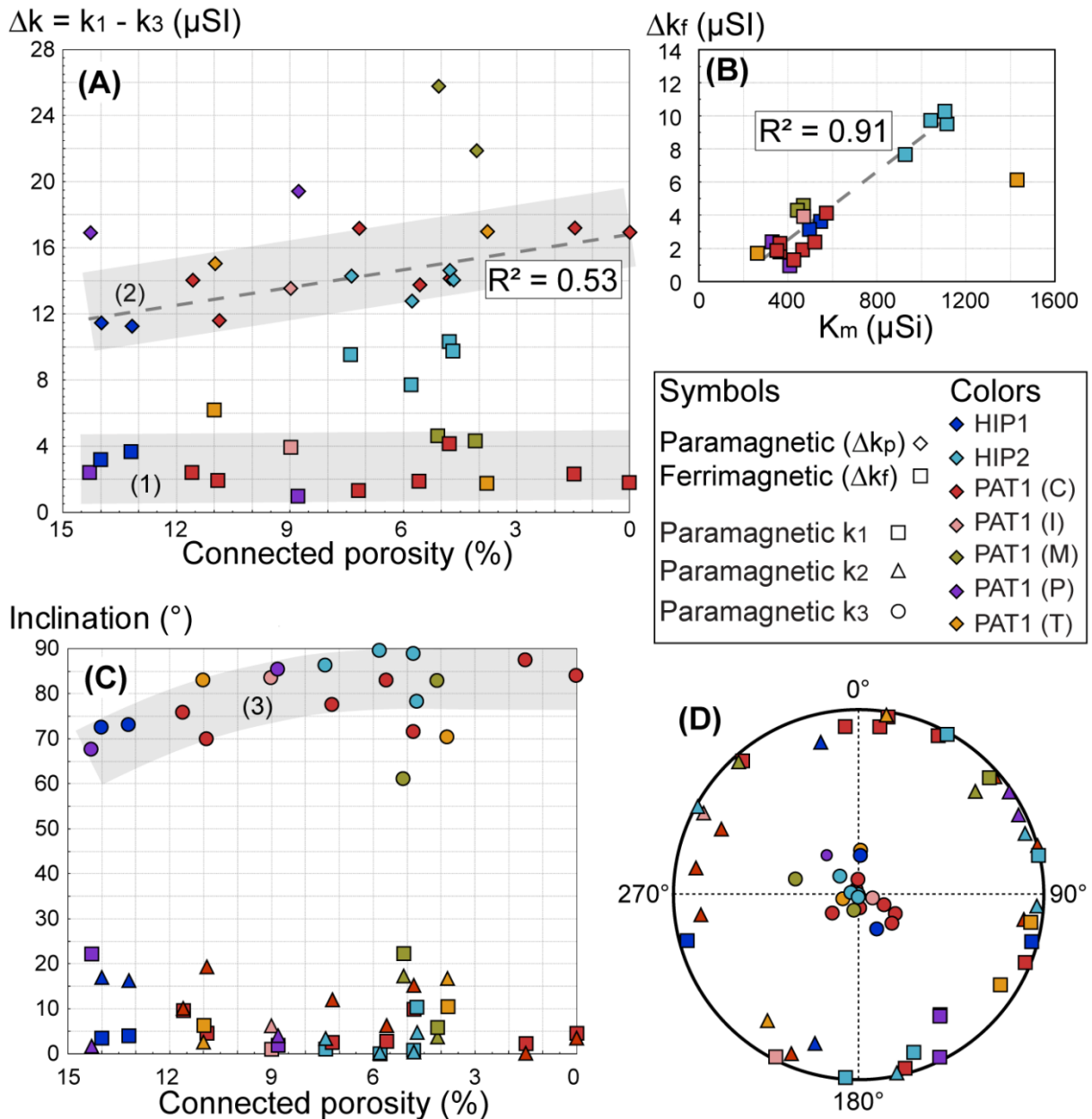


Figure 8.4. Results for high-field anisotropy of magnetic susceptibility (AMS) as a function of A) porosity for the paramagnetic and ferrimagnetic signal, and B) bulk magnetic susceptibility for the ferrimagnetic signal, color-coded according to compaction history (Table 8.1-2). Values in parentheses are labels for trend lines.

8.4: Discussion and conclusions

During sample preparation and experimental compaction, bulk magnetic susceptibility of illite shale powder is repeatedly altered, reflecting primarily changes of the ferrimagnetic minerals (Table 8.3, Fig. 8.1-2). Although not observed in intact fragments of Maplewood Shale (NAT), in the crushed state, magnetite/maghemite is the principal remanence-carrying mineral (Fig. 8.1). Intact Maplewood Shale shows negligible IRM acquisition, which is below the detection level of the VSM,

and has considerably lower magnetic susceptibility (Table 8.3). The suspected addition of magnetite/maghemite to Maplewood Shale powder (NAT (P)) is attributed to inadvertent admixing of concretions or iron-oxide-bearing veins. Magnetite/maghemite particles are heterogeneously distributed among the powder batches, as evidenced by the considerably varying bulk susceptibility of NAT (P) (Table 8.3). Contamination during the crushing procedure from an external source is excluded, because powder of similarly treated Silver Hill shale has lower values for K_m (Table 8.3). Reduced susceptibility in the synthesized metapelites is attributed to the combination of oxidation-reduction reactions and lowered sulfur fugacity during compaction stages 2 and 3, during which remanence-bearing iron-sulfides formed at the expense of magnetite/maghemite and pyrite [cf., *Rochette, 1987*]. The IRM acquisition curves and FORC distributions for synthetic metapelites indicate the dominant presence of high coercivity phases such as greigite and pyrrhotite, and confirm the disappearance of magnetite. Comparable susceptibility values for PAT1 and HIP1 samples (Table 8.3) suggests that the redox reactions completed during compaction stage 2. Higher susceptibility for HIP2 samples is attributed to higher initial magnetite/maghemite content, which resulted in a higher concentration of ferrimagnetic iron-sulfides after compaction stage 3a.

Both low-field and the ferrimagnetic AMS of all synthetic metapelite groups are unaffected by compaction (Fig. 8.3, 4A). As for bulk susceptibility, the signal of total AMS is explained by the dominant contribution of the ferrimagnetic minerals. Δk_f remains constant at a relative low value during compaction from 15 % to nearly 0 % porosity. The apparent higher Δk_f for HIP2 samples (Fig. 8.4A) is rather a consequence of higher bulk magnetic susceptibility than of enhanced preferred magnetocrystalline orientation for greigite and pyrrhotite, as indicated by the good matching of HIP2 samples to the best-fit linear line in the K_m - Δk_f diagram (Fig. 8.4B).

In this study, paramagnetic AMS increases with compaction (Fig. 8.4A trends (1) and (2)). Simultaneously as porosity decreases, the short axis of the paramagnetic susceptibility ellipsoid rotates towards steeper inclination without alignment of its declination, while the intermediate and long axes remain at shallow inclination with scattered declination (Fig. 8.4C-D). Recorded Δk_p values for PAT1 (CIT) samples plot within trend (2) of figure 8.4A, which also includes HIP1 and HIP2 samples. This behavior is explained by transformation of clay into mica. Compared with clay, mica has higher crystallinity and single crystal AMS [*Hrouda, 1993*]. As such, porosity and paramagnetic AMS are first-order measures of the progress of illite to phengite transformation. Higher Δk_p for PAT1 (M) metapelite is explained by enhanced anisotropic biotite formation, which is not accompanied by pore closure. Addition of gaseous pore pressure in compaction stage 3b tests enhanced Δk_p for PAT1 (P) samples compared with trend (2) (Fig. 8.4A), without affecting the mechanism behind AMS development. Fluids hamper (magnetic) foliation development, as they facilitate phengite nucleation and growth in random orientations away from illite grains. Pore pressure restricts phyllosilicate dehydroxylation and thus phengite mobility. Grain rotation as the primary mechanism of paramagnetic AMS development is excluded on two grounds. Firstly, sample

compaction by isostatic stress, confined torsion or compression yields a comparable Δk_p trend. Grain rotation, on the other hand, is a consequence of strain pathways (e.g. pure and simple shear), which in essence is the response of a material to applied stress fields. Distinctly different stress fields are likely to produce characteristic AMS during deformation or compaction. Secondly, grain rotation is a process primarily associated with mechanical compaction and is typically exhausted in argillaceous sediments below ~15 % porosity [e.g. *Vasseur et al.*, 1995; *Nygård et al.*, 2004; *Mondol et al.*, 2007; *Fawad et al.*, 2010]. The non-linear increase of strength of clays during mechanical compaction is the consequence of rapidly increasing resistance to clay rotation. Chemical compaction in clays by clay recrystallization and dissolution/precipitation processes is required to lower porosity below ~15 %. From the distinctly different paramagnetic and ferrimagnetic AMS development it is inferred that remanence-bearing minerals behave independent from clay and mica minerals during chemical compaction below 15 % porosity.

8.5: Acknowledgements

We thank S. Misra for running the HIP apparatus during compaction stage 2 and 3a experiments, and R. Hofmann for technical support. This research was funded by SNF projects 200020-132772 and 200021-116153.

Chapter 9

Discussion

Bertrand Russell once said, "The fundamental cause of trouble in the world is that the stupid are cocksure while the intelligent are full of doubt."

Preface

Chapters 7 and 8 presented data and images on compacted synthetic metapelites. This chapter discusses these results by relating the observations to clay transformation leading to chemical compaction. The data show that chemical compaction is the main compaction mechanism in all samples, regardless of compaction history. A technique for the chemical compaction of illite shale was for the first time established, offering new opportunities for further experimental research on the development of chemical and physical properties in clay-rich sediments buried to late-diagenetic/anchizone conditions. The first section discusses the evidence for chemical compaction in the porosity and density data (subchapter 9.1). A density trend is identified and explanations given for samples that do not fit this trend. The second subchapter focuses on the relationship between volumetric strain and porosity reduction in such a way that it becomes possible to ascribe a mechanism to the accommodation of volumetric strain (subchapter 9.2). Data from the metapelites is also compared with data from compacted sandstones. The discussion continues with the construction and interpretation of the sample deformation path from radial and axial strain data (subchapter 9.3). Plotted against each other, these properties give insight in the compaction efficiency during axial straining. It is subsequently shown that dilation by radial extension occurred for most metapelites after a certain axial strain, which resulted in decompaction. The topic of subchapter (9.4) is sample strength behavior. The wide range of sample strength in confined compression and torsion tests is discussed in light of the dominant deformation mechanism. Compaction hardening is associated with pore-space reduction, which is influenced mostly by the variations in pore compressibility due to anisotropy and varying pore alignment. Strain rate and temperature sensitive steady state flow and compaction weakening are associated with ductile flow by diffusion creep. Sample drainage and pore pressure restrict diffusion creep. Combined ductile flow and pore-space reduction resulted in strain rate sensitive compaction hardening. Confined torsion experiments suffered from reduced friction of the assembly interfaces, which resulted in localized slip at low shear strain values. As a consequence, deformation of metapelites by sample twist was not possible. Chemical processes during the compaction stages are addressed in subchapter 9.5. The progress of the mineral reactions for the various sample groups is discussed in pseudosections of the chemical model (Chapter 6). The discussion focuses on the progress of the reactions towards the expected equilibrium phase assemblages. When linked to the heating of hydrous minerals, fluids play an important role. The precise role of fluids in the accommodation of strain in the Paterson apparatus tests is discussed. The chapter continues with a discussion on the produced microfibrils (subchapter 9.6). Addressed subtopics include the illite-phengite transformation, pores, deformation structures, and authigenic biotite and quartz. A link with chapter 8 on the magnetic response to chemical compaction is made by relating magnetic fabric development to microstructures and phengite content. As quartz cementation

is source for recent debates in the sedimentary petrology and petroleum geology community, the subchapter is concluded with a short discussion on the presence of authigenic quartz. The final subchapter attempts to answer the main question in this investigation: how do variations in the stress field influence chemical compaction? Presented arguments are based on the points made in the previous subchapters and chapter 8.

9.1: Porosity and density

Porosity and density data permit to verify the dominant compaction mode in synthetic metapelites. This is important, as the density development trends provide a first insight into the effects of stress fields on compaction processes.

Due to predominantly lower porosities of HIP1, HIP2 and PAT1 samples (less than 15%), chemical compaction is considered the dominant compaction mode in all the synthetic metapelites used. To achieve this degree of compaction, two or three compaction stages were required. The majority of PAT1 and all HIP2 samples are more compacted than HIP1 samples. This implies that further compaction was achieved during most compaction stage 3 tests. As the porosity of most of the HIP1 samples is below 15 %, porosity reduction in subsequent stages 3a or 3b is primarily the result of chemical compaction processes. The porosity after compaction stage 1 in the hydraulic cold-press was likely greater than 15 %. It therefore seems that during compaction stage 2 HIP1 samples compacted by both mechanical and chemical processes. However, the confining pressure during compaction stage 2 in the hot isostatic press was smaller than the vertical load in stage 1 (subchapter 3.2). As mechanical compaction is a function of effective stress/pressure [e.g. *Hedberg, 1936; Rieke and Chilingarian, 1974*], mechanical compaction during the hot isostatic pressing is improbable, excluding the compensation for the minor decompaction after load removal in stage 1. During cold pressing in compaction stage 1, only mechanical processes are activated; reversed illite to smectite transformation can be excluded on the time scale of hours to days. HIP1 samples exhibit a combination of mechanical and chemical compaction processes. In HIP2 and PAT1 samples, chemical compaction is more dominant but not solely responsible for the end product metapelites. The effect of chemical compaction is isolated by considering the differences between HIP1, and HIP2 and PAT1 metapelites.

Maplewood Shale has porosity between 2.7 and 2.9 % (Fig. 7.1A). The high illite and low smectite content, together with the estimated burial depth of 5 km [*Friedman, 1987*] suggest that smectite transformation to illite was nearly completed when exhumation started. The fact that an illite-rich shale and synthetic metapelite have comparable density and porosity is explained by the presence of detrital micas in the former and by the small grain density contrast between illite (average 2.75 g cm^{-3}) and phengite (average 2.82 g cm^{-3}). The two subsets in density data of the metapelites, therefore, indicate variable mineral content or composition heterogeneities in Maplewood Shale, perhaps reflecting lateral changes in deposition conditions in the Appalachian Basin during Early

Silurian. HIP2 samples of subset 2 are quartz-richer than metapelites of subset 1. The inferred grain density is higher for metapelites of subset 1 than of subset 2 (Fig. 7.1A).

Having concluded that chemical processes dominated compaction of the illite shale powder in HIP2 and PAT1 samples, the question on how compaction conditions affect porosity and density can be addressed. Within subset 1 (Fig. 7.1A) metapelites a trend that describes the density development during compaction is identified (Fig. 9.1). This trend includes data points from all PAT1 sample groups. Hence, the stress field in compaction stage 3b tests hardly affected density development during compaction. Two sets of PAT1 samples deviate from this trend; six high porosity and two low porosity metapelites are denser than the trend at equivalent porosity (Fig. 9.1). For five of the six high porosity samples, dilation occurred during compaction stage 3b, which decompacted the samples (Fig. 7.2 and Table D1). Since samples are confined and/or compressed, pores are elastically strained. Upon pressure and stress release, strained pores, unaffected by chemical compaction, are restored. During restoration, pore throats and channels are potentially modified to create a more efficient pore network. Porosity measurements afterwards yield a greater value, because the connected porosity increased. Chemical compaction densified the solid framework while pore unloading enhanced porosity.

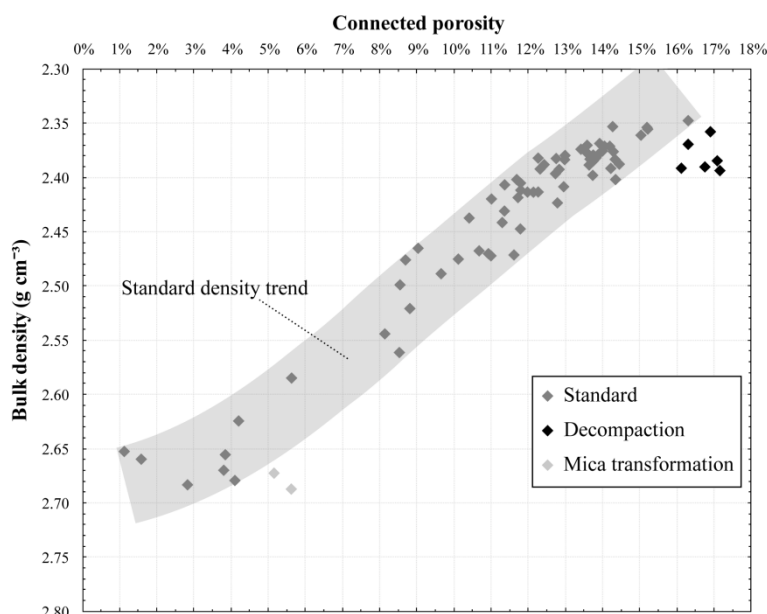


Figure 9.1: Porosity-density plot for subset 1 samples, with interpreted density development trend and recognition of out-of-sequence compacted samples.

The higher density of two low-porosity PAT1 (I) and PAT1 (M) metapelites results from mica transformation. The grain density of biotite (average 3.09 g cm⁻³) contrasts more with phengite than illite. Consequently, biotite production has a relatively larger effect on sample density than illite transformation. In mineral stability field IV (Fig. 6.1), biotite is stable, while phengite and illite are

not. Biotite formation at the expense of phengite results in metapelite densification, but is not necessarily accompanied by effective porosity reduction. This will be discussed in subchapter 9.6.

9.2: Accommodation of finite volumetric strain

The relationship between volumetric strain and porosity reduction gives a first insight in the strain accommodation mechanism. Compaction is directly related to pore-space collapse, whereas deformation of the solid grains leads to relatively low porosity reduction, and blocking of pore channels results in enhanced porosity reduction (Fig 7.2).

Most synthetic metapelites in this study predominantly accommodate strain by pore-space collapse, regardless of finite strain, temperature or stress kinetics (Fig. 7.2). For three samples with 10 % to 12 % volumetric strain, porosity reduction is relatively low (Fig. 7.2). These 700 °C samples were deformed by a combination of pore-space collapse and appreciable amount of solid grain deformation, but do not relate to a particular compaction stage 3b stress field (Fig. 7.2A). Quartz fracturing is observed in samples that were compacted isostatically and by confined compression (Fig. 7.9-10). It is probable that in these 700 °C samples, grain fracturing brought about sufficient grain rearrangement to accommodate measurable strain. Interestingly, for sandstones, comparable deviations from pore-space collapse are reported for room temperature shear-enhanced compaction (Fig. 9.2) [Wong *et al.*, 1997]. Solid grain deformation in these sandstones was accommodated by compactive cataclastic flow [Wong *et al.*, 1997]. Deformation features associated with cataclasis are not observed in any of the synthetic metapelites.

The volumetric strain-porosity reduction plot (Fig. 7.2) also shows the extent and controlling parameters of volumetric strain and compaction. The amount of finite volumetric strain (i.e. pore-space collapse) is evidently temperature controlled (Fig. 7.2B). The broad range of 700 °C PAT1 metapelites reflects not only experiment duration but also strain rate (or compaction rate) and effective pressure. The amount of compaction and strain in long-duration 700 °C isostatic stress tests is comparable with that in shorter 700 °C confined compression tests (Fig. 7.2). However, samples in 700 °C confined compression experiments with lower effective pressure (PAT1 (P)), compact and strain less (Fig. 7.2). Therefore, deformation (i.e. strain rate) and temperature promotes, but pore pressure restricts porosity reduction.

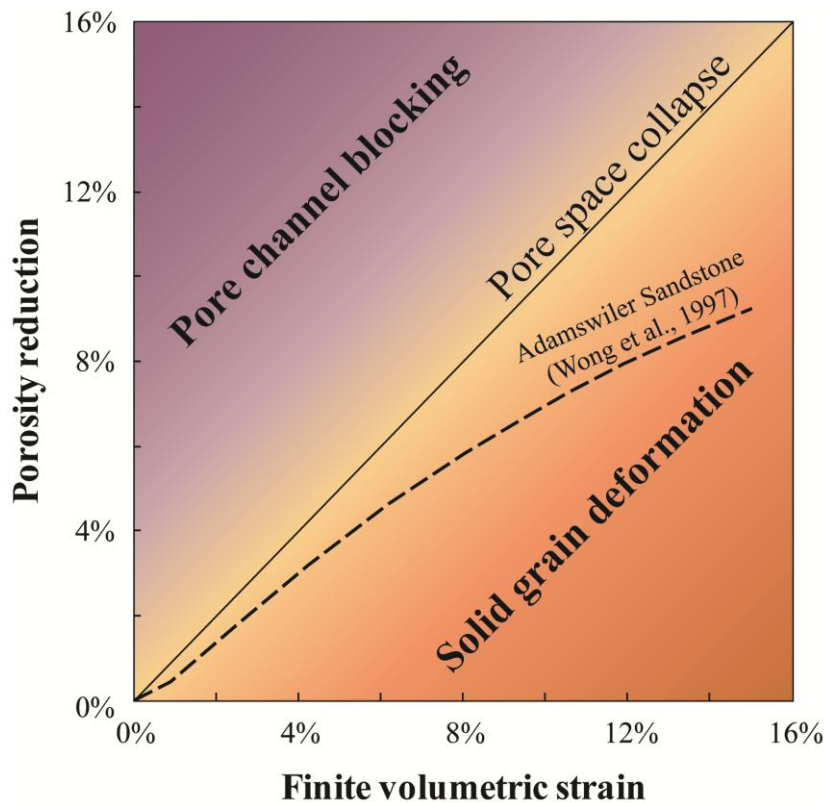


Figure 9.2: Finite volumetric strain/porosity reduction plot for room temperature shear-enhanced compaction of Adamswiler Sandstone (after Wong *et al.* [1997]).

9.3: Sample deformation path

From the relation between volumetric strain and porosity reduction it is clear that contraction is required for compaction of synthetic metapelites to take place. In a diagram of axial strain versus radial strain, compaction occurs anywhere in the strain field that satisfies this condition; for simple flattening this occurs above the line that denotes pure shear (Fig. 7.3) (i.e. critical state line of constant volume deformation). The deformation path describes the shape change and volumetric strain evolution during axial straining in $\epsilon_{ax}/\epsilon_{rd}$ -space. With axial strain, the line for continued pure shear (i.e. division between compaction and decompaction) shifts to higher axial strain values. Sample deformation paths are constructed from grouped data points in a ϵ_{ax} - ϵ_{rd} plot (Fig. 9.3). Grouping is based on temperature, with PAT1 (I) and PAT1 (T) samples excluded in this case. Deformation paths represent the best-fit lines through the data points. Key points for the deformation paths are their (extrapolated) intersections with the line of 0 % finite radial strain (i.e. uniaxial strain). These intersection points mark the axial strain beyond which no sample plots in the field of non-uniform contraction, and where axial strain is compensated by radial extension (Fig. 9.3). The intersection point moves to higher axial strain values for higher temperature, with a major change evident between 650 °C and 700 °C, although a large undefined error exists for $T \geq 650$ °C, possibly due to a change in deformation mechanism (discussed in subchapter 9.4). From each intersection point, a new critical

state line for pure shear is constructed. It separates the field of simple flattening for higher axially strained samples in contraction (right) and dilation (left). For 500 °C samples, the intersection point is placed at $\epsilon_{ax} = 3.5\%$, for 650 °C at $\epsilon_{ax} = 5.8\%$, for 700 °C at $\epsilon_{ax} = 12.2\%$ and for 750 °C at $\epsilon_{ax} = 13.3\%$. Beyond the 500 °C intersection point, 500 °C samples with higher axial strain plot to the left of the re-defined pure shear line, indicating that sample dilation (i.e. decompaction) took place for $\epsilon_{ax} > 3.5\%$. For 700 °C and 750 °C samples, decompaction occurred after axial straining of respectively 12.2 % and 13.3 %. Finally, based on the 650 °C intersection point and pure shear line, two samples experienced compaction and one sample experienced no volume change after 5.8 % axial straining. The position of the intersection points is critical for the interpretation of the onset of decompaction and requires tight constraints from data points, which is not always the case for the synthetic metapelites. It is most reliable for samples that plot near their deformation path, assuming that samples behave according to the deformation path they constrained.

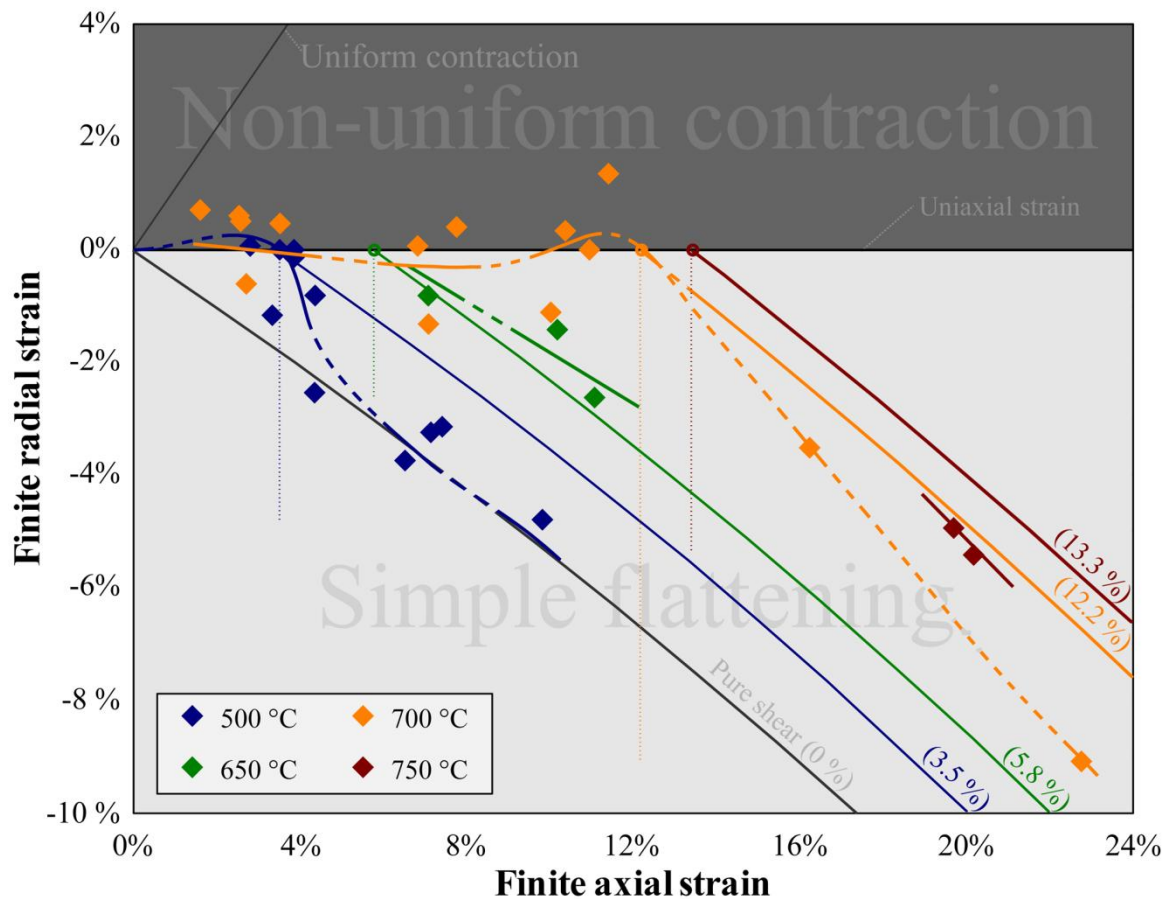


Figure 9.3: Deformation paths for temperature-grouped PAT1 (C), (P) and (M) samples. Dashed line sections represent low-confidence intervals. Circles and vertical dotted lines mark the (extrapolated) intersection points. Pure shear lines derived from intersection points are colored by temperature.

The deformation paths illustrate how axial deformation of synthetic metapelites is accommodated. At first samples are uniaxially compressed. Beyond the intersection point, radial extension partially to fully accommodates axial straining. In fact, for most samples, radial extension

leads to decompaction. Therefore, deformation paths and the related intersection points offer an explanation for the observation that compaction is not directly related to axial strain (Table D1).

9.4: Deformation mechanisms

Confined compression Paterson apparatus tests were performed under different conditions to investigate the effects of axial strain, temperature, strain rate, sample drainage, pore pressure and jacket material on synthetic metapelite compaction. From the obtained data (Fig. 7.4) it is evident that all these parameters have measurable effects. Two deformation mechanisms dominate the compaction of synthetic metapelites during compaction stage 3b confined compression tests. Compaction hardening during axial straining is ascribed to pore-space reduction. Steady state stress and compaction weakening are linked to ductile flow by diffusion creep.

Compaction hardening:

As metapelites compact in response to axial compression, their strength increases in a linear or near linear fashion; a behavior termed “compaction hardening”. The reduction of compressible pores and simultaneous increase of the stiff ‘solid’ framework with axial straining result in compaction hardening, without localized failure of the sample within an axial strain of 15 %. Comparable stress-strain behavior, albeit with lower σ_{diff} values, was recorded during high strain confined compression tests at room temperature on London clay and fluvio-marine shale [Jones and Addis, 1986, Fig. 4]. More recently, strain hardening ascribed partially to compaction was observed in 300 °C to 600 °C shearing of synthetic pure muscovite gouges [Van Diggelen et al., 2010]. Experimental compaction by pore space reduction in sandstones results in permanent deformation by grain crushing [Zhang et al., 1990; David et al., 1994; Menéndez et al., 1996; Klein et al., 2001], cataclastic flow [Menéndez et al., 1996; Wong et al., 1997; Wu et al., 2000], or compaction bands and shear fractures [Menéndez et al., 1996; Wu et al., 2000; Wong et al., 2001; Klein et al., 2001], depending on initial porosity, effective pressure and stress regime. The strength of compacting metapelites essentially reflects the pore-space/solid-space ratio (porosity). In this concept and by allowing for radial extension (Fig. 7.3 and Table D1), more than 14 % axial straining should lead to very low porosity metapelites. This concept is valid for the $T \geq 700$ °C tests, but does not hold for 650 °C and 500 °C tests (Fig. 7.2-3 and Table D1). Strain recovery and pore elasticity explain this conundrum. At the lower temperature range, the finite axial strain of a sample is much lower than the total axial strain during the compaction test. Axial strain is (partially) recovered upon unloading. The solid framework of the compacted metapelites can only partially account for observed strain recovery of up to 12 %. Previous experiments under similar conditions show that the inelastic yield point of natural mica schist is smaller than 1.7 % [Shea and Kronenberg, 1992; 1993]. The remaining

recoverable strain is ascribed to pores. Pore annihilation by chemical processes is required to keep synthetic metapelites compacted after unloading, and was more successful in tests in the higher than in the lower temperature range. For example, SEM data revealed that in 500 °C and 650 °C metapelites, the amount of clay micropores is much higher than in higher temperature PAT1 samples (Fig. 7.10). Strong elastic rebound has been reported for illite compaction tests before and was ascribed to illite flocculation [Olson and Mitronovas, 1962].

Most of the tests at 500 °C and 650 °C (confined compression) and some 700 °C experiments share a common sample strength evolution of unfinished compaction hardening (Fig. 7.4A). This behavior implies that strain rate and temperature have a negligible influence on strength development during pore space reduction.

During three tests (P1336, P1337 and P1346), a different strength evolution was recorded. After the first two tests, the samples were more porous than before. This decompaction was discussed in subchapter 9.1. The finite radial strain in these samples is smallest, whereas their finite axial strain is largest of all 500 °C samples. After P1346, the metapelite was still relatively porous considering its compaction temperature and total axial strain (Table D1). These observations and the realization that 500 °C samples have the strongest tendency to recover axial strain imply that pore elasticity recovered strain in both directions. Such isotropic behavior is typically associated with spherical pores, or in the case of phyllosilicate-rich material, with random distribution of sheet-like pores. The compressibility of pores is shape dependent. In 2D, depending on the pore aspect ratio elliptical pores have a two or more times lower compressibility than circular pores [Zimmerman, 1991, p. 91]. Aligned sheet-like pores, such as the abundant clay micropores in HIP1 samples (Fig. 7.9AB), are therefore much weaker than spherical pores or randomly oriented sheet-like pores. The stiffer sample behavior during P1336, P1337 and P1346 (Fig. 7.4A-B) supports the proposed poro-elastic response, and implies that the degree of compaction hardening is influenced by microfabric elements such as pores and pore shapes.

The application and increase of pore pressure (which has the effect of lowering effective pressure) has negligible effect on pore-space reduction and compaction hardening. Stress-strain curves for PAT1 (P) samples show a compaction hardening behavior (Fig. 7.4C) comparable to that in compression tests without pore pressure (Fig. 7.4A-B). In contrast, Jones and Addis [1986] reports faster compaction hardening with axial strain between 14 and 70 MPa confining pressure tests.

Sample drainage experiments conducted at 700 °C (P1339) resulted in compaction hardening (Fig. 7.4B), low finite axial strain and volumetric strain, and limited compaction (see Table D1 for details). These observations imply that elastic pore space reduction dominates strain accommodation in open systems up to higher temperatures.

Steady state flow and compaction weakening:

Compaction weakening, reduction of sample strength during constant strain rate compaction and steady state flow behavior were observed in four experiments at 700 °C and 750 °C (Fig. 7.4B-C). The stress sensitivity to the applied strain rate suggests that the dominant deformation mechanism during steady state flow is diffusion creep (Table 7.1 and Fig. 7.5B-C). Diffusion creep is a constant volume deformation mechanism and as such requires radial extension of the samples to counter balance the axial deformation. The deformation paths for 700 °C and 750 °C PAT1 (C) samples (Figure 9.3) show exactly that, with the samples plotting close to a shifted critical state line for pure shear, indicating that after 12.2 % and 13.3 % axial straining, respectively, the condition of constant volume deformation is met. Diffusion creep is temperature sensitive. Compared with 700 °C tests, 750 °C samples are weaker and reach mechanical steady state at lower strain values.

Strain rate sensitive compaction hardening:

The spread in compaction hardening rates in 700 °C tests is ascribed to varying contributions of diffusion creep and pore-space reduction. The 700 °C stress/strain curves, experiments P1339, P1345, P1346 and P1347 excluded, indicate stiffer behavior for higher strain rates (Fig. 7.4B), which is explained by a decreasing contribution of diffusion creep. The stress-strain curve for P1472 (650 °C) can also be interpreted as being slightly influenced by diffusion creep (Fig. 7.4A). In recent experimental shearing of pure muscovite, 700 °C was found to mark the temperature where a change in deformation mechanism from a mixture of brittle/frictional and crystal plastic processes to linear-viscous dislocation creep occurs at strain rates of approximately 10^{-5} s^{-1} [Mariani *et al.*, 2006]. In addition, from deformation studies on kaolinite and halite/kaolinite gouges, strain weakening was coupled with the activation of pressure solution processes solely in the polymineralic gouge [Bos *et al.*, 2000].

Effect of jacket material:

Copper-jacketed samples were found to be slightly weaker than iron-jacketed samples in the experiments conducted at 500 °C (Fig. 7.4A). At 700 °C, the unique copper-jacketed sample is stiffer than most iron-jacketed samples. This contradicting behavior suggests that the effect of jacket material on sample stiffness cannot be ascribed solely to the flow strength of the jackets. Also porosity, density and strain data show no evidence for jacket material effects (Table D1). Instead, variations in compaction hardening rates are attributed to sample-to-sample variations and related experiment reproducibility.

Confined torsion tests:

Slip along assembly pistons and spacer interfaces prevented confined torsion tests from reaching appreciable values for shear strain (Fig. 7.6). Such slip is commonly attributed to reduced

friction because of water vapor. Using a coefficient of friction (μ) of 0.67, the shear stress required to slip along alumina-alumina interfaces, compressed by 300 MPa normal stress, is approximately 200 MPa. This is supported by data comparing water content of samples before and after experiment P1211 (Fig. 7.8B and Table E1).

Sample P1211 displayed no permanent strain, because twist was primarily by slip on assembly interfaces (Fig. 7.6A). Torque data > 0 throughout the experiment indicate that minor deformation was however achieved. Assuming a minimum observable shear strain of 0.02, the actual sample strain rate must have been lower than $4 \times 10^{-6} \text{ s}^{-1}$. This strain rate approaches the minimum strain rate achievable by the torsion motor of the Paterson apparatus ($2 \times 10^{-6} \text{ s}^{-1}$).

During experiments P1212 and P1216, twist was accommodated solely by the sample until slip along assembly interfaces occurred. The permanent shear strain in the samples (Fig. 7.6B-C) matches with the strain values at the moment of slip (Fig. 7.4D). Shear stress values at the moment of slip are much lower than 200 MPa, so the slipped interfaces must have experienced some sort of lubrication to reduce the friction.

9.5: Chemistry

Mineral reactions:

As predicted by the pseudosection for Maplewood Shale (Fig. 6.1-2) and shown by XRD patterns (Fig. 7.7) and on SEM images (Fig. 7.9-10), the mineral content of the illite shale powder changed during compaction stages 2 and 3. It is evident that in none of the experiments sufficient time was available to reach the mineral equilibrium assemblage predicted for the experimental conditions. In PAT1 (M) samples, no partial melt was observed (Fig. 7.10E) and in 700 °C PAT1 samples there is no sign of authigenic K-feldspar, aluminosilicates or garnet (Fig. 7.10D). Instead, the nearly complete disappearance of illite and the presence of authigenic biotite and phengite suggest that mineral equilibrium field III was almost achieved (Fig. 7.10D, F). In lower temperature PAT1 and HIP1 samples illite is better preserved (Figs. 7.9A-B and 7.10A-C), albeit still in reduced quantities in favor of phengite formation. No authigenic biotite is observed, so at best the boundary between fields I and II was reached. There is no risk that water loss resulted in mineral reactions towards field VII, as no field VII minerals were observed. In HIP2 samples authigenic biotite and phengite was found, and illite content was found to be severely diminished (Fig. 7.9C), corresponding to the mineral assemblage for field II (Fig. 6.1).

Based also on XRD-patterns and SEM images, there is no evidence that different stress fields influence mineral reactions and reaction rates. Nevertheless, deformation-induced compaction resulted in lower porosities in shorter amount of time, but this was not achieved by different mineral reactions. In fact, compaction primarily reflects the transformation of illite into phengite. As porosity

decreases in the synthetic metapelites, the illite content seems to decrease in favor of authigenic phengite. This is best seen in the SEM images of figures 7.9 and 7.10.

Fluids:

The role of fluids in the chemical compaction of metapelites is best demonstrated by experiment P1339 during compaction stage 3b. Sample drainage limited diffusion creep, leaving pore space reduction the sole deformation mechanism. The activation or rate of diffusion creep depends on the fluid availability. Fluids likely originated from the dehydroxylation of phyllosilicates. TG analysis on HIP1 metapelites demonstrates that mica dehydroxylation occurs in a temperature range from 550 °C to 1000 °C (Fig. 6.3). KFT water content measurements indicate that water loss is a function of maximum temperature (Fig. 7.8 and Table E1). Phyllosilicates barely dehydroxylate when re-heated at lower temperatures, as is the case for 500 °C compaction stage 3b tests. During 650 °C to 750 °C tests, a sufficient amount of lattice water is released to facilitate diffusion creep.

The reliability of diffusion creep on fluid offers an alternative explanation for the strain rate sensitivity of mixed diffusion creep and pore space reduction. During compaction permeability of the system lowers. For faster compaction, faster diffusion creep is needed, while less time for fluid migration is available. Permeability of illite shale is strongly dependent of effective pressure and porosity. In general, clay/mudstones permeability data, derived from experiments, nature and theoretical considerations, show a decrease with compaction extending to porosity < 15 % [Neuzil, 1994; Yang and Aplin, 1998; 2007; 2010; Kwon *et al.*, 2004]. For example in illite-rich Wilcox Shale, water permeability decreases more than one order of magnitude in an effective pressure interval from 3 to 8 MPa [Kwon *et al.*, 2004].

9.6: Microfabric elements

Illite-phengite transformation:

The transformation of illite into phengite readily alters the microstructure of the synthetic metapelites. The porosity decreases as flocculated illite is replaced by tightly stacked phengite and biotite (Fig. 7.9-10). Simultaneously, isotropic illite orientations are transformed into anisotropic mica alignment that gives rise to foliation (Fig. 7.9-10). Anisotropic fabric development is frequently described in natural mudstones affected by the smectite to illite transformation and is believed to depend on temperature and thermal history rather than depth and effective stress [e.g. Bowles *et al.*, 1969; Ho *et al.*, 1999; Aplin *et al.*, 2003; 2006; Charpentier *et al.*, 2003; Worden *et al.*, 2005]. The paramagnetic AMS increase as a function of decreasing porosity (chapter 8) quantifies the development of the anisotropic phyllosilicate fabric.

Mica wrapping:

Detrital and authigenic mica wrapping around silt clasts render the foliation irregular in appearance (Fig. 7.9C-F and 7.10A, D-F). Clay particle alignment and clay wrapping have been proposed as porosity reducing mechanisms in experimental mechanical compaction tests on clay-silt mixtures [e.g. *Vasseur et al.*, 1995; *Fawad et al.*, 2010]. However, if this is applicable to mica as well, it implies that compaction occurred mechanically in the synthetic metapelites, which is improbable for all compaction stages except the first one. The origin of the irregular foliation, marked by authigenic mica, is believed to be related to fluid-driven mica nucleation and growth. As fluids are flowing through a sample, their flow direction is controlled by pressure gradients and permeability. The permeability in clay/mica-rich samples quickly becomes more anisotropic as phyllosilicates align themselves by compaction [*Vasseur et al.*, 1995]. Therefore, local enhanced phyllosilicate alignment essentially means permeability anisotropy, which determines the direction of fluid flow. As mica minerals precipitate from the solution, they orient according to the flow direction. Obstacles in the flow path, such as rigid silt clasts, force fluids to go around them. Authigenic micas mark the fluid flow path of fluid, resulting in “wavy” foliation.

Pores:

Clay micropores disappear, within the resolution of the SEM, as the illite fraction diminishes, but the amount of intragranular fractures in detrital clasts increases with compaction. Collapse of matrix-clast voids and matrix pores contributed least to compaction. Conversely, during mechanical compaction tests on clay-silt mixtures the pores most frequently collapsed are matrix-clast voids or related [e.g. *Fawad et al.*, 2010; *Schneider et al.*, 2011].

Some matrix-clast voids and the majority of intragranular fractures are not filled by authigenic mica. This implies that either they were formed in the absence of phyllosilicate dehydroxylation, or that they were not connected with the pore network, throughout the experiment. Intragranular fractures are related to stress-induced grain crushing. Due to unfavorable orientation, shape or pore space-solid space ratios, local stress values could overcome the cohesion and shear strength of the quartz grains, which led to fracturing, in a fashion comparable with what is commonly reported for sandstone [*Zhang et al.*, 1990; *David et al.*, 1994; *Menéndez et al.*, 1996; *Klein et al.*, 2001]. As the metapelites compact, more stress is transmitted to the quartz grains. Therefore, grain crushing likely occurs at or near the end of a test. In PAT1 (M) samples, despite the low porosity, intragranular fractures are seldom observed (Fig. 7.9E). This suggests that stress variations were relatively small and quartz grains were homogeneously loaded. If the pore-space solid-space ratio controls quartz fracturing, it can be inferred that diffusion creep reduces pore space relatively evenly. Alternatively if grain orientation or shape, are most important, diffusion creep leads to detrital quartz SPO or grain shape homogenization, respectively.

Deformation structures:

In low-porosity HIP2 and PAT1 (I) metapelites (Fig. 7.9C-D, F) and for the full porosity range for PAT1 (C), (P) and (M) metapelites (Fig. 7.10A,C-F), local space deficiency problems were overcome by mica folding and kinking. The absence of such deformation structures in HIP1 samples suggests that strain rate was higher than the rate at which pore space reduction could accommodate strain during confined compression tests at 500 °C. When sufficient time was available, spatial problems that arose during compaction could be overcome by clay transformation, leading to patches of illite-phengite transition material (Fig. 7.9A). This notion indirectly implies that the illite-phengite transformation is pressure sensitive. Illite preserved in pressure shadows of quartz clasts provides evidence (Fig. 7.9D) for this. Other indirect evidence comes from the PAT1 (P) samples, as lowered effective pressure results in lesser compaction (Fig. 7.1-2).

Authigenic biotite:

Authigenic biotite is frequently organized in complex patterns (Figs. 7.9C-D and 7.10D-E). This is believed to reflect nucleation from a trapped fluid. As authigenic biotite is mostly found in the metapelites with the lowest porosity, average and local permeability within the samples are very low. Fluids migrate through connected pores, but get increasingly more confined as compaction reduces the porosity. Remaining pores are mostly matrix-clast voids and matrix pores. The complex shape of some authigenic biotite patches reflects the triangular and sheet-like matrix pores. Phengite dehydroxylation is then a prerequisite for authigenic biotite.

Quartz precipitation:

Quartz precipitation is subject of debate in the study of sediment diagenesis. Silica released during the smectite to illite transformation is considered an important source for both sandstone [e.g. *Towe, 1962; Boles and Franks, 1979; Leder and Park, 1986; Land et al., 1997; Lynch et al., 1997; Land and Milliken, 2000; Van de Kamp, 2008; Day-Stirrat et al., 2010*] and mudstone cementation [*Hower et al., 1976; Yeh and Savin, 1977; Small, 1994; Peltonen et al., 2009; Thyberg et al., 2010*], depending on the permeability of the system. The illite-phengite transformation is less studied but also associated with silica release [*Van de Kamp, 2008*]. In the synthetic metapelites with porosity < 7 %, released silica is recognized in the form of clay-sized authigenic quartz, comparably with observations by *Thyberg et al. [2010]*. The elongated shape and alignment with the mica matrix suggests that the quartz precipitated from a silica-rich fluid. The correlation between temperature, porosity and occurrence of authigenic quartz strengthens the previously discussed importance of fluid availability for compaction by diffusion creep.

The presence of authigenic quartz occurs simultaneously with smoothing of detrital quartz grains. It was however not yet possible to distinguish whether the smoothing is the result of precipitation or dissolution processes.

Chapter 10

Conclusions

Mark Twain once said, “A banker is a fellow who lends you his umbrella when the sun is shining, but wants it back the minute it begins to rain.”

Preface

This chapter summarizes the study and presents conclusions. The problem statement and related questions, discussed in chapter 1 are re-iterated in subchapter 10.1. The most important findings, presented in chapters 7 and 8, are summarized in bullet form in subchapter 10.2. The next subchapter summarizes the discussion of chapter 9 and draws conclusions. This chapter concludes with a short outlook for research on chemical compaction of clay-rich sediments.

10.1: Problem statement

The fact that clay transformation and dissolution/precipitation processes greatly influence rock physical properties during mudstone/shale burial has been extensively demonstrated [e.g. *Van der Pluijm et al.*, 1998; *Ho et al.*, 1999; *Aplin et al.*, 2006; *Day-Stirrat et al.*, 2008; *Thyberg et al.*, 2010]. Implementation in modeling of basin evolution has been advocated by e.g. *Bjørlykke and Høeg* [1997]. Nevertheless, experimental simulation of clay diagenesis has previously focused almost exclusively on mechanical compaction, while chemical compaction was considered to be too slow for reliable laboratory simulations of diagenesis [e.g. *Nygård et al.*, 2004; *Mondol et al.*, 2007; *Fawad et al.*, 2010].

Numerical simulations of basin evolution have been shown to be accurate, especially when non-vertical tectonic stresses, as argued by *Aplin and Vasseur* [1998] and *Luo et al.* [1998], are incorporated [*Pouya et al.*, 1998]. However, experimental compaction studies supporting the theorized role of tectonic stress and providing an important opportunity to calibrate and validate such models are scarce [*Jones and Addis*, 1986; *Nygård et al.*, 2004].

This thesis reports the first laboratory simulations of mechanical and chemical compaction designed to replicate the conditions typical in deep sedimentary systems, using natural illite-rich sediment. Two main questions were posed:<

1. Can chemical compaction of clay be simulated in the laboratory?
2. How does the stress regime affect clay compaction?

To address these questions, experiments were designed along a three-stage compaction procedure. In the first compaction stage, natural illite shale powder, derived from Maplewood Shale (New York, USA), was compacted in a hydraulic cold-press with a vertical load of 200 MPa. Further compaction was achieved during the second compaction stage in a hot isostatic press with applied temperature of 590 °C and isostatic stress of 170 to 172 MPa. In the third and final stage, compaction was continued either in the hot isostatic press for a second run, or in a Paterson apparatus. In the latter case, an isostatic stress, confined compression or confined torsion stress regime at 300 MPa confining pressure, and a temperature of 500 °C, 650 °C, 700 °C or 750 °C were applied. The effect of other extrinsic parameters such as strain rate, fluid venting and effective pressure were also tested.

Forward modeling of the anticipated mineral reactions was done using a PERPLE_X build phase stability diagram for Maplewood Shale composition, taking into consideration water content, temperature and pressure.

10.2: Main findings

The progress and mechanism of compaction during the various stages of the experimental procedure were monitored by measuring porosity, density and magnetic properties after each compaction stage. Detailed chemical analysis was performed using XRD and KFT methods, while SEM imaging was used for mineral and pore identification, and fabric development during compaction. In Paterson apparatus tests, sample strength was monitored and when applicable, the stress exponent of the flow was determined. Sample strain (radial, axial and volumetric) was measured for the construction of deformation paths, which gave insight in the compaction efficiency during axial straining. A summary of the main findings follows:

- Experimental compaction of illite shale powder results in porous metapelites, with connected porosity ranging from 1.0 % to 17.1 %. Two sample subsets are identified from bulk density-porosity data, related to quartz/mica fractions in the samples. Density increases approximately linearly as a function of porosity reduction, regardless of the stress regime during compaction.
- Finite volumetric strain in relation to porosity reduction shows that strain is primarily accommodated by pore space collapse. A gradient of compaction increasing with temperature is identified. Room temperature tests result in nearly zero finite volumetric strain and porosity increase.
- Finite axial and radial strains confirm a stress regime dependency. The strain character of samples compacted in confined torsion and isostatic stress is described as non-uniform contraction, whereas that of confined compression samples is better described as flattening. The style of flattening of samples during confined compression tests is controlled by temperature and axial strain.
- Three types of strength evolution with axial straining are identified. Continuous nearly linear hardening, with no strain rate dependence, is displayed by all porous metapelites compressed at 500 °C and 650 °C, and by 700 °C metapelites when effective pressure is lowered or the sample is drained during the experiment. In other confined compression tests performed at 700 °C, strain-rate dependent continuous hardening is seen. The third deformation behavior is observed during confined compression experiments conducted between 700 °C and 750 °C. These stress/strain curves initially display hardening, but reach steady state flow or even strain weakening within 10 % axial strain. Calculated values for the stress exponent indicated diffusion creep flow behavior.
- The monitoring of sample strength during confined torsion tests is hampered by unwanted slip along assembly spacers or pistons. The maximum strain achieved during a single test is $\gamma = 0.10$.

- XRD spectra of synthetic metapelites of all samples groups reveal an enhanced phengite and biotite crystallinity, and the disappearance of smectite, clinochlore and apatite.
- The amount of dehydration and dehydroxylation of original Maplewood Shale is controlled by the maximum temperature during the experimental compaction stages. For half of the 500 °C PAT1 samples the remaining water content is lower than the critical value that marks the boundary of the modeled phase stability fields II and VII. For none of the higher temperature PAT1 metapelites, except for the single drained sample, the water content after compaction stage 3b is below 1.0 wt. %, which marks the boundary between fields IV and V, and field VI.
- SEM analysis on both isostatically compacted metapelites and those compacted by differential stress show a correlation between illite and mica content, and porosity. Porosity decreases as more illite is transformed to phengite.
- The illite to phengite transformation is accompanied by 1) enhanced grain alignment seen in SEM images and quantified by paramagnetic AMS, and 2) authigenic quartz formation.
- (Semi)-ductile deformation structures such as microfolds and mica kinks are observed in 1) low- to high-porosity metapelites that are compacted by differential stress, and 2) the low-porosity (< 5 %) isostatically compacted metapelites.
- As porosity decreases, clay micropores start to disappear. Other pore types are preserved and a new type of pores (intragranular fractures) associated with rigid clasts is generated.

10.3: Conclusions

In this study, mechanical and chemical compaction of clay-rich sediments was successfully simulated in the laboratory. In the first of three stages compaction was achieved by mechanical processes whereas in subsequent stages chemical compaction dominated. The transformation of illite into phengite, closing clay micropores, and mineral precipitation from fluids accounted for the chemical compaction. It is demonstrated that fluid availability, for which temperature and pressure are key parameters, is a prerequisite for chemical compaction. Heat is required to drive water molecules out of the crystal lattice, whereas fluid release is restricted by pore pressure, and illite is preserved in pressure shadows. Deformation enhances chemical compaction. Deformation structures appear locally when strain accommodation by clay transformation and mass transfer is exhausted (isostatic compaction) or too slow (deformation-induced compaction).

Deformation of compacting metapelites is described by a temperature controlled deformation path in radial and axial strain space. These paths give insight in the accommodation of axial strain. Strain is first accommodated by closure of pore space. Beyond the intersection point of the deformation path with the line for uniaxial strain (i.e. zero radial strain), axial straining is accommodated by radial extension. Radial extension is often associated with sample dilation and

preserves a minimum porosity. The onset of radial extension moves to higher axial strain for higher temperatures, and is coupled to the ability of diffusion creep to accommodate strain. Radial extension of the sample is organized predominantly, by diffusion creep that allows mass transfer along a pressure gradient. Pore space collapse is independent of strain rate or temperature and results in nearly linear compaction hardening; leading to sample strengths ≥ 500 MPa at 8 % axial strain. Diffusion creep weakens the sample by at least 50 %, depending on the strain rate and temperature. Strain rate sensitive hardening is the result of the combined effects of pore space closing and diffusion creep. The switch in dominant deformation mechanism, brought about by dehydroxylation and/or axial strain, is not accompanied by solid grain deformation. Permanent compaction is finally achieved only by clay transformation and mass transfer. However, pore space closure is temporary and reversed after unloading, leading, for some low-temperature experiments, to eventual decompaction and higher porosity.

The degree of compaction in the synthetic metapelites is controlled primarily by the progress of the illite to phengite transformation. The linear increase of the paramagnetic AMS with decreasing porosity reflects the gradual phengitization of the compacting metapelites. Biotite forms at the expense of phengite, without closing pores, but with greater AMS. Fluids hamper foliation development, as precipitation is steered by pressure gradients reflecting sample heterogeneities. Restricted fluid flow and on site illite to phengite transformation results in enhanced paramagnetic AMS.

This study demonstrates that chemical compaction processes can be simulated in the laboratory. To make this happen elevated temperature and pressure conditions are required. Forward phase stability modeling is useful for selecting these conditions. Furthermore, this study shows that, besides temperature and pressure, differential stress also is an actor of chemical compaction processes. To conclude, in deep basin systems, tectonic stress is unlikely to have a dramatic effect on the intrinsic properties of compacted argillaceous sediments.

10.4: Recommendations for further research

Now that chemical compaction of illite shale in the laboratory has been achieved, a wide range of follow-up studies may be developed, from detailed microstructural investigations, to physical properties measurements, and other compaction tests using specifically chosen source material. The following is a description of a small number of key questions worth investigating.

Authigenic quartz:

The origin of quartz cement in both sandstones and mudstones is poorly understood if not controversial. Detailed knowledge about the controlling parameters and boundary conditions are

essential for the correct interpretation of naturally occurring authigenic quartz and sediment cementation. Simulation of chemical compaction can provide that required knowledge.

To solve the uncertainties about the origin of the smoothing of detrital quartz, two methods are proposed. First, detailed image analysis may provide sufficient information on the grain size distribution of detrital quartz before and after compaction tests. Alternatively, high-resolution cathodoluminescence (CL) SEM analysis, (as used in e.g. *Peltonen et al.* [2009] and *Thyberg et al.* [2010]) can be used to discriminate authigenic from detrital quartz, provided the detrital quartz grains contain lattice defects.

Clay/mica texture development:

The smectite to illite transformation marks a prominent increase in crystal alignment [e.g. *Bowles et al.*, 1969; *Ho et al.*, 1999; *Aplin et al.*, 2003; *Charpentier et al.*, 2003; *Worden et al.*, 2005]. Similar observations are made with the illite to phengite transformation. Measurements of the magnetic fabric provided a first quantitative description of the texture development. However, it is recommended that quantitative texture analysis is performed on the synthetic metapelites. X-ray texture goniometry (XTG) [e.g. *Van der Pluijm et al.*, 1994; *Ho et al.*, 1999; *Day-Stirrat et al.*, 2011] and the recently developed synchrotron diffraction technique [e.g. *Bäckström et al.*, 1996; *Heidelbach et al.*, 1999, *Wenk et al.*, 2004; *Voltolini et al.*, 2009] are useful techniques for detailed quantification of phyllosilicates texture.

Silver Hill shale powder compaction tests:

Shales are notorious for their diversity. The effect of intrinsic parameters on chemical compaction should be investigated by applying the experimental procedure of this study to, for example, Silver Hill shale. It is expected that mica kinking and folding are more common in the silty Silver Hill shale than in the clayey Maplewood Shale. The formation conditions for ferrimagnetic iron-sulphides can be tested and constrained by compacting Silver Hill shale powder using the hot isostatic press.

Detailed SEM pore analysis on enhanced polished surfaces and mercury porosimetry analysis:

SEM image quality at high-resolution is strongly affected by the quality of the polish. Topographic effects severely affect the BSE images, especially in high-porosity synthetic metapelites, complicating mineral identification. Recent developments in SEM technology permit, very high quality sample polishing by argon milling [e.g. *Loucks et al.*, 2009] or focus-ion-beam (FIB) [e.g. *Desbois et al.*, 2009; *Heath et al.*, 2011]. Applying one of these polishing techniques to the synthetic metapelites and imaging in SEM will provide a clearer view of the pore types and their development during chemical compaction. Enhanced polish will also provide better chemical information.

Finally, a quantitative description of pore throat development further enhances the understanding of chemical compaction processes. Mercury porosimetry analysis can determine the contribution of each pore throat radius to the total connected porosity. Changes in pore throat radii contribution gives insight in which pore types during compaction are closing or remaining [e.g. *Armitage et al.*, 2010]. Such information is essential for permeability modeling [e.g. *Bernabé et al.*, 1982; *Yang and Aplin*, 1998; *Dewhurst et al.*, 1999; *Zhu et al.*, 1999], which, with the future continuous use of enhanced hydrocarbon extraction technologies from shales (such as hydraulic fracturing in shale gas), is likely to become a major goal.

References

- Abel, A., and Muir, H., 1972, The Bauschinger effect and discontinuous yielding: *Philosophical Magazine*, v. 26, no. 2, p. 489-504, doi: 10.1080/14786437208227444.
- Adams, F.D., and Nicolson, J.T., 1900, An experimental investigation into the flow of marble: *Philosophical Transactions of the Royal Society of London*, v. 195, p. 363-U80.
- Almqvist, B.S.G., Hirt, A.M., Schmidt, V., and Dietrich, D., 2009, Magnetic fabrics of the Morcles Nappe complex: *Tectonophysics*, v. 466, no. 1-2, p. 89-100, doi: 10.1016/j.tecto.2008.07.014.
- Anson, G.L., and Kodama, K.P., 1987, Compaction-induced inclination shallowing of the post-depositional remanent magnetization in a synthetic sediment: *Geophysical Journal of the Royal Astronomical Society*, v. 88, no. 3, p. 673-692, doi: 10.1111/j.1365-246X.1987.tb01651.x.
- Antao, S.M., and Hassan, I., 2010, Temperature dependence of the structural parameters in the transformation of aragonite to calcite, as determined from in situ synchrotron powder X-ray-diffraction data: *The Canadian Mineralogist*, v. 48, no. 5, p. 1225-1236, doi: 10.3749/canmin.48.5.1225.
- Antao, S.M., Hassan, I., Wang, J., Lee, P.L., and Toby, B.H., 2008, State-of-the-art high-resolution powder X-ray diffraction (HRPXRD) illustrated with Rietveld structure refinement of quartz, sodalite, tremolite, and meionite: *The Canadian Mineralogist*, v. 46, no. 6, p. 1501-1509, doi: 10.3749/canmin.46.5.1501.
- Aoyagi, K., and Asakawa, T., 1980, Primary migration theory of petroleum and its application to petroleum exploration: *Organic Geochemistry*, v. 2, p. 33-43, doi: 10.1016/0146-6380(80)90018-2.
- Aoyagi, K., Kazama, T., Sekiguchi, K., and Chilingarian, G.V., 1985, Experimental compaction of Namtormillonite clay mixed with crude oil and seawater: *Chemical Geology*, v. 49, p. 385-392, doi: 10.1016/0009-2541(85)90170-6.
- Aplin, A.C., and Vasseur, G., 1998, Some new developments for modelling the geological compaction of fine-grained sediments: introduction: *Marine and Petroleum Geology*, v. 15, p. 105-108, doi: 10.1016/S0264-8172(98)00007-5.
- Aplin, A.C., Matenaar, I.F., and Van der Pluijm, B.A., 2003, Influence of mechanical compaction and chemical diagenesis on the microfabric and fluid flow properties of Gulf of Mexico mudstones: *Journal of Geochemical Exploration*, v. 78-79, p. 449-451, doi: 10.1016/S0375-6742(03)00035-9.
- Aplin, A.C., Matenaar, I.F., McCarty, D.K., and Van der Pluijm, B.A., 2006, Influence of mechanical compaction and clay mineral diagenesis on the microfabric and pore-scale properties of deep-water Gulf of Mexico mudstones: *Clays and Clay Minerals*, v. 54, p. 500-514, doi: 10.1346/CCMN.2006.0540411.
- Arason, P., and Levi, S., 1990, Compaction and inclination shallowing in deep-sea sediments from the Pacific Ocean: *Journal of Geophysical Research*, v. 95, no. B4, p. 4501-4510, doi: 10.1029/JB095iB04p04501.
- Armitage, P.J., Worden, R.H., Faulkner, D.R., Aplin, A.C., Butcher, A.R., and Iliffe, J., 2010, Diagenetic and sedimentary controls on porosity in Lower Carboniferous fine-grained lithologies, Krechba field, Algeria: A petrological study of a caprock to a carbon capture site: *Marine and Petroleum Geology*, v. 27, p. 1395-1410, doi: 10.1016/j.marpetgeo.2010.03.018.
- Athy, L.F., 1930, Density, porosity, and compaction of sedimentary rocks: *American Association of Petroleum Geologists Bulletin*, v. 14, no. 1, p. 25-35.
- Audet, D.M., and Fowler, A.C., 1992, A mathematical model for compaction in sedimentary basins: *Geophysical Journal International*, v. 110, p. 577-590, doi: 10.1111/j.1365-246X.1992.tb02093.x.
- Audet, D.M., and McConnell, J.D.C., 1992, Forward modelling of porosity and pore pressure evolution in sedimentary basins: *Basin Research*, v. 4, p. 147-162, doi: 10.1111/j.1365-2117.1992.tb00137.x.
- Austin, N., Evans, B., Herwegh, M., and Ebert, A., 2008, Strain localization in the Morcles nappe (Helvetic Alps, Switzerland): *Swiss Journal of Geosciences*, v. 101, no. 2, p. 341-360, doi: 10.1007/s00015-008-1264-2.
- Bäckström, S.P., Riekkel, C., Abel, S., Lehr, H., and Wenk, H.-R., 1996, Microtexture analysis by synchrotron-radiation X-ray diffraction of nickel-iron alloys prepared by microelectroplating: *Journal of Applied Crystallography*, v. 29, p. 118-124, doi: 10.1107/S0021889895009733.

- Baker, D.W., Chawla, K.S., and Krizek, R.J., 1993, Compaction fabrics of pelites: experimental consolidation of kaolinite and implications for analysis of strain in slate: *Journal of Structural Geology*, v. 15, no. 9/10, p. 1123-1137, doi: 10.1016/0191-8141(93)90159-8.
- Baker, P.A., Kastner, M., Byerlee, J.D., and Lockner, D.A., 1980, Pressure solution and hydrothermal recrystallization of carbonate sediments — An experimental study: *Marine Geology*, v. 38, p. 185-203, doi: 10.1016/0025-3227(80)90058-4.
- Baldwin, B., 1971, Ways of deciphering compacted sediments: *Journal of Sedimentary Petrology*, v. 41, no. 1, p. 293-301.
- Baldwin, B., and Butler, C.O., 1985, Compaction curves: *American Association of Petroleum Geologists Bulletin*, v. 69, no. 4, p. 622-626.
- Barber, D.J., Wenk, H.-R., Gomez-Barreiro, J., Rybacki, E., and Dresen, G., 2006, Basal slip and texture development in calcite: new results from torsion experiments: *Physics and Chemistry of Minerals*, v. 34, no. 2, p. 73-84, doi: 10.1007/s00269-006-0129-3.
- Barnhoorn, A., Bystricky, M., Burlini, L., and Kunze, K., 2005a, Post-deformational annealing of calcite rocks: *Tectonophysics*, v. 403, p. 167-191, doi: 10.1016/j.tecto.2005.04.008.
- Barnhoorn, A., Bystricky, M., Burlini, L., and Kunze, K., 2004, The role of recrystallisation on the deformation behaviour of calcite rocks: large strain torsion experiments on Carrara marble: *Journal of Structural Geology*, v. 26, p. 885-903, doi: 10.1016/j.jsg.2003.11.024.
- Barnhoorn, A., Bystricky, M., Kunze, K., Burlini, L., and Burg, J.-P., 2005b, Strain localisation in bimineralic rocks: Experimental deformation of synthetic calcite–anhydrite aggregates: *Earth and Planetary Science Letters*, v. 240, no. 3, p. 748-763, doi: 10.1016/j.epsl.2005.09.014.
- Barnhoorn, A., Bystricky, M., Kunze, K., Burlini, L., and Burg, J.-P., 2005, Strain localisation in bimineralic rocks: Experimental deformation of synthetic calcite–anhydrite aggregates: *Earth and Planetary Science Letters*, v. 240, no. 3-4, p. 748-763, doi: 10.1016/j.epsl.2005.09.014.
- Bate, P.S., and Wilson, D.V., 1986, Analysis of the Bauschinger effect: *Acta Metallurgica*, v. 34, no. 6, p. 1097-1105, doi: 10.1016/0001-6160(86)90220-8.
- Bathurst, R.G.C., 1971, *Carbonate sediments and their diagenesis*: Elsevier Science Publishers, Amsterdam, the Netherlands.
- Baud, P., Klein, E., and Wong, T.-fong, 2004, Compaction localization in porous sandstones: spatial evolution of damage and acoustic emission activity: *Journal of Structural Geology*, v. 26, p. 603-624, doi: 10.1016/j.jsg.2003.09.002.
- Baud, P., Schubnel, A., and Wong, T.-fong, 2000, Dilatancy, compaction, and failure mode in Solnhofen limestone: *Journal of Geophysical Research*, v. 105, p. 19289-19303, doi: 10.1029/2000JB900133.
- Bauschinger, J., 1881, Changes of the elastic limit and the modulus of elasticity on various metals: *Zivilingenieur*, v. 21, p. 289-348.
- Beaumont, C., Quinlan, G., and Hamilton, J., 1988, Orogeny and stratigraphy: Numerical models of the Paleozoic in the eastern interior of North America: *Tectonics*, v. 7, no. 3, p. 389-416, doi: 10.1029/TC007i003p00389.
- Behrens, H., Romano, C., Nowak, M., Holtz, F., and Dingwell, D.B., 1996, Near-infrared spectroscopic determination of water species in glasses of the system MAlSi_3O_8 (M = Li, Na, K) : an interlaboratory study: *Chemical Geology*, v. 128, no. 1-4, p. 41-63, doi: 10.1016/0009-2541(95)00162-X.
- Bergmüller, F., Barlocher, C., Geyer, B., Grieder, M., Heller, F., and Zweifel, P., 1994, A torque magnetometer for measurements of the high-field anisotropy of rocks and crystals: *Measurement Science and Technology*, v. 5, no. 12, p. 1466-1470, doi: 10.1088/0957-0233/5/12/007.
- Berman, R.G., 1991, Thermobarometry using multi-equilibrium calculations: A new technique, with petrological applications: *Canadian Mineralogist*, v. 29, no. 4, p. 833-855.
- Berman, R.G., 2007, winTWQ version 2.3): a software package for performing internally-consistent thermobarometric calculations: Geological Survey of Canada, Ottawa, Canada.

- Bernabé, Y., Brace, W.F., and Evans, B., 1982, Permeability, porosity and pore geometry of hot-pressed calcite: *Mechanics of Materials*, v. 1, p. 173-183, doi: 10.1016/0167-6636(82)90010-2.
- Bestmann, M., Kunze, K., and Matthews, A., 2000, Evolution of a calcite marble shear zone complex on Thassos Island, Greece: microstructural and textural fabrics and their kinematic significance: *Journal of Structural Geology*, v. 22, p. 1789-1807, doi: 10.1016/S0191-8141(00)00112-7.
- Bésuelle, P., Baud, Patrick, and Wong, T.-F., 2003, Failure mode and spatial distribution of damage in Rothbach sandstone in the brittle-ductile transition: *Pure and Applied Geophysics*, v. 160, p. 851-868, doi: 10.1007/PL00012569.
- Bethke, C.M., 1985, A numerical model of compaction-driven groundwater flow and heat transfer and its application to the paleohydrology of intracratonic sedimentary basins: *Journal of Geophysical Research*, v. 90, no. B8, p. 6817-6828, doi: 10.1029/JB090iB08p06817.
- Biot, M.A., 1941, General Theory of Three-Dimensional Consolidation: *Journal of Applied Physics*, v. 12, p. 155, doi: 10.1063/1.1712886.
- Bish, D.L., and Von Dreele, R.B., 1989, Rietveld refinement of non-hydrogen atomic positions in kaolinite: *Clays and Clay Minerals*, v. 37, no. 4, p. 289-296, doi: 10.1346/CCMN.1989.0370401.
- Bjørlykke, K., 1988, Sandstone diagenesis in relation to preservation, destruction and creation of porosity, *in* Chilingarian, G.V. and Wolf, K.H. eds., *Diagenesis I, Developments in sedimentology 41*, Elsevier Science Publishers, Amsterdam, the Netherlands, p. 555-588.
- Bjørlykke, K., and Høeg, K., 1997, Effects of burial diagenesis on stresses, compaction and fluid flow in sedimentary basins: *Marine and Petroleum Geology*, v. 14, no. 3, p. 267-276, doi: 10.1016/S0264-8172(96)00051-7.
- Blackwelder, E., 1920, The origin of the central Kansas oil domes: *American Association of Petroleum Geologists Bulletin*, v. 4, no. 10, p. 39-94.
- Blow, R.A., and Hamilton, N., 1978, Effect of compaction on the acquisition of a detrital remanent magnetization in fine-grained sediments: *Geophysical Journal of the Royal Astronomical Society*, v. 52, no. 1, p. 13-23, doi: 10.1111/j.1365-246X.1978.tb04219.x.
- Bohlen, S.R., Peacor, D.R., and Essene, E.J., 1980, Crystal chemistry of a metamorphic biotite and its significance in water barometry: *American Mineralogist*, v. 65, no. 1-2, p. 55-62.
- Boles, J.R., and Franks, S.G., 1979, Clay diagenesis in Wilcox sandstones of southwest Texas: Implications of smectite diagenesis on sandstone cementation: *Journal of Sedimentary Petrology*, v. 49, no. 1, p. 55-70, doi: 10.1306/212F76BC-2B24-11D7-8648000102C1865D.
- Bons, P.D., and Urai, J.L., 1996, An apparatus to experimentally model the dynamics of ductile shear zones: *Tectonophysics*, v. 256, p. 145-164, doi: 10.1016/0040-1951(95)00161-1.
- Borradaile, G.J., and Henry, B., 1997, Tectonic applications of magnetic susceptibility and its anisotropy: *Earth-Science Reviews*, v. 42, no. 1-2, p. 49-93, doi: 10.1016/S0012-8252(96)00044-X.
- Bos, B., Peach, C.J., and Spiers, C.J., 2000, Frictional-viscous flow of simulated fault gouge caused by the combined effects of phyllosilicates and pressure solution: *Tectonophysics*, v. 327, p. 173-194, doi: 10.1016/S0040-1951(00)00168-2.
- Bowles, F.A., Bryant, W.R., and Wallin, C., 1969, Microstructure of unconsolidated and consolidated marine sediments: *Journal of Sedimentary Petrology*, v. 39, no. 4, p. 1546-1551, doi: 10.1306/74D71E7E-2B21-11D7-8648000102C1865D.
- Brace, W.F., 1978, Volume changes during fracture and frictional sliding: A review: *Pure and Applied Geophysics*, v. 116, no. 4-5, p. 603-614, doi: 10.1007/BF00876527.
- Bradley, D.C., and Kidd, W.S.F., 1991, Flexural extension of the upper continental crust in collisional foredeeps: *Geological Society of America Bulletin*, v. 103, no. 11, p. 1416-1438, doi: 10.1130/0016-7606(1991)103<1416:FEOTUC>2.3.CO;2.
- Brett, C.E., and Baird, G.C., 2002, Revised stratigraphy of the Trenton Group in its type area, central New York State: sedimentology and tectonics of a Middle Ordovician shelf-to-basin succession: *Physics and Chemistry of the Earth*, v. 27, p. 231-263, doi: 10.1016/S1474-7065(01)00007-9.

- Brett, C.E., Goodman, W.M., and LoDuca, S.T., 1990, Sequences, cycles, and basin dynamics in the Silurian of the Appalachian Foreland Basin: *Sedimentary Geology*, v. 69, no. 3-4, p. 191-244, doi: 10.1016/0037-0738(90)90051-T.
- Brett, C.E., Tepper, D.H., Goodman, W.M., LoDuca, S.T., and Eckert, B.-Y., 1995, Revised stratigraphy and correlations of the Niagaran Provincial Series (Medina, Clinton, and Lockport Groups) in the type area of western New York: *U.S. Geological Survey Bulletin*, v. 2086, p. 66.
- Brogly, P.J., Martini, I.P., and Middleton, G.V., 1998, The Queenston Formation: shale-dominated, mixed terrigenous-carbonate deposits of Upper Ordovician, semiarid, muddy shores in Ontario, Canada: *Canadian Journal of Earth Sciences*, v. 35, no. 6, p. 702-719, doi: 10.1139/cjes-35-6-702.
- Bunge, H.J., 1983, *Texture Analysis in Material Science*: Butterworth-Heinemann, London, United Kingdom.
- Burland, J.B., 1990, On the compressibility and shear strength of natural clays: *Géotechnique*, v. 40, no. 3, p. 329-378.
- Burst, J.F., 1969, Diagenesis of Gulf Coast clayey sediments and its possible relation to petroleum migration: *American Association of Petroleum Geologists Bulletin*, v. 53, no. 1, p. 73-93.
- Buxton, T.M., and Sibley, D.F., 1981, Pressure solution features in a shallow buried limestone: *Journal of Sedimentary Petrology*, v. 51, no. 1, p. 19-26.
- Bystricky, M., Heidelbach, F., and Mackwell, S., 2006, Large-strain deformation and strain partitioning in polyphase rocks: Dislocation creep of olivine–magnesiowüstite aggregates: *Tectonophysics*, v. 427, p. 115-132, doi: 10.1016/j.tecto.2006.05.025.
- Cameron, E.M., and Garrels, R.M., 1980, Geochemical compositions of some Precambrian shales from the Canadian Shield: *Chemical Geology*, v. 28, p. 181-197, doi: 10.1016/0009-2541(80)90046-7.
- de Capitani, C., and Brown, T.H., 1987, The computation of chemical equilibrium in complex systems containing non-ideal solutions: *Geochimica et Cosmochimica Acta*, v. 51, no. 10, p. 2639-2652, doi: 10.1016/0016-7037(87)90145-1.
- de Capitani, C., and Petrakakis, K., 2010, The computation of equilibrium assemblage diagrams with Theriak/Domino software: *American Mineralogist*, v. 95, no. 7, p. 1006-1016, doi: 10.2138/am.2010.3354.
- Carter, N.L., and Tsenn, M.C., 1987, Flow properties of continental lithosphere: *Tectonophysics*, v. 136, p. 27-63, doi: 10.1016/0040-1951(87)90333-7.
- Casagrande, A., 1932b, Research on the Atterberg limits of soils: *Public Roads*, v. 13, p. 121-136.
- Casagrande, A., 1932a, The structure of clay and its importance in foundation engineering: *Journal of the Boston Society of Civil Engineers*, v. 19, p. 168.
- Casey, M., Kunze, K., and Olgaard, D.L., 1998, Texture of Solnhofen limestone deformed to high strains in torsion: *Journal of Structural Geology*, v. 20, p. 255-267, doi: 10.1016/S0191-8141(97)00058-8.
- Chadwick, G.H., 1918, Stratigraphy of the New York Clinton: *Geological Society of America Bulletin*, v. 29, p. 327-368.
- Charpentier, D., Worden, R.H., Dillon, C.G., and Aplin, A.C., 2003, Fabric development and the smectite to illite transition in Gulf of Mexico mudstones: an image analysis approach: *Journal of Geochemical Exploration*, v. 78-79, p. 459-463, doi: 10.1016/S0375-6742(03)00073-6.
- Chilingar, G.V., 1961, Notes on compaction: *Journal of Alberta Society of Petroleum Geologists*, v. 9, p. 158-161.
- Chilingar, G.V., and Knight, L., 1960, Relationship between pressure and moisture content of kaolinite, illite, and montmorillonite clays: *American Association of Petroleum Geologists Bulletin*, v. 44, no. 1, p. 101-106.
- Chilingar, G.V., Rieke III, H.H., Sawabini, S.T., and Ershaghi, I., 1969, Chemistry of interstitial solutions in shales versus that in associated sandstones, *in* *Society of Petroleum Engineers*.
- Chilingar, G.V., Rieke, H.H., and Robertson, J.O., 1963, Relationship between high overburden pressures and moisture content of halloysite and dickite clays: *Geological Society of America Bulletin*, v. 74, p. 1041-1048, doi: 10.1130/0016-7606(1963)74[1041:RBHOPA]2.0.CO;2.
- Chilingarian, G.V., and Rieke III, H.H., 1968, Data on consolidation of fine-grained sediments: *Journal of Sedimentary Petrology*, v. 38, no. 3, p. 811-816, doi: 10.1306/74D71A7D-2B21-11D7-8648000102C1865D.

- Chilingarian, G.V., Sawabini, C.T., and Rieke III, H.H., 1973, Effect of compaction on chemistry of solutions expelled from montmorillonite clay saturated in sea water: *Sedimentology*, v. 20, p. 391-398, doi: 10.1111/j.1365-3091.1973.tb01617.x.
- Chopra, P.N., 1997, High-temperature transient creep in olivine rocks: *Tectonophysics*, v. 279, p. 93-111, doi: 10.1016/S0040-1951(97)00134-0.
- Chopra, P.N., and Paterson, M.S., 1981, The experimental deformation of dunite: *Tectonophysics*, v. 78, p. 453-473, doi: 10.1016/0040-1951(81)90024-X.
- Clarke, F.W., 1924, *The data of geochemistry*: Government Printing Office, Washington, D.C.
- Connolly, J.A.D., 1990, Multivariable phase-diagrams: An algorithm based on generalized thermodynamics: *American Journal of Science*, v. 290, no. 6, p. 666-718.
- Connolly, J.A.D., 2009, The geodynamic equation of state: What and how: *Geochemistry Geophysics Geosystems*, v. 10, no. 10, doi: 10.1029/2009GC002540.
- Cotter, E., 1988, Hierarchy of sea-level cycles in the medial Silurian siliciclastic succession of Pennsylvania: *Geology*, v. 16, no. 3, p. 242-245, doi: 10.1130/0091-7613(1988)016<0242:HOSLCL>2.3.CO;2.
- Coussy, O., 1991, *Mécanique des milieux poreux*: Technip, Paris.
- Covey-Crump, S.J., 1998, Evolution of mechanical state in Carrara marble during deformation at 400° to 700°C: *Journal of Geophysical Research*, v. 103, p. 29781-29794, doi: 10.1029/1998JB900005.
- Covey-Crump, S.J., 1994, The application of Hart's state variable description of inelastic deformation to Carrara marble at T < 450°C: *Journal of Geophysical Research*, v. 99, p. 19793-19808, doi: 10.1029/94JB01797.
- Covey-Crump, S.J., 1997, The normal grain growth behaviour of nominally pure calcitic aggregates: *Contributions to Mineralogy and Petrology*, v. 129, p. 239-254, doi: 10.1007/s004100050335.
- Crawford, B.R., Faulkner, D.R., and Rutter, E.H., 2008, Strength, porosity, and permeability development during hydrostatic and shear loading of synthetic quartz-clay fault gouge: *Journal of Geophysical Research*, v. 113, doi:10.1029/2006JB004634.
- Croizé, D., Bjørlykke, K., Jahren, J., and Renard, F., 2010, Experimental mechanical and chemical compaction of carbonate sand: *Journal of Geophysical Research*, v. 115, doi: 10.1029/2010JB007697.
- Curran, J.H., and Carroll, M.M., 1979, Shear Stress Enhancement of Void Compaction: *Journal of Geophysical Research*, v. 84, p. 1105-1112, doi: 10.1029/JB084iB03p01105.
- De Bresser, J.H.P., 2002, On the mechanism of dislocation creep of calcite at high temperature: Inferences from experimentally measured pressure sensitivity and strain rate sensitivity of flow stress: *Journal of Geophysical Research*, v. 107, doi: 10.1029/2002JB001812.
- De Bresser, J.H.P., and Spiers, C.J., 1993, Slip systems in calcite single crystals deformed at 300–800°C: *Journal of Geophysical Research*, v. 98, p. 6397-6409, doi: 10.1029/92JB02044.
- De Bresser, J.H.P., and Spiers, C.J., 1997, Strength characteristics of the r, f, and c slip systems in calcite: *Tectonophysics*, v. 272, p. 1-23, doi: 10.1016/S0040-1951(96)00273-9.
- De Bresser, J.H.P., Ter Heege, J., and Spiers, C.J., 2001, Grain size reduction by dynamic recrystallization: can it result in major rheological weakening?: *International Journal of Earth Sciences*, v. 90, no. 1, p. 28-45, doi: 10.1007/s005310000149.
- De Bresser, J.H.P., Urai, J.L., and Olgaard, D.L., 2005, Effect of water on the strength and microstructure of Carrara marble axially compressed at high temperature: *Journal of Structural Geology*, v. 27, no. 2, p. 265-281, doi: 10.1016/j.jsg.2004.10.002.
- David, C., Wong, T.-F., Zhu, W., and Zhang, J., 1994, Laboratory measurement of compaction-induced permeability change in porous rocks: Implications for the generation and maintenance of pore pressure excess in the crust: *Pure and Applied Geophysics PAGEOPH*, v. 143, p. 425-456, doi: 10.1007/BF00874337.
- Day-Stirrat, R.J., Aplin, A.C., Środoń, J., and Van der Pluijm, B.A., 2008, Diagenetic reorientation of phyllosilicate minerals in Paleogene mudstones of the Podhale Basin, Southern Poland: *Clays and Clay Minerals*, v. 56, no. 1, p. 100-111, doi: 10.1346/CCMN.2008.0560109.

- Day-Stirrat, R.J., Milliken, K.L., Dutton, S.P., Loucks, R.G., Hillier, S., Aplin, A.C., and Schleicher, A.M., 2010, Open-system chemical behavior in deep Wilcox Group mudstones, Texas Gulf Coast, USA: *Marine and Petroleum Geology*, v. 27, no. 9, p. 1804-1818, doi: 10.1016/j.marpetgeo.2010.08.006.
- Day-Stirrat, R.J., Schleicher, A.M., Schneider, J., Flemings, P.B., Germaine, J.T., and van der Pluijm, B.A., 2011, Preferred orientation of phyllosilicates: effects of composition and stress on resedimented mudstone microfabrics: *Journal of Structural Geology*, v. 33, p. 1347-1358, doi: 10.1016/j.jsg.2011.06.007.
- Deamer, G.A., and Kodama, K.P., 1990, Compaction-induced inclination shallowing in synthetic and natural clay-rich sediments: *Journal of Geophysical Research*, v. 95, no. B4, p. 4511-4529, doi: 10.1029/JB095iB04p04511.
- Delle Piane, C., and Burlini, L., 2008, Influence of strain history on the mechanical and micro-fabric evolution of calcite rocks: insights from torsion experiments: *Swiss Journal of Geosciences*, v. 101, no. 2, p. 361-375, doi: 10.1007/s00015-008-1257-1.
- Delle Piane, C., Burlini, L., and Kunze, K., 2009, The influence of dolomite on the plastic flow of calcite: rheological, microstructural and chemical evolution during large strain torsion experiments: *Tectonophysics*, v. 467, p. 145-166, doi: 10.1016/j.tecto.2008.12.022.
- Delle Piane, C., Wilson, C.J.L., and Burlini, L., 2009, Dilatant plasticity in high-strain experiments on calcite–muscovite aggregates: *Journal of Structural Geology*, v. 31, p. 1084-1099, doi: 10.1016/j.jsg.2009.03.005.
- Desbois, G., Urai, J.L., and Kukla, P.A., 2009, Morphology of the pore space in claystones – evidence from BIB/FIB ion beam sectioning and cryo-SEM observations: *eEarth*, v. 4, no. 1, p. 15-22, doi: 10.5194/ee-4-15-2009.
- Dewhurst, D.N., Aplin, A.C., and Sarda, J.-P., 1999, Influence of clay fraction on pore-scale properties and hydraulic conductivity of experimentally compacted mudstones: *Journal of Geophysical Research*, v. 104, p. 29261-29274, doi: 10.1029/1999JB900276.
- Dewhurst, D.N., Aplin, A.C., Sarda, J.-P., and Yang, Y., 1998, Compaction-driven evolution of porosity and permeability in natural mudstones: An experimental study: *Journal of Geophysical Research*, v. 103, p. 651-661, doi: 10.1029/97JB02540.
- Dickey, P.A., 1975, Possible primary migration of oil from source rock in oil phase: *American Association of Petroleum Geologists Bulletin*, v. 59, no. 2, p. 337-345.
- Dickinson, G., 1953, Geological aspects of abnormal reservoir pressures in the Gulf Coast Louisiana: *American Association of Petroleum Geologists Bulletin*, v. 37, no. 2, p. 410-432.
- Djéran-Maigre, I., Tessier, D., Grunberger, D., Velde, B., and Vasseur, G., 1998, Evolution of microstructures and of macroscopic properties of some clays during experimental compaction: *Marine and Petroleum Geology*, v. 15, p. 109-128, doi: 10.1016/S0264-8172(97)00062-7.
- Drits, V.A., Zviagina, B.B., McCarty, D.K., and Salyn, A.L., 2010, Factors responsible for crystal-chemical variations in the solid solutions from illite to aluminoceladonite and from glauconite to celadonite: *American Mineralogist*, v. 95, no. 2-3, p. 348-361, doi: 10.2138/am.2010.3300.
- Dunlop, D.J., and Özdemir, Ö., 1997, *Rock Magnetism: Fundamentals and frontiers*: Cambridge University Press, Cambridge, United Kingdom.
- Dunnington, H.V., 1954, Stylolite development post-dates rock induration: *Journal of Sedimentary Petrology*, v. 24, no. 1, p. 27-49, doi: 10.1306/D4269648-2B26-11D7-8648000102C1865D.
- Durmishyan, A.G., 1974, Compaction of argillaceous rocks: *International Geology Review*, v. 16, no. 6, p. 650-653.
- Earnest, C.M., 1991, Thermal analysis of selected illite and smectite clay minerals. Part I. Illite clay specimens, *in* Smykatz-Kloss, W. and Warne, S.S.J. eds., *Thermal Analysis in the Geosciences*, Springer-Verlag, Berlin/Heidelberg, p. 270-286.
- Eberl, D.D., 1993, Three zones for illite formation during burial diagenesis and metamorphism: *Clays and Clay Minerals*, v. 41, no. 1, p. 26-37, doi: 10.1346/CCMN.1993.0410103.
- Ehrenberg, S.N., 2006, Porosity destruction in carbonate platforms: *Journal of Petroleum Geology*, v. 29, p. 41-52, doi: 10.1111/j.1747-5457.2006.00041.x.

- El Bied, A., Sulem, J., and Martineau, F., 2002, Microstructure of shear zones in Fontainebleau sandstone: *International Journal of Rock Mechanics and Mining Sciences*, v. 39, p. 917-932, doi: 10.1016/S1365-1609(02)00068-0.
- Engelder, T., 1979, The nature of deformation within the outer limits of the central appalachian foreland fold and thrust belt in New York state: *Tectonophysics*, v. 55, no. 3-4, p. 289-310, doi: 10.1016/0040-1951(79)90181-1.
- von Engelhardt, W., and Gaida, K.H., 1963, Concentration changes of pore solutions during the compaction of clay sediments: *Journal of Sedimentary Petrology*, v. 33, no. 4, p. 919-930.
- England, W.A., Mackenzie, A.S., Mann, D.M., and Quigley, T.M., 1987, The movement and entrapment of petroleum fluids in the subsurface: *Journal of the Geological Society, London*, v. 144, p. 327-347, doi: 10.1144/gsjgs.144.2.0327.
- Ettensohn, F.R., 1991, Flexural interpretation of relationships between Ordovician tectonism and stratigraphic sequences, central and southern Appalachians, U.S.A., *in* Barnes, C.R. and Williams, S.H. eds., *Advances in Ordovician geology, Energy, Mines, and Resources Canada*, Ottawa, Canada, p. 213-224.
- Ettensohn, F.R., 2008, The Appalachian Foreland Basin in Eastern United States, *in* Miall, A. ed., *Sedimentary Basins of the United States and Canada, Sedimentary Basins of the World*, Elsevier, Amsterdam, the Netherlands, p. 105-179.
- Evans, B., and Kohlstedt, D., 1995, Rheology of rock, *in* Ahrends, T.J. ed., *Rock Physics and Phase Relations: A Handbook of Physical Constants*, AGU Reference Shelf 3, AGU, Washington, D.C., p. 148-165.
- Fail, R.T., 1997, A geological history of the north-central Appalachians, Part 2: The Appalachian basin from the Silurian through the Carboniferous: *American Journal of Science*, v. 297, no. 7, p. 729-761.
- Fawad, M., Mondol, N.H., Jahren, J., and Bjørlykke, K., 2010, Microfabric and rock properties of experimentally compressed silt-clay mixtures: *Marine and Petroleum Geology*, v. 27, p. 1698-1712, doi: 10.1016/j.marpetgeo.2009.10.002.
- Ferrill, D.A., 1998, Critical re-evaluation of differential stress estimates from calcite twins in coarse-grained limestone: *Tectonophysics*, v. 285, p. 77-86, doi: 10.1016/S0040-1951(97)00190-X.
- Fichter, L.S., and Diecchio, R.J., 1986, Stratigraphic model for timing the opening of the Proto-Atlantic Ocean in northern Virginia: *Geology*, v. 14, no. 4, p. 307-309, doi: 10.1130/0091-7613(1986)14<307:SMFTTO>2.0.CO;2.
- Fischer, G.J., and Paterson, M.S., 1989, Dilatancy during rock deformation at high temperatures and pressures: *Journal of Geophysical Research*, v. 94, p. 17607-17618, doi: 10.1029/JB094iB12p17607.
- Fowler, S.R., White, R.S., and Loudon, K.E., 1985, Sediment dewatering in the Makran accretionary prism: *Earth and Planetary Science Letters*, v. 75, no. 4, p. 427-438, doi: 10.1016/0012-821X(85)90186-4.
- Fraser, H.J., 1935, Experimental Study of the porosity and permeability of clastic sediments: *The Journal of Geology*, v. 43, no. 8, p. 910-1010, doi: 10.1086/624388.
- Fredrich, J.T., Evans, B., and Paterson, T.-F., 1989, Micromechanics of the brittle to plastic transition in Carrara marble: *Journal of Geophysical Research*, v. 94, p. 4129-4145, doi: 10.1029/JB094iB04p04129.
- Frey, M., and Robinson, D., 1998, *Low-Grade Metamorphism*: Blackwell Science Ltd., Oxford, United Kingdom.
- Friedman, G.M., 1987, Vertical movements of the crust: Case histories from the northern Appalachian Basin: *Geology*, v. 15, no. 12, p. 1130-1133, doi: 10.1130/0091-7613(1987)15<1130:VMOTCC>2.0.CO;2.
- Frost, H.J., and Ashby, M.F., 1982, *Deformation-Mechanism Maps: The Plasticity and Creep of Metals and Ceramics*: Pergamon Press, Oxford, United Kingdom.
- Fruth Jr., L.S., Orme, G.R., and Donath, F.A., 1966, Experimental compaction effects in carbonate sediments: *Journal of Sedimentary Petrology*, v. 36, no. 3, p. 747-754, doi: 10.1306/74D7155F-2B21-11D7-8648000102C1865D.
- González-Casado, J.M., Jiménez-Berrocó, Á., García-Cuevas, C., and Elorza, J., 2003, Strain determinations using inoceramid shells as strain markers: a comparison of the calcite strain gauge technique and the Fry method: *Journal of Structural Geology*, v. 25, p. 1773-1778, doi: 10.1016/S0191-8141(03)00040-3.
- Goulet, N.R., 1998, Relationships between porosity and effective stress in shales: *First Break*, v. 16, no. 12, p. 413-419.

- Gray, M.B., and Zeitler, P.K., 1997, Comparison of clastic wedge provenance in the Appalachian foreland using U/Pb ages of detrital zircons: *Tectonics*, v. 16, no. 1, p. 151-160, doi: 10.1029/96TC02911.
- Griggs, D., 1936, Deformation of rocks under high confining pressures: I. Experiments at room temperature: *The Journal of Geology*, v. 44, no. 5, p. 541-577.
- Griggs, D., and Miller, W.B., 1951, Deformation of Yule marble: part I – compression and extension experiments on dry Yule marble at 10,000 atmospheres confining pressure, room temperature: *Geological Society of America Bulletin*, v. 62, p. 853-862, doi: 10.1130/0016-7606(1951)62[853:DOYMPI]2.0.CO;2.
- Gromet, L.P., Dymek, R.F., Haskin, L.A., and Korotev, R.L., 1984, The “North American shale composite”: Its compilation, major and trace element characteristics: *Geochimica et Cosmochimica Acta*, v. 48, no. 12, p. 2469-2482, doi: 10.1016/0016-7037(84)90298-9.
- Groshong, R.H., 1975, “Slip” cleavage caused by pressure solution in a buckle fold: *Geology*, v. 3, no. 7, p. 411-413, doi: 10.1130/0091-7613(1975)3<411:SCCBPS>2.0.CO;2.
- Groshong, R.H., Teufel, L.W., and Gasteiger, C., 1984, Precision and accuracy of the calcite strain-gage technique: *Geological Society of America Bulletin*, v. 95, no. 3, p. 357-363, doi: 10.1130/0016-7606(1984)95<357:PAAOTC>2.0.CO;2.
- Ham, H.H., 1966, New charts help estimate formation pressures: *Oil and Gas Journal*, v. 65, no. 51, p. 58-63.
- Hansen, S., 1996, A compaction trend for Cretaceous and Tertiary shales on the Norwegian shelf based on sonic transit times: *Petroleum Geoscience*, v. 2, no. 2, p. 159-166, doi: 10.1144/petgeo.2.2.159.
- Hantschel, T., and Kauerauf, A.I., 2009, *Fundamentals of Basin and Petroleum Systems Modeling*: Springer-Verlag, Berlin Heidelberg.
- Harrison, R.J., and Feinberg, J.M., 2008, FORCinel: An improved algorithm for calculating first-order reversal curve distributions using locally weighted regression smoothing: *Geochemistry Geophysics Geosystems*, v. 9, no. 5, doi: 10.1029/2008GC001987.
- Hart, B.S., Flemings, P.B., and Deshpande, A., 1995, Porosity and pressure: Role of compaction disequilibrium in the development of geopressures in a Gulf Coast Pleistocene basin: *Geology*, v. 23, p. 45, doi: 10.1130/0091-7613(1995)023<0045:PAPROC>2.3.CO;2.
- Hasegawa, T., Yakou, T., and Kocks, U., 1986, Forward and reverse rearrangements of dislocations in tangled walls: *Materials Science and Engineering*, v. 81, p. 189-199, doi: 10.1016/0025-5416(86)90262-4.
- Heard, H.C., 1963, Effects of large changes in strain rate in the experimental deformation of Yule marble: *The Journal of Geology*, v. 71, no. 2, p. 162-195.
- Heard, H.C., and Raleigh, C.B., 1972, Steady-state flow in marble at 500° to 800°C: *Geological Society of America Bulletin*, v. 83, no. 4, p. 935, doi: 10.1130/0016-7606(1972)83[935:SFIMAT]2.0.CO;2.
- Heath, J.E., Dewers, T.A., McPherson, B.J.O.L., Petrusak, R., Chidsey, T.C., Rinehart, A.J., and Mozley, P.S., 2011, Pore networks in continental and marine mudstones: Characteristics and controls on sealing behavior: *Geosphere*, v. 7, no. 2, p. 429-454, doi: 10.1130/GES00619.1.
- Hedberg, H.D., 1936, Gravitational compaction of clays and shales: *American Journal of Science*, v. 31, no. 184, p. 241-287.
- Hedberg, H.D., 1926, The effect of gravitational compaction on the structure of sedimentary rocks: *American Association of Petroleum Geologists Bulletin*, v. 10, no. 10, p. 1035-1072.
- Hedberg, H.D., 1927, The effect of gravitational compaction on the structure of sedimentary rocks: a reply to a discussion by W. W. Rubey: *American Association of Petroleum Geologists Bulletin*, v. 11, p. 875-886.
- Heidelbach, F., Riekkel, C., and Wenk, H.-R., 1999, Quantitative texture analysis of small domains with synchrotron radiation X-rays: *Journal of Applied Crystallography*, v. 32, p. 841-849, doi: 10.1107/S0021889899004999.
- Herwegh, M., and Kunze, K., 2002, The influence of nano-scale second-phase particles on deformation of fine grained calcite mylonites: *Journal of Structural Geology*, v. 24, no. 9, p. 1463-1478, doi: 10.1016/S0191-8141(01)00144-4.

- Hirt, A.M., Evans, K.F., and Engelder, T., 1995, Correlation between magnetic anisotropy and fabric for Devonian shales on the Appalachian Plateau: *Tectonophysics*, v. 247, no. 1-4, p. 121-132, doi: 10.1016/0040-1951(94)00176-A.
- Ho, N.-C., Peacor, D.R., and Van der Pluijm, B.A., 1999, Preferred orientation of phyllosilicates in Gulf Coast mudstones and relation to the smectite-illite transition: *Clays and Clay Minerals*, v. 47, no. 4, p. 495-504.
- Holland, T.J.B., and Powell, R., 1998, An internally consistent thermodynamic data set for phases of petrological interest: *Journal of Metamorphic Geology*, v. 16, no. 3, p. 309-343, doi: 10.1111/j.1525-1314.1998.00140.x.
- Holtzman, B.K., and Kohlstedt, D.L., 2007, Stress-driven melt segregation and strain partitioning in partially molten rocks: effects of stress and strain: *Journal of Petrology*, v. 48, no. 12, p. 2379-2406, doi: 10.1093/petrology/egm065.
- Hower, J., Eslinger, E.V., Hower, M.E., and Perry, E.A., 1976, Mechanism of burial metamorphism of argillaceous sediment: 1. Mineralogical and chemical evidence: *Geological Society of America Bulletin*, v. 87, no. 5, p. 725, doi: 10.1130/0016-7606(1976)87<725:MOBMOA>2.0.CO;2.
- Hrouda, F., 1993, Theoretical models of magnetic anisotropy to strain relationship revisited: *Physics of the Earth and Planetary Interiors*, v. 77, no. 3-4, p. 237-249, doi: 10.1016/0031-9201(93)90101-E.
- Hubbert, M.K., and Rubey, W.W., 1959, Role of fluid pressure in mechanics of overthrust faulting: I. Mechanics of fluid-filled porous solids and its application to overthrust faulting: *Geological Society of America Bulletin*, v. 70, no. 2, p. 115-166.
- Hughes, J., M., Cameron, M., and Crowley, K.D., 1989, Structural variations in natural F, OH, and Cl apatites: *American Mineralogist*, v. 74, no. 7-8, p. 870-876.
- Jackson, M.J., Banerjee, S.K., Marvin, J.A., Lu, R., and Gruber, W., 1991, Detrital remanence, inclination errors, and anhysteretic remanence anisotropy: quantitative model and experimental results: *Geophysical Journal International*, v. 104, no. 1, p. 95-103, doi: 10.1111/j.1365-246X.1991.tb02496.x.
- Jacobi, R.D., 1981, Peripheral bulge—a causal mechanism for the Lower/Middle Ordovician unconformity along the western margin of the Northern Appalachians: *Earth and Planetary Science Letters*, v. 56, p. 245-251, doi: 10.1016/0012-821X(81)90131-X.
- Jamison, W.R., and Spang, J.H., 1976, Use of calcite twin lamellae to infer differential stress: *Geological Society of America Bulletin*, v. 87, no. 6, p. 868-872, doi: 10.1130/0016-7606(1976)87<868:UOCTLT>2.0.CO;2.
- Jelínek, V., 1981, Characterization of the magnetic fabric of rocks: *Tectonophysics*, v. 79, no. 3-4, p. T63-T67, doi: 10.1016/0040-1951(81)90110-4.
- Jelínek, V., 1978, Statistical processing of anisotropy of magnetic susceptibility measured on groups of specimens: *Studia Geophysica et Geodaetica*, v. 22, p. 50-62, doi: 10.1007/BF01613632.
- Ji, S., Jiang, Z., Rybacki, E., Wirth, R., Prior, D., and Xia, B., 2004, Strain softening and microstructural evolution of anorthite aggregates and quartz–anorthite layered composites deformed in torsion: *Earth and Planetary Science Letters*, v. 222, no. 2, p. 377-390, doi: 10.1016/j.epsl.2004.03.021.
- Johnson, M.E., Jia-Yu, R., and Xue-Chang, Y., 1985, Intercontinental correlation by sea-level events in the Early Silurian of North America and China (Yangtze Platform): *Geological Society of America Bulletin*, v. 96, no. 11, p. 1384, doi: 10.1130/0016-7606(1985)96<1384:ICBSEI>2.0.CO;2.
- Jones, O.T., 1944, The compaction of muddy sediments: *Quarterly Journal of the Geological Society*, v. 100, p. 137-160, doi: 10.1144/GSL.JGS.1944.100.01-04.09.
- Jones, M.E., and Addis, M.A., 1986, The application of stress path and critical state analysis to sediment deformation: *Journal of Structural Geology*, v. 8, no. 5, p. 575-580, doi: 10.1016/0191-8141(86)90006-4.
- Van de Kamp, P.C., 2008, Smectite-illite-muscovite transformations, quartz dissolution, and silica release in shales: *Clays and Clay Minerals*, v. 56, no. 1, p. 66-81, doi: 10.1346/CCMN.2008.0560106.
- Karig, D.E., and Hou, G., 1992, High-stress consolidation experiments and their geologic implications: *Journal of Geophysical Research*, v. 97, p. 289-300, doi: 10.1029/91JB02247.

- Kaszuba, J.P., Janecky, D.R., and Snow, M.G., 2005, Experimental evaluation of mixed fluid reactions between supercritical carbon dioxide and NaCl brine: Relevance to the integrity of a geologic carbon repository: *Chemical Geology*, v. 217, no. 3-4, p. 277-293, doi: 10.1016/j.chemgeo.2004.12.014.
- Kim, J.-W., Bryant, W.R., Watkins, J.S., and Tieh, T.T., 1999, Electron microscopic observations of shale diagenesis, offshore Louisiana, USA, Gulf of Mexico: *Geo-Marine Letters*, v. 18, p. 234-240, doi: 10.1007/s003670050073.
- Kinnison, C.S., 1915, *A Study of the Atterberg Plasticity Method*: U.S. Government Printing Office, Washington, D.C.
- Kirby, S.H., 1983, Rheology of the lithosphere: *Reviews of Geophysics*, v. 21, no. 6, p. 1458-1487, doi: 10.1029/RG021i006p01458.
- Kittel, C., 2005, *Introduction to solid state physics*: Wiley, Hoboken NJ, United States.
- Klein, E., Baud, P., Reuschle, T., and Wong, T.-F., 2001, Mechanical behaviour and failure mode of bentheim sandstone under triaxial compression: *Physics and Chemistry of the Earth, Part A: Solid Earth and Geodesy*, v. 26, p. 21-25, doi: 10.1016/S1464-1895(01)00017-5.
- Kodama, K.P., and Sun, W.W., 1990, SEM and magnetic fabric study of a compacting sediment: *Geophysical Research Letters*, v. 17, no. 6, p. 795, doi: 10.1029/GL017i006p00795.
- Kohlstedt, D.L., Evans, B., and Mackwell, S.J., 1995, Strength of the lithosphere: constraints imposed by laboratory experiments: *Journal of Geophysical Research*, v. 100, p. 17587-17602, doi: 10.1029/95JB01460.
- Kübler, B., 1968, Evaluation quantitative du métamorphisme par la cristallinité de l'illite: *Bulletin Centre Recherche Pau-SNPA*, v. 2, p. 385-397.
- Kwon, O., Kronenberg, A.K., Gangi, A.F., Johnson, B., and Herbert, B.E., 2004, Permeability of illite-bearing shale: 1. Anisotropy and effects of clay content and loading: *Journal of Geophysical Research*, v. 109, no. B10205, doi: 10.1029/2004JB003052.
- Lambe, T.W., and Whitman, R.V., 1969, *Soil Mechanics*: Wiley, New York.
- Land, L.S., and Milliken, K.L., 2000, Regional loss of SiO₂ and CaCO₃, and gain of K₂O during burial diagenesis of Gulf Coast mudrocks, USA, *in* Worden, R.H. and Morad, S. eds., *Quartz Cementation in Sandstones*, Special Publication International Association of Sedimentologists 29, Blackwells, Oxford, United Kingdom.
- Land, L.S., Mack, L.E., Milliken, K.L., and Lynch, F.L., 1997, Burial diagenesis of argillaceous sediment, south Texas Gulf of Mexico sedimentary basin: A reexamination: *Geological Society of America Bulletin*, v. 109, no. 1, p. 2-15, doi: 10.1130/0016-7606(1997)109<0002:BDOASS>2.3.CO;2.
- Larsen, G., and Chilingar, G.V., 1983, *Diagenesis in Sediments and Sedimentary Rocks, 2*: Elsevier Science Publishers, Amsterdam, the Netherlands.
- Leder, F., and Park, W.C., 1986, Porosity reduction in sandstone by quartz overgrowth: *American Association of Petroleum Geologists Bulletin*, v. 70, no. 11, p. 1713-1728.
- Lehmann, D., Brett, C.E., Cole, R., and Baird, G., 1995, Distal sedimentation in a peripheral foreland basin: Ordovician black shales and associated flysch of the western Taconic foreland, New York State and Ontario: *Geological Society of America Bulletin*, v. 107, no. 6, p. 708-724, doi: 10.1130/0016-7606(1995)107<0708:DSIAPF>2.3.CO;2.
- Lerche, I., 1990, *Basin analysis : quantitative methods*: Academic press, San Diego ;;New York ;;Boston [etc.].
- LoDuca, S.T., and Brett, C.E., 1994, Revised stratigraphic facies relationships of the lower part of the Clinton Group (Middle Llandoveryan) of western New York State, *in* Landing, E. ed., *Studies in stratigraphy and paleontology in honor of Donald W. Fisher*, New York State Museum Bulletin, New York State Museum, Albany, New York, p. 161-182.
- Loucks, R.G., Reed, R.M., Ruppel, S.C., and Jarvie, D.M., 2009, Morphology, genesis, and distribution of nanometer-scale pores in siliceous mudstones of the Mississippian Barnett Shale: *Journal of Sedimentary Research*, v. 79, no. 12, p. 848-861, doi: 10.2110/jsr.2009.092.
- Lu, R., Banerjee, S.K., and Marvin, J.A., 1990, Effects of clay mineralogy and the electrical conductivity of water on the acquisition of depositional remanent magnetization in sediments: *Journal of Geophysical Research*, v. 95, no. B4, p. 4531-4538, doi: 10.1029/JB095iB04p04531.

- Luo, X., Vasseur, G., Pouya, A., Lamoureux-Var, V., and Poliakov, A., 1998, Elastoplastic deformation of porous media applied to the modelling of compaction at basin scale: *Marine and Petroleum Geology*, v. 15, p. 145-162, doi: 10.1016/S0264-8172(97)00061-5.
- Lynch, F.L., 1997, Frio Shale Mineralogy and the Stoichiometry of the Smectite-to-Illite Reaction: The Most Important Reaction in Clastic Sedimentary Diagenesis: *Clays and Clay Minerals*, v. 45, no. 5, p. 618-631, doi: 10.1346/CCMN.1997.0450502.
- Lynch, F.L., Mack, L.E., and Land, L.S., 1997, Burial diagenesis of illite/smectite in shales and the origins of authigenic quartz and secondary porosity in sandstones: *Geochimica et Cosmochimica Acta*, v. 61, no. 10, p. 1995-2006, doi: 10.1016/S0016-7037(97)00066-5.
- Magara, K., 1968, Compaction and migration of fluids in Miocene mudstones, Nagaoka plain, Japan: *American Association of Petroleum Geologists Bulletin*, v. 52, no. 12, p. 2466-2501.
- Mariani, E., Brodie, K.H., and Rutter, E.H., 2006, Experimental deformation of muscovite shear zones at high temperatures under hydrothermal conditions and the strength of phyllosilicate-bearing faults in nature: *Journal of Structural Geology*, v. 28, no. 9, p. 1569-1587, doi: 10.1016/j.jsg.2006.06.009.
- Martín-Hernández, F., and Hirt, A.M., 2001, Separation of ferrimagnetic and paramagnetic anisotropies using a high-field torsion magnetometer: *Tectonophysics*, v. 337, no. 3-4, p. 209-221, doi: 10.1016/S0040-1951(01)00116-0.
- McAuliffe, C., 1966, Solubility in water of paraffin, cycloparaffin, olefin, acetylene, cycloolefin, and aromatic hydrocarbons: *Journal of Physical Chemistry*, v. 70, p. 1267-1275, doi: 10.1021/j100876a049.
- Meade, R.H., 1966, Factors influencing the early stages of the compaction of clays and sands: *Journal of Sedimentary Petrology*, v. 36, p. 1085-1101, doi: 10.1306/74D71604-2B21-11D7-8648000102C1865D.
- Menéndez, B., Zhu, W., and Wong, T.-F., 1996, Micromechanics of brittle faulting and cataclastic flow in Berea sandstone: *Journal of Structural Geology*, v. 18, no. 1, p. 1-16, doi: 10.1016/0191-8141(95)00076-P.
- Merriman, R.J., and Frey, M., 1998, Patterns of very low-grade metamorphism in metapelitic rocks, *in* Frey, M. and Robinson, D. eds., *Low-Grade Metamorphism*, Blackwell Science, p. 61-107.
- Merriman, R.J., and Peacor, D.R., 1998, Very Low-Grade Metapelites: Mineralogy, Microfabrics and Measuring Reaction Progress, *in* Frey, M. and Robinson, D. eds., *Low-Grade Metamorphism*, Blackwell Science Ltd., Oxford, UK, p. 10-60.
- Minshull, T., and White, R.S., 1989, Sediment compaction and fluid migration in the Makran accretionary prism: *Journal of Geophysical Research*, v. 94, p. 7387-7402, doi: 10.1029/JB094iB06p07387.
- Misra, S., Burlini, L., and Burg, J.-P., 2009, Strain localization and melt segregation in deforming metapelites: *Physics of the Earth and Planetary Interiors*, v. 177, no. 3-4, p. 173-179, doi: 10.1016/j.pepi.2009.08.011.
- Mitra, S., 1976, A quantitative study of deformation mechanisms and finite strain in quartzites: *Contributions to Mineralogy and Petrology*, v. 59, p. 203-226, doi: 10.1007/BF00371309.
- Mondol, N.H., Bjørlykke, K., Jahren, J., and Høeg, K., 2007, Experimental mechanical compaction of clay mineral aggregates—Changes in physical properties of mudstones during burial: *Marine and Petroleum Geology*, v. 24, no. 5, p. 289-311, doi: 10.1016/j.marpetgeo.2007.03.006.
- Monnett, V.E., 1922, Possible origin of some of the structures of the Mid-Continent oil field: *Economic Geology*, v. 17, p. 194-200, doi: 10.2113/gsecongeo.17.3.194.
- Moore, C.H., 2001, *Carbonate Reservoirs: Porosity Evolution and Diagenesis in a Sequence Stratigraphic Framework*: Elsevier Science Publishers, Amsterdam, the Netherlands.
- Neuzil, C.E., 1994, How permeable are clays and shales?: *Water Resources Research*, v. 30, no. 2, p. 145-150, doi: 10.1029/93WR02930.
- Nygård, R., Gutierrez, M., Gautam, R., and Høeg, K., 2004, Compaction behavior of argillaceous sediments as function of diagenesis: *Marine and Petroleum Geology*, v. 21, no. 3, p. 349-362, doi: 10.1016/j.marpetgeo.2004.01.002.
- Olgaard, D.L., 1990, The role of second phase in localizing deformation, *in* Knipe, R.J. and Rutter, E.H. eds., *Deformation Mechanisms, Rheology and Tectonics*, Special Publications 54, Geological Society, London, United Kingdom, p. 175-181.

- Olson, R.E., and Mitronovas, F., 1962, Shear strength and consolidation characteristics of calcium and magnesium illite: *Clays and Clay Minerals*, v. 9, p. 162-184.
- Ord, A., Vardoulakis, I., and Kajewski, R., 1991, Shear band formation in Gosford Sandstone: *International Journal of Rock Mechanics and Mining Sciences & Geomechanics Abstracts*, v. 28, no. 5, p. 397-409, doi: 10.1016/0148-9062(91)90078-Z.
- Park, H., Barbeau Jr., D.L., Rickenbaker, A., Bachmann-Krug, D., and Gehrels, G., 2010, Application of foreland basin detrital-zircon geochronology to the reconstruction of the southern and central Appalachian orogen: *Journal of Geology*, v. 118, no. 1, p. 23-44, doi: 10.1086/648400.
- Passchier, C.W., and Trouw, R.A.J. (Eds.), 2005, *Microtectonics*: Springer Verlag, Berlin/Heidelberg.
- Paterson, M.S., 1990, Rock deformation experimentation, *in* Duba, A.G. ed., *The Brittle-Ductile Transition in Rocks. The Heard Volume*, Geophysical Monograph, AGU, Washington, D.C., p. 187-194.
- Paterson, M.S., and Olgaard, D.L., 2000, Rock deformation tests to large shear strains in torsion: *Journal of Structural Geology*, v. 22, no. 9, p. 1341-1358, doi: 10.1016/S0191-8141(00)00042-0.
- Pavese, A., Ferraris, G., Pischedda, V., and Ibberson, R., 1999, Tetrahedral order in phengite 2M(1) upon heating, from powder neutron diffraction, and thermodynamic consequences: *European Journal of Mineralogy*, v. 11, no. 2, p. 309-320.
- Peltonen, C., Marcussen, Ø., Bjørlykke, K., and Jahren, J., 2009, Clay mineral diagenesis and quartz cementation in mudstones: The effects of smectite to illite reaction on rock properties: *Marine and Petroleum Geology*, v. 26, no. 6, p. 887-898, doi: 10.1016/j.marpetgeo.2008.01.021.
- Perry Jr., E.A., and Hower, J., 1972, Late-stage dehydration in deeply buried pelitic sediments: *Clays and Clay Minerals*, v. 56, no. 10, p. 2013-2021, doi: 10.1346/CCMN.1970.0180306.
- Pfiffner, O.A., 1982, Deformation mechanisms and flow regimes in limestones from the Helvetic zone of the Swiss Alps: *Journal of Structural Geology*, v. 4, no. 4, p. 429-442, doi: 10.1016/0191-8141(82)90034-7.
- Pieri, M., Burlini, L., Kunze, K., Stretton, I., and Olgaard, D.L., 2001, Rheological and microstructural evolution of Carrara marble with high shear strain: results from high temperature torsion experiments: *Journal of Structural Geology*, v. 23, p. 1393-1413, doi: 10.1016/S0191-8141(01)00006-2.
- Pieri, M., Kunze, K., Burlini, L., Stretton, I., Olgaard, D.L., Burg, J.-P., and Wenk, H.-R., 2001, Texture development of calcite by deformation and dynamic recrystallization at 1000K during torsion experiments of marble to large strains: *Tectonophysics*, v. 330, p. 119-140, doi: 10.1016/S0040-1951(00)00225-0.
- Pike, C.R., Roberts, A.P., and Verosub, K.L., 1999, Characterizing interactions in fine magnetic particle systems using first order reversal curves: *Journal of Applied Physics*, v. 85, no. 9, p. 6660, doi: 10.1063/1.370176.
- Poirier, J.-P., 1985, *Creep of Crystals: High-temperature Deformation Processes in Metals, Ceramics and Minerals*: Cambridge University Press, Cambridge, United Kingdom.
- Poirier, J.-P., 1980, Shear localization and shear instability in materials in the ductile field: *Journal of Structural Geology*, v. 2, p. 135-142, doi: 10.1016/0191-8141(80)90043-7.
- Pouya, A., Djéran-Maigre, I., Lamoureux-Var, V., and Grunberger, D., 1998, Mechanical behaviour of fine grained sediments: experimental compaction and three-dimensional constitutive model: *Marine and Petroleum Geology*, v. 15, p. 129-143, doi: 10.1016/S0264-8172(98)00011-7.
- Powell, R., and Holland, T.J.B., 1988, An internally consistent dataset with uncertainties and correlations: 3. Applications to geobarometry, worked examples and a computer program: *Journal of Metamorphic Geology*, v. 6, no. 2, p. 173-204, doi: 10.1111/j.1525-1314.1988.tb00415.x.
- Powell, R., Holland, T.J.B., and Worley, B., 1998, Calculating phase diagrams involving solid solutions via non-linear equations, with examples using THERMOCALC: *Journal of Metamorphic Geology*, v. 16, no. 4, p. 577-588, doi: 10.1111/j.1525-1314.1998.00157.x.
- Powers, M.C., 1967, Fluid-release mechanisms in compacting marine mudrocks and their importance in oil exploration: *American Association of Petroleum Geologists Bulletin*, v. 51, no. 7, p. 1240-1254.
- Powers, S., 1922, Reflected buried hills and their importance in petroleum geology: *Economic Geology*, v. 17, p. 233-259, doi: 10.2113/gsecongeo.17.4.233.

- Powers, S., 1920, The Sabine uplift, Louisiana: American Association of Petroleum Geologists Bulletin, v. 4, p. 117-136.
- Proshlyakov, B.K., 1960, Reservoir properties of rocks as a function of their depth and lithology: Geol. Nefti i Gaza, v. 12, p. 24-29.
- Quinlan, G.M., and Beaumont, C., 1984, Appalachian thrusting, lithospheric flexure, and the Paleozoic stratigraphy of the Eastern Interior of North America: Canadian Journal of Earth Sciences, v. 21, no. 9, p. 973-996, doi: 10.1139/e84-103.
- Ramsay, J.R., and Huber, M.I., 1984, The Techniques of Modern Structural Geology, Volume 1: Strain Analyses: Academic Press, London, United Kingdom.
- Renner, J., Evans, B., and Siddiqi, G., 2002, Dislocation creep of calcite: Journal of Geophysical Research, v. 107, doi: 10.1029/2001JB001680.
- Rieke III, H.H., and Chilingarian, G.V. (Eds.), 1974, Compaction of argillaceous sediments.: Elsevier Scientific Pub. Co., Amsterdam, the Netherlands.
- Rieke III, H.H., Chilingar, G.V., and Robertson Jr., J.O., 1964, High-pressure (up to 500,000 p.s.i.) compaction studies on various clays, *in* 15, New Delhi, p. 22-38.
- Roberts, A.P., Chang, L., Rowan, C.J., Horng, C.-S., and Florindo, F., 2011, Magnetic properties of sedimentary greigite (Fe₃S₄): An update: Reviews of Geophysics, v. 49, no. 1, doi: 10.1029/2010RG000336.
- Roberts, A.P., Liu, Q., Rowan, C.J., Chang, L., Carvallo, C., Torrent, J., and Horng, C.-S., 2006, Characterization of hematite (α -Fe₂O₃), goethite (α -FeOOH), greigite (Fe₃S₄), and pyrrhotite (Fe₇S₈) using first-order reversal curve diagrams: Journal of Geophysical Research, v. 111, doi: 10.1029/2006JB004715.
- Roberts, A.P., Pike, C.R., and Verosub, K.L., 2000, First-order reversal curve diagrams: A new tool for characterizing the magnetic properties of natural samples: Journal of Geophysical Research, v. 105, no. B12, p. 28461-28475, doi: 10.1029/2000JB900326.
- Rochette, P., 1987, Metamorphic control of the magnetic mineralogy of black shales in the Swiss Alps: toward the use of "magnetic isogrades." Earth and Planetary Science Letters, v. 84, no. 4, p. 446-456, doi: 10.1016/0012-821X(87)90009-4.
- Rogers, W.B., Isachsen, Y.W., Mock, T.D., and Nyahay, R.E., 1990, New York State Geological Highway Map: New York State Museum/Geological Survey.
- Ronov, A.B., and Migdisov, A.A., 1971, Geochemical history of the crystalline basement and the sedimentary cover of the Russian and North American platforms: Sedimentology, v. 16, no. 3-4, p. 137-185, doi: 10.1111/j.1365-3091.1971.tb00227.x.
- Rosenbaum, M.S., 1976, Effect of compaction on the pore fluid chemistry of montmorillonite: Clays and Clay Minerals, v. 24, p. 118-121.
- Ross, N., L., and Reeder, R.J., 1992, High-pressure structural study of dolomite and ankerite: American Mineralogist, v. 77, no. 3-4, p. 412-421.
- Rowe, K.J., and Rutter, E.H., 1990, Palaeostress estimation using calcite twinning: experimental calibration and application to nature: Journal of Structural Geology, v. 12, p. 1-17, doi: 10.1016/0191-8141(90)90044-Y.
- Rowley, D.B., and Kidd, W.S.F., 1981, Stratigraphic relationships and detrital composition of the medial Ordovician flysch of western New England: implications for the tectonic evolution of the Taconic orogeny: Journal of Geology, v. 89, p. 199-218.
- Rubey, W.W., 1927, The effect of gravitational compaction on the structure of sedimentary rocks: American Association of Petroleum Geologists Bulletin, v. 11, p. 621-633.
- Rubey, W.W., and Hubbert, M.K., 1959, Role of fluid pressure in mechanics of overthrust faulting: II. Overthrust belt in geosynclinal area of western Wyoming in light of fluid-pressure hypothesis: Geological Society of America Bulletin, v. 70, no. 2, p. 167-206.
- Rutter, E.H., 1995, Experimental study of the influence of stress, temperature, and strain on the dynamic recrystallization of Carrara marble: Journal of Geophysical Research, v. 100, no. B12, p. 24651-24663, doi: 10.1029/95JB02500.

- Rutter, E.H., 1999, On the relationship between the formation of shear zones and the form of the flow law for rocks undergoing dynamic recrystallization: *Tectonophysics*, v. 303, p. 147-158, doi: 10.1016/S0040-1951(98)00261-3.
- Rutter, E.H., 1974, The influence of temperature, strain rate and interstitial water in the experimental deformation of calcite rocks: *Tectonophysics*, v. 22, p. 311-334, doi: 10.1016/0040-1951(74)90089-4.
- Rutter, E.H., 1998, Use of extension testing to investigate the influence of finite strain on the rheological behaviour of marble: *Journal of Structural Geology*, v. 20, p. 243-254, doi: 10.1016/S0191-8141(97)00060-6.
- Rutter, E.H., and Rusbridge, M., 1977, The effect of non-coaxial strain paths on crystallographic preferred orientation development in the experimental deformation of a marble: *Tectonophysics*, v. 39, p. 73-86, doi: 10.1016/0040-1951(77)90089-0.
- Rybacki, E., and Dresen, G., 2006, Strength and ductile failure of homogeneously mixed and layered two-phase anorthite-diopside aggregates, in *American Geophysical Union, San Francisco, California USA*.
- Rybacki, E., Paterson, M.S., Wirth, R., and Dresen, G., 2003, Rheology of calcite-quartz aggregates deformed to large strain in torsion: *Journal of Geophysical Research*, v. 108, doi: 10.1029/2002JB001833.
- Rybacki, E., Wirth, R., and Dresen, G., 2008, High-strain creep of feldspar rocks: implications for cavitation and ductile failure in the lower crust: *Geophysical Research Letters*, v. 35, no. 4, doi: 10.1029/2007GL032478.
- Schmid, S.M., 1976, Rheological evidence for changes in the deformation mechanism of Solenhofen limestone towards low stresses: *Tectonophysics*, v. 31, p. T21-T28, doi: 10.1016/0040-1951(76)90160-8.
- Schmid, S.M., 1975, The Glarus Overthrust: field evidence and mechanical model: *Eclogae Geologicae Helvetiae*, v. 68, p. 247-280.
- Schmid, S.M., Boland, J.N., and Paterson, M.S., 1977, Superplastic flow in finegrained limestone: *Tectonophysics*, v. 43, p. 257-291, doi: 10.1016/0040-1951(77)90120-2.
- Schmid, S.M., Panozzo, R., and Bauer, S., 1987, Simple shear experiments on calcite rocks: rheology and microfabric: *Journal of Structural Geology*, v. 9, p. 747-778, doi: 10.1016/0191-8141(87)90157-X.
- Schmid, S.M., Paterson, M.S., and Boland, J.N., 1980, High temperature flow and dynamic recrystallization in carrara marble: *Tectonophysics*, v. 65, p. 245-280, doi: 10.1016/0040-1951(80)90077-3.
- Schmidt, V., Burlini, L., Hirt, A.M., and Leiss, B., 2008, Fabrication of synthetic calcite-muscovite rocks with variable texture — an analogue to cataclasite fabrics?: *Tectonophysics*, v. 449, p. 105-119, doi: 10.1016/j.tecto.2007.11.055.
- Schneider, J., Flemings, P.B., Day-Stirrat, R.J., and Germaine, J.T., 2011, Insights into pore-scale controls on mudstone permeability through resedimentation experiments: *Geology*, v. 39, no. 11, p. 1011-1014, doi: 10.1130/G32475.1.
- Schneider, F., Potdevin, J.L., Wolf, S., and Faille, I., 1996, Mechanical and chemical compaction model for sedimentary basin simulators: *Tectonophysics*, v. 263, p. 307-317, doi: 10.1016/S0040-1951(96)00027-3.
- Sclater, J.G., and Christie, P.A.F., 1980, Continental stretching: an explanation of the post-mid-Cretaceous subsidence of the central North Sea Basin: *Journal of Geophysical Research*, v. 85, p. 3711-3739, doi: 10.1029/JB085iB07p03711.
- Shaw, E.W., 1918, Anomalous Dips: *Economic Geology*, v. 13, p. 598-610.
- Shaw, E.W., and Munn, M.J., 1911, Coal, oil, and gas of the Foxburg Quadrangle, Pa.: *United States Geological Survey Bulletin*, v. 454.
- Shea, W.T., and Kronenberg, A.K., 1992, Rheology and deformation mechanisms of an isotropic mica schist: *Journal of Geophysical Research*, v. 97, no. B11, p. 15201-15237, doi: 10.1029/92JB00620.
- Shea, W.T., and Kronenberg, A.K., 1993, Strength and anisotropy of foliated rocks with varied mica contents: *Journal of Structural Geology*, v. 15, no. 9/10, p. 1097-1121, doi: 10.1016/0191-8141(93)90158-7.
- Shi, Y., and Wang, C.-Y., 1986, Pore pressure generation in sedimentary basins: overloading versus aquathermal: *Journal of Geophysical Research*, v. 91, no. B2, p. 2153-2162, doi: 10.1029/JB091iB02p02153.

- Shinn, E.A., and Robbin, D.M., 1983, Mechanical and chemical compaction in fine-grained shallow-water limestones: *Journal of Sedimentary Petrology*, v. 53, no. 2, p. 595-618, doi: 10.1306/212F8242-2B24-11D7-8648000102C1865D.
- Shinn, E.A., Halley, R.B., Hudson, J.H., and Lidz, B.H., 1977, Limestone compaction: An enigma: *Geology*, v. 5, no. 1, p. 21-24, doi: 10.1130/0091-7613(1977)5<21:LCAE>2.0.CO;2.
- Skempton, A.W., 1953, Soil mechanics in relation to geology: *Proceedings of the Yorkshire Geological Society*, v. 29, p. 33-62.
- Skempton, A.W., and Jones, O.T., 1944, Notes on the compressibility of clays: *Quarterly Journal of the Geological Society*, v. 100, p. 119-135, doi: 10.1144/GSL.JGS.1944.100.01-04.08.
- Small, J.S., 1994, Fluid Composition, mineralogy and morphological changes associated with the smectite-to-illite reaction: an experimental investigation of the effect of organic acid anions: *Clay Minerals*, v. 29, no. 4, p. 539-554, doi: 10.1180/claymin.1994.029.4.11.
- Smith, J.E., 1971, The dynamics of shale compaction and evolution of pore-fluid pressures: *Journal of the International Association for Mathematical Geology*, v. 3, no. 3, p. 239-263, doi: 10.1007/BF02045794.
- Sorby, H.C., 1908, On the application of quantitative methods to the study of the structure and history of rocks: *Quaternary Journal of the Geological Society of London*, v. 64, p. 171-232.
- Stockdale, P.B., 1943, Stylolites, primary or secondary?: *Journal of Sedimentary Petrology*, v. 13, no. 1, p. 3-12, doi: 10.1306/D4269175-2B26-11D7-8648000102C1865D.
- Stoltz, R.E., and Pelloux, R.M., 1976, The Bauschinger effect in precipitation strengthened aluminum alloys: *Metallurgical Transactions A: Physical Metallurgy and Material Sciences*, v. 7, no. 9, p. 1295-1306, doi: 10.1007/BF02658814.
- Stout, M.G., and Rollett, A.D., 1990, Large-strain Bauschinger effects in fcc metals and alloys: *Metallurgical Transactions A: Physical Metallurgy and Material Sciences*, v. 21, no. 12, p. 3201-3213, doi: 10.1007/BF02647315.
- Suetnova, E., and Vasseur, G., 2000, 1-D Modelling rock compaction in sedimentary basins using a visco-elastic rheology: *Earth and Planetary Science Letters*, v. 178, p. 373-383, doi: 10.1016/S0012-821X(00)00074-1.
- Sulem, J., and Ouffroukh, H., 2006, Shear banding in drained and undrained triaxial tests on a saturated sandstone: Porosity and permeability evolution: *International Journal of Rock Mechanics and Mining Sciences*, v. 43, p. 292-310, doi: 10.1016/j.ijrmms.2005.07.001.
- Sun, W.W., and Kodama, K.P., 1992, Magnetic anisotropy, scanning electron microscopy, and X-ray pole figure goniometry study of inclination shallowing in a compacting clay-rich sediment: *Journal of Geophysical Research*, v. 97, no. B13, p. 19599-19615, doi: 10.1029/92JB01589.
- Tarling, D.H., and Hrouda, F., 1993, *The Magnetic Anisotropy of Rocks*: Chapman & Hall, London, United Kingdom.
- Tauxe, L., 2010, *Essentials of paleomagnetism*: University of California Press, Berkeley (Ca), United States.
- Taylor, S.R., and McLennan, S.M., 1985, *The Continental Crust: Its Composition and Evolution: An Examination of the Geochemical Record Preserved in Sedimentary Rocks*: Blackwell Scientific Publications, Oxford, United Kingdom.
- Teas, L.P., 1923, Differential compacting the cause of certain Clairborne dips: *American Association of Petroleum Geologists Bulletin*, v. 9, p. 370-373.
- Ter Heege, J.H., De Bresser, J.H.P., and Spiers, C.J., 2002, The influence of dynamic recrystallization on the grain size distribution and rheological behaviour of Carrara marble deformed in axial compression, *in* De Meer, S., Drury, M.R., De Bresser, J.H.P., and Pennock, G.M. eds., *Deformation Mechanisms, Rheology and Tectonics: Current Status and Future Perspectives*, Geological Society Special Publications, Geological Society, London, United Kingdom, p. 331-353.
- Terzaghi, K., 1925, *Erdbaumechanik auf bodenphysikalischer Grundlage*: F. Deuticke, Leipzig Vienna.
- Terzaghi, K., 1927, Principles of final soil classification: *Public Roads*, v. 8, p. 41-53.
- Thyberg, B., Jahren, J., Winje, T., Bjørlykke, K., Faleide, J.I., and Marcussen, Ø., 2010, Quartz cementation in Late Cretaceous mudstones, northern North Sea: Changes in rock properties due to dissolution of smectite and

- precipitation of micro-quartz crystals: *Marine and Petroleum Geology*, v. 27, no. 8, p. 1752-1764, doi: 10.1016/j.marpetgeo.2009.07.005.
- Towe, K.M., 1962, Clay mineral diagenesis as a possible source of silica cement in sedimentary rocks: *Journal of Sedimentary Petrology*, v. 32, no. 1, p. 26-28, doi: 10.1306/74D70C3B-2B21-11D7-8648000102C1865D.
- Tribble, J.S., Mackenzie, F.T., and Urmos, J., 1991, Physical property changes accompanying deep burial of clay-rich sediments, Barbados convergent margin, *in* Bennett, R.H., Bryant, W.R., and Hulbert, M.H. eds., *Microstructure of Fine-Grained Sediments: From Mud To Shale*, *Frontiers in Sedimentary Geology*, Springer-Verlag, New York, p. 93-99.
- Tucker, M.E., 1981, *Sedimentary Petrology: an Introduction*: Blackwell Science Ltd., Oxford, United Kingdom.
- Tumarkina, E., Misra, S., Burlini, L., and Connolly, J.A.D., 2011, An experimental study of the role of shear deformation on partial melting of a synthetic metapelite: *Tectonophysics*, v. 503, no. 1-2, p. 92-99, doi: 10.1016/j.tecto.2010.12.004.
- Turner, F.J., Griggs, D.T., and Heard, H., 1954, Experimental deformation of calcite crystals: *Geological Society of America Bulletin*, v. 65, no. 9, p. 883-934, doi: 10.1130/0016-7606(1954)65[883:EDOCC]2.0.CO;2.
- Ungerer, P., Burrus, J., Doligez, B., Chenet, P.Y., and Bessis, F., 1990, Basin evaluation by integrated two-dimensional modeling of heat transfer, fluid flow, hydrocarbon generation, and migration: *American Association of Petroleum Geologists Bulletin*, v. 74, no. 3, p. 309-335.
- Vajdova, V., Baud, P., and Wong, T.-fong, 2004, Compaction, dilatancy, and failure in porous carbonate rocks: *Journal of Geophysical Research*, v. 109, doi: 10.1029/2003JB002508.
- Van der Pluijm, B.A., Ho, N.-C., and Peacor, D.R., 1994, High-resolution X-ray texture goniometry: *Journal of Structural Geology*, v. 16, no. 7, p. 1029-1032, doi: 10.1016/0191-8141(94)90084-1.
- Van der Pluijm, B.A., Ho, N.-C., Peacor, D.R., and Merriman, R.J., 1998, Contradictions of slate formation resolved?: *Nature*, v. 392, no. 6674, p. 348.
- Van Diggelen, E.W.E., De Bresser, J.H.P., Peach, C.J., and Spiers, C.J., 2010, High shear strain behaviour of synthetic muscovite fault gouges under hydrothermal conditions: *Journal of Structural Geology*, v. 32, p. 1685-1700, doi: 10.1016/j.jsg.2009.08.020.
- Vasseur, G., Djéran-Maigre, I., Grunberger, D., Rousset, G., Tessier, D., and Velde, B., 1995, Evolution of structural and physical parameters of clays during experimental compaction: *Marine and Petroleum Geology*, v. 12, no. 8, p. 941-954, doi: 10.1016/0264-8172(95)98857-2.
- Vassoevich, N.B., 1960, Experiment in constructing typical curve of gravitational compaction of clayey sediments: *Nov. Neft. Tekh. Geol. Ser.*, v. 1960, no. 4, p. 11-15.
- Velde, B., 1996, Compaction trends of clay-rich deep sea sediments: *Marine Geology*, v. 133, p. 193-201, doi: 10.1016/0025-3227(96)00020-5.
- Voltolini, M., Wenk, H.-R., Mondol, N.H., Bjørlykke, K., and Jahren, J., 2009, Anisotropy of experimentally compressed kaolinite-illite-quartz mixtures: *Geophysics*, v. 74, no. 1, p. D13, doi: 10.1190/1.3002557.
- Walker, A.N., Rutter, E.H., and Brodie, K.H., 1990, Experimental study of grain-size sensitive flow of synthetic, hot-pressed calcite rocks, *in* Knipe, R.J. and Rutter, E.H. eds., *Deformation Mechanisms, Rheology and Tectonics*, *Geological Society Special Publications*, Geological Society, London, United Kingdom, p. 259-284.
- Wanless, H.R., 1979, Limestone response to stress: pressure solution and dolomitization: *Journal of Sedimentary Petrology*, v. 49, no. 2, p. 437-462, doi: 10.1306/212F7766-2B24-11D7-8648000102C1865D.
- Warner, D.L., 1964, *An Analysis of the Influence of Physical-Chemical Factors Upon the Consolidation of Fine-Grained Clastic Sediments*: University of California Press, Berkeley (Ca), United States.
- Weertman, J., 1957, Steady-state creep of crystals: *Journal of Applied Physics*, v. 28, no. 10, p. 1185-1189, doi: 10.1063/1.1722604.
- Welch, M.D., and Marshall, W.G., 2001, High-pressure behavior of clinocllore: *American Mineralogist*, v. 86, no. 11-12, p. 1380-1386.
- Weller, J.M., 1959, Compaction of sediments: *American Association of Petroleum Geologists Bulletin*, v. 43, no. 2, p. 273-310.

- Wenk, H.-R., Lonardeli, I., Pehl, J., Devine, J., Prakapenka, V., Shen, G., and Mao, H.-K., 2004, In situ observation of texture development in olivine, ringwoodite, magnesiowüstite and silicate perovskite at high pressure: *Earth and Planetary Science Letters*, v. 226, p. 507-519, doi: 10.1016/j.epsl.2004.07.033.
- Wenk, H.-R., Matthies, S., Donovan, J., and Chateigner, D., 1998, BEARTEX: a Windows-based program system for quantitative texture analysis: *Journal of Applied Crystallography*, v. 31, p. 262-269, doi: 10.1107/S002188989700811X.
- White, W.A., 1949, Atterberg plastic limits of clay minerals: *American Mineralogist*, v. 34, p. 508-512.
- Wilson, J.T., 1966, Did the Atlantic Close and then re-open?: *Nature*, v. 211, p. 676-681, doi: 10.1038/211676a0.
- Wong, T.-F., Baud, P., and Klein, E., 2001, Localized failure modes in a compactant porous rock: *Geophysical Research Letters*, v. 28, no. 13, p. 2521-2524, doi: 10.1029/2001GL012960.
- Wong, T.-F., David, C., and Zhu, W., 1997, The transition from brittle faulting to cataclastic flow in porous sandstones: Mechanical deformation: *Journal of Geophysical Research*, v. 102, p. 3009-3025, doi: 10.1029/96JB03281.
- Wong, T.-F., Szeto, H., and Zhang, J., 1992, Effect of loading path and porosity on the failure mode of porous rocks: *Applied Mechanics Reviews*, v. 45, no. 8, p. 281-293, doi: 10.1115/1.3119759.
- Worden, R.H., Charpentier, D., Fisher, Q.J., and Aplin, A.C., 2005, Fabric development and the smectite to illite transition in Upper Cretaceous mudstones from the North Sea: an image analysis approach, *in* Shaw, R.P. ed., *Understanding the Micro to Macro Behaviour of Rock-Fluid Systems*, Geological Society Special Publication 249, The Geological Society, London, United Kingdom, p. 167.
- Wu, X.Y., Baud, P., and Wong, T.-F., 2000, Micromechanics of compressive failure and spatial evolution of anisotropic damage in Darley Dale sandstone: *International Journal of Rock Mechanics and Mining Sciences*, v. 37, p. 143-160, doi: 10.1016/S1365-1609(99)00093-3.
- Yang, Y., and Aplin, A.C., 2010, A permeability–porosity relationship for mudstones: *Marine and Petroleum Geology*, v. 27, p. 1692-1697, doi: 10.1016/j.marpetgeo.2009.07.001.
- Yang, Y., and Aplin, A.C., 1998, Influence of lithology and compaction on the pore size distribution and modelled permeability of some mudstones from the Norwegian margin: *Marine and Petroleum Geology*, v. 15, p. 163-175, doi: 10.1016/S0264-8172(98)00008-7.
- Yang, Y., and Aplin, A.C., 2007, Permeability and petrophysical properties of 30 natural mudstones: *Journal of Geophysical Research*, v. 112, doi: 10.1029/2005JB004243.
- Yeh, H.-W., and Savin, S.M., 1977, Mechanism of burial metamorphism of argillaceous sediments: 3. O-isotope evidence: *Geological Society of America Bulletin*, v. 88, no. 9, p. 1321, doi: 10.1130/0016-7606(1977)88<1321:MOBMOA>2.0.CO;2.
- Zhang, S., Paterson, M.S., and Cox, S.F., 1994, Porosity and permeability evolution during hot isostatic pressing of calcite aggregates: *Journal of Geophysical Research*, v. 99, p. 15741-15760, doi: 10.1029/94JB00646.
- Zhang, X., Spiers, C.J., and Peach, C.J., 2010, Compaction creep of wet granular calcite by pressure solution at 28°C to 150°C: *Journal of Geophysical Research*, v. 115, doi: 10.1029/2008JB005853.
- Zhang, J., Wong, T.-F., and Davis, D.M., 1990, Micromechanics of pressure-induced grain crushing in porous rocks: *Journal of Geophysical Research*, v. 95, no. B1, p. 341-352, doi: 10.1029/JB095iB01p00341.
- Zhu, W., Evans, B., and Bernabé, Y., 1999, Densification and permeability reduction in hot-pressed calcite: a kinetic model: *Journal of Geophysical Research*, v. 104, p. 25501-25511, doi: 10.1029/1999JB900230.
- Zimmerman, R.W., 1991, *Compressibility of sandstones*: Elsevier Science Publishers, Amsterdam, the Netherlands.

Appendix A

This appendix lists the physical quantities and established constants used in this thesis (Table A1). The list in table A1 is sorted by quantity/constant's first mention of in the thesis.

TABLE A1: LIST OF PHYSICAL QUANTITIES AND ESTABLISHED CONSTANTS

Symbol	Quantity	First mention	Value	Units
F_c	Tectonic compressive forces	ch. 2.1		N
h_{ct}	Depth of confined tension where $\sigma_H = \sigma_v$	ch. 2.1		m
M	Torque	ch. 2.1		Nm
P_c	Confining pressure in confined compression	ch. 2.1		MPa
P_i	Confining pressure in isostatic stress	ch. 2.1		MPa
P_t	Confining pressure in confined torsion	ch. 2.1		MPa
r	Radius of cylindrical sample	ch. 2.1		mm
σ	Stress scalar	ch. 2.1		MPa
σ_1	Maximum principal stress	ch. 2.1		MPa
σ_2	Intermediate principal stress	ch. 2.1		MPa
σ_3	Minimum principal stress	ch. 2.1		MPa
σ_H	Sum of horizontal stresses	ch. 2.1		MPa
σ_{ij}	Stress tensor with $i, j = 1, 2$ or 3	ch. 2.1		MPa
σ_t	Sub-horizontal tectonic stress	ch. 2.1		MPa
σ_t^*	Critical horizontal tectonic stress	ch. 2.1		MPa
τ	Shear stress	ch. 2.1		MPa
g	Acceleration due to gravity	eq. 2.1	9.81	$m\ s^{-2}$
h	Depth of base of sediments	eq. 2.1		m
h_w	Depth of base of water level	eq. 2.1		m
p_l	Lithostatic pressure	eq. 2.1		MPa
z	Depth below sea level	eq. 2.1		m
ρ_b	Bulk density of overlying sediments	eq. 2.1		$g\ cm^{-3}$ or $kg\ m^{-3}$
ρ_{sea}	Density of seawater	eq. 2.1		$g\ cm^{-3}$ or $kg\ m^{-3}$
ν	Poisson ratio	eq. 2.2	material constant	-
σ_h	Gravity load induced horizontal stress	eq. 2.2		MPa
σ_v	Vertical stress	eq. 2.2		MPa
P_p	Pore pressure	eq. 2.3		MPa
σ'	Effective stress	eq. 2.3		MPa
σ_n	Normal stress	eq. 2.3		MPa
P_{eff}	Effective pressure	eq. 2.4		MPa
σ_{ii}	Diagonal components of stress tensor with $i = 1, 2$ or 3	eq. 2.4B		MPa
σ'_{ii}	Diagonal components of effective stress tensor	eq. 2.4B		MPa
LL	Atterberg liquid limit	ch. 2.2		%
PI	Atterberg plasticity index	ch. 2.2		%
PL	Atterberg plastic limit	ch. 2.2		%
e	Void ratio	eq. 2.5		-
V_b	Bulk volume	eq. 2.5		cm^3
V_g	Grain volume	eq. 2.5		cm^3
V_p	Pore volume	eq. 2.5		cm^3
ϕ	Porosity	eq. 2.5		%
e_{100}	Void ratio at 100 kPa	eq. 2.6A		-
e_{1000}	Void ratio at 1000 kPa	eq. 2.6A		-
I_v	Void index	eq. 2.6A		%
C_c	Intrinsic compression index	eq. 2.6B		-
P^*	Transition point from linear to non-linear compaction	ch. 2.3		MPa
P^{**}	Inflection point in type 4 isostatic stress compaction	ch. 2.3		MPa
σ_{diff}	Differential stress ($\sigma_1 - \sigma_3$)	ch. 2.3		MPa

KI	Kübler index for illite crystallinity	ch. 2.5	°
H	Applied magnetic field	ch. 2.6	A/m or mT
k	magnetic susceptibility	ch. 2.6	S.I.
k ₁	Maximum principal axes k _{ij}	ch. 2.6	S.I.
k ₂	Intermediate principal axes k _{ij}	ch. 2.6	S.I.
k ₃	Minimum principal axes k _{ij}	ch. 2.6	S.I.
M	Magnetization	ch. 2.6	A/m
M _{ind}	Induced magnetization	ch. 2.6	A/m
M _{rem}	Remanent magnetization	ch. 2.6	A/m
M _s	Magnetization value at saturation	ch. 2.6	A/m
H _j	Applied magnetic field vector	eq. 2.7	A/m or mT
k _{ij}	Magnetic susceptibility tensor	eq. 2.7	SI
M _i	Magnetization vector	eq. 2.7	A/m
P _{max}	Maximum pressure	ch. 3.2	MPa
T _{max}	Maximum temperature	ch. 3.2	°C
ν	Sample twist rate	ch. 3.3	rev s ⁻¹
D	Load cell internal position	eq. 3.1A	mm
D ₀	Load cell internal position at “touch point”	eq. 3.1A	mm
L	Sample length	eq. 3.1A	m
l	Initial sample length	eq. 3.1A	m
ε _{tot}	Total axial strain	eq. 3.1B	%
A	Sample cross section area	eq. 3.2A	m ²
F ₀	Internal force at “touch point”	eq. 3.2A	kN
F _i	Internal force	eq. 3.2A	kN
S	Sample strength	eq. 3.2A	MPa
A ₀	sample cross section area at onset of experiment	eq. 3.2B	m ²
A _f	sample cross section area at end of experiment	eq. 3.2B	m ²
t	Absolute time during experiment	eq. 3.2B	s
t ₀	Absolute time at start of experiment	eq. 3.2B	s
t _f	Absolute time at end of experiment	eq. 3.2B	s
d	Initial sample diameter	eq. 3.3	m
n	Stress exponent	eq. 3.3	-
π	Pi	eq. 3.3	material constant 3.14159etc
ν	Rotary motor speed	eq. 3.4	RPM
γ	Shear strain	eq. 3.4	-
γ̇	Shear strain rate	eq. 3.4	s ⁻¹
ψ	Shear angle	eq. 3.5	rad
θ	XRD incident angle	ch. 3.4	°
m	Mass	ch. 3.5	g
φ _c	Connected porosity	eq. 3.6	%
R	Sample cut distance from axis	ch. 3.6	mm
R'	Sample cut distance from periphery	ch. 3.6	mm
Δk	k ₁ – k ₃	ch. 3.7	SI
H _c / H _c '	Coercivity (ascending/descending)	ch. 3.7	mT
H _{cr}	Remanent coercivity	ch. 3.7	mT
k _i	Principal axes k _{ij}	ch. 3.7	S.I.
K _M	Hysteresis initial slope	ch. 3.7	
K _m	Bulk magnetic susceptibility	ch. 3.7	S.I.
M _r	Measured remanent magnetization	ch. 3.7	A/m
ΔM	Hysteresis loop magnetization difference	ch. 3.7	A/m
η _i	Natural logarithms of k _i	ch. 3.7	
P	Standard measure for anisotropy of k _{ij}	eq. 3.7A	-
P _j	Extended measure for anisotropy of k _{ij}	eq. 3.7A	-
η	Average of η _i	eq. 3.7B	- or S.I.

η_1	Natural logarithm of k_1	eq. 3.7B	- or S.I.
η_2	Natural logarithm of k_2	eq. 3.7B	- or S.I.
η_3	Natural logarithm of k_3	eq. 3.7B	- or S.I.
λ	Grain aspect ratio (length / width)	ch. 5.3	-
ϵ_{ax}	Finite axial strain	ch. 7.2	%
ϵ_{rd}	Finite radial strain	ch. 7.2	%
μ	Coefficient of friction	ch. 9.4	-

Appendix B

This appendix lists the working conditions of compaction stage 3b experiments in the Paterson apparatus (Table 1). Experiments are sorted in groups, temperature and total axial strain. Group codes reflect compaction stage 3b operation conditions other than those mentioned in the table already: (C) = confined compression, (I) = isostatic stress, (IP) = isostatic stress and applied pore pressure, (M) = confined compression with suspected partial melting, (P) = confined compression and applied pore pressure, (T) = confined torsion. Assembly codes refer to the jacket material and drained (open) or undrained (closed) sample conditions. Strain rate values are those imposed on the sample calculated using motor speed, and are slightly higher than strain rate values measured from rate of internal position change. Three room-temperature tests were performed in isostatic stress mode to verify the effect of sample pressurization on sample.

Strain rate and strain values for PAT1 (T) tests are in fact shear strain rate and shear strain. The sample in experiment P1212 was re-jacketed and compacted further in experiment P1216.

TABLE B1: LIST OF COMPACTION STAGE 3B EXPERIMENTS

Experiment	Group	Length (mm)	Diameter (mm)	Assembly	Temperature (°C)	P _c (MPa)	P _p (MPa)	Duration (min)	Strain rate (s ⁻¹)	Total axial strain (%)
P1307	PAT1 (C)	12.47	14.87	Fe-closed	500	300	-	181	1 x 10 ⁻⁵	6.9%
P1282	PAT1 (C)	14.77	14.86	Cu-closed	500	300	-	2	1 x 10 ⁻³	7.5%
P1284	PAT1 (C)	12.52	14.86	Cu-closed	500	300	-	190	1 x 10 ⁻⁵	8.1%
P1242	PAT1 (C)	15.03	14.9	Cu-closed	500	300	-	20	1 x 10 ⁻⁴	8.3%
P1331	PAT1 (C)	7.1	9.84	Fe-closed	500	300	-	377	7 x 10 ⁻⁶	10.4%
P1313	PAT1 (C)	7.49	9.89	Fe-closed	500	300	-	263	1 x 10 ⁻⁵	11.0%
P1336 ¹	PAT1 (C)	19.14	9.8	Fe-closed	500	300	-	245	1 x 10 ⁻⁵	12.3%
P1336a	PAT1 (C)	6.52	9.8	Fe-closed	500	300	-	245	1 x 10 ⁻⁵	12.3%
P1336b	PAT1 (C)	6.88	9.86	Fe-closed	500	300	-	245	1 x 10 ⁻⁵	12.3%
P1336c	PAT1 (C)	5.74	9.86	Fe-closed	500	300	-	245	1 x 10 ⁻⁵	12.3%
P1337	PAT1 (C)	8.28	9.88	Fe-closed	500	300	-	35	1 x 10 ⁻⁴	13.9%
P1472	PAT1 (C)	18.67	9.86	Fe-closed	650	300	-	224	1 x 10 ⁻⁵	12.6%
P1332	PAT1 (C)	6.78	9.83	Fe-closed	650	300	-	320	1 x 10 ⁻⁵	13.1%
P1243	PAT1 (C)	11.64	14.93	Cu-closed	700	300	-	22	1 x 10 ⁻⁴	8.2%
P1306	PAT1 (C)	10.99	14.81	Fe-closed	700	240	-	2	1 x 10 ⁻³	8.3%
P1330	PAT1 (C)	6.83	9.85	Fe-closed	700	300	-	25	1 x 10 ⁻⁴	10.8%
P1328	PAT1 (C)	9.5	9.9	Fe-closed	700	300	-	178	2 x 10 ⁻⁵	11.6%
P1305	PAT1 (C)	10.9	14.85	Fe-closed	700	300	-	30	1 x 10 ⁻⁴	13.1%
P1339	PAT1 (C)	7	9.9	Fe-open	700	300	-	311	1 x 10 ⁻⁵	13.3%
P1304	PAT1 (C)	11.4	14.8	Fe-closed	700	300	-	150	2 x 10 ⁻⁵	14.4%
P1346	PAT1 (C)	10.28	9.89	Fe-closed	700	300	-	158	2 x 10 ⁻⁵	14.5%
P1347	PAT1 (C)	11.4	9.95	Fe-closed	700	300	-	199	2 x 10 ⁻⁵	15.8%
P1345	PAT1 (C)	21.1	9.9	Fe-closed	700	300	-	136	Stepping	20.2%
P1317	PAT1 (I)	6.32	9.89	Fe-open	500	300	-	20	-	-
P1302	PAT1 (I)	5.53	9.9	Fe-open	700	300	-	25	-	-
P1312	PAT1 (I)	10.57	14.8	Fe-closed	700	300	-	0	-	-
P1320	PAT1 (I)	5.72	9.95	Fe-closed	700	300	-	600	-	-

P1322	PAT1 (I)	7.16	9.88	Fe-closed	700	300	-	300	-	-
P1354	PAT1 (I)	9.57	9.84	Fe-closed	room	300	-	4056	-	0.6%
P1411	PAT1 (I)	21.95	9.9	Fe-closed	room	320	-	?	-	1.8%
P1476- P1477	PAT1 (I)	10.01	14.62	Fe-closed	room	100	-	?	-	4.0%
P1490	PAT1 (IP)	10.85	9.89	Fe-pore	700	350	20	3	-	-
P1471	PAT1 (M)	14.63	9.91	Fe-closed	750	300	-	218	Stepping	19.5%
P1469	PAT1 (M)	12.15	9.96	Fe-closed	750	300	-	96	Stepping	27.4%
P1487	PAT1 (P)	7.58	9.85	Fe-pore	500	300	50	160	2×10^{-5}	12.8%
P1488	PAT1 (P)	21.95	9.9	Fe-pore	650	300	50	122	2×10^{-5}	12.5%
P1489	PAT1 (P)	6.35	9.86	Fe-pore	700	300	50	167	2×10^{-5}	12.2%
P1211	PAT1 (T)	6.08	9.86	Cu-closed	700	300	-	90	3×10^{-5}	~ 0
P1212+ P1216	PAT1 (T)	5.17	9.88	Cu-closed	700	300	-	78 + 60	3×10^{-5}	0.11 + 0.08

¹ During experiment P1336 the sample was comprised of three pieces, denoted a, b and c.

Appendix C

This appendix lists the compaction-related rock physical properties of synthetic metapelites after their stage 2 or stage 3a compaction in the hot isostatic press (Table C1). Samples are sorted in groups and sample ID. When the sample was further compacted in the Paterson apparatus during stage 3b, the number of the experiment is presented.

TABLE C1: SAMPLE PROPERTIES AFTER COMPACTION STAGES 2 AND 3A

Experiment	Sample ID	Group	Bulk density (g cm ⁻³)	Porosity (%)
P1211	WS_HIP_01	HIP1	2.42 ²	-
P1212	WS_HIP_02 ¹	HIP1	2.42	11 ^b
P1216				
P1242	WS_HIP_03	HIP1	2.4	14.0
P1243	WS_HIP_04	HIP1	2.41	11.8
P1282	WS_HIP_05	HIP1	2.4	13.9
P1284	WS_HIP_06	HIP1	2.4	12.7
P1305	WS_HIP_07	HIP1	2.39	12.4
P1306	WS_HIP_08	HIP1	2.41	11.4
P1304	WS_HIP_09	HIP1	2.39	12.3
P1307	WS_HIP_10	HIP1	2.40	11.8
P1469	WS_HIP_11	HIP1	2.36	15.0
P1490	WS_HIP_11AB	HIP1	2.36	16.3
P1302	WS_HIP_12a	HIP1	-	-
P1339	WS_HIP_12b	HIP1	-	-
P1322	WS_HIP_12c	HIP1	2.38	13.7
P1317	WS_HIP_12d	HIP1	2.40	14.3
P1330	WS_HIP_13a	HIP1	2.43	11.3
P1313	WS_HIP_13b	HIP1	2.42	11.7
P1320	WS_HIP_13c	HIP1	2.39	12.8
	WS_HIP_13d	HIP1	2.38	13.0
P1331	WS_HIP_14a	HIP1	2.41	12.1
P1328	WS_HIP_14b	HIP1	2.37	10.6
P1489	WS_HIP_15a	HIP1	2.38	14.3
P1332	WS_HIP_15b	HIP1	2.37	14.2
P1337	WS_HIPc_16	HIP1	2.39	14.2
P1336	WS_HIP_17a ³	HIP1	2.4	13.7
	WS_HIP_17b ³	HIP1	2.37	13.4
	WS_HIP_17c ³	HIP1	2.38	13.6
P1345	WS_HIPc_18	HIP1	-	-
P1411	WS_HIPc_20 ⁴	HIP1	2.38	13.7
P1488				
P1472	WS_HIPc_21	HIP1	2.37	14.0
P1471	WS_HIPc_22	HIP1	2.39	13.6
P1347	WS_HIPc_23	HIP1	2.41	12.3
P1346	WS_HIPc_24	HIP1	2.36	15.2
P1354	WS_HIPc_25	HIP1	2.40	13.7
-	WS_HIPc_30	HIP1	2.38	13.0
-	WS_HIPc_31	HIP1	2.37	13.6
-	WS_HIPc_32	HIP1	2.38	12.7
-	WS_HIPc_33	HIP1	2.38	12.3
-	WS_HIPc_34	HIP1	2.38	14.3
-	WS_HIPc_35	HIP1	2.38	13.8
P1477	WS_HIPc_X1	HIP1	2.37	13.9

-	RS_01_01	HIP2	2.53	5.8
-	RS_01A	HIP2	2.52	5.3
-	RS_01B	HIP2	2.50	7.4
-	RS_01C	HIP2	2.52	6.1
-	RS_02	HIP2	2.52	4.8
-	RS_02_02	HIP2	2.51	5.0
-	RS_03A	HIP2	2.56	2.2
-	RS_03B	HIP2	2.56	2.7
-	RS_01_01	HIP2	2.53	5.8
-	RS_01A	HIP2	2.52	5.3
-	RS_01B	HIP2	2.50	7.4
-	RS_01C	HIP2	2.52	6.1
-	RS_02	HIP2	2.52	4.8
-	RS_02_02	HIP2	2.51	5.0

¹ re-jacketed sample, affected by first test

² assumed value

³ part of stacked sample

⁴ re-used sample, unaffected by first test

Appendix D

This appendix lists compaction-related rock physical properties of synthetic metapelites after their stage 3b experiments in the Paterson apparatus. Samples are sorted in groups, temperature and total axial strain (Table B1). Group codes reflect compaction stage 3b operation conditions other than those mentioned in the table already: (C) = confined compression, (I) = isostatic stress, (IP) = isostatic stress and applied pore pressure, (M) = confined compression with suspected partial melting, (P) = confined compression and applied pore pressure, (T) = confined torsion.

TABLE D1: SAMPLE PROPERTIES AFTER COMPACTION STAGE 3B EXPERIMENTS

Experiment	Group	Temperature (°C)	Bulk density (g cm ⁻³)	Porosity (%)	Porosity reduction (%)	Finite axial strain (%)	Finite radial strain (%)	Finite volumetric strain (%)
P1307	PAT1 (C)	500	2.48	10.1	1.7	2.8	0.1	2.9
P1282	PAT1 (C)	500	2.5	10.9	3.0	3.9	-0.1	3.6
P1284	PAT1 (C)	500	2.49	9.6	3.1	3.5	0.0	3.5
P1242	PAT1 (C)	500	2.5	11.6	2.4	3.9	0.0	3.9
P1331	PAT1 (C)	500	2.47	10.7	1.5	4.4	-0.8	2.8
P1313	PAT1 (C)	500	2.44	10.4	1.3	3.3	-1.2	1.1
P1336	PAT1 (C)	500	2.4	17.2	-3.4	9.8	-4.8	1.0
P1336	PAT1 (C)	500	2.38	17.1	-3.7	7.4	-3.1	1.5
P1336	PAT1 (C)	500	2.39	16.8	-3.2	7.1	-3.2	1.0
P1337	PAT1 (C)	500	2.36	16.9	-2.7	6.5	-3.7	-0.6
P1472	PAT1 (C)	650	2.56	8.5	5.5	10.2	-1.4	7.6
P1332	PAT1 (C)	650	2.50	8.5	5.6	7.1	-0.8	5.6
P1243	PAT1 (C)	700	2.52	4.8	7.0	3.5	0.5	4.4
P1306	PAT1 (C)	700	2.58	5.6	5.7	6.8	0.1	7.0
P1330	PAT1 (C)	700	2.65	1.1	10.2	7.8	0.4	8.5
P1328	PAT1 (C)	700	2.66	3.9	6.8	10.9	0.0	10.9
P1305	PAT1 (C)	700	2.66	1.5	10.9	10.4	0.3	1.0
P1339	PAT1 (C)	700	2.4	9.5	3.7 ^c	2.7	-0.6	1.5
P1304	PAT1 (C)	700	2.76 ^b	0.0 ^a	12.3	11.4	1.4	13.8
P1346	PAT1 (C)	700	2.55	8.2	7.0	10.0	-1.1	8.0
P1347	PAT1 (C)	700	2.68	2.8	9.4	16.2	-3.5	10.2
P1345	PAT1 (C)	700		5.0 ^c	7.5	22.7	-9.1	8.1
P1317	PAT1 (I)	500	2.41	12.0	2.4	0.3	0.3	0.9
P1302	PAT1 (I)	700	2.44	11.3 ^c	2.0	1.6	0.7	3.0
P1312	PAT1 (I)	700	2.46	9.0	4.3	2.9	0.8	4.5
P1320	PAT1 (I)	700	2.62	4.5	8.4	3.8	2.8	9.2
P1322	PAT1 (I)	700	2.7	5.6	8.1	6.3	2.8	11.5
P1354	PAT1 (I)	room	2.39	16.1	-2.4	0.0	-0.1	-0.2
P1411	PAT1 (I)	room	2.39	14.4 ^c	-0.7 ^c	-0.1	0.1	0.1
P1476+P 1477	PAT1 (I)	room	2.35	15.2	-1.3	0.0	-0.2	-0.4
P1490	PAT1 (IP)	700	2.45	11.8	4.5	2.5	0.6	3.7
P1490	PAT1 (IP)	700	2.40	11.7	4.6	1.6	0.7	3.0
P1490	PAT1 (IP)	700	2.42	12.8	3.5	2.6	0.5	3.6
P1471	PAT1 (M)	750	2.68	4.1	9.5	19.7	-4.9	11.5
P1469	PAT1 (M)	750	2.67	5.1	9.9	20.2	-5.4	11.3

P1487	PAT1 (P)	500	2.35	14.3	-0.6	4.4	-2.5	-0.6
P1488	PAT1 (P)	650	2.52	8.8	4.9	11.1	-2.6	6.3
P1489	PAT1 (P)	700	2.48	8.7	5.6	7.1	-1.3	4.6
P1211	PAT1 (T)	700	2.47	11.0	2.2 ^c	1.2	0.9	2.9
P1212+P 1216	PAT1 (T)	700	2.67	3.8	7.2	7.9	1.5	10.7

^a measurements yielded negative value for porosity. Data not included in figure 7.1

^b unrealistic value for density

^c assumed value

Appendix E

This appendix lists the water content of synthetic metapelites and Maplewood Shale, measured by Karl-Fischer-Titration (KFT) technique (Table E1). Samples are sorted in groups, temperature and duration. Group codes reflect compaction history (Table 3.1). For Paterson apparatus experiments in compaction stage 3b, (C) = confined compression, (I) = isostatic stress, (M) = confined compression with suspected partial melting, (P) = confined compression and applied pore pressure, (T) = confined torsion. Data is summarized and graphically represented in figure 7.8AB.

TABLE E1: KFT WATER CONTENT DATA

Sample ID	Group	Experiment	Temperature (°C)	Drainage	Duration (hrs)	Average water content (wt. %)
R07a	NAT					3.79
R07b	NAT					4.04
R39	NAT					3.41
R05	HIP1		590	Closed	24	2.56
R11	HIP1		590	Closed	24	2.85
R06	HIP1		590	Closed	24	2.65
RS	HIP2		480	Closed	15	2.71
R03	PAT1 (C)	P1282	500	Closed	< 0.1	2.56
R01	PAT1 (C)	P1242	500	Closed	0.3	2.61
R27	PAT1 (C)	P1337	500	Closed	2.6	2.34
R14	PAT1 (C)	P1307	500	Closed	3.0	2.62
R04	PAT1 (C)	P1284	500	Closed	3.2	2.39
R24	PAT1 (C)	P1336	500	Closed	4.1	2.34
R25	PAT1 (C)	P1336	500	Closed	4.1	2.48
R26	PAT1 (C)	P1336	500	Closed	4.1	2.19
R16	PAT1 (C)	P1313	500	Closed	4.4	2.54
R22	PAT1 (C)	P1331	500	Closed	6.3	2.07
R38	PAT1 (C)	P1472	650	Closed	3.7	2.22
R23	PAT1 (C)	P1332	650	Closed	5.3	1.98
R12	PAT1 (C)	P1306	700	Closed	< 0.1	2.53
R02	PAT1 (C)	P1243	700	Closed	0.4	2.17
R21	PAT1 (C)	P1330	700	Closed	0.4	2.13
R09	PAT1 (C)	P1305	700	Closed	0.5	2.68
R29	PAT1 (C)	P1345	700	Closed	2.3	2.05
R13	PAT1 (C)	P1304	700	Closed	2.5	2.56
R30	PAT1 (C)	P1346	700	Closed	2.6	1.72
R20	PAT1 (C)	P1328	700	Closed	3.0	2.33
R31	PAT1 (C)	P1347	700	Closed	3.3	2.31
R28	PAT1 (C)	P1339	700	Open	5.2	0.64
R17	PAT1 (I)	P1317	500	Open	0.3	2.83
R10	PAT1 (I)	P1302	700	Open	0.4	1.88
R15	PAT1 (I)	P1312	700	Closed	0.3	2.31
R19	PAT1 (I)	P1322	700	Closed	5.0	2.31
R18	PAT1 (I)	P1320	700	Closed	10.0	2.40
R35	PAT1 (M)	P1469	750	Closed	1.6	2.23
R33	PAT1 (M)	P1471	750	Closed	3.6	1.87

R36	PAT1 (P)	P1487	500	Closed	2.7	2.44
R37	PAT1 (P)	P1488	650	Closed	2.0	2.15
R34	PAT1 (P)	P1489	700	Closed	2.8	1.85
R32	PAT1 (T)	P1211	700	Closed	1.5	1.69

Acknowledgements

It is hard to believe that after nearly 4 years of living, working and experiencing the PhD-life, it has come to an end. They say that all things good and bad end sometime. I guess now it is time to finish the Zurich chapter of my life. When I look back to the past years in Switzerland, I look back feeling proud of what I could accomplish, learn and overcome in this time. A whole new world opened up for me when I met people from all continents, hiked in the majestic Swiss Alps, skied on the snow-covered valley plains and biked through the forests and farmland of the Swiss countryside. I am grateful to all people that helped me accomplish this. The list of people is too great to mention everyone, but there are some people that deserve my gratitude more than anyone. First, I would like to thank Luigi and Jean-Pierre for giving me the chance to do a PhD with them in the Rock Deformation Laboratory, and allowing me to learn from my mistakes. It has been almost two years since Luigi passed away, but no day goes by without thinking of how wonderful a person he was, not only as lab manager and supervisor, but also as family man and friend of everyone. He showed me his vision of the world and people; a vision I admire and will always keep in mind. The PhD life, and especially the one in a busy and crowded lab such as the rock deformation lab, is full of social events and interactions, most of them memorable, some of them forgettable. I would like to thank the students, post-docs and staff at ETH for sharing their world with me. This applies foremost to my rock def lab colleagues Barbara, Liza, Sebastien, Santanu, Claudio and Alba, my office mates Vangelis and Daniel, but especially to my close friends Bjarne, Nicola, Marilu, Luca, Jara, Mattia, Michaela and Sifra. Without you guys and girls my life would not have been the same. Thank you all, you are the best!

That said the work of few people and institutes deserve proper acknowledgement. I thank Robert and Reto for their essential technical support in the lab. Your magical fingers and impressive machines saved my project at least a couple of times. I am furthermore grateful to the doctoral examination committee, comprised of Prof. Jean-Pierre Burg, Dr. Phil Benson and Dr. Dan Faulkner, for their efforts in reviewing my thesis and providing valuable suggestions for improvements. I can say with certainty that I've learned a great deal thanks to your efforts to support me in whatever way. To conclude I would like to thank the Institute of Geochemistry and Petrology for teaching me the use of and allowing me to run some of their machines, Karsten Kunze of the Electron Microscopy Center for teaching me how to operate the SEM and for providing scientific suggestions, Frowin Pirovino of the Geological Institute for always preparing excellent quality thin sections and polished rock slices, Christian Mensing of the Laboratory of Inorganic Chemistry for performing the TG analyses, Lydia Zehnder of the Institute of Geochemistry and Petrology for performing the XRF analyses, Prof. Ann Hirt of the Institute of Geophysics for letting me use the sensitive equipment in her Laboratory of Natural Magnetism, and Jan Pleuger, Daniel Egli and Michaela Erni for translating the abstract into

German. Last but not least many thanks go out to Regula and Ingrid. Their work on the often underappreciated duty of administration kept me out of the blue on many occasions.